THE UNIVERSITY OF HULL

Applications of Laser Generated Ultrasound using an Interferometric Sensor

being a Thesis submitted for the Degree of

Doctor of Philosophy

in the University of Hull

by

Andrew Duncan William McKie, B.Sc. (Hull)

December 1987

SUMMARY

Summary of Thesis Submitted for PhD Degree

by Andrew Duncan William McKie

on

Applications of Laser Generated Ultrasound using an Interferometric Sensor

To compliment non-contacting ultrasonic generation using lasers, it is ideal to have a remote, non-contacting detector. An interferometer, based on the Michelson design, has been constructed for the purpose of this thesis, enabling laser generated ultrasonic displacements of the order of 25 pm to be resolved. The design and operation of this device is described fully, and its performance compared with two other non-contacting devices, namely a capacitance transducer and an electromagnetic acoustic transducer (EMAT), and a contacting piezoelectric probe. Experimentally observed waveforms, from laser generation of ultrasound in both the thermoelastic and plasma regimes, are shown to be in excellent agreement with wave propagation theory.

The depth estimation of surface breaking defects by the detection of Rayleigh surface waves, generated in both the thermoelastic and plasma regimes, is described, and an empirical formula is given which is valid for narrow slots of < 0.3 mm width. The experimentally determined mechanism for the interaction of Rayleigh waves with slots is also compared with a theoretical computer model.

The measurement of ultrasonic velocity at elevated temperatures has been investigated in a number of materials, namely dural, aluminium, stainless steel, iron and graphite. Data is presented for non-contact ultrasonic detection at temperatures of up to 1000 degrees centigrade in iron and stainless steel.

Finally, the measurement of the thickness of thin metal sheets is investigated using both a pulse-echo technique, and Lamb waves.

To my parents

Acknowledgements

My thanks must go to my supervisors Dr. R. J. Dewhurst, and Prof. S. B. Palmer for their constant support and friendship throughout the work of this thesis. I would also like to thank my friends and colleagues for useful discussions and collaborative work. Thanks are also due to Mr. J. Lawrence for technical assistance and Mr. H. Pashby, and other members of the mechanical workshop staff for their help and cooperation in the building of the interferometer, and subsequent manufacture of numerous test samples. I would also like to thank Dr. C. B. Scruby, Mr. B. C. Moss, and Dr. L. E. Drain of AERE Harwell for support and advice on designing the interferometer.

Last but by no means least, my special thanks go to Sue for her help, encouragement, and for "being there" over the last 4 years.

CONTENTS

CHAPTER 1

Introduction

Examination of the structural integrity and quality of a manufactured product, without destroying or damaging it in the process, forms the basis for a technique known as nondestructive evaluation (NDE). Early NDE techniques included methods such as visual inspection, physical measurement, and analysis of sound produced by tapping. For example, large internal defects may be detected in castings by the change in ringing note when the specimen is struck with a hammer. In recent years these practices have been supplemented by techniques such as eddy current testing, electrical resistivity measurements, magnetic particle inspection and X-ray techniques. Certainly the nuclear industry, with its necessity for high specification materials for safety requirements, has highlighted the need for reliable NDE techniques. Additionally, in other industries the role of NDE is now being fully recognised for its contribution to producing quality components at reduced cost, and with high productivity.

Ultrasound, has now probably superceded many of these techniques in research and become one of the most widely used safe energy beams available for the inspection and characterisation of engineering materials. However, the ultrasonic techniques applied today have potential for improvement. Piezoelectric transducers are inexpensive, but it is difficult to commercially produce them to generate a controlled radiation pattern, or a reproducible amplitude and frequency response. Additionally, piezoelectric transducer sensitivities tend to change with time and usage, with an average life expectancy limited to a few months of continuous use.*

* B. G. W. Yee and J. C. Couchman, IEEE Trans. Son. Ultrason. SU-23 299 (1976).

In typical NDE applications, ultrasound is launched into a specimen with a view to detecting its scatter or reflection from internal or surface defects, or other parts of the specimen. For this reason it is usual to employ pulses of ultrasound rather than continuous wave generation. Additionally, in order to resolve signals that may arrive at the detector at comparable times, very short pulses of ultrasound are required if analysis is to be performed in the time domain. The use of laser generated ultrasound satisfies both of these requirements.

In chapter 2, the basic physical principles of the laser generation of ultrasound will be summarised. To compliment the non-contact generation of ultrasonic transients, it is ideal to have a remote non-contact detector. Many optical sensors have been developed, each having advantages and disadvantages. The most common and useful techniques will also be reviewed.

For the purpose of this project a stabilised interferometer based on a Michelson design was constructed. The design, operating characteristics and absolute calibration of the interferometer will be described in detail in chapter 3, and its performance along side other ultrasonic detectors will be assessed in chapter 4.

Signal processing systems are not widely used to determine defect dimensions. In many situations only the amplitude of the detected signals is used to indicate the presence of a defect. In chapter 5, the interaction of laser generated Rayleigh pulses wih surface breaking defects, in the form of machined slots, will be investigated, with a view to quantitative depth estimation.

The application of non-contacting laser generation and detection of ultrasound to the measurement of material properties at temperatures up to 1000 ^{0}C will be investigated in chapter 6. Further applications to the

ultrasonic measurement of thin materials using pulse-echo and Lamb wave techniques will be described in chapter 7.

Finally, a summmary of the work covered by the thesis will be presented in chapter 8, including some suggestions for future work.

CHAPTER 2

Laser Generation and Detection of Ultrasound

2.0 Introduction

The use of pulsed laser irradiation for the generation of broadband ultrasonic transients in solids, has been the subject of many papers since the first publication by White in 1963. Reviews on this subject have been published by Scruby et. al. (1982), Birnbaum and White (1984) and most recently by Hutchins (1987), which described the generation mechanisms, and characterised the resultant ultrasonic waveforms. In the first part of this chapter, a brief outline of the fundamental generation mechanisms will be given. The latter half of the chapter will review a number of the techniques for optical sensing of ultrasound which compliment the non-contacting generation, to produce a totally remote system.

There are a number of acoustic modes which may propagate in a solid. In the bulk material, both longitudinal and shear waves can propagate, together with surface waves at the solid boundaries. Ledbetter and Moulder (1979) have demonstrated that the focussing of a Q-switched Nd:GLASS laser pulse onto an aluminium surface producing material ablation resulted in the generation of longitudinal, shear and Rayleigh waves. Other work by Aindow et. al. (1981) showed that these modes could also be generated at lower laser power densities, where no material ablation, and hence no visible surface damage occurred. Two distinct regimes for the generation of ultrasound have been reported. These depend on the incident laser power density and will be described below.

2.1 The Thermoelastic Source

Consider a laser pulse incident on a metal surface. At low laser power densities the incident laser pulse rapidly heats the material causing radial thermal expansion close to the solid surface. In the case of an unconstrained surface, forces acting in a direction normal to the surface are small. The result is a source which is dominated by horizontal force dipoles which exists close to the surface (fig. (2.1a)), with a small vertical force dipole (Dewhurst et. al., 1982). This source has a step-like or Heaviside time dependence and is known as the thermoelastic source.

2.2 The Plasma Source

In the thermoelastic regime, the surface temperature increases linearly with incident laser power density. As the laser power density is increased, either by increasing the energy per pulse, or by focussing a constant energy onto a smaller surface area, the temperature of the material surface rises until its melting point is reached. At higher incident power densities, the surface temperature reaches the boiling point of the material, and material is "blown off" or ablated from the sample surface. As a consequence of the ablation of material and the high temperatures involved, a plasma is formed at and above the material surface. This results in a normal recoil force at the sample surface (fig. (2.1b))*. There exists a range of laser power densities from which plasma generation occurs. As the laser power density is increased from a level producing a "weak" plasma to that generating a "strong" plasma, the normal force due to ablation becomes increasingly dominant. The normal force component varies temporally with power density, becoming more

* (Scruby et. al., 1982)

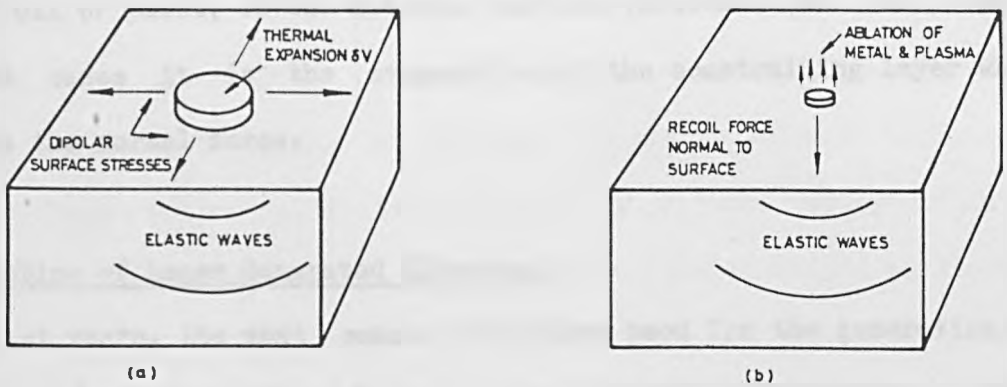

Fig. (2.1) (a) In the thermoelastic regime a temperature rise cause thermal expansion at the material surface. Th thermoelastic source can be approximated by dipole stresses in the surface.

(b) At high power densities in the plasma regime the ris in temperature is so large that material is ablate from the surface. There is now a recoil force norma to the surface.

asymmetric with increasing power density. At sufficiently high laser power densities, the time dependence of the force approaches that of the Heaviside function (Dewhurst et. al., 1982). However these high laser power densities inevitably lead to damage of the material surface.

However, a normal force, having a delta-like time dependence, similar to that generated by a weak plasma, can be generated at the sample surface, without causing any material damage. This can be achieved by laser irradiation of the material through a thin coating, such as a layer of oil or paint, on the material surface (Hutchins et. al., 1981). In these cases it is the evaporation of the constraining layer which generates the normal force.

2.3 Detection of Laser Generated Ultrasound

In past years, the most common technique used for the generation and detection of ultrasound was to use a piezoelectric transducer. Since piezoelectric devices are unquestionably sensitive, and relatively inexpensive, one may ask why we need to consider alternative methods of generating and detecting ultrasound. However, piezoelectric transducers have a number of serious limitations which are as follows;

(a) The couplant necessary to transmit the acoustic signal from the sample to the transducer adds an unknown impedance into the signal path. Problems are also associated with non-uniformity in thickness of the couplant. The necessity of using such a couplant also limits ultrasonic detection at elevated temperatures.(see chapter

(b) Most transducers load the sample surface, and distort the signals being measured.

(c) The bandwidth of most transducers is limited (typically < 2 MHz) and the recorded signals are dominated by electrical and

mechanical resonances.

(d) Absolute calibration of the transducer can only be achieved in its operating environment, and it must be recalibrated if it is removed. Thus for most purposes the transducer is a qualitative device.

In 1982 , the processes involved in the laser generation of ultrasonic transients were investigated in a more quantitative manner.* Non-contacting ultrasonic transducers have been developed, with capacitative devices (Scruby and Wadley, 1978, and Aindow et. al., 1987), electro-magnetic acoustic transducers (EMATs) (Frost, 1979), and optical sensors being the most commonly used. Of these techniques, the capacitative pickup is limited to operating of the order of a few microns from the sample surface, with EMATs normally operating at standoff distances of 1 mm or less. Both devices also have limited bandwidths due to the size of their useful active areas. It is thus optical sensing techniques that offer truly remote wideband ultrasonic detection.

Optical techniques have significant advantages which make them a useful addition to the existing range of transducers, both for generation and detection of ultrasound. A number of advantages are listed below;

(a) Optical techniques are truly non-contacting, and the surface motion of the sample is not damped or distorted by the optical sensing beam.

(b) High frequency bandwidths in excess of 50 MHz are easily obtainable.

(c) Automated scanning of a surface with an optical beam is faster than conventional scanning with a transducer.

(d) Measurements can be made at high and low temperatures, or in radioactive environments hostile to conventional transducers.

(e) The sensors can be absolutely calibrated and hence yield

* (Scruby et. al., 1982)

quantitative data.

Obvious disadvantages are the relatively high cost and complexity associated with optical systems, and most techniques require smooth polished sample surfaces for sensitive detection. However, more recently, a number of techniques have been developed for optical ultrasonic detection on rough surfaces as will be mentioned later in this chapter.

There exists a variety of optical sensing techniques developed for the detection of ultrasound and these are described below.

2.4 Optical Sensing of Ultrasound: An Historical Background

2.4.1 Knife-Edge Techniques

The operation of the knife-edge technique has been reviewed by Whitman and Korpel (1969), and more recently by Palmer and Green (1983), so that only the basic principles will be reviewed here.

A schematic diagram showing the principle of operation of the knife-edge technique is shown in fig. (2.2). As the name suggests, a knife-edge obstructs half of a light beam reflected from a polished sample surface, and allows the remainder to be measured at a photodetector. The periodic tilting of the sample surface, caused by the passage of an acoustic wave, modulates the light reflected from the surface, producing amplitude modulation at the detector. A photodetector sensing this light will generate an electric signal at the frequency of the surface wave. This signal contains both phase and amplitude information about the surface wave. It has been found by Whitman and Korpel (1969) that optimum sensitivity is achieved when the incident beam diameter is approximately half the acoustic wavelength.

The knife-edge technique of Adler et. al. (1968) was a simple optical

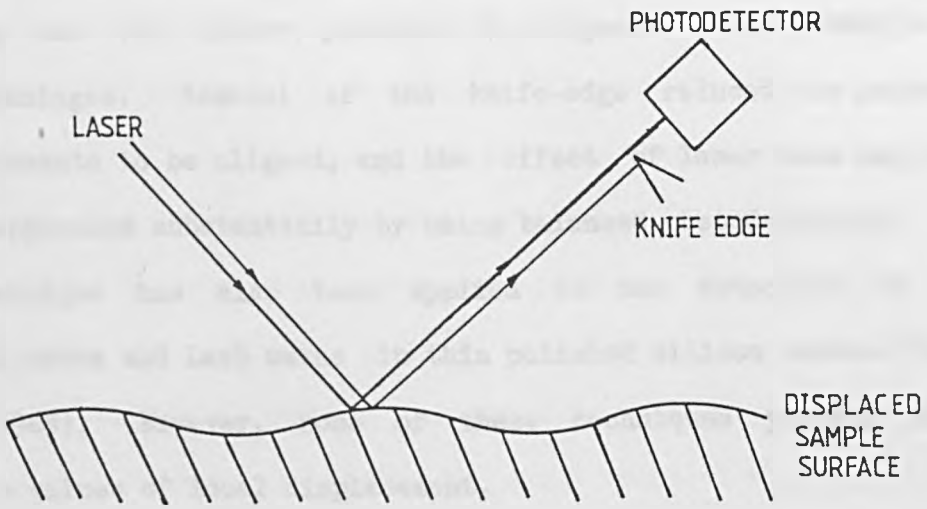

Fig. (2.2) The principle of operation of the knife-edge technique.

technique for the visualisation of Rayleigh surface waves. The technique was devised for the detection of single frequency ultrasonic waves, and as such had excellent sensitivity ($\sim$ 0.1 Angstroms). Experimental pictures clearly showed a variety of surface wave phenomena such as reflection and diffraction. However, the technique will not sense acoustic waves moving in a direction at right angles to the knife-edge.

Engan (1978) has modified the technique by replacing the knife-edge by a double photodiode system, where the difference of the electrical signals from the two diodes yielded the signal. This technique had several advantages. Removal of the knife-edge reduced the number of optical components to be aligned, and the effect of laser beam amplitude noise was suppressed substantially by using balanced photodetectors.

The technique has also been applied to the detection of both longitudinal waves and Lamb waves in thin polished silicon wafers (Sontag and Tam, 1985). However, none of these techniques yielded direct quantitative values of local displacement.

2.5 Interferometric Sensors

Optical interferometers have been used since their invention by Michelson in the 1890's to quantify surface finish and flatness, particularly of optical components. More recently, with the advent of the laser, interest has turned to the sensing of ultrasound.

One of the main problems with interferometrically sensing ultrasound is that naturally occurring environmental disturbances often produce displacements of the order of numbers of fringe shifts in the interferometer. Detection of ultrasonic displacements much smaller than the wavelength of light requires that the interferometer be stabilised so that the instrument sensitivity remains a maximum and constant throughout

a measurement. A number of approaches to overcome this problem have been developed and will be discussed in the following sections.

2.5.1 Differential Interferometer

The differential interferometer technique was developed by Palmer (1973) for the detection of surface waves, and modified (Palmer et. al., 1974) to make bulk measurements in transparent media. The theory and operation of a two beam differential interferometer for measurement of both surface and bulk waves was presented by Palmer et. al. in 1977. A simplified schematic diagram of the simple differential interferometer is given in fig. (2.3). A laser beam was suitably beam expanded and split into two beams. The focussed beams were reflected from a sample surface and superimposed to give an interference pattern. This pattern was spatially filtered with a Ronchi grating, and changes in the filtered optical field monitored with a photodetector. If a surface acoustic wave (SAW) passed under the probe, the light focussed at A travelled a shorter distance (by twice the SAW amplitude) to the grating than did the light focussed at B. The optical fringes shifted across the grating, and caused a corresponding variation in the light transmitted by the grating to the photodetector. The signal produced at the output of the interferometer was proportional to the differential particle displacement at the two detection spots, but insensitive to uniform specimen motion from ambient disturbances. The interferometer was most sensitive to those wavelengths that exhibited the largest phase difference. Hence, for maximum interferometer sensitivity the two detection points were separated by half the wavelength of the acoustic wave to be measured. The varifocal length lens assembly allowed the separation between the detection points to be varied, thus changing the frequency response of

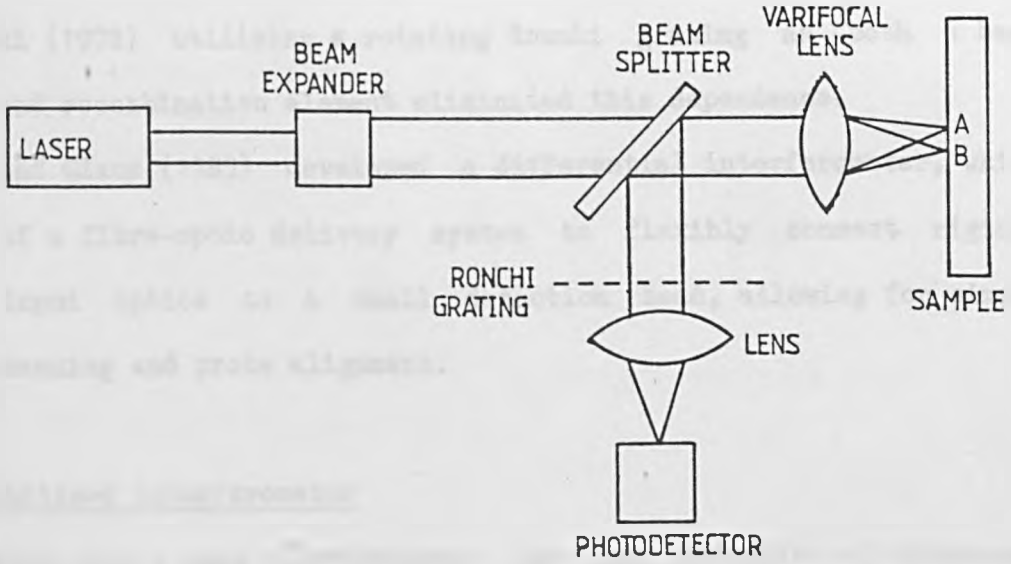

Fig. (2.3) A differential interferometer (after Palmer et. al., 1977).

the interferometer. Quite obviously, this technique was only suitable for continuous ultrasonic wave experiments. The technique does however have applications in the calibration of transducers at particular frequencies.

Since both signal and reference beams were reflected from the same sample surface, they remained parallel regardless of any sample tilt. The interferometer was therefore not as sensitive to surface orientation as the standard Michelson design. However orientation of the Ronchi grating was critical for optimum sensitivity. A technique developed by Jablonowski (1978) utilising a rotating Ronchi grating as both a beam splitter and recombination element eliminated this dependence.

Garg and Claus (1983) developed a differential interferometer, which made use of a fibre-optic delivery system to flexibly connect rigidly mounted input optics to a small detection head, allowing for simple surface scanning and probe alignment.

2.5.2 Stabilised Interferometer

The most widely used interferometer for the detection of ultrasound has been the stabilised interferometer. Most of the systems used are based on a Michelson interferometer. A schematic diagram of the most simple configuration often used is shown in fig. (2.4). Light incident on the photodetector generates a photocurrent having both high and low frequency components. The signal frequencies (i.e. detected ultrasonic signals), typically in the range 10 KHz to 5 MHz are amplified, displayed on an oscilloscope, and stored on a mini-computer for subsequent analysis. The low frequency component of the photocurrent (0 to 5 KHz), which results from room vibrations and other environmental disturbances is used to drive a high voltage amplifier, which provides a piezoelectric element

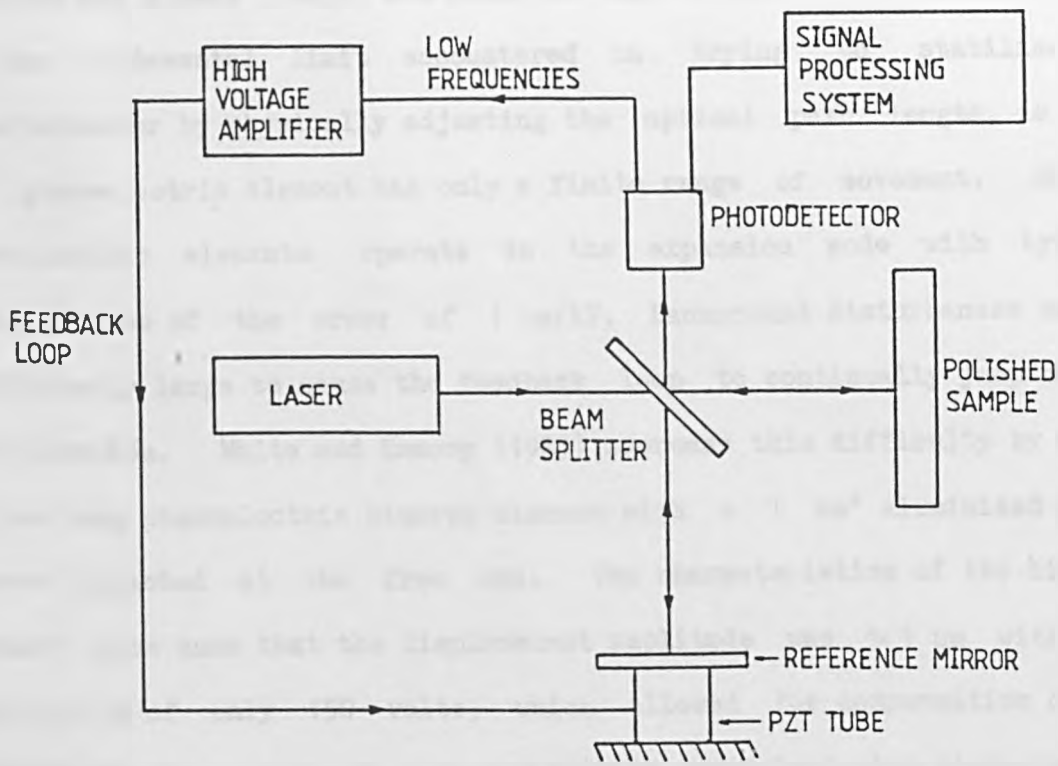

Fig. (2.4) A stabilised Michelson interferometer for measuring ultrasonic displacements.

with a feedback signal to displace the reference mirror, and so maintain the correct phase difference in the two interferometer arms. This technique has been successfully operated by several authors including Bondarenko et. al. (1976), Palmer and Green (1977), Jette et. al. (1977), Hutchins and Nadeau (1983), and Cielo et. al. (1985).

The fundamental limit encountered in trying to stabilise an interferometer by physically adjusting the optical path length, is that the piezoelectric element has only a finite range of movement. Single piezoelectric elements operate in the expansion mode with typical sensitivities of the order of 1 μm/kV. Background disturbances can be sufficiently large to cause the feedback loop to continually jump out of stabilisation. White and Emmony (1985) overcame this difficulty by using a 3 mm long piezoelectric bimorph element with a 1 mm^2 aluminised mylar mirror attached at the free end. The characteristics of the bimorph element were such that the displacement amplitude was $\sim$ 1 μm with the application of only 150 volts, which allowed for compensation over a greater displacement range compared with an equivalent size piezoelectric slab. An alternative approach by Kwaaitaal (1974) made use of a condenser microphone, which had a sensitivity of the order of 100 times that of a piezoelectric slab.

Palmer (1986) developed an in-line stabilised interferometer as shown in fig. (2.5). An expanded collimated laser beam was focussed onto the specimen surface. The beamsplitter ,BS, reflected half the light back to a focus on the reference mirror , M_r . Light reflected from both the specimen and from the reference mirror was recombined at the beamsplitter, where it was directed to a photodetector. With this in-line configuration of the interfering optical paths, the resulting fringe pattern was reasonably stable, without the use of a control system.

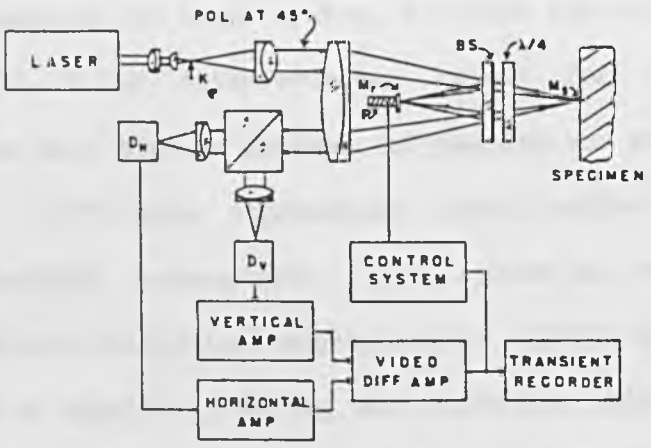

Fig. (2.5) A stabilised in-line interferometer (after Palmer, 1986).

Further stabilisation was implemented, again, by use of a piezoelectric device attached to the reference mirror.

A stabilised in-line system based on the Fizeau interferometer has also been reported by Jette et. al. (1977).

Calder and Wilcox (1980) have used a modified Michelson interferometer, which differed in that the photomultiplier tube was pulsed on just prior to the arrival of an ultrasonic signal, and the recording time was short, so that low frequency disturbances were not a problem. It was not necessary, in their system, to limit the displacement to the linearised portion of the interferometer output for their particular experiments, since only time of arrival information was required.

Drain et. al. (1977) have implemented stabilisation by means of an electro-optic feedback arrangement. The system is, conceptually, very similar to the electro-mechanical piezoelectric system already described. However, instead of physically moving the reference mirror to compensate for low frequency vibrations, this method altered the phase of the light in the reference arm. The optical layout is shown in fig. (2.6). Plane polarised light from a He-Ne laser was passed through a suitably orientated quarter wave plate converting it to circularly polarised light which then entered an electro-optic Kerr cell. About 95% of the light passed unaltered through the cell with the other 5% converted to the reverse circular polarisation which was also shifted in frequency. A further quarter wave plate at the exit of the modulator converted the circular polarisations into two orthogonal linearly polarised beams which were then separated by a polarising cube beamsplitter. Most of the light retained its original vertical polarisation and was incident on the target, with the horizontally polarised frequency shifted light selected as the reference beam of the interferometer. In this mode of operation

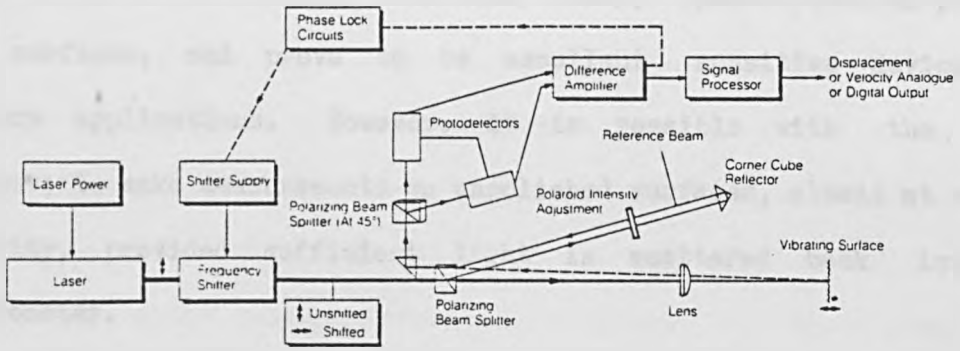

Fig. (2.6) Optical arrangement of a laser interferometer incorporating electro-optic stabilisation (after Drain et. al., 1977).

the Kerr cell controlled the phase of the reference beam, in accordance with a feedback signal from the output of the balanced photodetectors. In this way the phase was "locked" so that the interferometer remained at its most sensitive position in the presence of low frequency vibrations. The feedback was ineffective at high frequencies so that ultrasonic signals were not distorted. However the inclusion of a frequency shifter did increase the cost of the interferometer considerably, and for some cases may not be necessary.

All of the interferometers described above, operate best on polished sample surfaces, and prove to be excellent sensitive devices for laboratory applications. However, it is possible with the above techniques, to make measurements on unpolished surfaces, albeit at reduced sensitivity, provided sufficient light is scattered back into the interferometer.

2.5.3 Swept Path Interferometer

A technique proposed by Mezrich et. al. (1976) was to purposely vary the relative phase difference in the two arms of a Michelson interferometer over at least 180^0, by continually vibrating the reference mirror with a piezoelectric device. The effect was that at sometime during every sweep of the reference mirror, the phase difference was $\pi/2$, regardless of large thermal or mechanical variations, and the interferometer sensitivity was a maximum. An objection to using the technique for detecting short pulses of ultrasound was that the chance of observing the desired ultrasonic pulse, at the instant the interferometer was at its most sensitive position, was small.

2.5.4 Time Delay Interferometer

A schematic diagram of a time delay interferometer is shown in fig. (2.7). Unlike the displacement interferometer of fig. (2.4), here the interferometer does not make use of the sample surface as a mirror, but views the light scattered from it. The beam is then split, and part of it is delayed before being recombined with the undelayed portion of the beam. Extremely high temporal coherence was required, since one of the two interfering beams may be delayed with respect to the other by as much as 10^6 light frequency periods. Thus a single frequency laser is required. Barker and Hollenbach (1972) have used a time delay interferometer based on a wide-angled Michelson interferometer for shock wave research applications, and Kaule (1976) has used a Mach-Zender design for the detection of ultrasound.

The output of the interferometer was maximum for those frequencies whose half oscillation period was the same as the fixed delay. In this way the technique was selective to a certain ultrasonic frequency range, and was insensitive to low frequency ambient disturbances whose half oscillation periods were large compared with the delay time. Unfortunately, the production of an optical bandwidth appropriate to the detection of ultrasound in the megahertz frequency range, leads to long delay path lengths. A bandwidth of 25 MHz requires a time delay of 20 ns or an optical path difference of 6 m, with a bandwidth of 1 MHz requiring a path length difference of 75 m. Clearly even with folded pathlengths these interferometers are very bulky.

A solution which overcame this problem was to use a multiple wave interferometer, such as the Fabry-Perot. A confocal Fabry-Perot interferometer was constructed by Monchalin (1985a) which had the additional advantage of increased light gathering potential, enabling

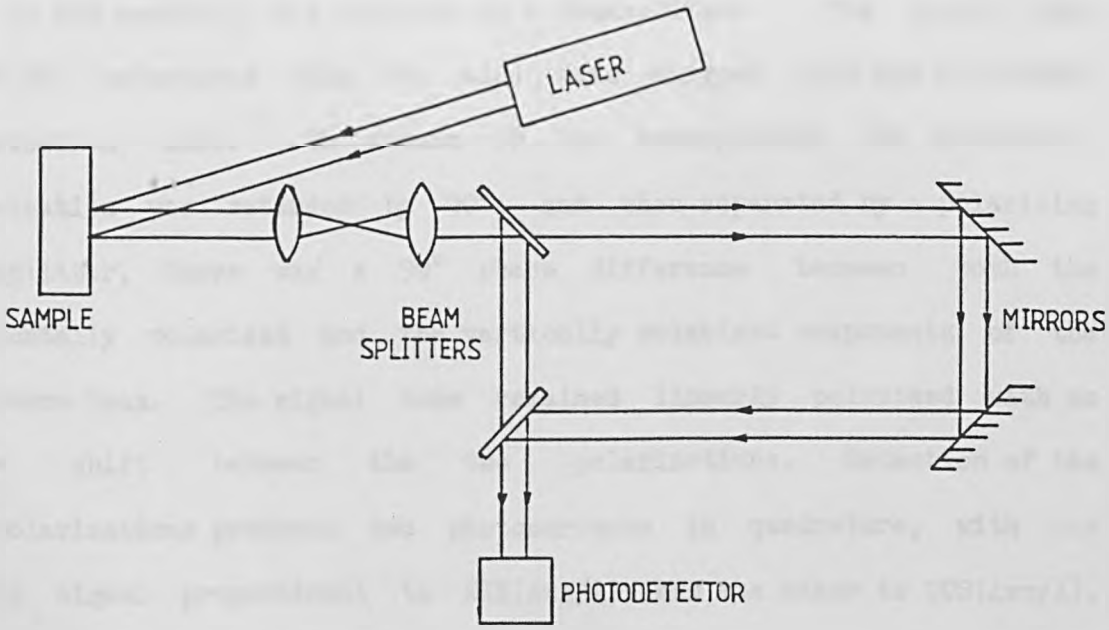

Fig. (2.7) Schematic diagram of a time-delay interferometer.

measurements to be made off machined, rather than polished, surfaces.

2.5.5 Quadrature-Dual Interferometer

A quadrature-dual interferometer, whose output never had a zero in sensitivity, was suggested in 1953 by Peck and Obetz. Fig. (2.8) shows a schematic diagram of the most common configuration as used by Vilkomerson (1976). The output of a 10 mW polarised He-Ne laser was orientated at 45^0 to the vertical, and incident on a beamsplitter. The eighth wave plate was orientated with its slow axis aligned with the horizontal polarisation axis. On return to the beamsplitter the horizontal polarisation was retarded by 90^0, and when separated by a polarising beamsplitter, there was a 90^0 phase difference between both the horizontally polarised and the vertically polarised components of the reference beam. The signal beam remained linearly polarised with no phase shift between the two polarisations. Detection of the two polarisations produced two photocurrents in quadrature, with one output signal proportional to $SIN(4\pi x/\lambda)$ and the other to $COS(4\pi x/\lambda)$. Thus squaring and summing the two signals effectively stabilised the operating point of the interferometer at the high sensitivity point, independent of the large low frequency variations in optical path difference caused by ambient disturbances. The main disadvantage with this technique was that phase information was lost.

A technique proposed by Godfrey and Emmony (1986) has been developed to overcome the problem of directional ambiguity. The operation of a quadrature-dual interferometer necessitates that when the signal from one photodetector is small, the signal in the other is comparitively large. The principle of their modified technique was to select which of the interferometer outputs was most sensitive at a particular instant in time.

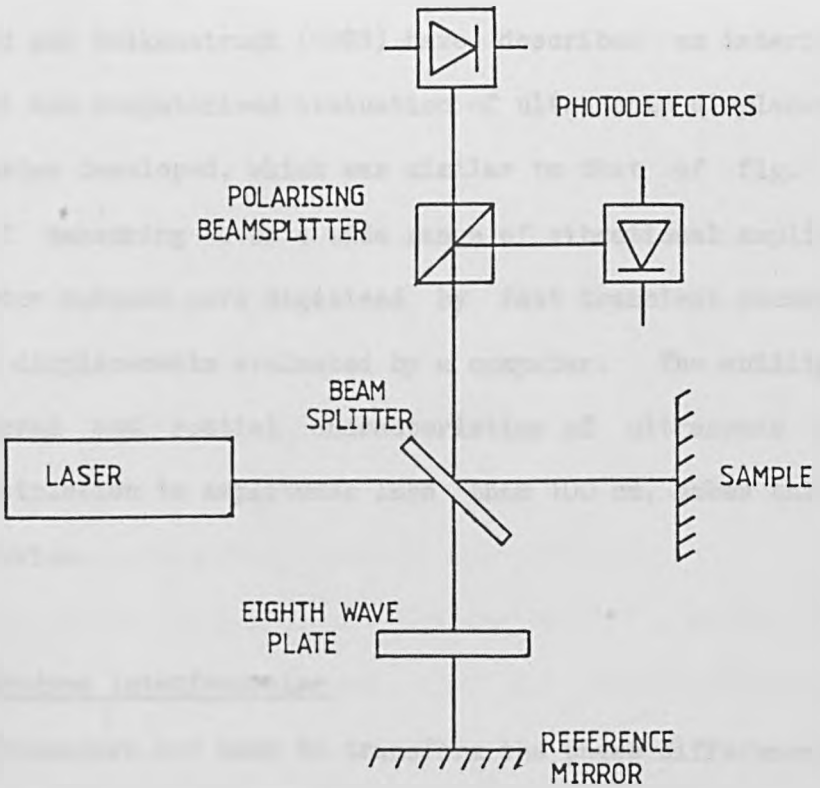

Fig. (2.8) A quadrature-dual interferometer (after Vilkomerson, 1976).

Such an interferometer will again have a sensitivity which is always non-zero, and in addition the single output will yield directional information. Due to the electronic method used to decide which interferometer output should be used, the sensitivity of this interferometer varied slightly as the optical path lengths varied, leading to an error in the calibrated output signal of ± 18%, which for some applications would be acceptable.

Reibold and Molkenstruck (1981) have described an interferometer for measurement and computerised evaluation of ultrasonic displacements. The interferometer developed, which was similar to that of fig. (2.8), was capable of measuring over a wide range of vibrational amplitudes. Both photodetector outputs were digitised by fast transient recorders and the ultrasonic displacements evaluated by a computer. The ability to measure both temporal and spatial characteristics of ultrasonic transducers, without restriction to amplitudes less than 100 nm, makes this instrument a useful device.

2.5.6 Heterodyne Interferometer

Interferometers are used to transform the phase difference between two optical fields into detectable intensity variations. In classical or homodyne interferometry, the two optical fields have identical frequencies. In heterodyne interferometry the two optical frequencies are chosen to differ by a small amount. The superposition then leads to a time dependent intensity, and the interference phase of the two optical fields is transformed into phase modulation of the beat frequency signal (Dandliker, 1981).

Eberhardt and Andrews were the first authors to use a heterodyne system in 1970. Many systems based on the heterodyne interferometer

technique have since been described in the literature, which mainly differ in their optical or electronic processing technique. Generally, a Bragg cell is used to shift the optical frequency in one arm of the interferometer. Fig. (2.9) shows a schematic diagram of the interferometer used by Monchalin (1984, 1985b). The acousto-optic cell was adjusted such that most of the light passed through the cell without any frequency shift or deviation, and was incident on a sample surface. Approximately 10% of the laser intensity was frequency shifted and diffracted for use in the reference arm. Both beams were recombined at a photodetector where the signal included a carrier at the shift frequency which was phase modulated by the sample vibration. Sophisticated processing electronics yielded an output signal proportional to the surface velocity. This interferometer was used for measurement of both in-plane and out of plane components of ultrasonic displacment. Techniques have been reported in which the interferometer output was proportional to surface displacement (Rudd, 1983).

The technique eliminated low frequency drift problems since the beat signal amplitude no longer changed with the phase difference between the two interfering beams, since the beams were continually changing relative phase at a MHz rate.

Paul et. al. (1987) have also used the heterodyne technique, but have used phase conjugation techniques to enable ultrasonic measurements to be made off rough aluminium surfaces. At present the displacement sensitivity is limited to 1 nm, but a more stable optical source and optimisation of the phase conjugation technique will considerably improve the device.

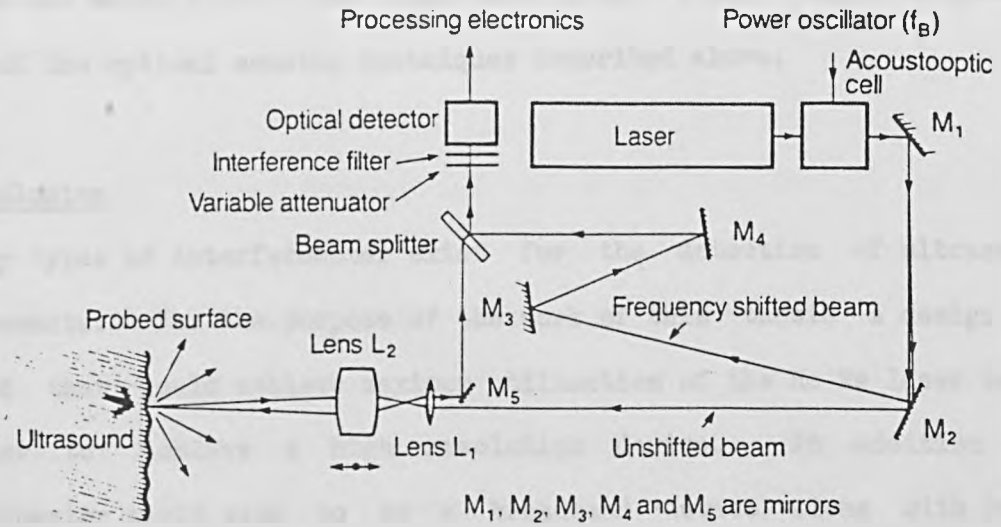

Fig. (2.9) A heterodyne interferometer for the detection of ultrasound (after Monchalin, 1984).

2.5.7 Fibre-Optic Interferometer

The problem of random variations in the optical paths of an interferometer can be significantly reduced by the use of optical fibres in the reference and signal arms, and their placement inside the same cable. This minimises thermal or mechanical variations affecting one of the arms without affecting the other. A review devoted to fibre-optic interferometry has been published by Culshaw (1984).

Several other review papers have been published by Monchalin (1986), Birnbaum and White (1984), and Palmer and Green (1983) which discuss a number of the optical sensing techniques described above.

2.6 Conclusion

Many types of interferometer exist for the detection of ultrasonic displacements. For the purpose of the work of this thesis a design was required that would achieve maximum utilisation of the He-Ne laser used, in order to achieve a high resolution device. In addition the interferometer would need to be a broadband device along with being simplistic in operation, and of a relatively cheap design.
An interferometer based on a Michelson interferometer was built the design and operation of which will be described in the following chapter.

2.7 References

A. M. Aindow, J. A. Cooper, R. J. Dewhurst, and S. B. Palmer, J. Phys. E: Sci. Instrum. 20 204 (1987).

A. M. Aindow, R. J. Dewhurst, D. A. Hutchins and S. B. Palmer, J. Acoust. Soc. Am. 69 449 (1981).

R. Adler, A. Korpel, and P. Desmares, IEEE Trans. Son. Ultrason. SU-15 157 (1968).

L. M. Barker and E. R. Hollenbach, J. Appl. Phys. 43 4669 (1972).

G. Birnbaum and G. S. White, in "Research Techniques in Nondestructive Testing" (Edited by R. S. Sharpe, Academic Press, London) Vol. 7, p.259 (1984).

A. N. Bondarenko, Yu. B. Drobot, and S. V. Kruglov, Sov. J. NDT 12 655 (1976).

C. A. Calder and W. W. Wilcox, Mater. Eval. 38 86 (1980).

P. Cielo, F. Nadeau, and M. Lamontagne, Ultrasonics 23 55 (1985).

B. Culshaw, in "Research Techniques in Nondestructive Testing" (Edited by R. S. Sharpe, Academic Press, London) Vol. 7, p.191 (1984).

R. Dandliker, Laser 81 Opto-Elektronik, Munich 1-4 June, (1981).

R. J. Dewhurst, D. A. Hutchins, S. B. Palmer and C. B. Scruby, J. Appl. Phys. 53 4064 (1982).

L. E. Drain, J. H. Speake, and B. C. Moss, in "Proceedings of the First European Congress on Optics Applied to Metrology", SPIE 136 52 (1977).

F. J. Eberhardt and F. A. Andrews, J. Acoust. Soc. Am. 48 603 (1970).

H. Engan, IEEE Trans. Son. Ultrason. SU-25 372 (1978).

H. M. Frost, in "Physical Acoustics" (Edited by W. P. Mason and R. N. Thurston, Academic Press, New York) Vol. 14, p.179 (1979).

A. O. Garg and R. O. Claus, Mater. Eval. 41 106 (1983).

M. W. Godfrey and D. C. Emmony, in "Review of Progress in Quantitative Nondestructive Evaluation" (Edited by D. O Thompson and D. E. Chimenti, Plenum Press, New York) Vol. 5A, p. 587 (1986).

D. A. Hutchins, in "Physical Acoustics" (Edited by W. P. Mason and R. N. Thurston, Academic Press, London) in press, (1987).

D. A. Hutchins, R. J. Dewhurst, S. B. Palmer and C. B. Scruby, Appl. Phys. Lett. 38 677 (1981).

D. A. Hutchins and F. Nadeau, in "1983 Ultrasonic Symposium of the IEEE" p. 1175 (1983).

D. P. Jablonowski, Appl. Opt. 17 2064 (1978).

A. N. Jette, M. S. Morris, J. C. Murphy and J. G. Parker, Mater. Eval. 35 90 (1977).

W. Kaule, in "Proceedings of the eighth World Conference on Nondestructive Testing" paper 3J5 (1976).

Th. Kwaaitaal, Rev. Sci. Instrum. 45 39 (1974).

H. M. Ledbetter and J. C. Moulder, J. Acoust. Soc. Am. 65 840 (1979).

R. Mezrich, D. Vilkomerson, and K. Etzold, Appl. Opt. 15 1499 (1976).

A. A. Michelson, Phil. Mag. XXX1 338 (1891).

J. -P. Monchalin, Can. J. Soc. Nondest. Test. 6 48 (1984).

J. -P. Monchalin, Appl.Phys. Lett. 47 14 (1985a).

J. -P. Monchalin, Rev. Sci. Instrum. 56 543 (1985b).

J. -P. Monchalin, IEEE Trans. Ultrason. Ferroelec. and Freq. Cont. UFFC-33 485 (1986).

C. H. Palmer, in "Review of Progress in Quantitative Nondestructive Evaluation" (Edited by D. O. Thompson and D. E. Chimenti, Plenum Press, New York) Vol. 5A, p. 651 (1986).

C. H. Palmer, J. Acoust. Soc. Am. 53 948 (1973).

C. H. Palmer, H. M. South, T. H. Mak, Ultrasonics 12 106 (1974).

C. H. Palmer, R. O. Claus, and S. E. Fick, Appl. Opt. 16 1849 (1977).

C. H. Palmer and R. E. Green, Appl. Opt. 16 2333 (1977).

C. H. Palmer and R. E. Green, in "Nondestructive evaluation of Materials" (Edited by J. J. Burke and V. Weiss, Plenum Press, New York) p.347 (1983).

M. Paul, B. Betz and W. Arnold, submitted to Appl. Phys. Lett. (1987).

E. R. Peck, and S. W. Obetz, J. Opt. Soc. Amer. 43 483 (1953).

R. Reibold and W. Molkenstruck, Acustica 49 205 (1981).

M. J. Rudd, in "Review of Progress in Quantitative Nondestructive Evaluation" (Edited by D. O. Thompson and D. E. Chimenti, Plenum Press, New York) p. 1763 (1983).

C. B. Scruby, R. J. Dewhurst, D. A. Hutchins, and S. B. Palmer, in "Research Techniques in Nondestructive Testing" (Edited by R. S. Sharpe, Academic Press, London) Vol. 5, p. 281 (1982).

C. B. Scruby and H. N. G. Wadley, J. Phys. D: Appl. Phys. 11 1487 (1978).

H. Sontag and A. C. Tam, Appl. Phys. Lett. 46 725 (1985).

G. I. Stegeman, IEEE Trans. Son. Ultrason. SU-23 33 (1976).

D. Vilkomerson, Appl. Phys. Lett. 29 183 (1976).

R. G. White and D. C. Emmony, J. Phys. E: Sci. Instrum. 18 658 (1985).

R. L. Whitman and A. Korpel, Appl. Opt. 8 1567 (1969).

R. M. White, J. Appl. Phys. 34 3559 (1963).

CHAPTER 3

A Modified Michelson Interferometer System

3.0 Introduction

In this chapter, the design and construction of a Micheslson interferometer, modified for the absolute measurement of displacements produced by laser generated ultrasonic transients, is discussed. The derivation of the cailbration of the interferometer is given, as well as some important coherence requirements for two beam interferometry. The detection of optical radiation is analysed for an N-type silicon p-i-n photodiode detection system, and the minimum detectable displacement of the interferometer is calculated.

3.1 Description of the Interferometer

A schematic diagram of the interferometer is shown in fig. (3.1a) with a photograph of the actual interferometer built shown in fig. (3.1b). The light source used was a 5 mW output helium-neon (He-Ne) laser (Hughes Corporation 3225H-PC) operating at a wavelength of 632.8 nm. The output from the laser was linearly polarised, with the orientation set at 45^0 to the first polarising beamsplitter.

3.1.1 Amplitude Beamsplitting

Consider light waves that are incident on a half silvered mirror. Part of the wave would be transmitted, and part would be reflected, with both components having lower amplitudes than the original one. i.e. the beam has been amplitude split. If the two separate beams are recombined at a photodetector, interference will result providing the original

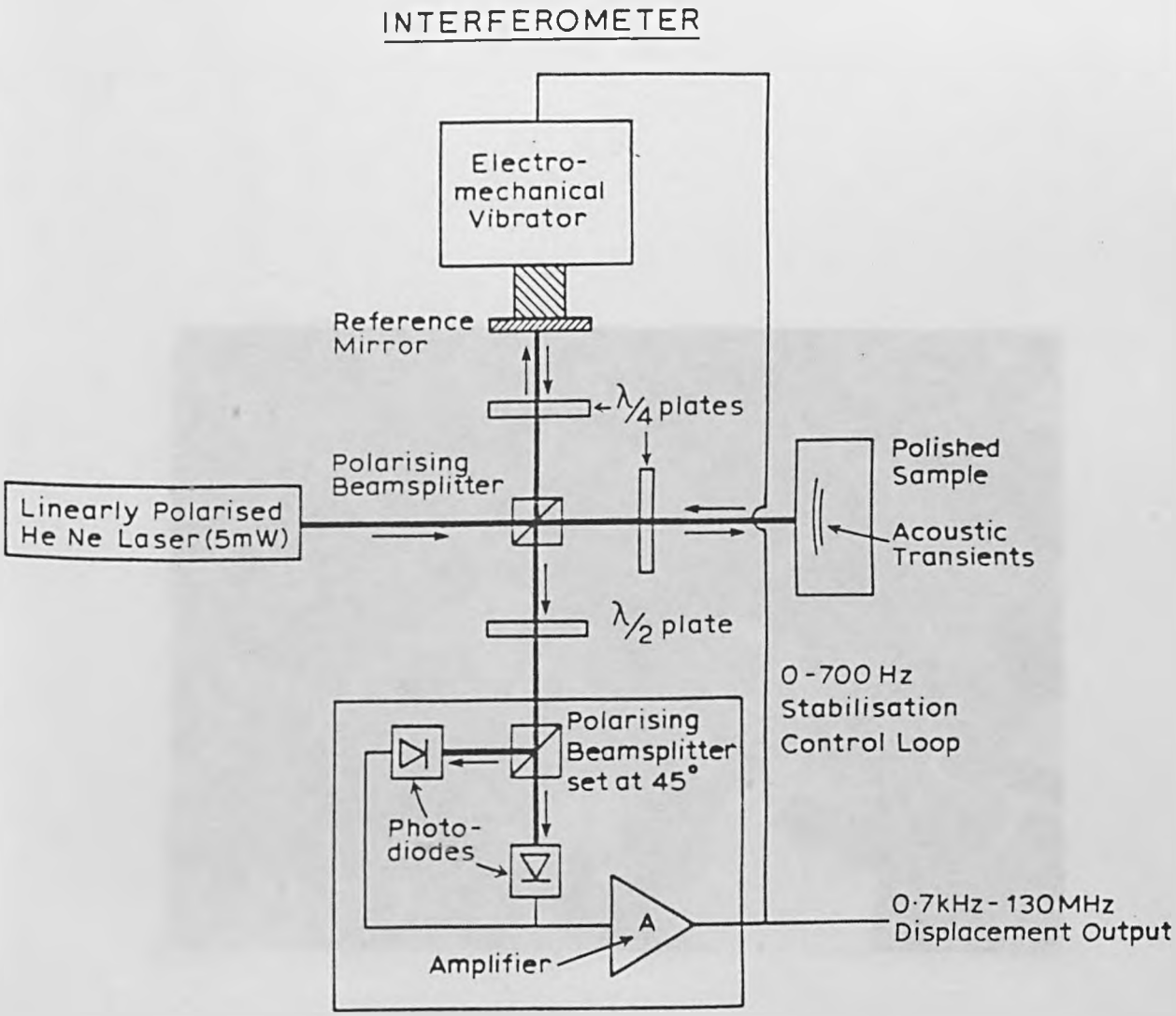

Fig. (3.1a) Schematic diagram of the modified Michelson interferometer.

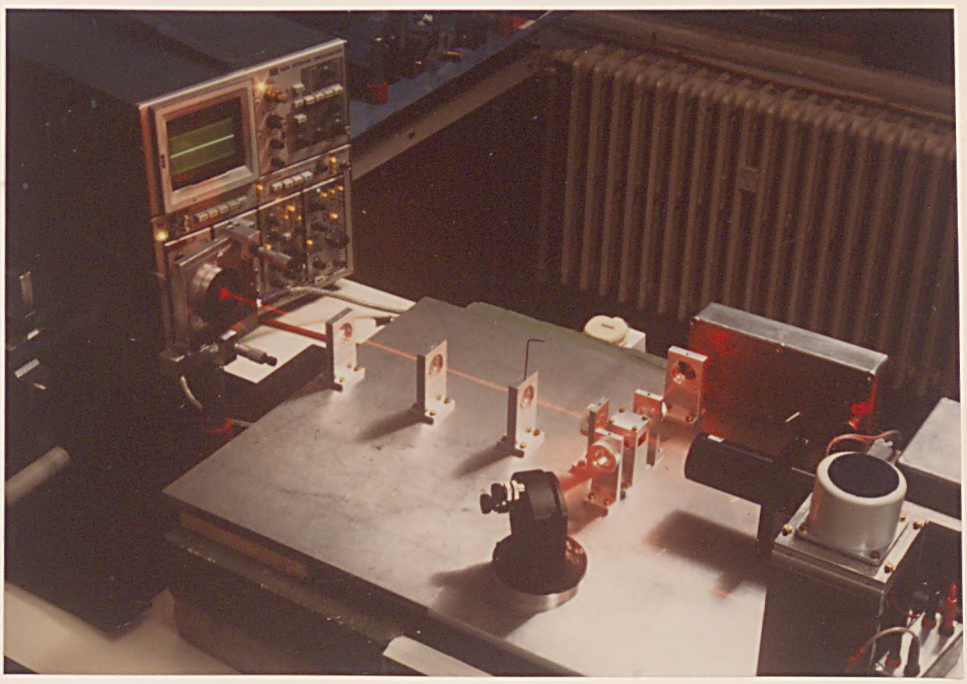

Fig. (3.1b) Photograph of the modified Michelson interferometer

coherence between the two beams has been maintained.

An important consideration in selecting the type of beam splitter to use, is the occurrence of "ghost" reflections (Hecht and Zajac, p.287, 1980). Where an uncoated plate-type beamsplitter is to be used, a weak reflection from the back face would produce a ghost image in both reflection and transmission. As fig. (3.2) suggests, these reflections are essentially parallel (if the plate surfaces are parallel) and hence in some applications may be of little importance. However in an interferometer system these reflections could confuse the fringe count. A method of minimising unwanted reflections is to broadband anti-reflection coat the back surface of the plate-type beamsplitter.

A method that avoids these problems is to use a cube beamsplitter, which has both pairs of entrance and exit faces anti-reflection coated. Pairs of right angled prisms are cemented together hypotenuse face to hypotenuse face with a special multilayer dielectric film in between. The total thickness of the multilayer film is only a few wavelengths, so ghost reflections are absent. Cube beamsplitters also deform less in response to external mechanical stress, and eliminate the need for a compensation plate in one arm of the interferometer, as used in a conventional Michelson interferometer. This latter restriction can be excluded anyway provided a quasi-monochromatic light source is to be used, since optical path length differences become less critical.

The beamsplitters used in the interferometer are in fact polarising beamsplitters. These are designed to separate the incident polarised laser beam into two orthogonally polarised beams, which emerge from the cube through adjacent faces, and in directions which are 90^0 apart, as shown in fig. (3.3). These beamsplitters are designed to transmit the P polarised component, and deflect the S component. Polarising

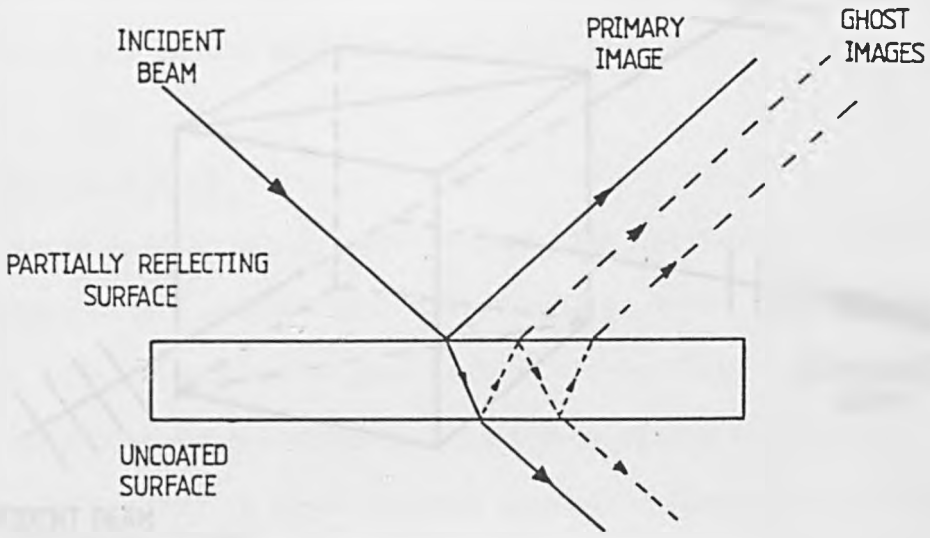

Fig. (3.2) Schematic diagram showing the formation of "ghost" images in a plate-type beamsplitter.

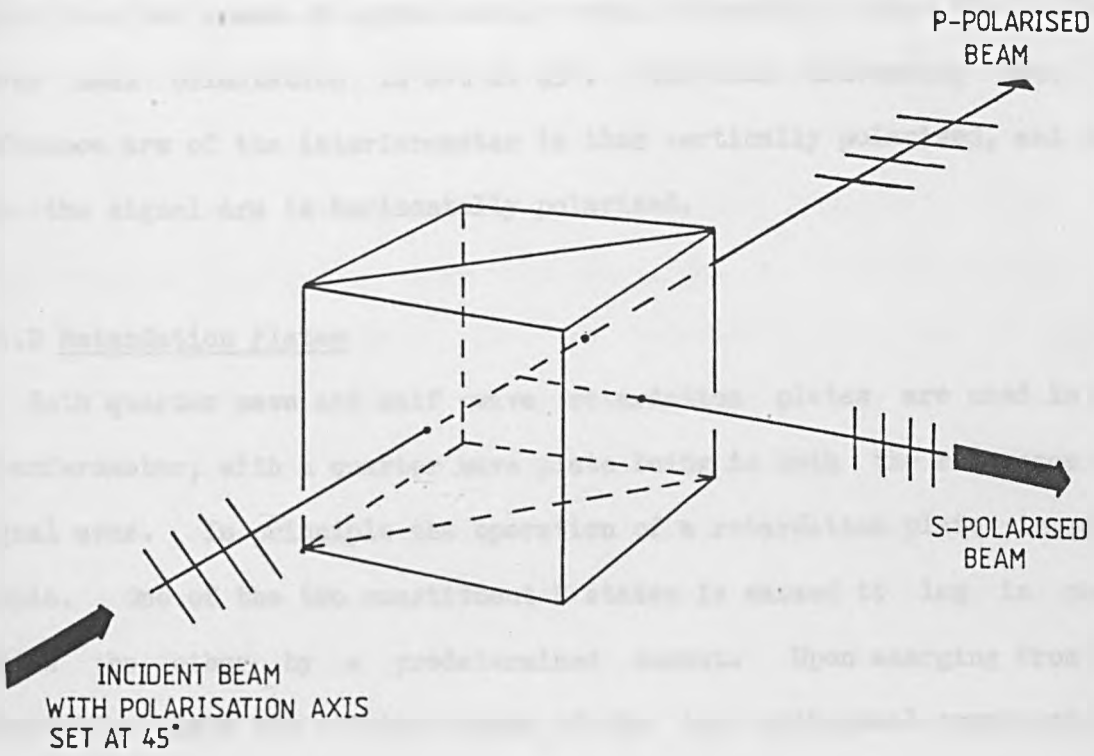

Fig. (3.3) Action of a polarising beamsplitter. The incident light, which is linearly polarised at 45^0, is split into approximately equal amplitude orthogonally polarised components.

beamsplitters have the advantage that the ratio of intensities of the two emergent beams can easily be adjusted by rotation of the incident laser beam orientation. This can be easily achieved by rotating a half wave retardation plate in front of the laser, or as is used in this case, the laser itself is mechanically rotated. This makes polarising cube beamsplitters particularly useful in balanced photodetection systems.

The light incident on the polarising beamsplitter is thus amplitude split into two beams of approximately equal intensity, since the incident laser beam orientation is set at 45^0. The beam traversing into the reference arm of the interferometer is then vertically polarised, and that into the signal arm is horizontally polarised.

3.1.2 Retardation Plates

Both quarter wave and half wave retardation plates are used in the interferometer, with a quarter wave plate being in both the reference and signal arms. In principle the operation of a retardation plate is quite simple. One of the two constituent P states is caused to lag in phase behind the other by a predetermined amount. Upon emerging from the retardation plate the relative phase of the two orthogonal components is different than it was initially, and thus the polarisation state is also different. This is achieved in practice by inserting a sheet of double refracting material in the polarised beam. If the thickness of this sheet is carefully selected so that the retarded component is a quarter of a cycle, or 90^0 out of phase with the other, then it is known as a quarter wave ($\lambda/4$) retardation plate. Similarly a half wave ($\lambda/2$) retardation plate causes the two orthogonal components to emerge half a cycle or 180^0 out of phase with each other (Hecht and Zajac, p.248, 1980).

The retardation plate has two axes, namely slow (S) and fast (F). The S axis of the quarter wave plate may be placed at 45^0 to the right or left of the polarisation axis of the incident laser beam. If the S axis is to the right, then the light emerges from the quarter wave plate as right handed circularly polarised light, and if to the left it emerges as left handed circularly polarised light.

Consider the signal beam path as shown in fig. (3.1). Before passing through the quarter wave plate, the beam is horizontally polarised. After transmission through the quarter wave plate twice, and a reflection at the sample surface, causing a phase change of 180^0, the light returns to the polarising beamsplitter as vertically polarised light, as illustrated in fig.(3.4). From here the light is reflected towards the photodetectors. Similarly for the reference path, the initially vertically polarised light is converted into horizontally polarised light on returning to the polarising beamsplitter, where it is transmitted towards the photodetectors. This method of using polarisation sensitive optical components offers an increase in sensitivity of a factor two over many forms of Michelson interferometer, since the maximum amount of light possible is utilised. More importantly, in many other forms of Michelson interferometer, 50% of the signal and reference beams is fed back into the laser, which can result in fluctuations in laser intensity, and spurious interference signals. In fact the total system of laser plus interferometer operates as a system of coupled resonant optical cavities, and in general the laser output beam should not be reflected back into the laser. In this respect, the polarising beamsplitter acts as an optical isolator.

A half wave retardation plate is inserted in front of the photodetection head. This provides a more accurate adjustment for

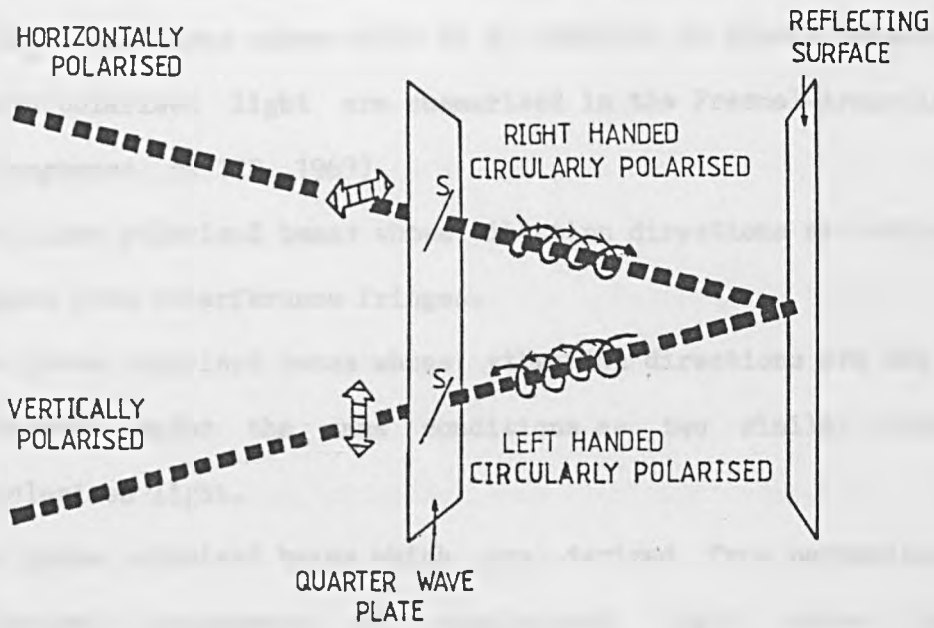

Fig. (3.4) Action of a quarter wave plate in the signal arm of the interferometer.

equalising beam intensities falling on the photodetectors. This is orientated so that the two photodetectors can be balanced such that the d.c. components of the two photocurrents will cancel.

3.1.3 The Balanced Photodetection System

It should be noted that the signal and reference beams, when recombined, have orthogonal polarisations, and as such will not interfere to give intensity fluctuations unless further polarising components are used. The conditions under which it is possible to obtain interference fringes with polarised light are summarised in the Fresnel-Arago laws as follows (Longhurst, p. 122, 1967).

(a) Two plane polarised beams whose vibration directions are orthogonal cannot give interference fringes.

(b) Two plane polarised beams whose vibration directions are the same, interfere under the same conditions as two similar beams of unpolarised light.

(c) Two plane polarised beams which are derived from perpendicularly polarised components of unpolarised light never produce interference fringes, even if their planes of vibration are rotated until parallel.

The first of the Fresnel-Arago laws does not imply that there is no interaction when two orthogonally polarised beams are superposed. In fact the result is to create either a linearly, elliptically, or circularly polarised beam, depending on the phase difference between the two beams, which has a total intensity equal to the sum of the intensities of the two components.

In practice, the polarisation orientations required for interference to occur are obtained by passing the two beams through another polarising

cube beamsplitter, which has its axes set at 45^0, to select the 45^0 components of the reference and signal beams. A schematic diagram of the process is shown in fig. (3.5). This technique provides two interference channels whose phases differ by 180^0 (Moss, 1982). The operation of this technique is of course critically dependent upon the maintenance of polarisation on scattering. Any depolarisation reduces the difference between the two photodetectors.

Two N-type silicon p-i-n photodiodes (type RCA C30808) have been used to monitor the intensity fluctuations arising from the interference. Electronic subtraction of the output of the photodetectors yields the output signal, which is amplified using a fast settling wideband operational amplifier (Comlinear Corporation, type CLC 103A1). The voltage gain of the amplifier is x 40, with a corresponding bandwidth of 0 to 130 MHz. The circuit diagram for the photodetection head, and amplifier electronics are shown in figs. (3.6) and (3.7) respectively. Table (3.1) shows the typical mechanical and electrical characteristics of the photodetectors used in the interferometer.

This balanced photodetection technique reduces high frequency noise due to laser relaxation oscillations and laser power fluctuations (Palmer, 1984).

3.1.4 Mechanical Stabilisation of the Interferometer

For large displacements of the sample surface, fig. (3.1), it is possible to count whole numbers of fringes at the photodetectors, with each fringe representing a sample displacement of $\lambda/4$, where λ is the wavelength of the light source used. If the interferometer was stable enough so that the photodetectors monitored one fringe, then a measure of sample displacements less than $\lambda/4$ could be obtained from the variation in

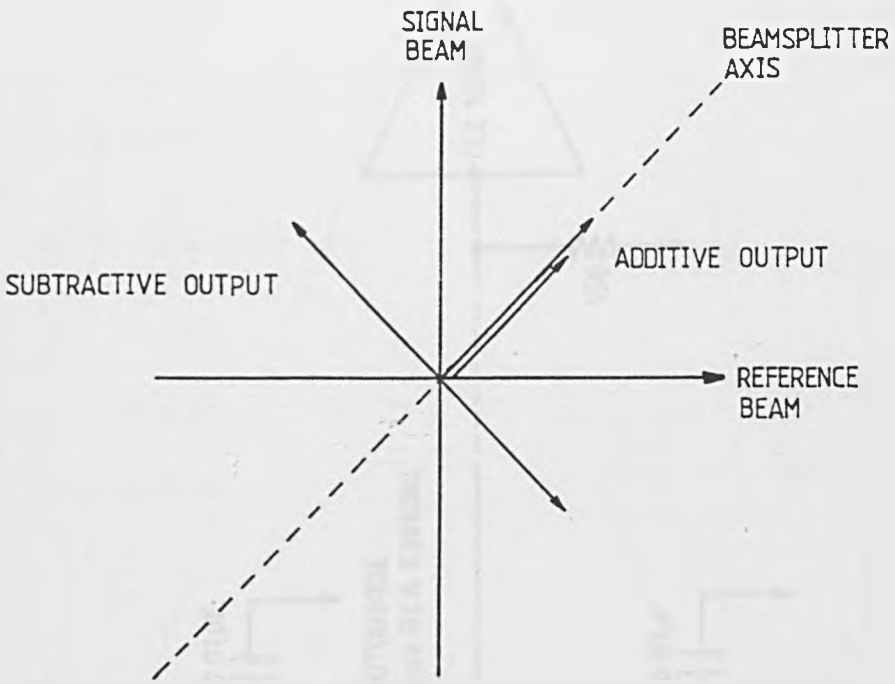

Fig. (3.5) Vector diagram for interference in the photodetectors. One photodiode receives the additive optical field components, and the other the subtractive components.

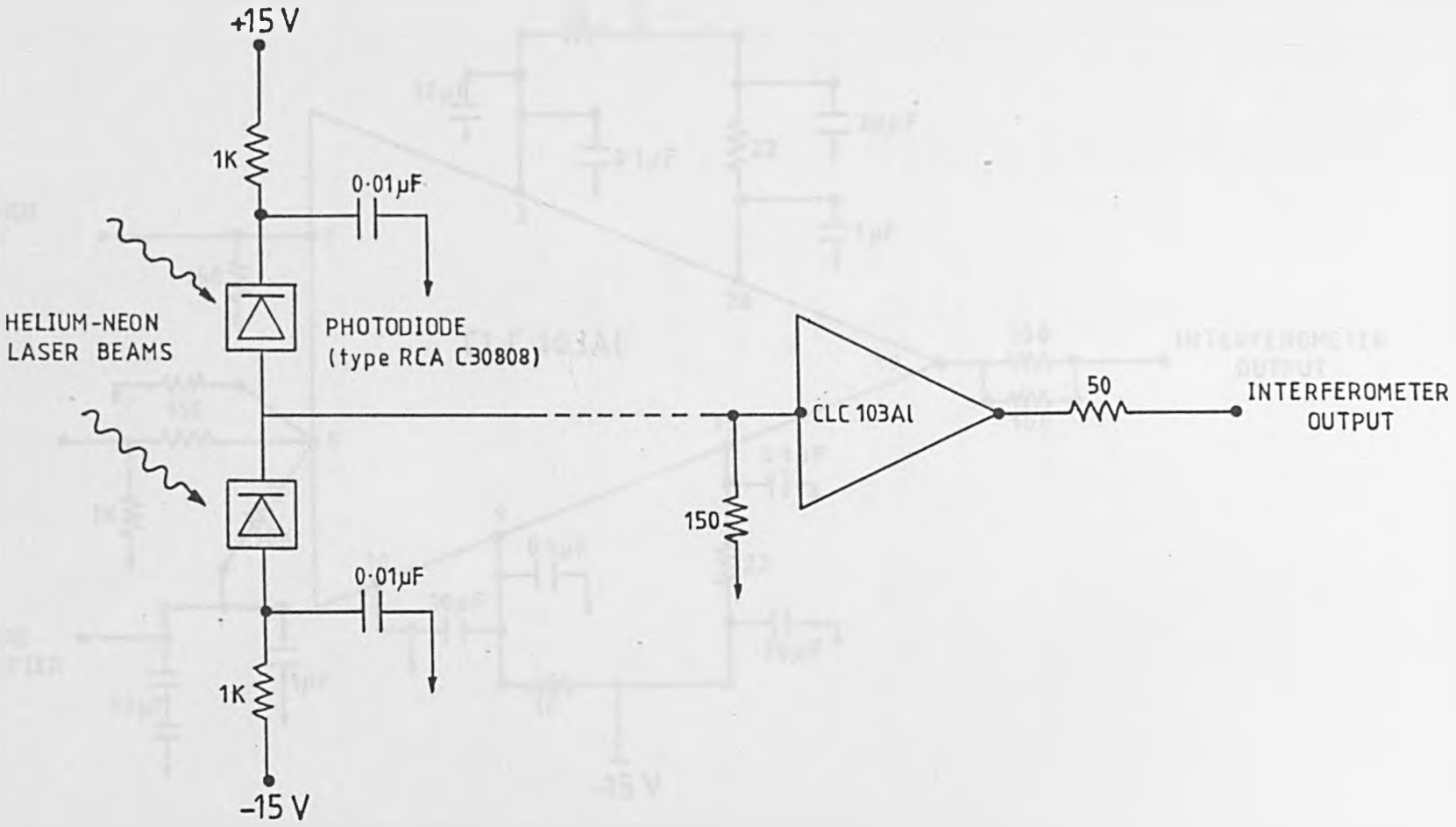

Fig. (3.6) Circuit diagram of the photodetection head.

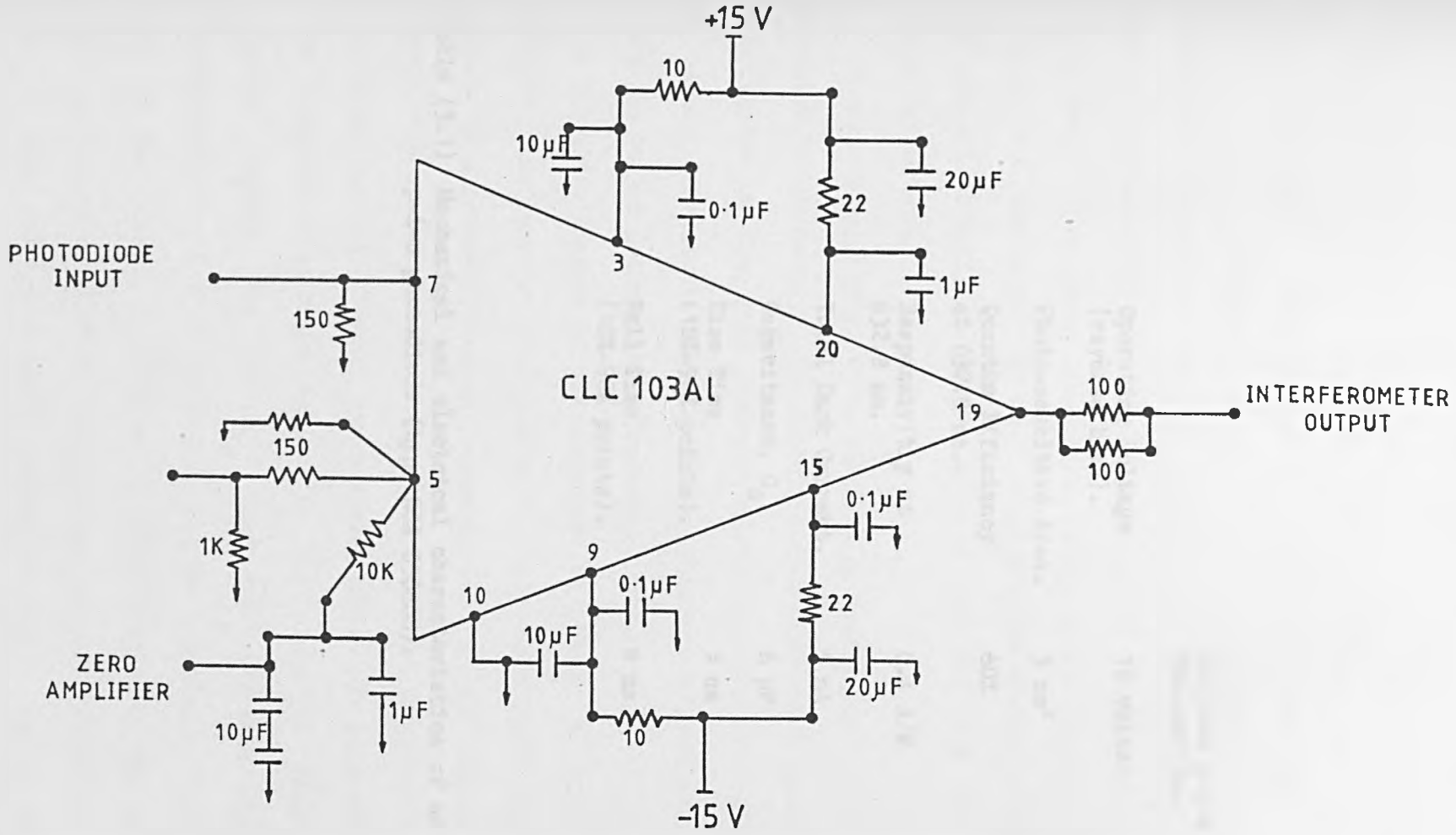

Fig. (3.7) Circuit diagram of the amplifier electronics.

	Silicon p-i-n Photodiode.
Operating Voltage (reverse bias).	15 volts
Photo-sensitive Area.	5 mm^2
Quantum Efficiency at 632.8 nm.	60%
Responsivitiy at 632.8 nm.	0.4 A/W
Total Dark Current.	5 nA
Capacitance, C_d.	6 pF
Rise Time (10%-90% points).	5 ns
Fall Time (10%-90% points).	8 ns

Table (3.1) Mechanical and electrical characteristics of an N-type silicon p-i-n photodiode (type RCA C30808).

fringe intensity. In practical situations however, environmental disturbances such as building vibrations, and refractive index variations etc. produce a randomly varying interference signal due to optical path length changes. These path length changes can have amplitudes of the order of several microns, in the 0 to 1 KHz frequency range. In later experiments, it will be seen that typical transient displacements arising from a laser acoustic source are typically of the order of hundreds of picometers, representing fractional fringe shifts in the interferometer. Clearly, the interferometer must be stabilised against any low frequency extraneous mechanical and thermal effects that may alter the optical path length difference.

Several methods exist for accomplishing stabilisation and have been described in chapter 2. The technique used here is a feedback technique in which the low frequency component of the photocurrent is used to drive an electro-mechanical vibrator (Ling Dynamics Systems, model No. V101) connected to the interferometer reference mirror.

A schematic diagram of the vibrator is shown in fig. (3.8). The vibrator functions by the interaction between a steady magnetic field, produced by a permanent magnet, concentrated in the annular gap formed between the pole tip and the central bore in the front plate, and an oscillating current flowing in a moving coil. In such circumstances a force is generated at right angles to the lines of flux and to the conductor carrying the current. Thus the reference mirror of the interferometer, which is attached to the spindle, is displaced. The drive for the vibrator is provided by amplification of the interferometer output by a power oscillator (Ling Dynamics Systems, model No. TP025). A peak to peak voltage of approximately 2.5 volts across the vibrator terminals, is sufficient to maintain the interferometer in its most

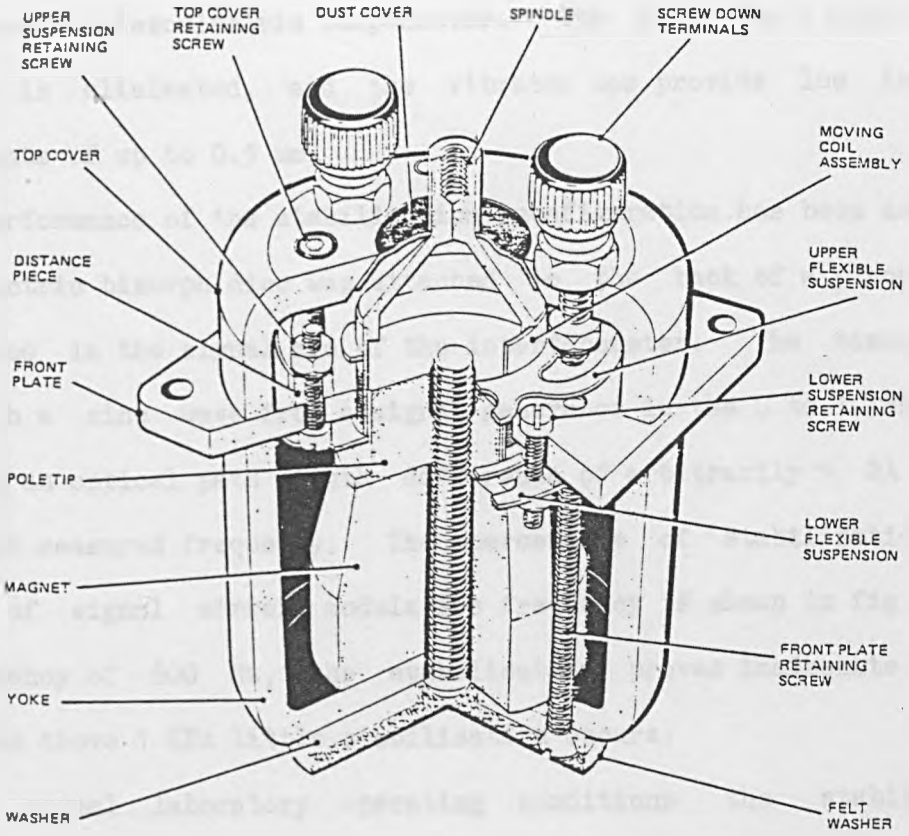

Fig. (3.8) Sectioned view of the Ling Dynamics Systems electro-mechanical vibrator.

sensitive position. Since the fringe intensity varies sinusoidally as a function of optical path difference, the most sensitive position corresponds to a point half way up the interference curve, i.e. with the phase difference between the reference and signal beams equal to $\pi/2$ (see section 3.2).

The use of the mechanical vibrator offers a number of advantages over the more common piezoelectric compensator. The need for a high voltage amplifier is eliminated, and the vibrator can provide low frequency displacements of up to 0.5 mm.

The performance of the stabilisation configuration has been assessed. A piezoelectric bimorph disc was attached to the back of a plane mirror and mounted in the signal arm of the interferometer. The bimorph was driven with a sine wave from a signal generator in the 0 to 1 KHz range, generating an optical path length difference of arbitrarily $\sim 2\lambda$ (~ 1.3 μm) at each measured frequency. The percentage of stabilisation as a function of signal mirror modulation frequency is shown in fig. (3.9). At a frequency of 600 Hz, the stabilisation proves inadequate, and at frequencies above 1 KHz little stabilisation occurs.

Under normal laboratory operating conditions the stabilisation feedback loop is 97% efficient. The sensitivity of the interferometer output will be shown below to be equal to,

$$\frac{dV}{dx} = V_0 \mathrm{SIN}\left(\frac{4\pi x}{\lambda}\right)$$

where V_0 is the peak voltage output of the interferometer when unstabilised, i.e. for variations in path difference greater than $\lambda/2$, and x is the sample displacement. The maximum sensitivity of the interferometer corresponds to a phase difference of $\pi/2$, or an optical path length difference of $\lambda/8$. The 3% instability represents an uncertainty in optical path length difference of $\sim$ 1 nm, which proves to

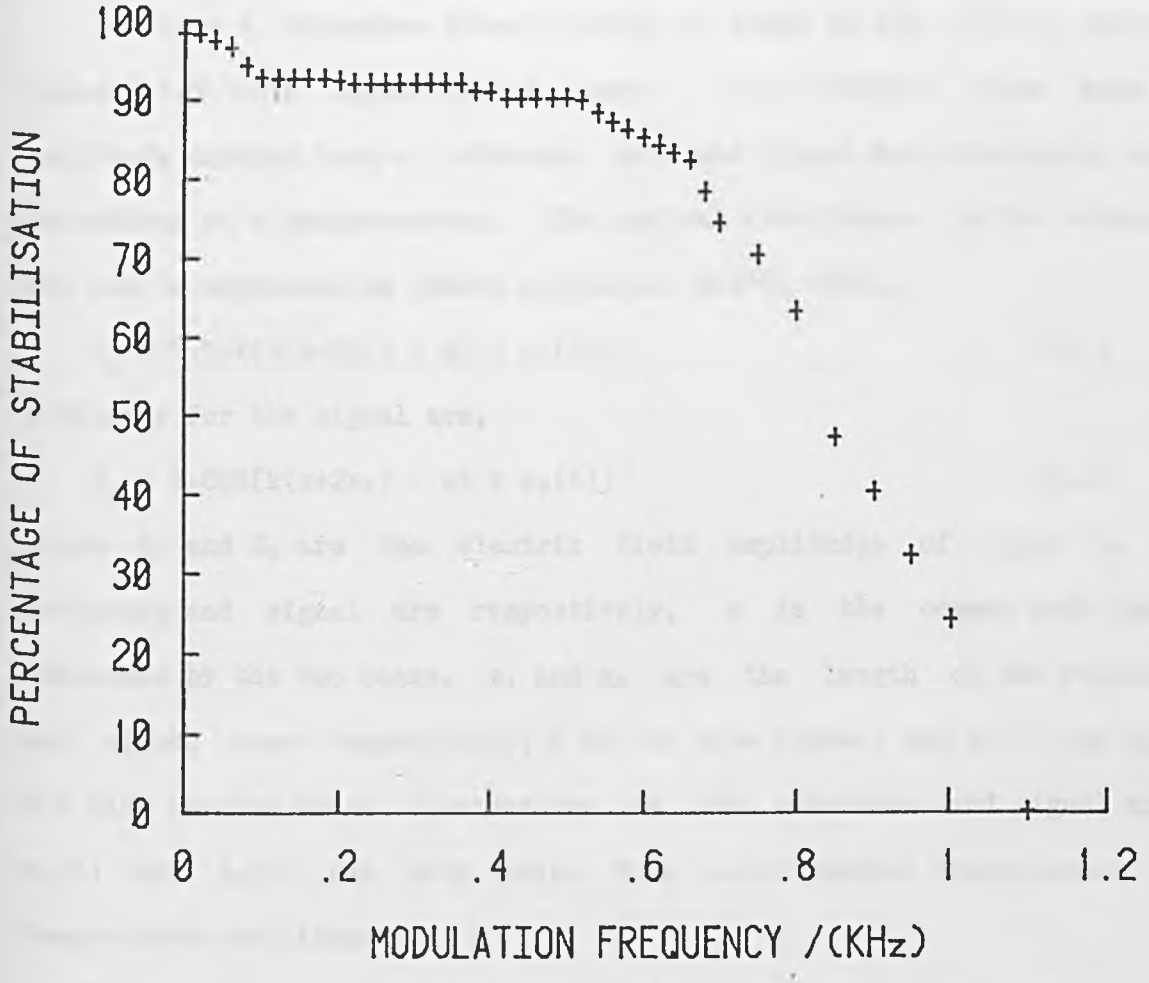

Fig. (3.9) The performance of the stabilisation circuit. Laboratory conditions yielded a figure of 97% stabilisation.

be insignificant in altering the interferometer sensitivity, and calibration.

3.2 Displacement Calibration of a Stabilised Two-Beam Interferometer

Presented below is the derivation of light intensity measured at the photodetector of a simple Michelson interferometer.

Consider a Michelson interferometer as shown in fig. (3.10), which is illuminated with light from a laser. The incident laser beam is amplitude divided into a reference arm and signal arm, eventually being recombined at a photodetector. The optical disturbance in the reference arm can be expressed as (Hecht and Zajac, p.277, 1980),

$$E_R = E_1 COS[k(x+2x_1) - wt + \phi_1(t)] \qquad (3.1)$$

Similarly for the signal arm,

$$E_S = E_2 COS[k(x+2x_2) - wt + \phi_2(t)] \qquad (3.2)$$

where E_1 and E_2 are the electric field amplitudes of light in the reference and signal arm respectively, x is the common path length traversed by the two beams, x_1 and x_2 are the length of the reference and signal arms respectively, k is the wave number, and $\phi_1(t)$ and $\phi_2(t)$ are time varying noise fluctuations in the reference and signal arms. $\phi_1(t)$ and $\phi_2(t)$ can both arise from environmental disturbances, and temperature variations etc.

In accordance with the principle of superposition, the total electric field, E_T, is given by,

$$E_T = E_R + E_S \qquad (3.3)$$

The intensity at the photodetector can be expressed as (Hecht and Zajac, p.46, 1980),

$$I = \varepsilon c \langle E_T^2 \rangle \qquad (3.4)$$

where the angular brackets signify a time average which is long with

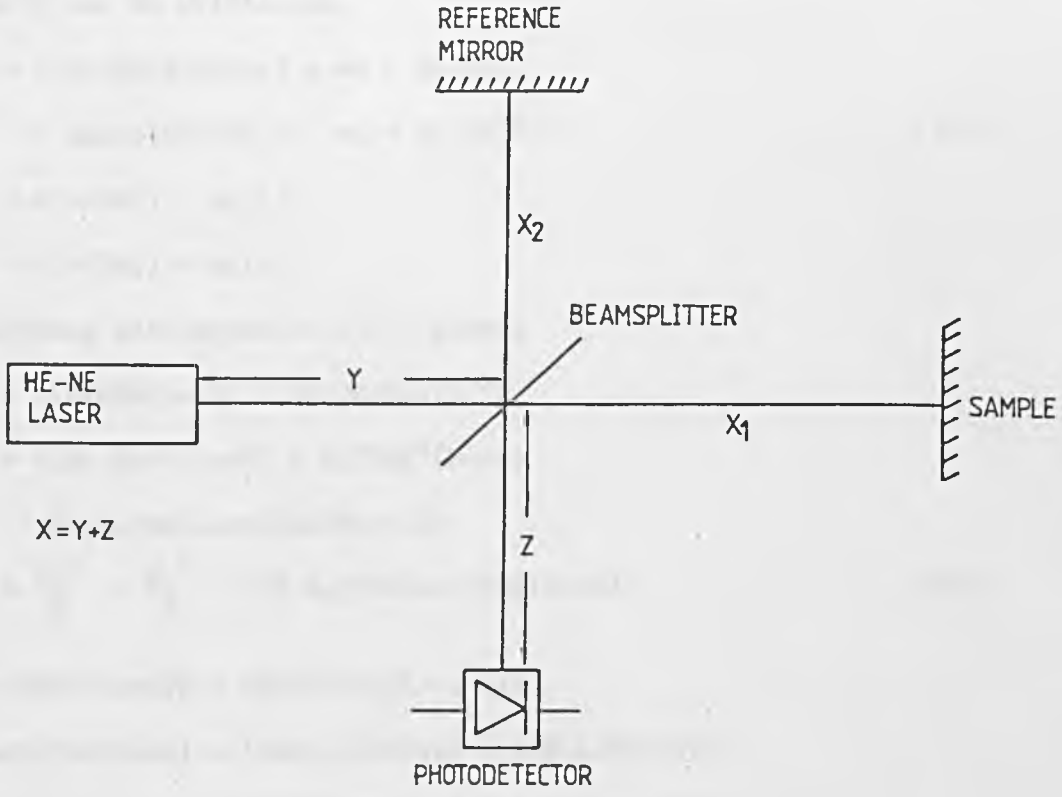

Fig. (3.10) Schematic diagram of a simple Michelson interferometer. The common path lengths are Y and Z.

respect to the optical period, but small compared to the time of observation, ε is the relative permittivity in air, and c is the velocity of light. It is only the relative intensity fluctuations that are of interest, so for the sake of brevity the constants will be ommitted in the following derivation. Thus, combining equations (3.1) to (3.4), the intensity can be written as,

$$I = \langle [E_1 \cos[k(x+2x_1) - wt + \phi_1(t)] + E_2 \cos[k(x+2x_2) - wt + \phi_2(t)]^2 \rangle \qquad (3.5)$$

Let $L = k(x+2x_1) + \phi_1(t)$

$M = k(x+2x_2) + \phi_2(t)$

Substituting into equation (3.5) gives,

$$I = \langle [E_1 \cos(L-wt) + E_2 \cos(M-wt)]^2 \rangle$$

$$I = \langle [E_1^2 \cos^2(L-wt) + E_2^2 \cos^2(M-wt) + 2E_1E_2 \cos(L-wt)\cos(M-wt)] \rangle$$

$$I = \frac{E_1^2}{2} + \frac{E_2^2}{2} + \langle 2E_1E_2 \cos(L-wt)\cos(M-wt) \rangle \qquad (3.6)$$

where $\langle \cos^2(L-wt) \rangle = \langle \cos^2(M-wt) \rangle = 1/2$

$$\cos(L-wt)\cos(M-wt) = [\cos(L)\cos(wt) + \sin(L)\sin(wt)] \times [\cos(M)\cos(wt) + \sin(M)\sin(wt)]$$

$$= \cos(L)\cos(M)\cos^2(wt) + \sin(L)\sin(M)\sin^2(wt) + \sin(L)\sin(wt)\cos(M)\cos(wt) + \cos(L)\cos(wt)\sin(M)\sin(wt)$$

Here it is noted that $\langle \cos^2(wt) \rangle = 1/2$, $\langle \sin^2(wt) \rangle = 1/2$ and $\langle \cos(wt)\sin(wt) \rangle = 0$. Therefore, substituting back into equation (3.6), the intensity can now be written as,

$$I = \frac{E_1^2}{2} + \frac{E_2^2}{2} + E_1E_2[\cos(L)\cos(M) + \sin(L)\sin(M)]$$

$$= \frac{E_1^2}{2} + \frac{E_2^2}{2} + E_1E_2[\cos(L-M)] \qquad (3.7)$$

and on substituting back for L and M into equation (3.7),

$$I = \frac{E_1^2}{2} + \frac{E_2^2}{2} + E_1E_2\cos[2k(x_1-x_2) + \phi_1(t) - \phi_2(t)]$$

Let $I_1 = \frac{E_1^2}{2}$ and $I_2 = \frac{E_2^2}{2}$, giving $E_1E_2 = 2\sqrt{I_1I_2}$, so that,

$$I = I_1 + I_2 + 2\sqrt{I_1I_2}\cos(2k\delta x + \phi) \qquad (3.8)$$

where δx is the mirror displacement x_1-x_2, and $\phi = \phi_1(t) - \phi_2(t)$.

It is evident that there will be a maxima of intensity,

$$I_{max} = I_1 + I_2 + 2\sqrt{I_1I_2} \qquad (3.9)$$

when $(2k\delta x + \phi) = 0, 2\pi, 4\pi$ etc.

and a minima of intensity,

$$I_{min} = I_1 + I_2 - 2\sqrt{I_1I_2} \qquad (3.10)$$

when $(2k\delta x + \phi) = \pi, 3\pi, 5\pi$ etc.

For the special case of both beams having the same amplitude, then $I_1 = I_2 = I_0$, and it follows from equation (3.8) that,

$$I = 2I_0 + 2I_0\cos(2k\delta x + \phi)$$

$$= 2I_0[1 + \cos(2k\delta x + \phi)] \qquad (3.11)$$

which can be written alternatively as,

$$I = 4I_0\cos^2[(2k\delta x + \phi)/2] \qquad (3.12)$$

and the intensity varies between a maximum value of $I_{max} = 4I_0$ and minimum value $I_{min} = 0$. This variation of intensity with path difference is plotted in fig. (3.11).

The voltage output of a photodetector is proportional to the light intensity incident on it. Rewriting equation (3.8) gives,

$$V = A + V_1\cos(2kx + \phi) \qquad (3.13)$$

where V is the voltage output of the photodetectors created by a sample displacement of x, and A is a d.c. term. In the balanced photodetection system already described in section 3.1.3, the d.c. terms are electronically removed so that the output oscillates about ground. When used to measure small displacements the interferometer is also stabilised

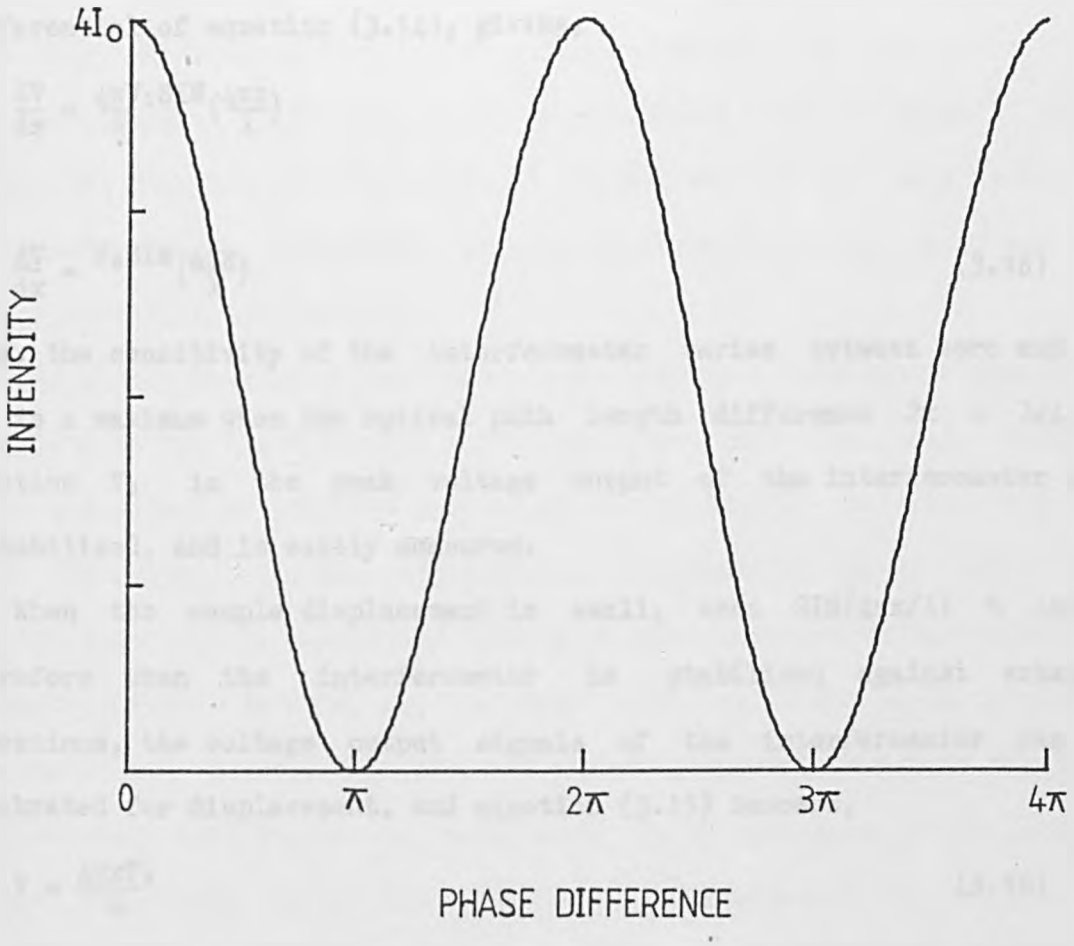

Fig. (3.11) Variation of intensity with phase difference observed at the photodetector of a Michelson interferometer.

against environmental path length changes so that ϕ is zero. Under these conditions equation (3.13) becomes,

$$V = V_1 COS(2kx)$$

or alternatively,

$$V = V_1 COS \frac{4\pi x}{\lambda} \qquad (3.14)$$

The sensitivity of the interferometer to small displacements is the differential of equation (3.14), giving,

$$\frac{dV}{dx} = \frac{4\pi V_1}{\lambda} SIN\left(\frac{4\pi x}{\lambda}\right)$$

or

$$\frac{dV}{dx} = V_0 SIN\left(\frac{4\pi x}{\lambda}\right) \qquad (3.15)$$

Thus, the sensitivity of the interferometer varies between zero and V_0, and is a maximum when the optical path length difference $2x = \lambda/4$. In practice V_0 is the peak voltage output of the interferometer when unstabilised, and is easily measured.

When the sample displacement is small, then $SIN(4\pi x/\lambda) \sim 4\pi x/\lambda$. Therefore when the interferometer is stabilised against external vibrations, the voltage output signals of the interferometer can be calibrated for displacement, and equation (3.15) becomes,

$$V = \frac{4\pi x V_0}{\lambda} \qquad (3.16)$$

This equation has been used exclusively throughout the work of this thesis, in the graph plotting routines. As long as the unstabilised interferometer sensitivity is noted before an experiment, then subsequent waveforms may be processed and absolutely calibrated.

3.3 Coherence Requirements For Two-Beam Interferometry

The classical description of two-beam interferometry has always required that for maximum fringe visibility the optical path lengths traversed by the two light beams be equal or near equal. The allowable path length difference decreases as the spectral width of the light source increases. When a Michelson interferometer is illuminated with a white light source, interference fringes will only be visible if the optical path length difference is zero, or differs from zero by not more than a few wavelengths. If the light source used was a laser of single frequency, then the spectral width of the source would be very narrow, so that path length differences of many metres could be tolerated and good fringe visibility maintained.

For single frequency laser operation only one mode can be allowed to oscillate in the laser cavity. This requires that the laser cavity be short and should be operated very close to threshold. Unfortunately this leads to very low laser output power. For increased power output the cavity length can be increased and the laser operated further above the threshold level. In doing so, the laser spectral line width gradually increases and several longitudinal modes will reach threshold for laser oscillation. This results in multi-mode laser operation, which for good fringe visibility means that path length differences of only a few centimetres can be tolerated. The path length difference that reduces the interference signal to a fraction of its maximum value is known as the coherence length, L_c, and although it is not a precisely defined quantity, it is usually quoted as (Drain, 1980),

$$L_c = c/\Delta\nu$$

where $\Delta\nu$ is the linewidth of the laser, and c the velocity of light. For a typical He-Ne laser this is of the order of 20 cm.

However, if the near zero path length condition is not practically possible, an alternative approach which still maintains good fringe visibility, is to have the optical path length difference equal to an integer multiple of twice the laser cavity length (Drain et. al., 1977). A laser mode can be described as a self consistent field configuration, i.e. the optical field distribution reproduces itself after one round trip in the laser resonator. Therefore constructive interference from all oscillating laser modes will only occur at optical path length differences equal to 0, 2L, 4L, 6L etc., where L is the laser cavity length. Any positions in between these will result in decreased fringe visibility, and in the case of the optical path length difference equal to L, 3L, 5L, 7L etc., the fringe visibility can be reduced to zero (depending on mode distribution within the linewidth, and relative mode intensities). i.e. total destructive interference can occur.

3.3.1 Theory of Interference with Multi-mode Gas Laser Radiation

Consider a cw (continuous wave) laser in which a number of longitudinal modes are oscillating simultaneously. The angular frequencies w of the longitudinal modes are given by ,

$$w = n\pi c/L \qquad (3.17)$$

where n is an integer, c is the velocity of light in free space, and L is the laser cavity length.

From equation (3.11) the intensity for two-beam interference has been derived as,

$$I = 2I_0[1 + \cos(kx)]$$

where x is the optical path length difference, and it has been assumed that the two interfering beams are of equal intensity. The intensity due

to laser modes having wavenumbers in the range k to k + dk is given by (Born and Wolf, p.267, 1964),

$$idk = 2i_1(k)[1 + COS(kx)]dk \tag{3.18}$$

where $i_1(k)$ represents the spectral distribution of intensity of either beam. The total intensity received at the photodetectors due to all the oscillating laser modes is,

$$I = 2\int i_1(k)[1 + COS(kx)]dk \tag{3.19}$$

For any one specific mode, $i_1(k)$ will be negligible except in a small range of k, about some mean wavenumber k_0. Let $k-k_0 = \bar{k}$ and $i_1(k) = i_1(\bar{k}+k_0) = I_1$.

$$I = 2\int I_1[1 + COS(k_0x+\bar{k}x)]d\bar{k} \tag{3.20}$$

Using the identity,

$COS(k_0x+\bar{k}x) = COS(k_0x)COS(\bar{k}x) - SIN(k_0x)SIN(\bar{k}x)$,

equation (3.20) becomes,

$$I = 2[\int I_1 d\bar{k} + \int I_1 COS(k_0x)COS(\bar{k}x)d\bar{k} - \int I_1 SIN(k_0x)SIN(\bar{k}x)d\bar{k}]$$

or alternatively,

$$I = P + C(x)COS(k_0x) - S(x)SIN(k_0x) \tag{3.21}$$

where $P = 2\int I_1 d\bar{k}$

$$C(x) = 2\int I_1 COS(\bar{k}x)d\bar{k}$$

$$S(x) = 2\int I_1 SIN(\bar{k}x)d\bar{k}$$

Evaluating equation (3.21) to find maximum and minimum values for I gives,

$$\frac{dI}{dx} = -k_0SIN(k_0x)C - k_0COS(k_0x)S = 0$$

$$C.SIN(k_0x) = -S.COS(k_0x)$$

or

$$TAN(k_0x) = -\frac{S}{C} \tag{3.22}$$

The quality of fringes produced by an interferometric system can be described quantitatively using the visibility, V(x), which as first

formulated by Michelson (1891), is given by,

$$V(x) = \frac{I_{max} - I_{min}}{I_{max} + I_{min}} \qquad (3.23)$$

where I_{max} and I_{min} correspond to the intensity of a maximum and minimum fringe respectively. From equations (3.21) and (3.22) it can be shown that the visibility due to interference from a quasi-monochromatic source is (Born and Wolf, p.269, 1964),

$$V(x) = \frac{(C^2 + S^2)^{1/2}}{P}$$

The fringe visibility for interference from a laser which has N oscillating modes is given by (Foreman, 1967),

$$V(x) = \frac{(A^2 + B^2)^{1/2}}{Z} \qquad (3.24)$$

where $A = \Sigma_{n=1}^{N} I_n COS(\bar{k}_n x)$

$B = \Sigma_{n=1}^{N} I_n SIN(\bar{k}_n x)$

$Z = \Sigma_{n=1}^{N} I_n$

The fringe visibilities have been evaluated for a 35 cm long laser cavity, which has N = 1 to 7 oscillating modes. These results are shown in fig.(3.12), in which the values of relative mode intensity used have been calculated assuming symmetrically spaced modes, equi-spaced under a gaussian linewidth.

Most commercially available helium-neon lasers are operated well above threshold for increased power output, where the width of the gain curve will approach the Doppler-broadened line width of the atomic transition for neon, which participates in the laser action.

The Doppler-broadened linewidth between the half-maximum value points can be expressed by (O' Shea et. al., p. 83, 1978),

$$\Delta\nu_{HM} = 2.35\nu(kT/mc^2)^{1/2}$$

where k is Boltzmann's constant, T is the absolute temperature of the discharge, m is the atomic mass, c is the velocity of light and ν is the

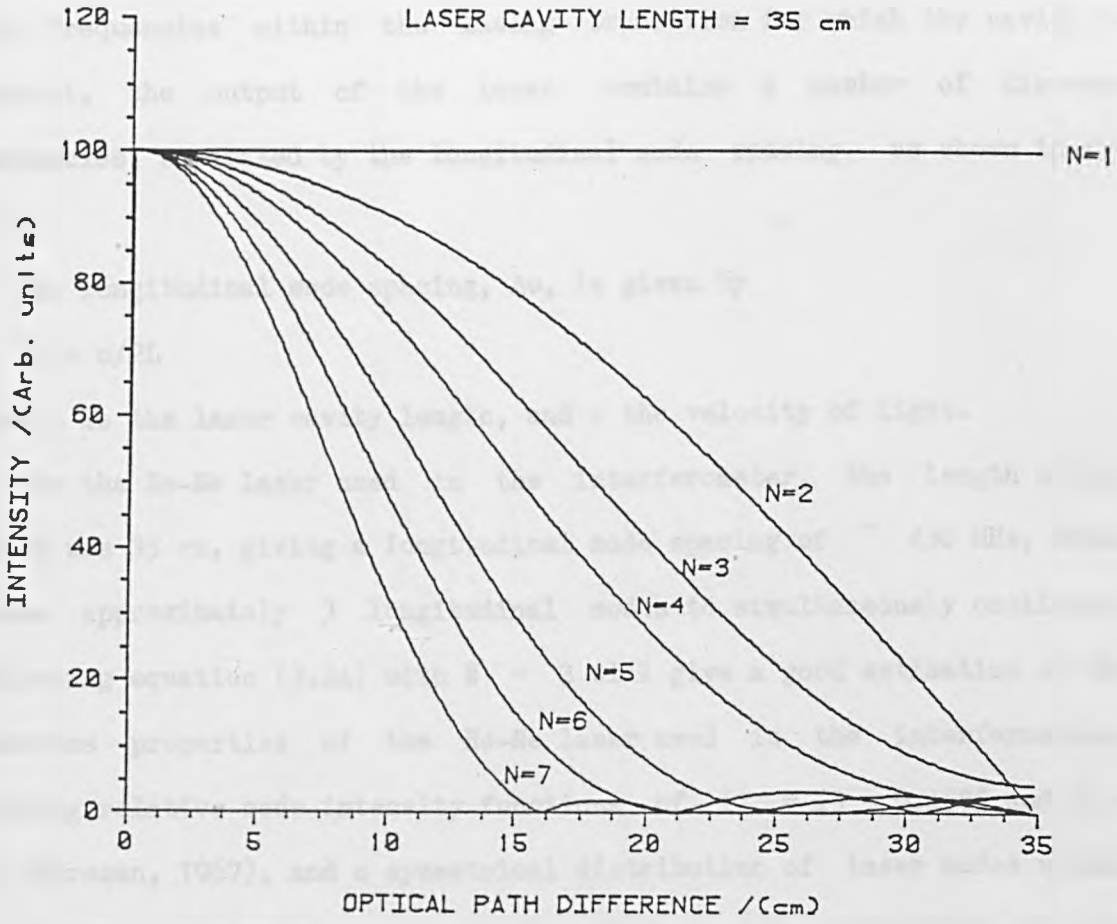

Fig. (3.12) Dependence of the interference signal quality with optical path difference, for various numbers of oscillating longitudinal laser modes.

optical frequency emitted by the atoms. Thus in the case of the 632.8 nm He-Ne laser transition, assuming a discharge temperature of about 400 K and a neon atomic mass of 20, the half maximum linewidth is about 1500 MHz. Consequently, there can be a number of longitudinal modes within the broadened linewidth. Since sustained laser action can occur only at those frequencies within the lasing transition for which the cavity is resonant, the output of the laser contains a number of discrete frequencies, separated by the longitudinal mode spacing, as shown in fig (3.13).

The longitudinal mode spacing, $\Delta\nu$, is given by

$$\Delta\nu = c/2L$$

where L is the laser cavity length, and c the velocity of light.

For the He-Ne laser used in the interferometer, the length of the cavity was 35 cm, giving a longitudinal mode spacing of ~ 430 MHz, which allows approximately 3 longitudinal modes to simultaneously oscillate. Evaluating equation (3.24) with N = 3 will give a good estimation of the coherence properties of the He-Ne laser used in the interferometer. Assuming relative mode intensity functions of I1 = I3 = 0.4585 and I2 = 1.0 (Foreman, 1967), and a symmetrical distribution of laser modes within the linewidth, the theoretical plot of the way the intensity at the photodetectors varies with optical path difference in the interferometer, is shown in fig (3.14).

Experimentally this relationship was investigated with the interferometer initially setup at the zero path length position, with the He-Ne laser beam incident on a plane silvered mirror. The interferometer was aligned for maximum interference, and the mirror traversed away from the interferometer, along an optical bench, in 2 cm divisions. The maximum modulation depth was recorded as a function of mirror distance up

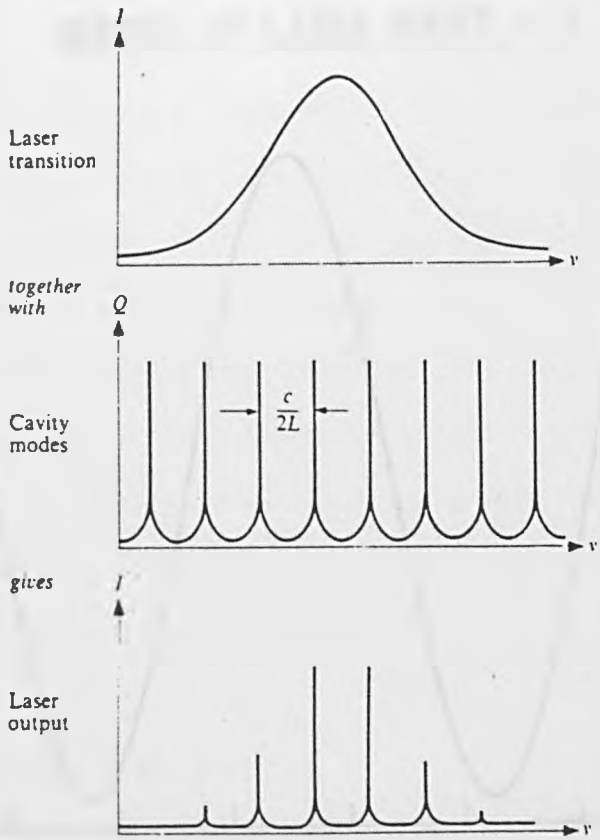

Fig. (3.13) The combination of the lasing transition with the resonant longitudinal modes gives the resulting laser output (after O' Shea et. al., 1978).

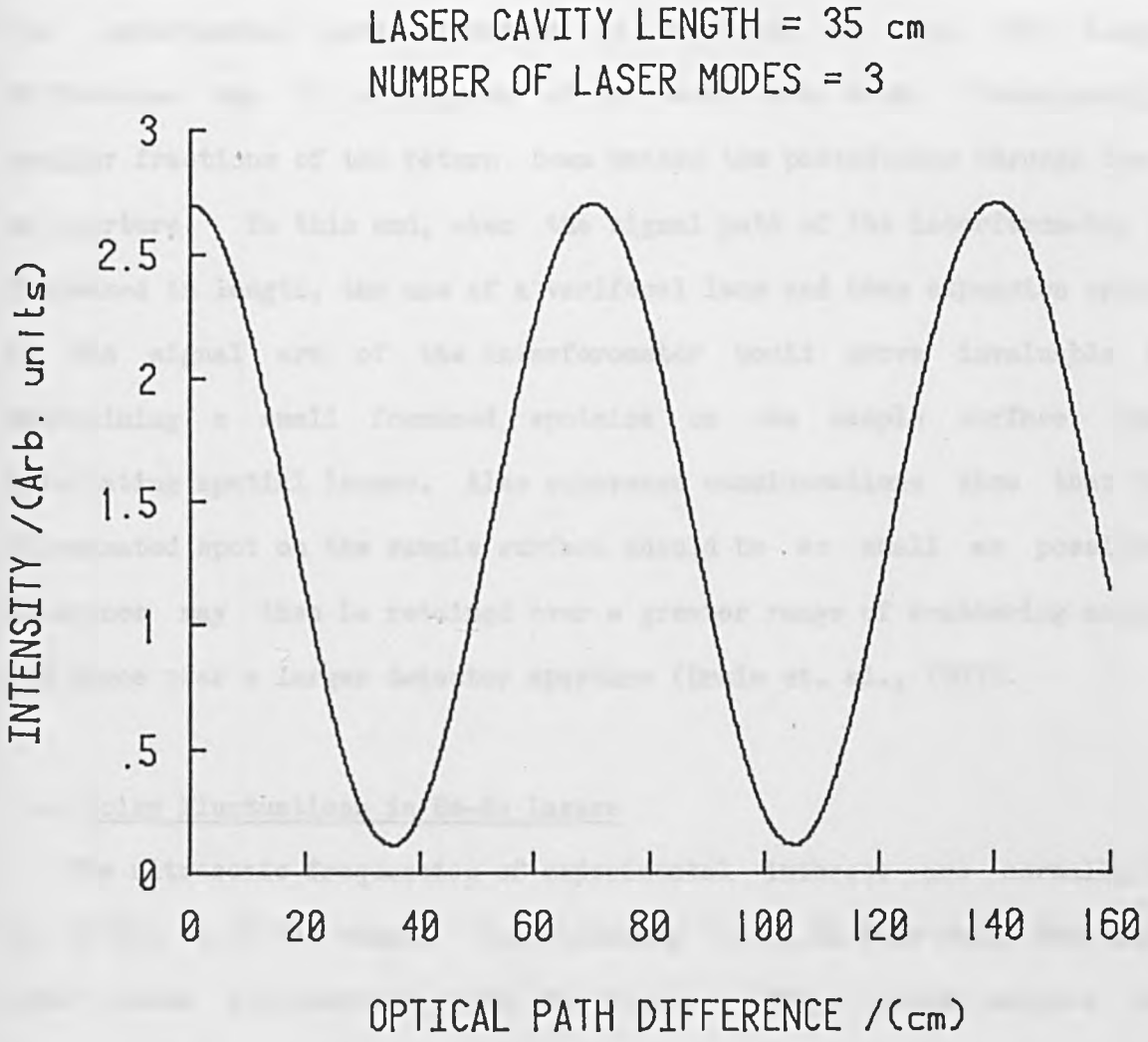

Fig. (3.14) Theoretical variation of intensity with optical path difference for interference with a laser having 3 symmetrically spaced oscillating longitudinal modes within the linewidth.

to a distance of 80 cm away from the initial position. The experimental data is presented in fig. (3.15).

It should be noted that both theoretical and experimental data show maxima at optical path length differences equal to 0, 2L, 4L, and minima at optical path length differences equal to L and 3L as already predicted. The experimental data decreases in amplitude at long path length differences due to divergence of the He-Ne laser beam. Consequently, smaller fractions of the return beam enters the photodiodes through the 1 mm aperture. To this end, when the signal path of the interferometer is increased in length, the use of a varifocal lens and beam expansion optics in the signal arm of the interferometer would prove invaluable in maintaining a small focussed spotsize on the sample surface, thus eliminating spatial losses. Also coherence considerations show that the illuminated spot on the sample surface should be as small as possible. Coherence may then be retained over a greater range of scattering angle, and hence over a larger detector aperture (Drain et. al., 1977).

3.4 Noise Fluctuations in He-Ne Lasers

The ultrasonic frequencies of experimental interest are normally in the 10 KHz to 20 MHz range. Unfortunately it is in this range that most laser noise fluctuations tend to occur. These noise sources can superpose a varying high frequency component on the ultrasonic signal of interest, obscuring the desired signal.

One source of laser noise is that of laser relaxation oscillations which occur in the 100 KHz to 10 MHz region (Yariv, p. 147, 1976). In multimode lasers another source originates from intermode beating which appears as a swept frequency distorted sine wave which is superposed on the mean laser intensity (Kwaaitaal et. al., 1980). An example of this

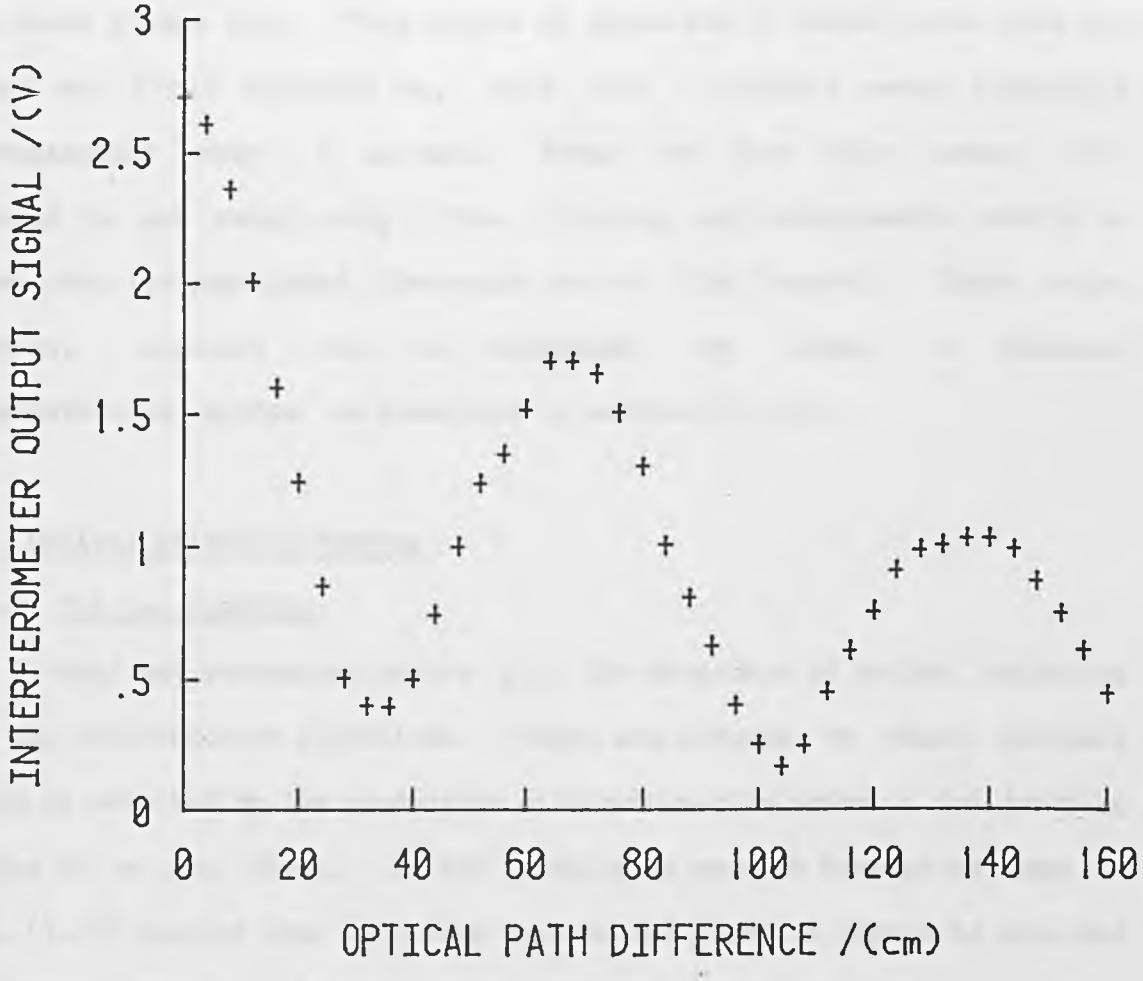

Fig. (3.15) Experimentally determined variation of interferometer output signal with optical path difference. The results indicate the presence of 3 oscillating longitudinal modes in the He-Ne laser.

effect is shown in fig. (3.16), where the interferometer was stabilised, and the digitiser was externally triggered to capture an ultrasonic Rayleigh surface wave. The waveform of fig. (3.16a) shows a signal waveform when mode interference is absent. In contrast, fig. (3.16b) shows a signal superposed with a distorted sine wave. The duration of the sweep and its repetition rate depended on the temperature change of the laser plasma tube. This source of noise was of course worst when the laser was first switched on, with the frequency sweep repeating approximately every 3 seconds. After one hour this sweep rate reduced to one sweep every five minutes, and measurements should be taken when the superposed frequency was at its lowest. These noise sources, however, can be minimised by using a balanced photodetection system as described in section (3.1.3).

3.5 Optical Detection Systems

3.5.1 The p-n Junction

A cheap and convenient device for the detection of optical radiation is the semiconductor photodiode. These are devices in which incident light is detected by the production of electron-hole pairs in the junction region of a p-n diode. If the junction is reverse biassed as shown in fig. (3.17) current does not flow because the junction region is depleted of charge carriers. However illumination by light of the appropriate wavelength generates electron and hole carriers which are drawn to the n and p sides respectively, by the electric field in the junction, before they can recombine. This produces a leakage current proportional to the incident light intensity, and an output voltage may be developed across a resistor, R.

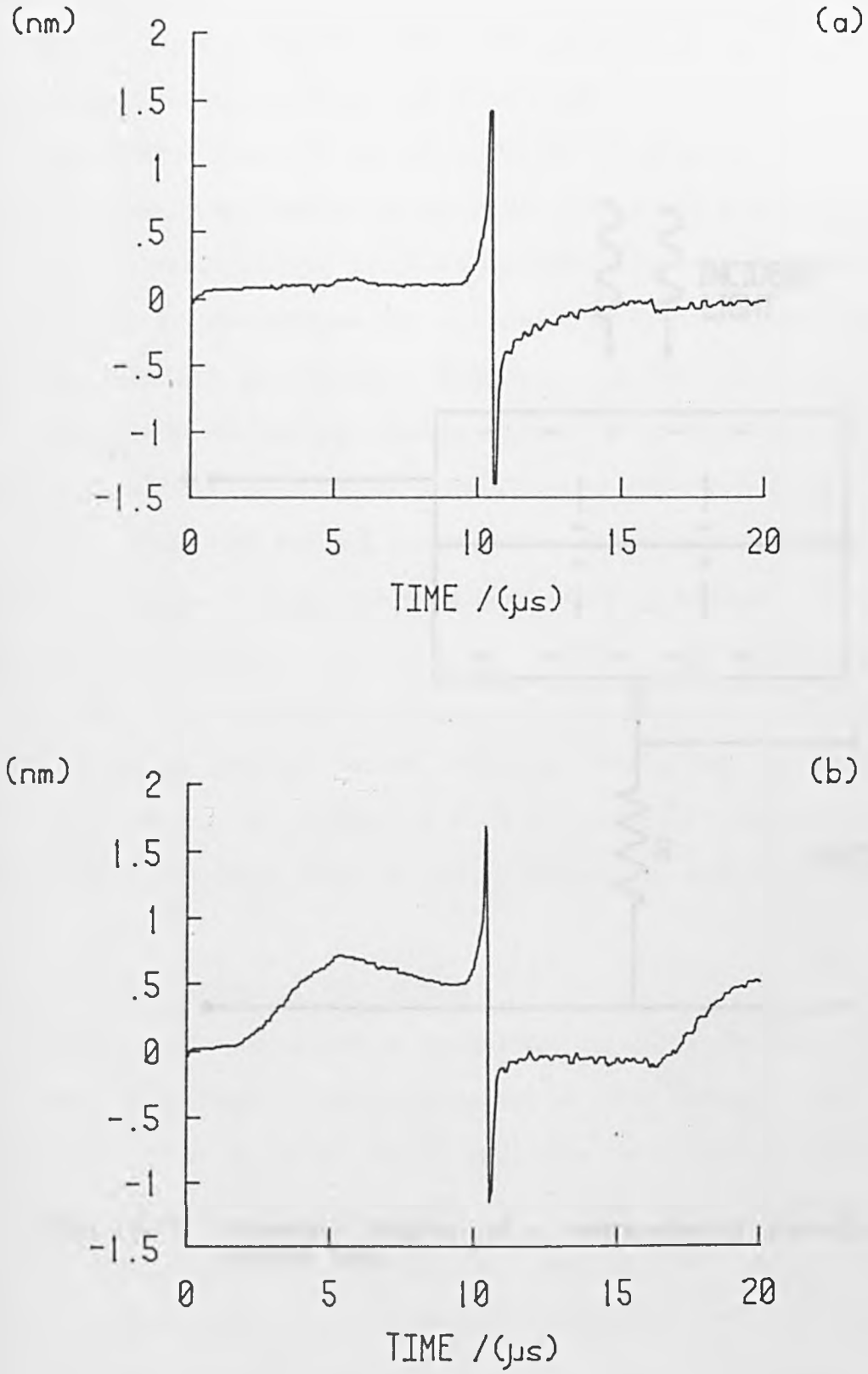

Fig. (3.16) The effect of noise fluctuations in heliun-neon lasers.

(a) Detection of a Rayleigh surface wave without mode interference gives the true sample displacement.

(b) Detection of a Rayleigh surface wave in the presence of mode interference gives a waveform superposed with a distorted sine wave.

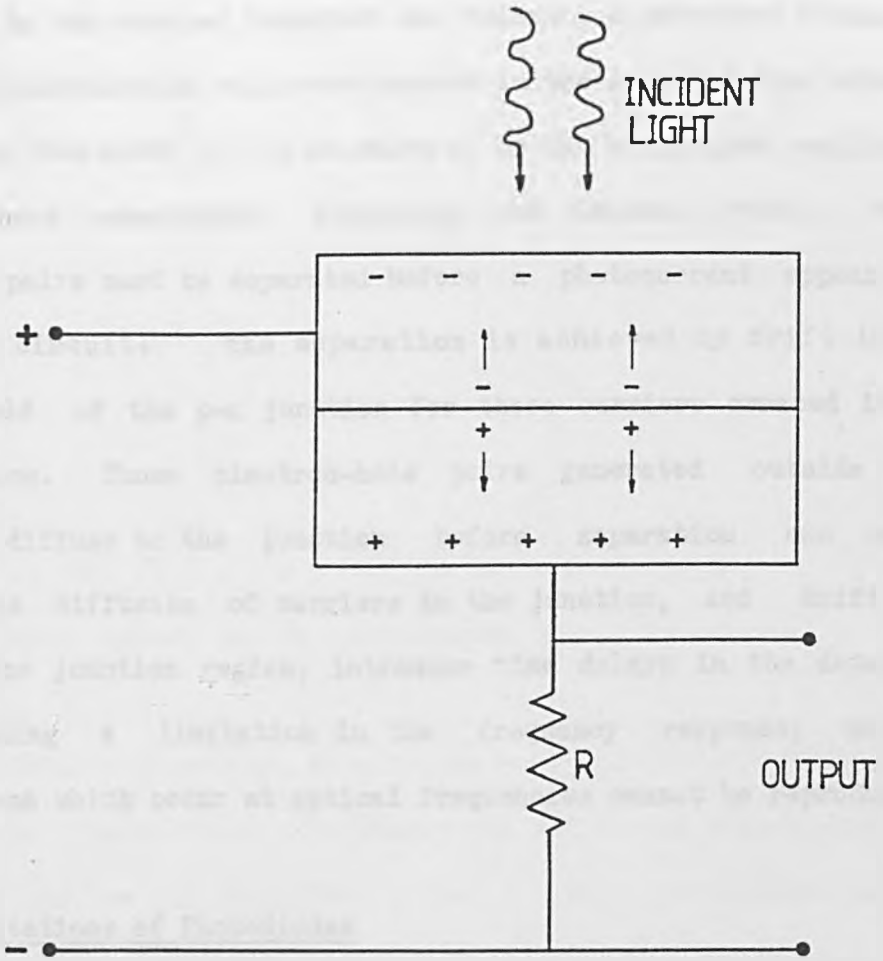

Fig. (3.17) Schematic diagram of a semiconductor photodiode in reverse bias.

3.5.2 Frequency Response of a p-n Junction Photodiode

The p-n junction photodiode is a square law detector that responds to the intensity of incident light averaged over a number of optical cycles (Johnson, 1965). This is because the speed of response of the detector is determined by the carrier transport and relaxation processes within the detector. Electron-hole pairs are created in the semiconductor material to a depth of the order of $1/\alpha$ cm where α is the absorption coefficient at the incident wavelength (Lucovsky and Emmons, 1965). These electron-hole pairs must be separated before a photocurrent appears in the external circuit. The separation is achieved by drift in the electric field of the p-n junction for those carriers created in the junction region. Those electron-hole pairs generated outside the junction must diffuse to the junction before separation can occur. Thus both the diffusion of carriers to the junction, and drift of carriers in the junction region, introduce time delays in the detection process, creating a limitation in the frequency response, so that field variations which occur at optical frequencies cannot be reproduced.

3.5.3 RC Limitations of Photodiodes

The speed of response of a photodiode is also determined by the inherent resistance and capacitance of the device. The junction capacitance can be shown to be equivalent to that of a parallel plate capacitor (Solymar and Walsh, 1979). This capacitance decreases as the reverse bias is increased, because the depletion layer becomes wider, and at a reverse bias of 45 volts the capacitance of the RCA C30808 photodiodes is typically 6 pF for a 5 mm^2 active area device. For high frequency response it is essential that this capacitance be kept as low as possible.

The photodiode resistance in a reverse biassed configuration is usually very large, typically of the order of 10^6 to 10^8 ohms, which compared with the resistance of any external load can usually be neglected. Fig. (3.18) (Lucovsky and Emmons, 1965) shows an equivalent circuit for a photodiode, where C_d and R_d represent the junction capacitance and resistance respectively. R_s is the series resistance and I_{sig} is the equivalent light current generator. R_s arises from resistance of the contacts to the semiconductor, and is usually less than 1 ohm. The frequency cutoff, f_c, of the photodiode at the -3dB (half power) point occurs at a frequency given by (Lucovsky and Emmons, 1965),

$$f_c = \frac{1}{2\pi R_T C_d}$$

where $1/R_T = 1/R_s(1+R_s/R_d)$

Hence the frequency cutoff may be approximated by,

$$f_c = \frac{1}{2\pi R_s C_d} \qquad (3.25)$$

Practical detection systems, however, have lower cutoff frequencies because of the finite load resistance and additional capacitance (and inductance) of the load or amplifier circuit. Fast photodiodes usually have planar junctions that are 50 μm to 1 mm in diameter, in order to keep the capacitance small. For photodiodes with very small diameter active areas, focussing of the incident light is required, which makes optical alignment more critical.

Unfortunately for good sensitivity, the active area of the photodiode should be as large as possible, and a compromise between frequency response and sensitivity may be required, depending on the application.

The major requirements imposed on optical detectors thus include,

(a) sufficiently wide bandwidth to detect high frequency modulation in the incident optical signal,

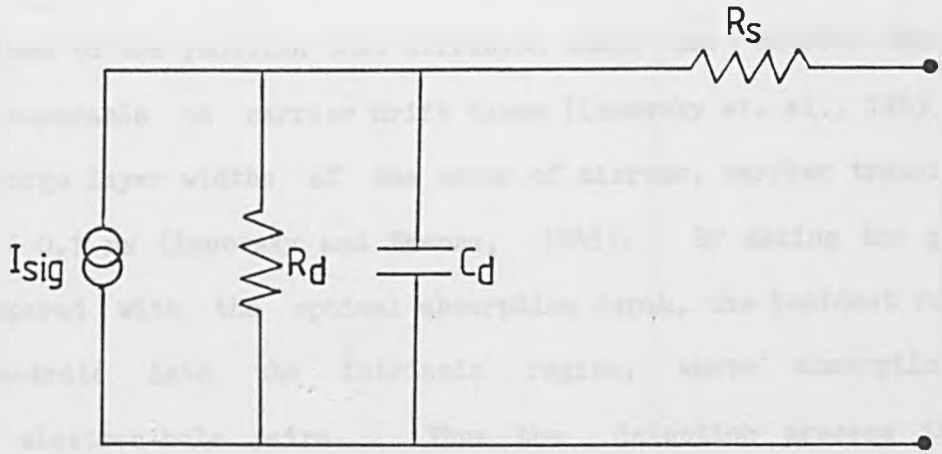

Fig. (3.18) Equivalent circuit of a p-i-n photodiode.

(b) large quantum efficiency for the incident optical signal,

(c) relatively low noise devices for good signal to noise ratios.

3.5.4 The p-i-n Junction

Instead of employing an abrupt p-n junction, a p-i-n photodiode incorporates an intrinsic region between the p and n sides of the junction. Diffusion processes are slow compared to the drift of carriers in the high field region. Therefore, in high speed photodiodes, the carriers have to be excited within the high field region of the junction, or so close to the junction that diffusion times are shorter than, or at least comparable to carrier drift times (Lucovsky et. al., 1963). For space charge layer widths of the order of microns, carrier transit times can be < 0.1 ns (Lucovsky and Emmons, 1965). By making the p region thin compared with the optical absorption depth, the incident radiation will penetrate into the intrinsic region, where absorption will produce electron-hole pairs. Thus the detection process in p-i-n photodiodes is dominated by drift through the region, and the frequency response of a p-i-n photodiode can be higher than that of a p-n junction of the same material. The construction of a typical p-i-n photodiode is shown schematically in fig.(3.19) (Gower, 1984). To maximise the amount of incident optical radiation reaching the semiconductor region, the access window of the photodetector is anti-reflection coated.

3.5.5 Practical Operation of Junction Photodiodes

In practical applications most photodiodes are operated in the reverse bias configuration. Unilluminated, the voltage-current characteristic of a junction photodiode would be expected to have the form of curve (1) in

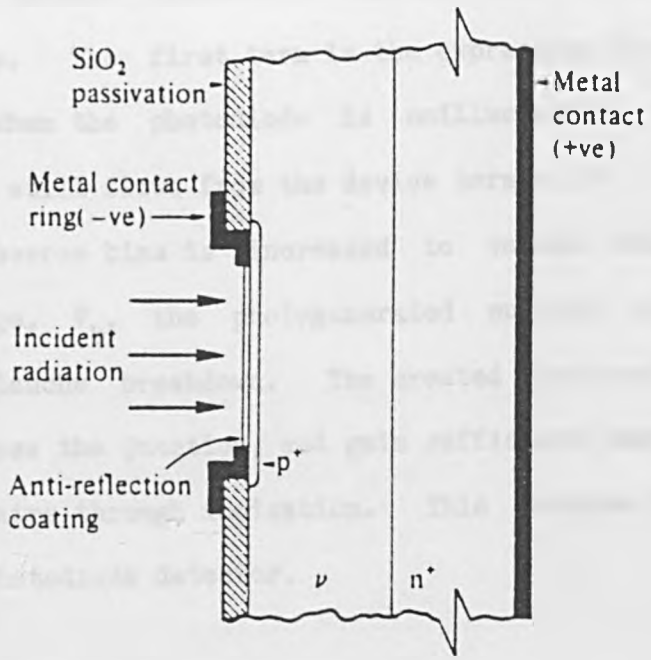

Fig. (3.19) Schematic diagram of a silicon p-i-n photodiode (after Gower, 1984).

fig.(3.20) (Gower, 1984). However when light of the appropriate wavelength is incident on the junction, the effect is to shift the voltage-current characteristic by an amount given by the photocurrent I_{sig} as shown in curve (2) in fig.(3.20). The total current generated when the junction is illuminated is given by (Verdeyen, p.397, 1981),

$$I = I_0[EXP(eV/kT) - 1] - I_{sig} \qquad (3.26)$$

where I_0 is the reverse saturation current, and V is the externally applied voltage. The first term in the expression is equivalent to the dark current. When the photodiode is unilluminated, a small reverse leakage current still flows from the device terminals.

When the reverse bias is increased to values which approach the breakdown voltage, V_b, the photogenerated current is multiplied as a result of avalanche breakdown. The created electron-hole carriers are accelerated across the junction, and gain sufficient energy to release new electron-hole pairs through ionization. This process forms the basis of the avalanche photodiode detector.

3.6 Signal to Noise Ratio of a Photodiode

The ultimate sensitivity of a photodiode is determined by the random voltage and current fluctuations that appear at its output terminals during practical operation. A number of noise sources that arise in photodiodes will be discussed in the following sections.

3.6.1 Shot Noise in Photodiodes

Shot noise generated in a photon detector is due to the discrete nature of photoelectric generation. Whenever current carriers cross a barrier such as a junction, each carrier causes a slight transient current surge as it travels across the junction, the combined effect being a

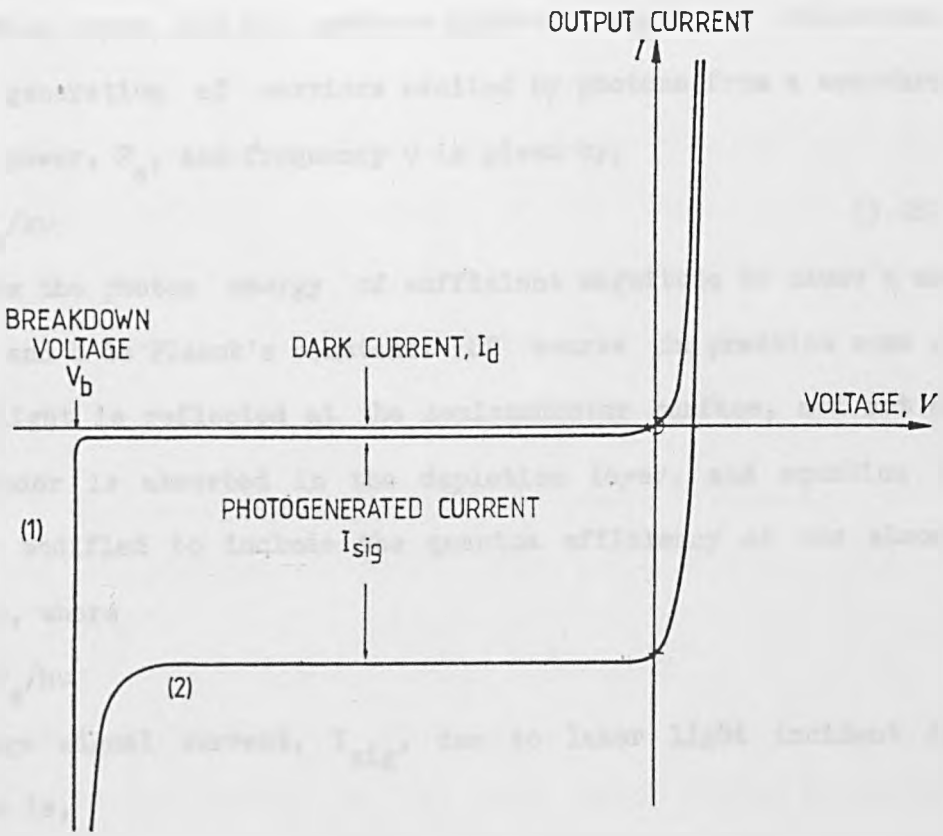

Fig. (3.20) Voltage-current characteristics of a p-n junction photodiode (after Gower, 1984).

random current fluctuation. It can be shown that the mean square shot noise current is given by (Yariv, p.280, 1976),

$$I_S^2 = 2eI_{sig}B \tag{3.27}$$

where I_{sig} is the average signal current due to the incident laser light, e is the electronic charge, and B is the system bandwidth.

In the ideal photodiode all the incident light would be absorbed in the depletion layer, and all carriers generated would be collected. The rate of generation of carriers excited by photons from a monochromatic source of power, P_s, and frequency ν is given by,

$$r = P_s/h\nu \tag{3.28}$$

where $h\nu$ is the photon energy of sufficient magnitude to cause a carrier emission, and h is Planck's constant. Of course in practice some of the incident light is reflected at the semiconductor surface, and not all of the remainder is absorbed in the depletion layer, and equation (3.28) should be modified to include the quantum efficiency of the absorption process, η, where

$$r = \eta P_s/h\nu$$

The average signal current, I_{sig}, due to laser light incident on the photodiode is,

$$I_{sig} = e\eta P_s/h\nu \tag{3.29}$$

assuming no reflection loss at the entrance window. From equation (3.27) and (3.29) the mean square shot noise current can be rewritten as,

$$I_S^2 = 2\eta e^2 P_s B/h\nu \tag{3.30}$$

Consider the detector illuminated with both signal and background radiation. The latter may be due to visible light scatter entering the photodiode. The mean square shot noise current is then given by,

$$I_S^2 = 2\eta e^2 (P_s + P_b)B/h\nu \tag{3.31}$$

where P_b is the power associated with the background radiation. Also

included in P_b is the dark noise current component. Note however that the current associated with the desired optical signal remains that of equation (3.29). The signal to noise ratio for a photodiode is thus given by,

$$\frac{S}{N} = \frac{I_{sig}^2}{I_S^2}$$

which from equations (3.29) and (3.31) gives,

$$\frac{S}{N} = \frac{\eta P_s^2}{2h\nu B(P_s + P_b)} \qquad (3.32)$$

Note that if background power levels are negligible, or can be made negligible by suitable filtering of the light incident on the photodetector, then equation (3.32) can be reduced to the maximum signal to noise ratio attainable with a real photon detector, given by,

$$\frac{S}{N} = \frac{\eta P_s}{2h\nu B} \qquad (3.33)$$

From (3.33) it follows that the minimum power detectable, which by definition is that yielding a signal to noise ratio of unity, is given by,

$$(P_s)_{min} = \frac{2h\nu B}{\eta} \qquad (3.34)$$

This corresponds to the quantum limit of optical detection, where the signal detected is limited by the shot noise in the photodetection process.

3.6.2 Amplification of Photodetected Signals

Most optical photodetection systems require an amplifier to increase the output from the photodetectors to a level which can be measured on an oscilloscope. In doing so, the amplifier contributes its own noise power, which must be included in any signal to noise analysis. The primary causes of noise in an amplifier is shot noise from charge transport in the active devices (i.e. transistors), and amplified thermal

or Johnson noise from the resistive components. The net result is that there is a noise component superimposed on the voltage (or current) output of the amplifier, even when there is no signal input.

In the previous section, signal to noise ratios for the photodetection process were calculated assuming that the photodetector was followed by a noise free amplifier. In practice it is imperative that the amplifier noise be taken into account in any signal to noise analysis.

Another noise contribution is the Johnson noise generated by the output load of the photodetector. The mean square Johnson noise current is (Yariv, p. 282, 1976),

$$I_J^2 = 4kTB/R \qquad (3.35)$$

where R is the value of the load resistance, and T is the absolute temperature. Johnson or thermal noise fluctuations are caused by the thermal motion of charge carriers, and so can be minimised, if necessary, by cooling of the resistor or increasing the resistance value, but the latter may not be desireable if a wide bandwidth is required.

A number of other sources of noise are present in any photodetection system and include (Dereniak and Crowe, p. 100, 1984),

(a) generation-recombination noise,

(b) 1/f noise,

(c) and noise due to temperature fluctuations.

In general these noise sources are negligible and in the analysis given here have been neglected.

Noise powers from different sources can be added directly to obtain the resultant noise. Therefore noise current and voltage sources must be added in quadrature. It follows that in practical photodetection systems, the total noise current is given by,

$$I_T = (I_S^2 + I_J^2 + I_{amp}^2)^{1/2} \qquad (3.36)$$

where I_{amp} is the noise associated with any amplifier used in the system.

3.7 Theoretical Minimum Detectable Displacement of the Interferometer

The photodiode configuration depicted in fig. (3.6) can be redrawn for noise analysis purposes as that shown in fig. (3.21). The total noise in the interferometer system is thus due to shot noise in both photodiodes, Johnson noise of the amplifier input load resistance, and the noise associated with the amplifier itself. The thermal noise components generated by the 1 KΩ diode input resistors are decoupled by the 0.01 μF capacitors (fig. 3.6), and so do not contribute to the output noise current. Rewriting equation (3.36), the total theoretical noise voltage at the output of the interferometer can be evaluated by,

$$V_T = G[(2I_S^2 + I_J^2)R^2 + V_{amp}^2]^{1/2} \qquad (3.37)$$

where R is the amplifier input load resistance, V_{amp} is the amplifier equivalent input noise voltage, and G is the amplifier voltage gain. The signal to noise ratio of the interferometer is thus given by combining equations (3.16) and (3.37) so that,

$$\frac{S}{N} = \frac{(4V_0\pi x/\lambda)^2}{G^2[(2I_S^2 + I_J^2)R^2 + V_{amp}^2]} \qquad (3.38)$$

The minimum detectable displacement, by definition corresponds to a signal to noise ratio of unity, and from equation (3.38) can be expressed as,

$$x_{min} = \frac{\lambda G}{4\pi V_0}[(2I_S^2 + I_J^2)R^2 + V_{amp}^2]^{1/2} \qquad (3.39)$$

or

$$x_{min} = \frac{\lambda G}{4\pi V_0}[4\eta e^2 P_S BR^2 + (4kTBR) + V_{amp}^2]^{1/2} \qquad (3.40)$$

Evaluation of equation (3.41) for an optical power of 0.5 mW incident on photodiodes of quantum efficiency, $\eta = 0.6$, with $e = 1.6 \times 10^{-19}$ C, B = 130 MHz, $h = 6.626 \times 10^{-34}$ Js, $\nu \sim 4.7 \times 10^{14}$ Hz, $k = 1.38 \times 10^{-23}$ J/K,

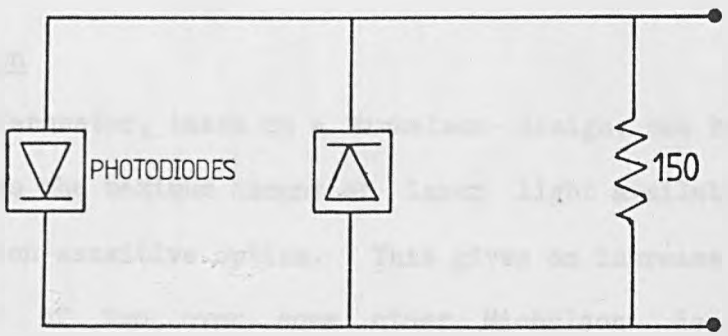

Fig. (3.21) Equivalent photodetection circuit for signal to noise analysis.

R = 150 Ω, T = 300 K, and an amplifier with a voltage gain of 40, and equivalent input noise voltage of 25 μV, and an unstabilised interferometer sensitivity of 3 volts peak to peak, gives a total theoretical minimum displacement detectable with the interferometer of ∿ 47 pm. This figure is somewhat pessimistic with the system noise measured experimentally. Fig. (3.22) shows the base line noise obtained in the output channel of the interferometer when stabilised. It shows that the noise level is ∿ 1 mV_{p-p}, equivalent to a displacement resolution of ∿ 25 pm. This discrepancy between theory and experiment is not understood.

3.8 Conclusion

An interferometer, based on a Michelson design, has been constructed, which utilises the maximum amount of laser light available, with the use of polarisation sensitive optics. This gives an increase in sensitivity by a factor of two over some other Michelson designs. Absolute calibration of the interferometer to give a displacement output is easily implemented. Stabilisation of the interferometer, by means of an electro-mechanical vibrator attached to the reference mirror, has proved effective up to a frequency of ∿ 600 Hz for displacements of ∿ 1.3 μm. Under normal laboratory conditions, stabilisation of 97% was readilly achieved, with environmental disturbances measured to be ∿ 1 μm in the 0 to 100 Hz range. The effects of laser noise have been reduced with use of a balanced photodetection system.

The effect of interference with multi-mode laser radiation has been analysed. It has been shown, both theoretically and experimentally, that maxima in constructive interference can be obtained for the widely used zero path length condition, and additionally at optical path length

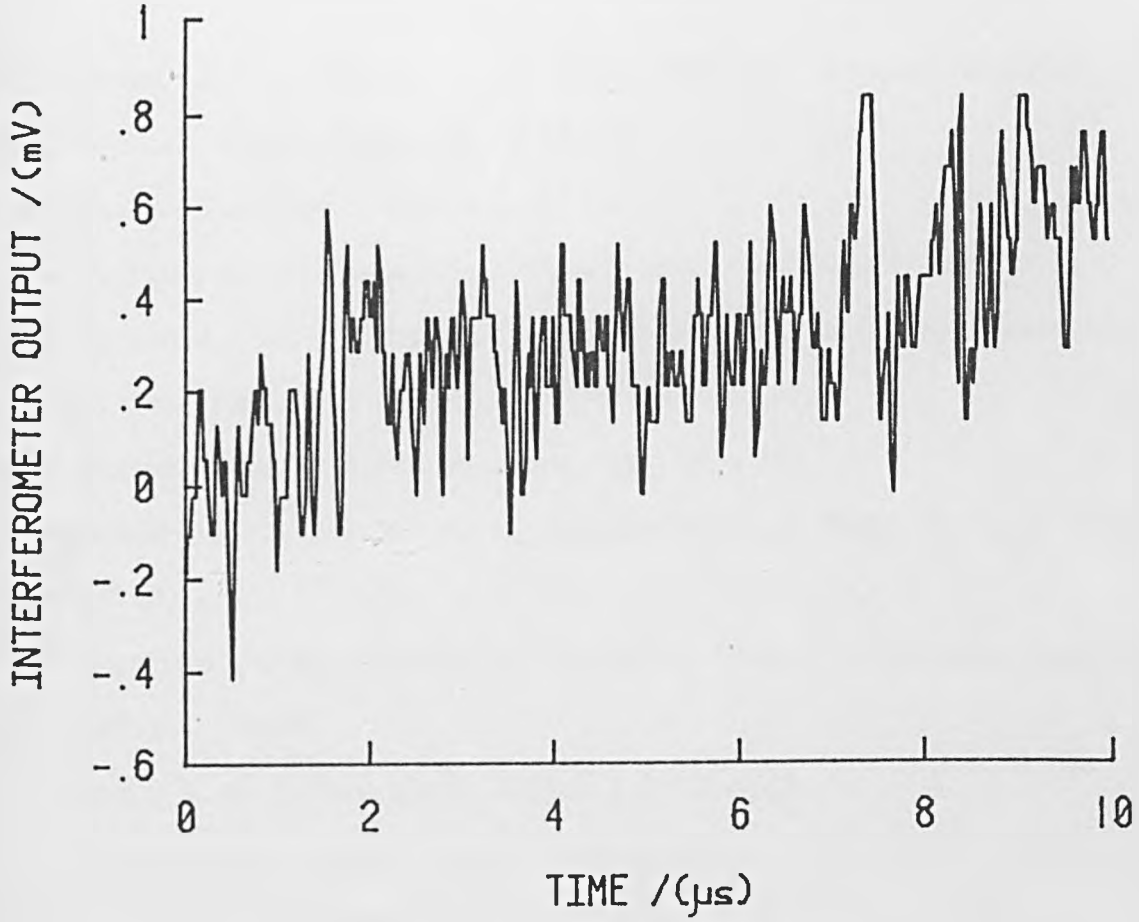

Fig. (3.22) Typical noise waveform of the stabilised Michelson interferometer.

differences equal to an integer multiple of twice the laser cavity length.

The experimentally determined displacement resolution of the interferometer was found to be $\sim$ 25 pm.

3.9 References

M. Born and E. Wolf, "Principles of Optics" (Pergamon Press, New York, second edition, 1964).

E. L. Dereniak, D. G. Crowe, "Optical Radiation Detectors" (John Wiley and Sons, New York, 1984).

L. E. Drain, "The Laser Doppler Technique" (John Wiley and Sons, New York, 1980).

L. E. Drain, J. H. Speake, B. C. Moss, SPIE 1st European Congress on Optics Applied to Metrology, 136 52 (1977).

J. W. Foreman, Jr., Appl. Optics 6 821 (1967).

J. Gower, "Optical Communication Systems" (Prentice/Hall, London, 1984).

E. Hecht and A. Zajac, "Optics" (Addison Wesley Publishing, Amsterdam, sixth edition, 1980).

A. M. Johnson, IEEE J. Quant. Electron. QE-1 99 (1965).

Th. Kwaaitaal, B. J. Luymes, G. A. van der Pijll, J. Phys. D: Appl. Phys. 13 1005 (1980).

R. S. Longhurst, "Geometrical and Physical Optics" (Longmans, London, second edition, 1967).

G. Lucovsky, R. B. Emmons, Appl. Optics 4 697 (1965).

G. Lucovsky, M. E. Lasser, R. B. Emmons, Proc. IEEE 51 166 (1963).

A. A. Michelson, Phil. Mag. XXX1 338 (1891).

B. C. Moss, "The Harwell Laser Interferometer" AERE report no. R10417 (1982).

C. H. Palmer, Appl. Optics 23 3510 (1984).

D. C. O' Shea, W. R. Callen, and W. T. Rhodes, "Introduction to Lasers and their Applications" (Addison Wesley, Amsterdam, 1978).

L. Solymar and D. Walsh, "Lectures on the Electrical Properties of Materials" (Oxford University Press, Oxford, second edition, 1979).

J. T. Verdeyen, "Laser Electronics" (Prentice-Hall, Inc., New Jersey, 1981).

A. Yariv, "Introduction to Optical electronics" (Holt, Rinehart, and Winston, New York, second edition, 1976).

CHAPTER 4

Characterisation and Performance of the Modified Michelson Interferometer

4.0 Introduction

In this chapter the performance of the modified Michelson interferometer is assessed. Both bulk and surface acoustic transients, generated by thermoelastic and plasma sources have been detected in duraluminium, with the interferometer. A comparison of the experimental waveforms has been made with existing theoretical predictions. Experimental results are also presented for generation and detection of ultrasound in a graphite sample. The performance of the Michelson interferometer compared with another absolute device, the capacitance transducer, will be assessed. Finally, two types of electromagnetic acoustic transducers (EMATs), and a broadband piezoelectric transducer will be examined. The comparison will include a study of the risetimes and typical signal to noise ratios of the different detectors.

4.1 Experimental Arrangement

The laser used was a Spectron Laser Systems Ltd. Q-switched neodymium yttrium-aluminium-garnet (Nd:YAG) laser (type SL402), which was capable of a maximum energy output of 250 mJ in a multi-mode 1.06 μm pulse, with typical rise times of 20 ns. The laser energy was stable to within 5% on a shot to shot basis. The acoustic transients were displayed on an oscilloscope, and captured on a Tektronix 7912AD digitiser, which was triggered from the incident laser pulse via a beam

splitter and fast photodiode. The waveforms were stored on a Tektronix MS4101 mini computer for subsequent analysis. All waveforms presented are single shot measurements produced without any surface modification (i.e. grease or oil on the surface) of the sample under investigation, unless otherwise stated.

4.2 Linearity of the Interferometer

It has been shown previously (Dewhurst et. al., 1982) that the amplitudes of the ultrasonic transients produced by a thermoelastic source in a metallic medium, are directly proportional to the incident laser energy. To confirm the linearity of the interferometer, ultrasonic transients were generated in a 50 mm diameter, $\sim$ 24.5 mm thick duraluminium disc in the thermoelastic regime. One face of the sample was irradiated with laser pulses in the energy range 10 to 100 mJ, whilst the interferometer monitored the opposite face, on epicentre. The amplitude of the thermoelastic waveform, which was measured from the zero base line down to the minimum of the waveform at the shear arrival, generated at various incident laser energies is shown plotted in fig. (4.1). The data forms a straight line which passes through the origin, with a gradient of $\sim$ 38 $\pm$ 1 mJ/nm, indicating that the interferometer has a linear response for measuring ultrasonic transients, up to amplitudes of at least 2.5 nm. This gradient agrees with previous data of the variation of the ultrasonic amplitude with laser energy, in the thermoelastic regime (Dewhurst et. al., 1982). They obtained a gradient of $\sim$ 37 mJ/nm using a capacitance transducer as the detector.

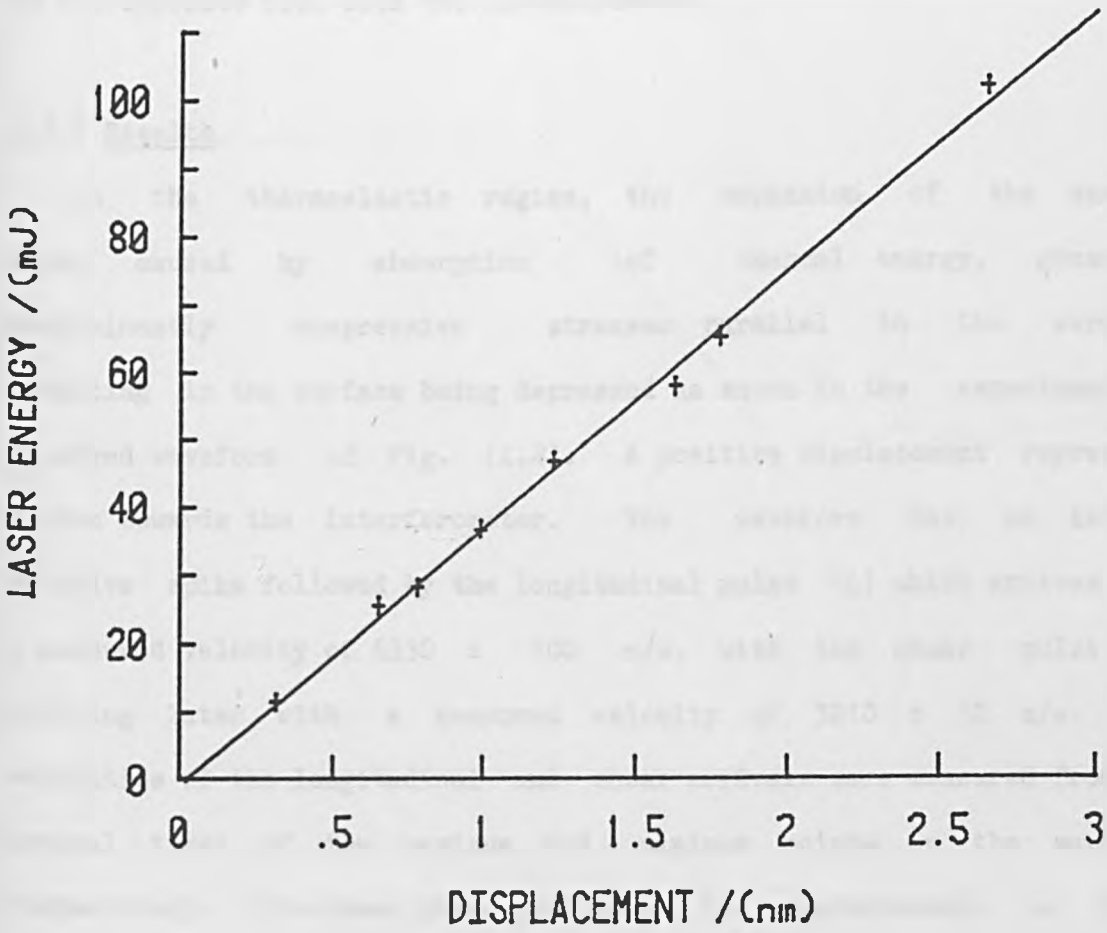

Fig. (4.1) Variation of ultrasonic displacement with laser energy. Interferometric detection is linear up to ultrasonic displacements of at least 2.5 nm.

4.3 Interferometric Detection of Bulk waves in the Thermoelastic Regime

The sample used was a 25 cm square duraluminium plate of thickness 24.5 mm. The dimensions of the plate were chosen so that side wall reflections arrived much later than the direct longitudinal and shear pulses. Laser pulses of $\sim$ 40 mJ energy irradiated one face of the plate. Epicentral detection of the ultrasonic transients was performed on the opposite face with the interferometer.

4.3.1 Results

In the thermoelastic regime, the expansion of the surface layer caused by absorption of thermal energy, generates predominantly compressive stresses parallel to the surface, resulting in the surface being depressed as shown in the experimentally observed waveform of fig. (4.2). A positive displacement represents motion towards the interferometer. The waveform has an initial positive spike followed by the longitudinal pulse (L) which arrives with a measured velocity of 6330 ± 100 m/s, with the shear pulse (S) arriving later with a measured velocity of 3210 ± 50 m/s. The velocities of the longitudinal and shear arrivals were measured from the arrival times of the maximum and minimum points on the waveform respectively. The shear pulse amplitude is approximately 4 times the amplitude of the longitudinal pulse. This empirical relationship was first reported by Scruby et. al. (1980). Fig. (4.3a) was obtained on a longer timescale of 20 μs, where it is evident that there is very little variation in surface displacement with time, after the arrival of the direct shear wave. It should be noted that this latter result was obtained with an incident laser energy of $\sim$ 110 mJ, hence the increase in

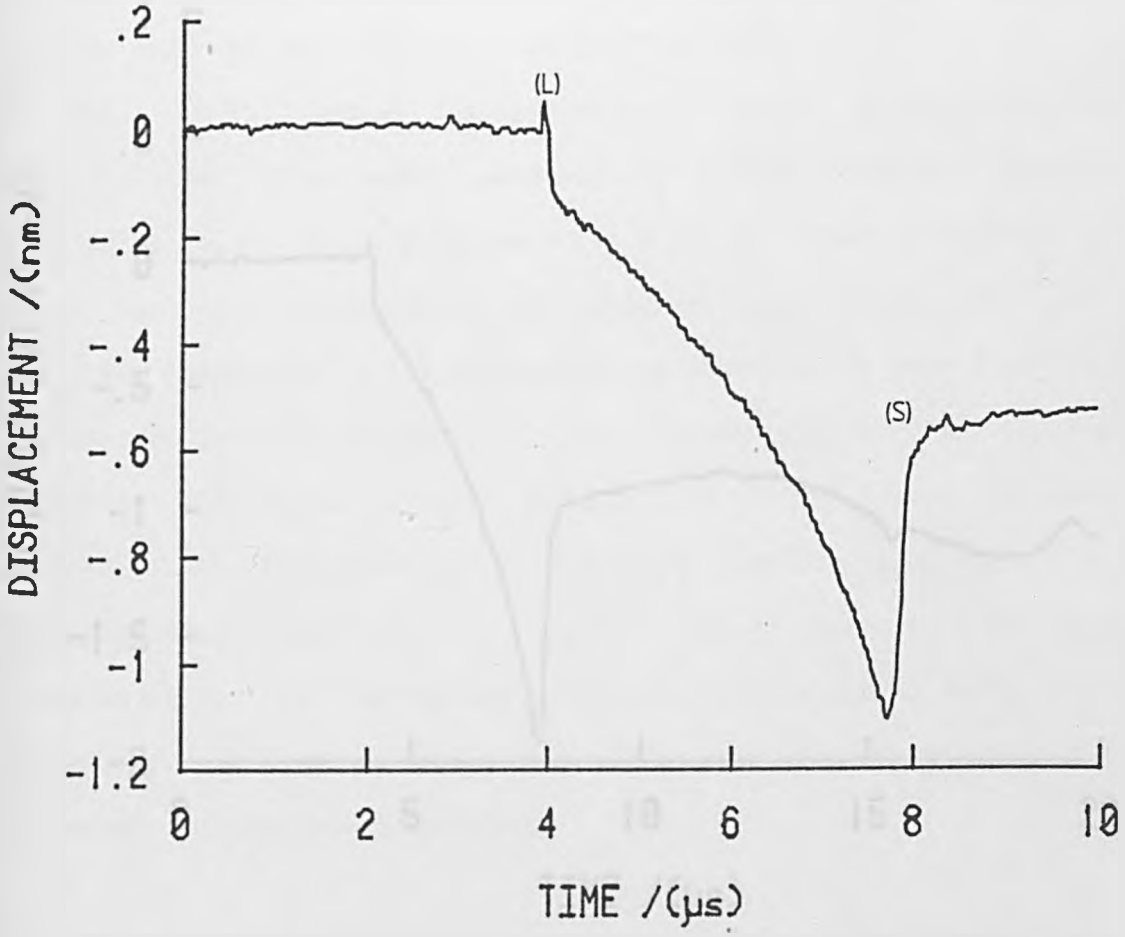

Fig. (4.2) Experimentally observed epicentral waveform in the thermoelastic regime, detected with the interferometer.
(L) denotes the longitudinal wave arrival and
(S) the shear arrival.

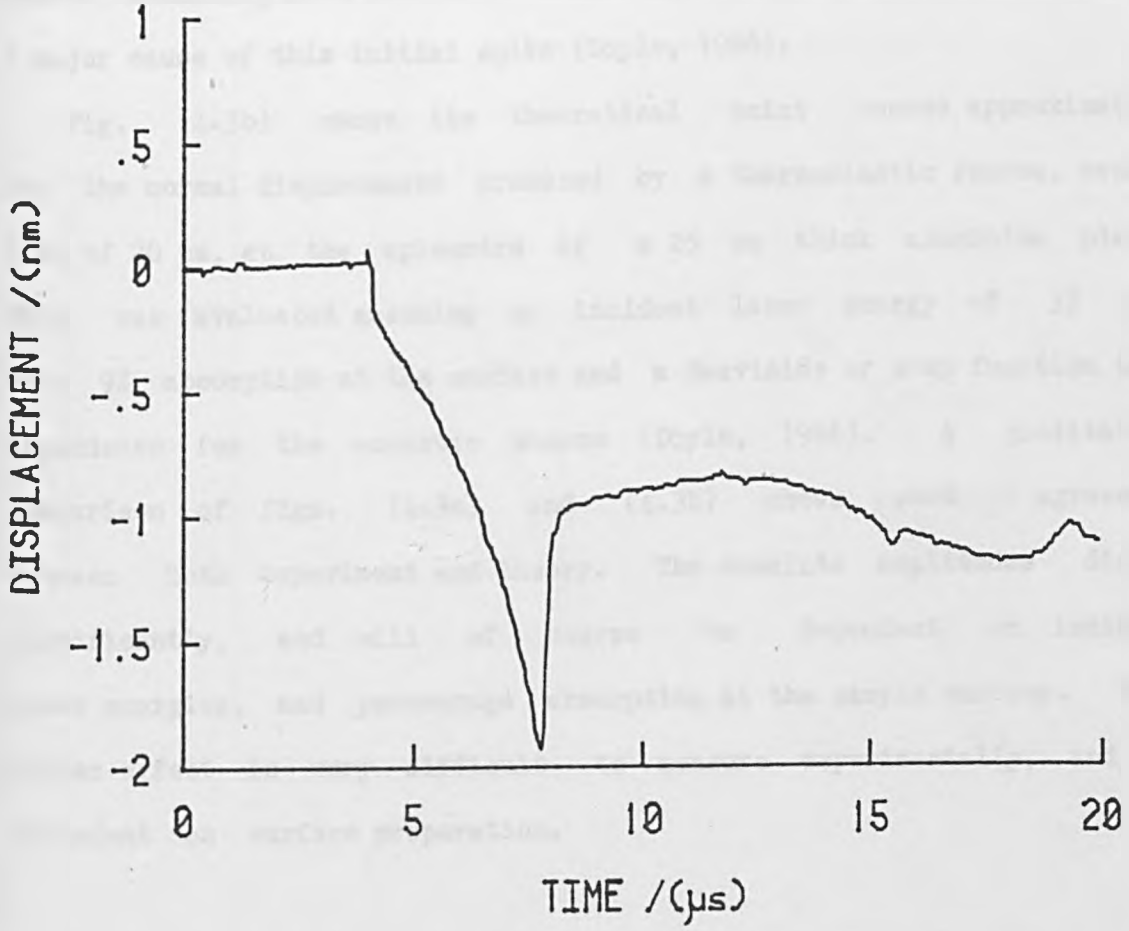

Fig. (4.3a) Experimentally observed epicentral waveform in the thermoelastic regime, detected with the interferometer.

waveform amplitude.

4.3.2 Comparison of Experimental Results with Theoretical Predictions

The initial outward displacement of fig. (4.2) is not predicted by the point source approximation of the thermoelastic source (Rose, 1984), and it has been reported that the finite size of the source, resulting from thermal diffusion into the bulk of the material, is a major cause of this initial spike (Doyle, 1986).

Fig. (4.3b) shows the theoretical point source approximation for the normal displacement produced by a thermoelastic source, over a time of 20 μs, at the epicentre of a 25 mm thick aluminium plate. This was evaluated assuming an incident laser energy of 35 mJ, with 9% absorption at the surface and a Heaviside or step function time dependence for the acoustic source (Doyle, 1986). A qualitative comparison of figs. (4.3a) and (4.3b) shows good agreement between both experiment and theory. The absolute amplitudes differ significantly, and will of course be dependent on incident laser energies, and percentage absorption at the sample surface. This latter effect is very difficult to measure experimentally, and is dependent on surface preparation.

4.4 Interferometric Detection of Bulk Waves in the Plasma Regime

The sample used was a 50 mm diameter, $\sim$ 24 mm thick duraluminium disc, which was polished on one face. Laser pulses of $\sim$ 40 mJ energy, irradiated one face of the sample surface. Interferometric detection of the acoustic transients was performed on the opposite polished face, on epicentre. A 15 cm focal length convex lens was inserted into the generating laser beam path. The incident power

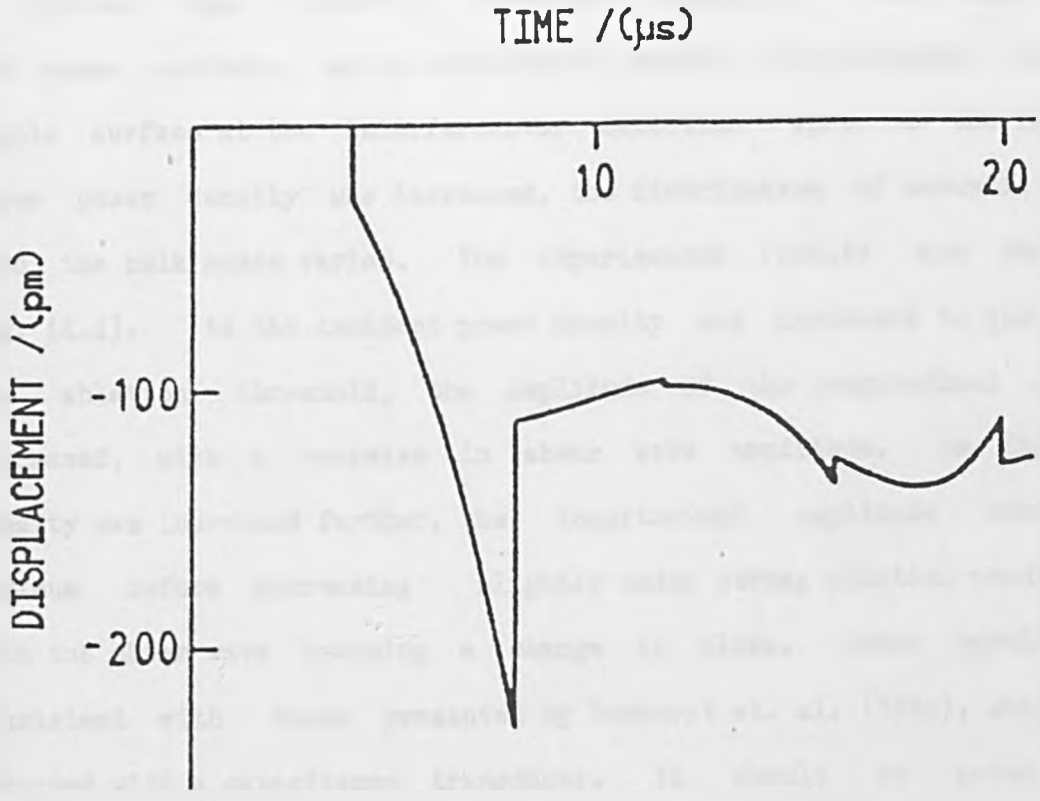

Fig. (4.3b) Normal displacement produced by a thermoelastic source at the epicentre of a 25 mm thick aluminium plate (after Doyle, 1986).

density at the sample surface was increased from the thermoelastic regime, to that producing a strong plasma, by decreasing the focal spot size on the sample surface, while maintaining a constant laser energy.

4.4.1 Results

Typical bulk acoustic waveforms contained both longitudinal and shear arrivals, which constituted vertical displacements of the sample surface at the interferometer detection spot. As the incident laser power density was increased, the distribution of acoustic energy into the bulk modes varied. The experimental results are shown in fig. (4.4). As the incident power density was increased to just above the ablation threshold, the amplitude of the longitudinal arrival increased, with a decrease in shear wave amplitude. As the power density was increased further, the longitudinal amplitude reached a maximum before decreasing slightly under strong ablation conditions, with the shear wave becoming a change in slope. These results are consistent with those presented by Dewhurst et. al. (1982), which were recorded with a capacitance transducer. It should be noted that the thermoelastic waveform represents an overall depression of the sample surface, in a direction away from the interferometer, while the strong plasma produces displacements in a direction towards the interferometer.

A qualitative comparison has been made between the waveforms of fig. (4.4) detected with the interferometer, and the waveforms of fig. (4.5) detected with a capacitance transducer. Both sets of data were captured under similar irradiation conditions on duraluminium samples whose thicknesses differed slightly, and are in excellent agreement. However, as expected, results obtained using the broadband interferometer

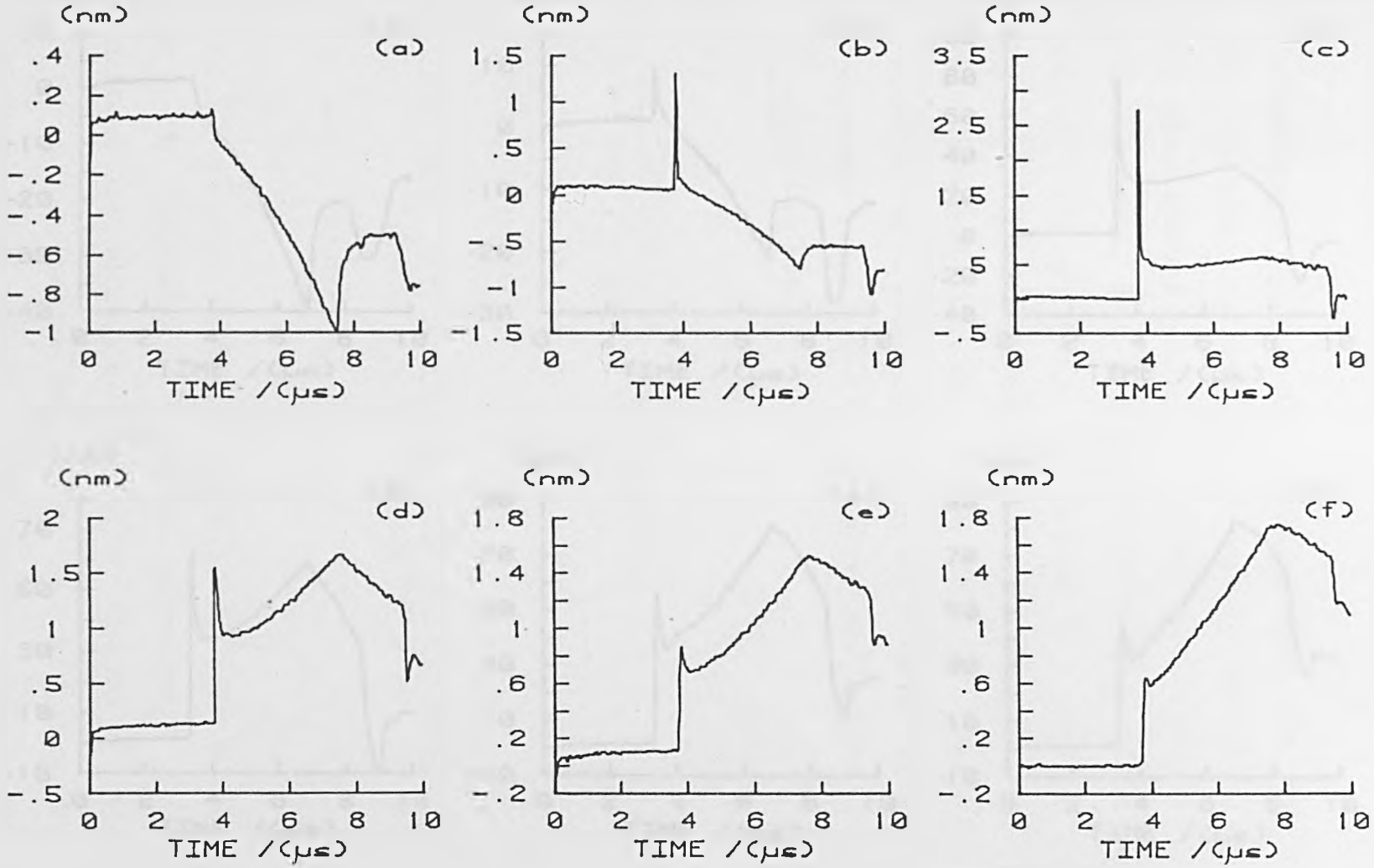

Fig. (4.4) Acoustic waveforms detected with the interferometer in an aluminium sample, for increasing incident laser power density.

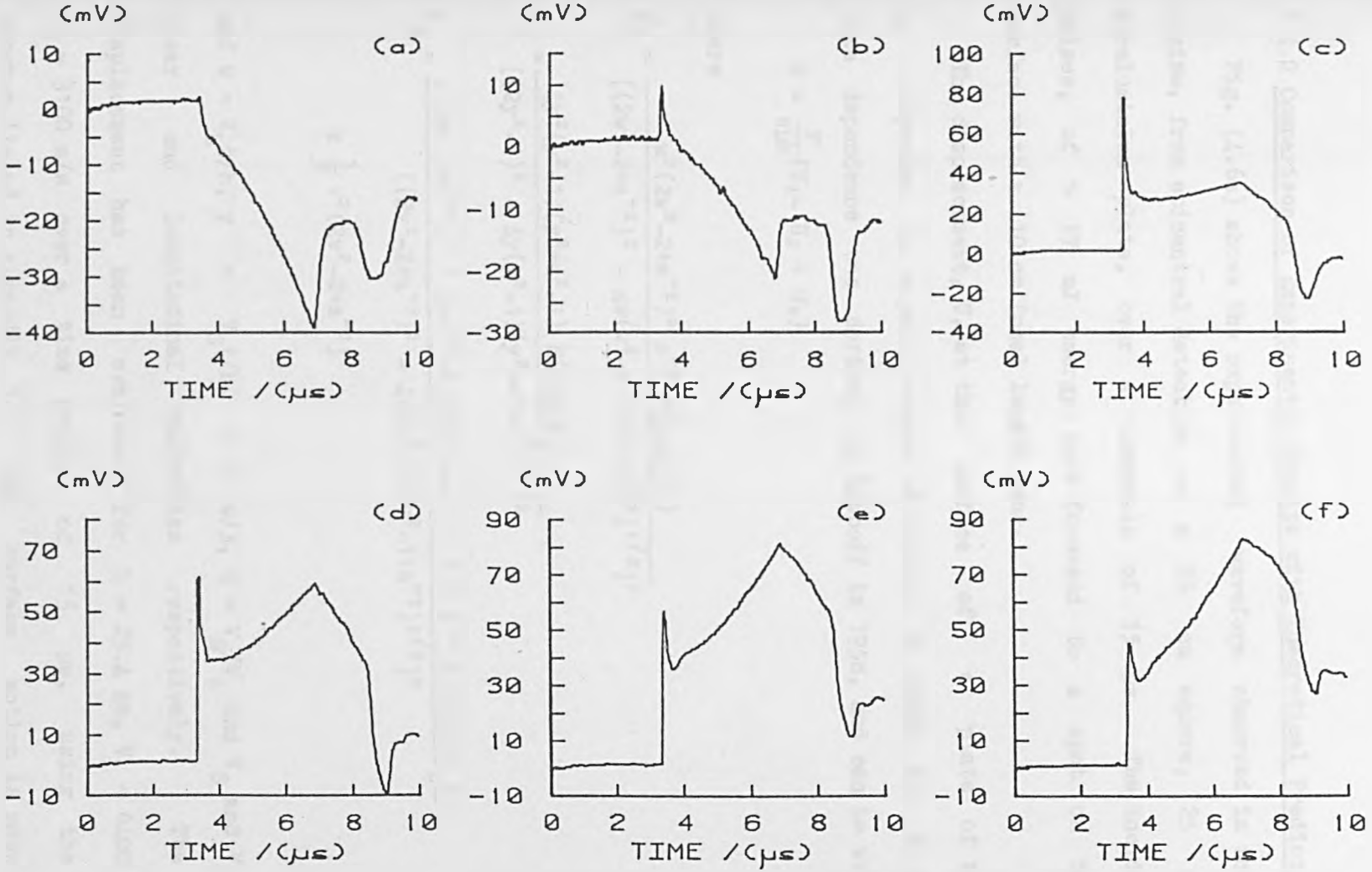

Fig. (4.5) Acoustic waveforms detected with a capacitance transducer in an aluminium sample, for increasing incident laser power density.

display sharper acoustic transients than those recorded with the capacitance transducer.

4.4.2 Comparison of Experimental Results with Theoretical Predictions

Fig. (4.6a) shows the experimental waveform observed in the plasma regime, from epicentral detection on a 25 cm square, 25 mm thick duraluminium plate, over a timescale of 15 μs. The incident laser pulses, of ∿ 17 mJ energy, were focussed to a spot on the sample surface with a 10 cm focal length lens.

The displacement, U, at the surface of a plate of thickness, h, subjected to a point source of stress, F, which has a Heaviside time dependence was derived by Knopoff in 1958, and can be written as,

$$U = \frac{F}{\pi\mu h}[U_1 - U_2 + U_3]$$

where

$$U_1 = \frac{w^2(2w^2-2+a^{-2})^2\ a^{-2}\ H(t-h/V_L)}{[(2w^2-2+a^{-2})^2 - 4w(w^2-1)(w^2-1+a^{-2})^{1/2}]^2}$$

$$U_2 = \frac{4y^2(y^2-1)(y^2+a^2-1)\ H(t-h/V_S)}{[(2y^2-1)^2 - 4y(y^2-1)(y^2+a^2-1)^{1/2}]^2}$$

$$U_3 = \frac{[(2v^2-2+a^{-2})^2 + 4v(v^2-1)(v^2-1+a^{-2})^{1/2}]^2\ a^{-4}\ H(t-3h/V_L)}{[(2v^2-2+a^{-2})^2 - 4v(v^2-1)(v^2-1+a^{-2})^{1/2}]^4}$$

$$\times \frac{1}{3}\ v^2(2v^2-2+a^{-2})$$

and $w = V_L t/h$, $y = V_S t/h$, $v = w/3$, $a = V_S/V_L$ and V_S and V_L are the shear and longitudinal velocities respectively. The surface displacement has been evaluated for $h = 25.4$ mm, $V_L = 6400$ m/s, and $V_S = 3100$ m/s over a time period of 15 μs, using the computer program listed in appendix 1. The surface motion is shown in fig. (4.6b) displayed with arbitrary units of amplitude. Both figures

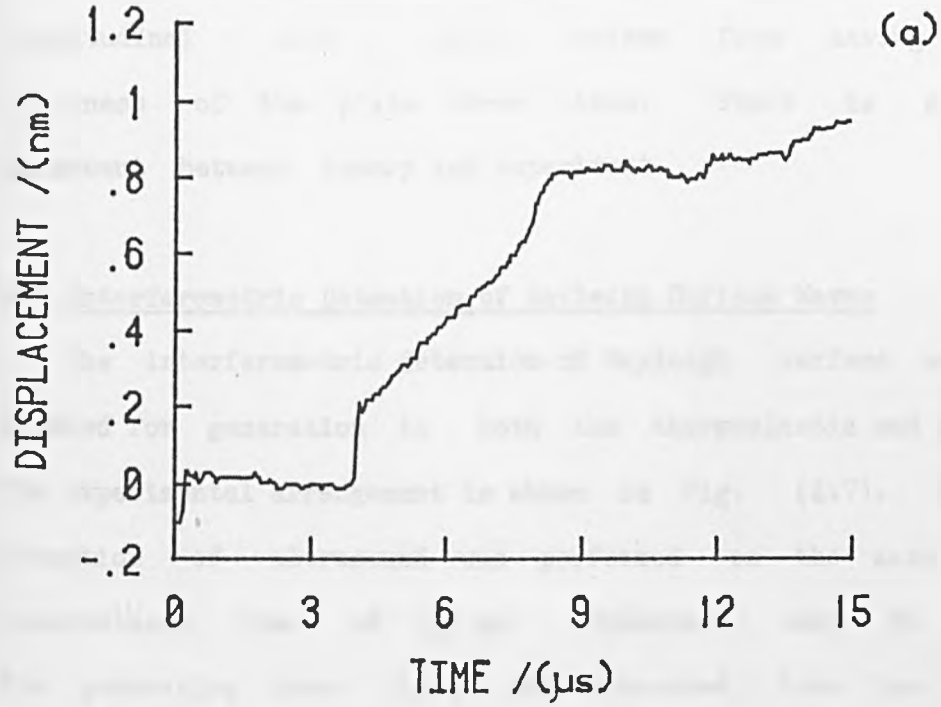

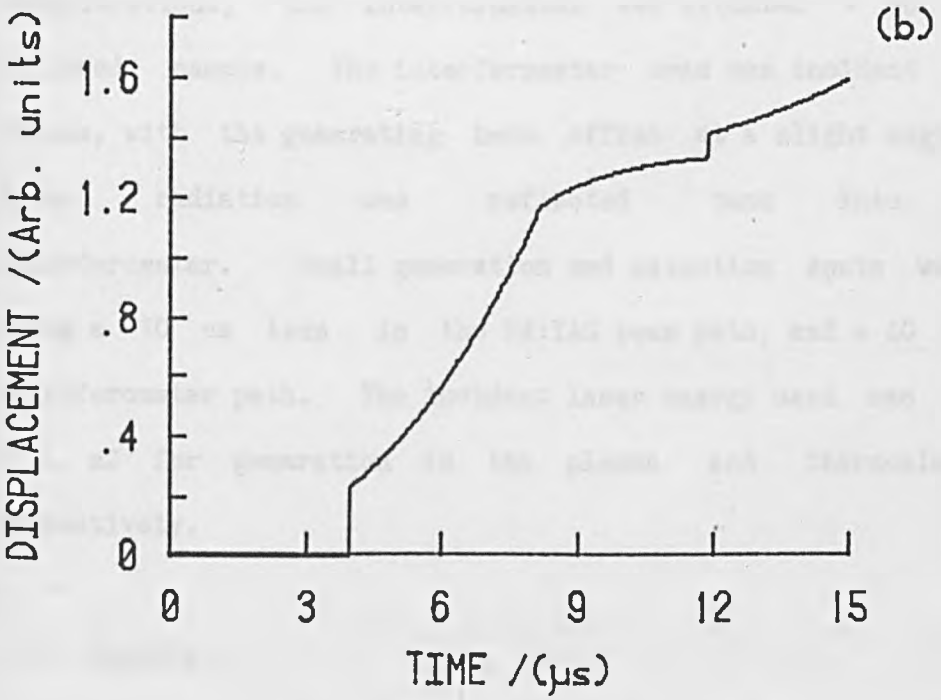

Fig. (4.6) A comparison of experimental and theoretical waveforms in the plasma regime
(a) detected with the interferometer.
(b) Model based on the theory of Knopoff (1958), evaluated using the program in appendix 1.

show the direct longitudinal and shear waves, and the first reflected longitudinal wave which arises from having traversed the thickness of the plate three times. There is again excellent agreement between theory and experiment.

4.5 Interferometric Detection of Rayleigh Surface Waves

The interferometric detection of Rayleigh surface waves has been studied for generation in both the thermoelastic and plasma regimes. The experimental arrangement is shown in fig. (4.7). Generation and detection of ultrasound was performed on the same side of a duraluminium disc of 130 mm diameter, and 50 mm thickness. The generating laser beam was separated from the interferometer detection spot by $\sim$ 12 mm for the plasma regime and $\sim$ 15 mm for the thermoelastic regime. For ease of optical alignment and coherence considerations, the interferometer was situated $\sim$ 50 cm from the polished sample. The interferometer beam was incident normal to the sample, with the generating beam offset at a slight angle such that no laser radiation was reflected back into the laser interferometer. Small generation and detection spots were obtained by using a 10 cm lens in the Nd:YAG beam path, and a 40 cm lens in the interferometer path. The incident laser energy used was $\sim$ 20 mJ and $\sim$ 4 mJ for generation in the plasma and thermoelastic regimes respectively.

4.5.1 Results

Figs. (4.8a) and (4.8b) show Rayleigh surface waves which were generated in the thermoelastic and plasma regimes respectively. The Rayleigh wave amplitude (R) is much greater than that of the

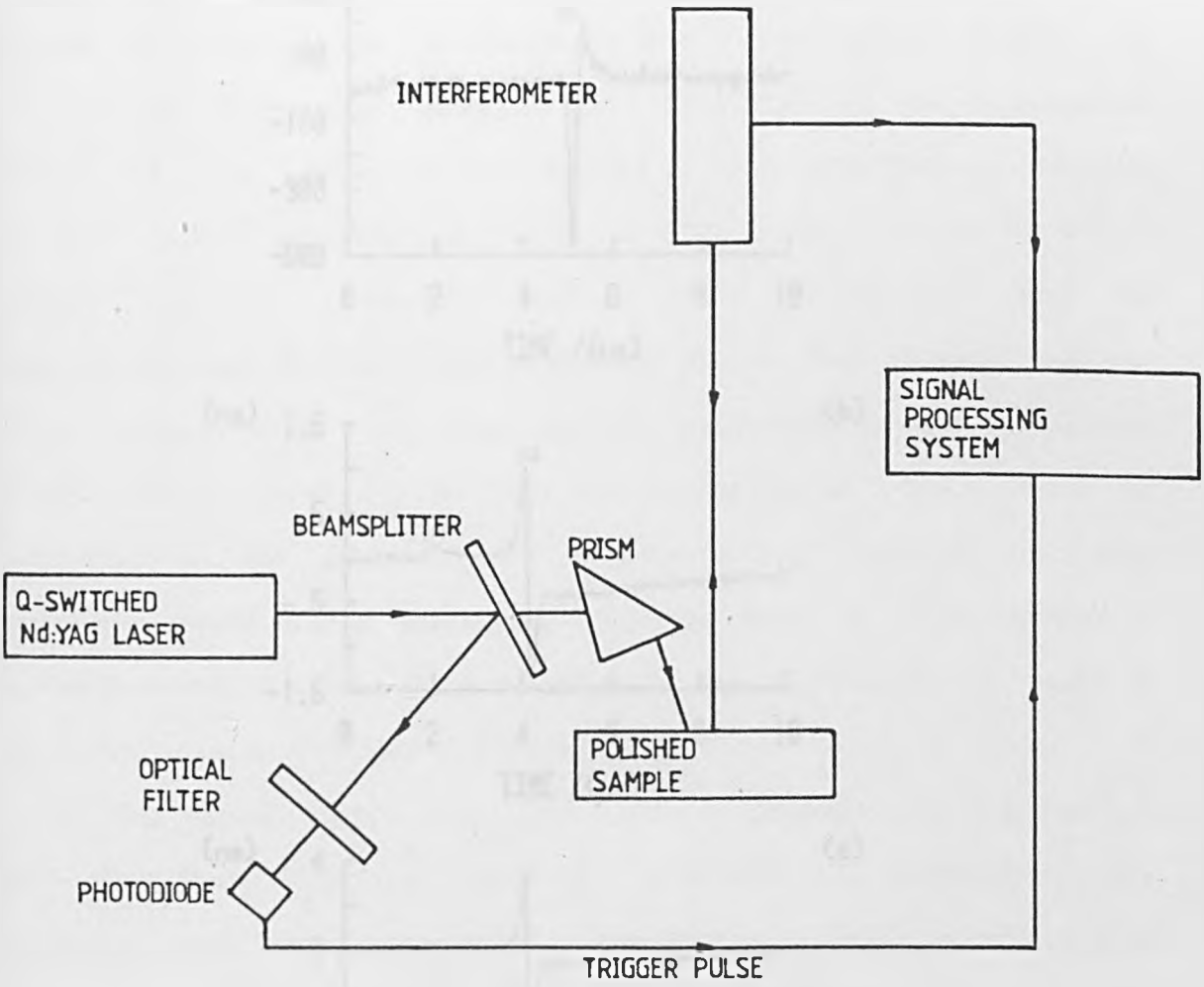

Fig. (4.7) Schematic diagram of the experimental arrangement used for the detection of surface waves.

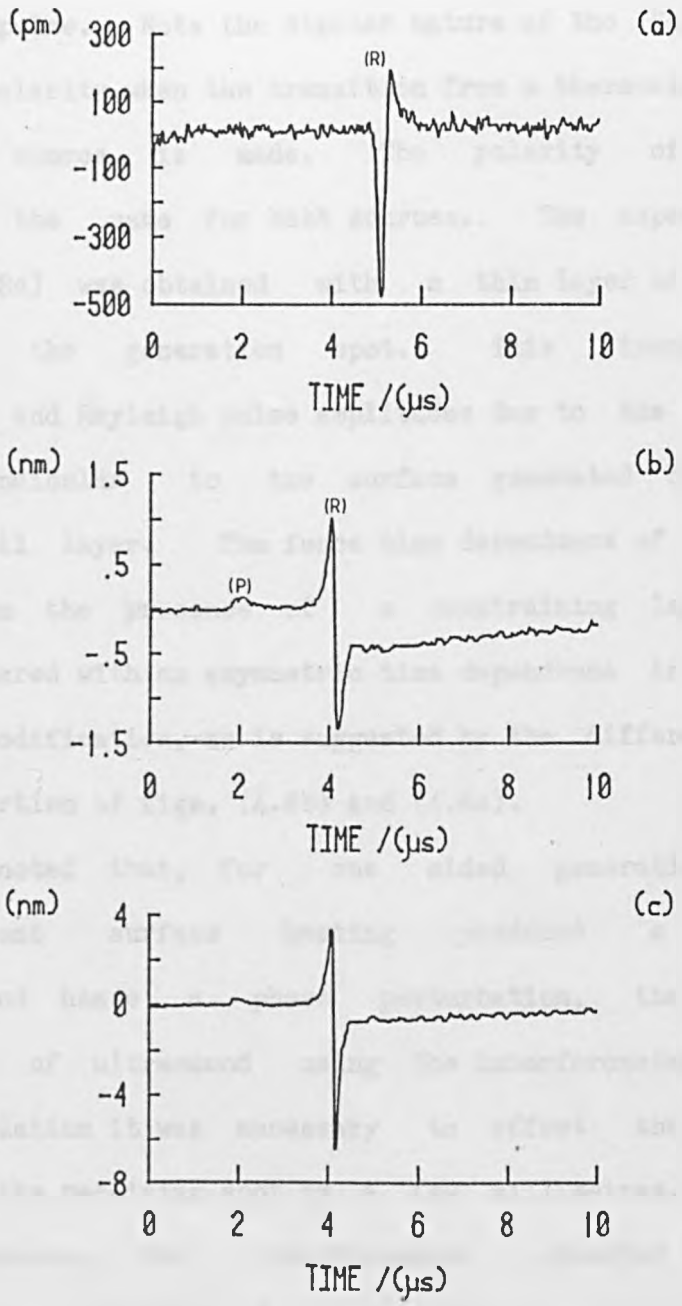

Fig. (4.8) Surface acoustic waveforms detected with the interferometer.
(a) Thermoelastic source
(b) Plasma source
(c) Oil layer source

longitudinal arrival (P). The shear arrival is not separately observed since its velocity is only just greater than that of the Rayleigh wave, which was evaluated as 2920 ± 62 m/s. The Rayleigh wave velocity has been evaluated from the time of arrival of the first peak of the Rayleigh pulse. Note the dipolar nature of the Rayleigh pulse which inverts its polarity when the transition from a thermoelastic source to a plasma source is made. The polarity of the longitudinal arrival is the same for both sources. The experimental waveform of fig. (4.8c) was obtained with a thin layer of oil on the sample surface at the generation spot. This increased both the longitudinal and Rayleigh pulse amplitudes due to the momentum transfer force perpendicular to the surface generated by the evaporation of the thin oil layer. The force time dependence of the source is delta-like in the presence of a constraining layer on the sample surface, compared with an asymmetric time dependence in the absence of any surface modification, as is suggested by the difference in shape of the latter portion of figs. (4.8b) and (4.8c).

It was noted that, for one sided generation and detection, the transient surface heating produced a refractive index variation, and hence a phase perturbation, that interfered with the detection of ultrasound using the interferometer. In the case of surface ablation it was necessary to offset the generating spot from that of the receiving spot by a few millimetres. Even then, on longer timescales, the interferometer detected a large amplitude displacement due to the refractive index variation caused by the plasma blast wave, as shown in fig. (4.9).

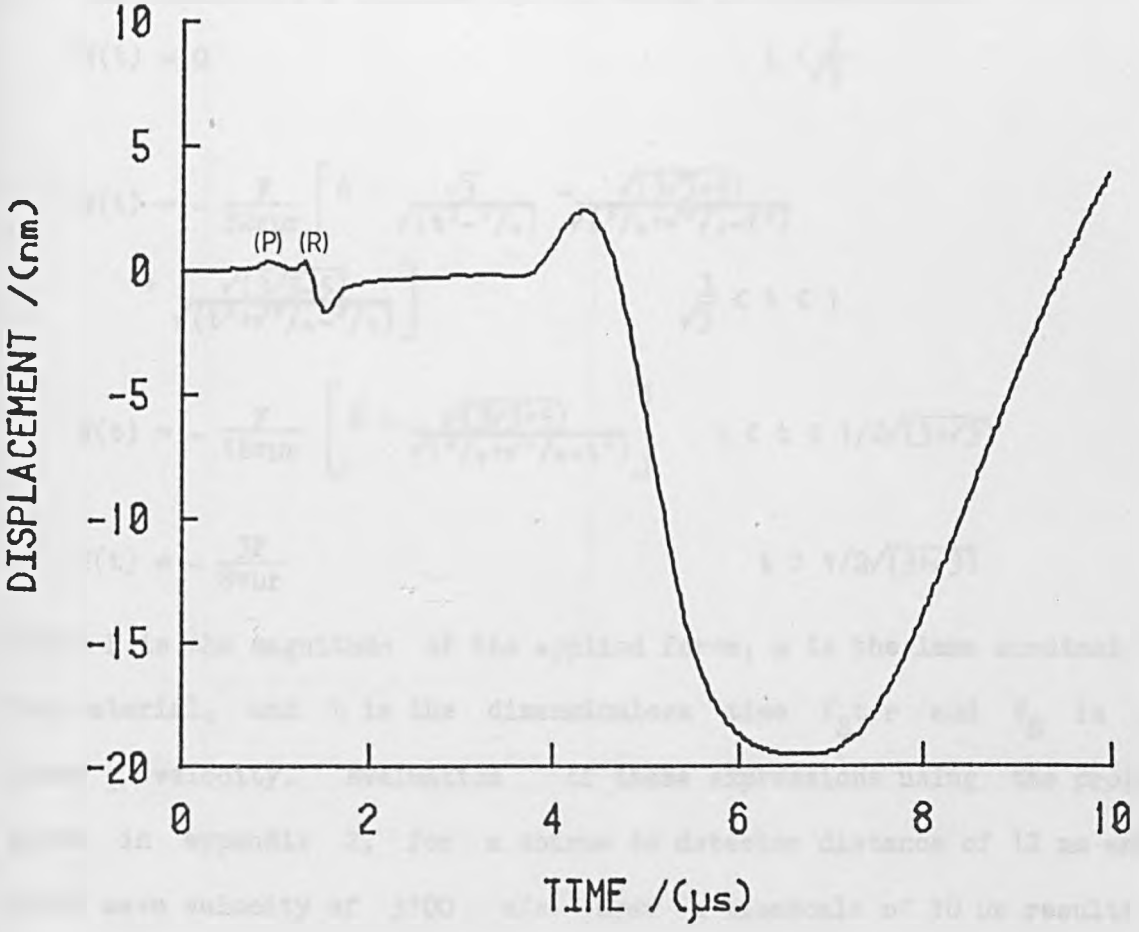

Fig. (4.9) Acoustic waveform showing the large displacement detected by the interferometer, produced by a plasma "blast" wave travelling along the sample surface. Initial features show the longitudinal (P) and Rayleigh (R) pulses.

4.5.2 Comparison of Experimental Results with Theoretical Predictions

The motion of the surface of a uniform elastic half space, produced by the application at the surface of a normal point loading, with a Heaviside time dependence has been the subject of a number of papers, with Lamb's paper being the first in 1904. In 1955 Pekeris presented a complete solution for the displacement W(t) of the surface at a distance r, from which it follows that,

$$W(t) = 0 \qquad t < \frac{1}{\sqrt{3}}$$

$$W(t) = -\frac{F}{32\pi\mu r}\left[6 - \frac{\sqrt{3}}{\sqrt{(t^2-1/4)}} - \frac{\sqrt{(3\sqrt{3}+5)}}{\sqrt{(3/4+\sqrt{3}/4-t^2)}} + \frac{\sqrt{(3\sqrt{3}-5)}}{\sqrt{(t^2+\sqrt{3}/4-3/4)}}\right] \qquad \frac{1}{\sqrt{3}} < t < 1$$

$$W(t) = -\frac{F}{16\pi\mu r}\left[6 - \frac{\sqrt{(3\sqrt{3}+5)}}{\sqrt{(3/4+\sqrt{3}/4-t^2)}}\right] \qquad 1 < t < 1/2\sqrt{(3+\sqrt{3})}$$

$$W(t) = -\frac{3F}{8\pi\mu r} \qquad t > 1/2\sqrt{(3+\sqrt{3})}$$

where F is the magnitude of the applied force, μ is the lame constant for the material, and t is the dimensionless time $V_S t/r$ and V_S is the shear velocity. Evaluation of these expressions using the program given in appendix 2, for a source to detector distance of 12 mm and a shear wave velocity of 3100 m/s over a timescale of 10 μs results in the theoretical surface displacement depicted in fig. (4.10). As in the experimentally obtained waveforms, the surface displacement is dominated by the Rayleigh wave, with a small precursor associated with the longitudinal arrival. The constant negative step predicted in the theoretical model differs from the experimental waveform since the laser source does not have an exact Heaviside dependence.

A more rigorous analysis calculating the vertical displacement

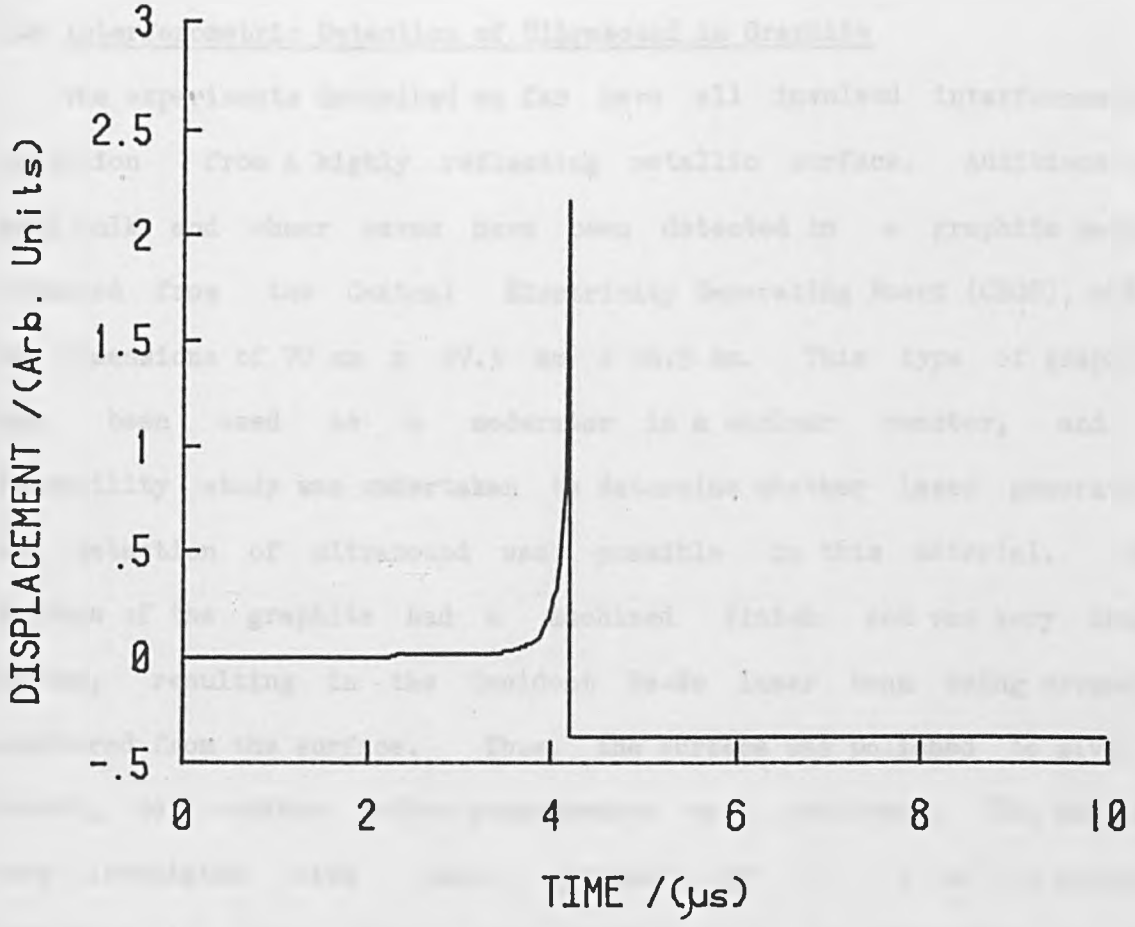

Fig. (4.10) Theoretically predicted displacement on the surface of a uniform elastic half space, produced by the application at the surface of a normal point loading, having a Heaviside time dependence.
Theory derived from Pekeris (1957) and evaluated with the program in appendix 2.

for a normal force which has a gaussian time dependence, results in fig. (4.11a) (Scruby et. al., 1982). The same authors also calculated the theoretical thermoelastic source, assuming the source to be a horizontal force dipole lying in the surface, resulting in fig. (4.11b). Comparison of figs. (4.8) and (4.11) gives excellent agreement between experiment and theory.

4.6 Interferometric Detection of Ultrasound in Graphite

The experiments described so far have all involved interferometric detection from a highly reflecting metallic surface. Additionally, both bulk and shear waves have been detected in a graphite sample obtained from the Central Electricity Generating Board (CEGB), which had dimensions of 70 mm x 27.5 mm x 26.5 mm. This type of graphite has been used as a moderator in a nuclear reactor, and a feasability study was undertaken to determine whether laser generation and detection of ultrasound was possible in this material. The surface of the graphite had a machined finish and was very badly pitted, resulting in the incident He-Ne laser beam being severely scattered from the surface. Thus, the surface was polished to give a smooth, dull surface before measurements were performed. The samples were irradiated with laser pulses of $\sim$ 17 mJ in energy, resulting in figs. (4.12a) and (4.12b) taken on epicentre in the thermoelastic and plasma regimes respectively. Although only 17 mJ of laser energy was used in the thermoelastic regime, the black sample surface gave rise to high absorption and hence the large amplitude longitudinal arrival shown in fig. (4.12a). Repetition of these experiments at different points on the sample surface changed the form of the structure between the longitudinal and shear arrivals, seen in

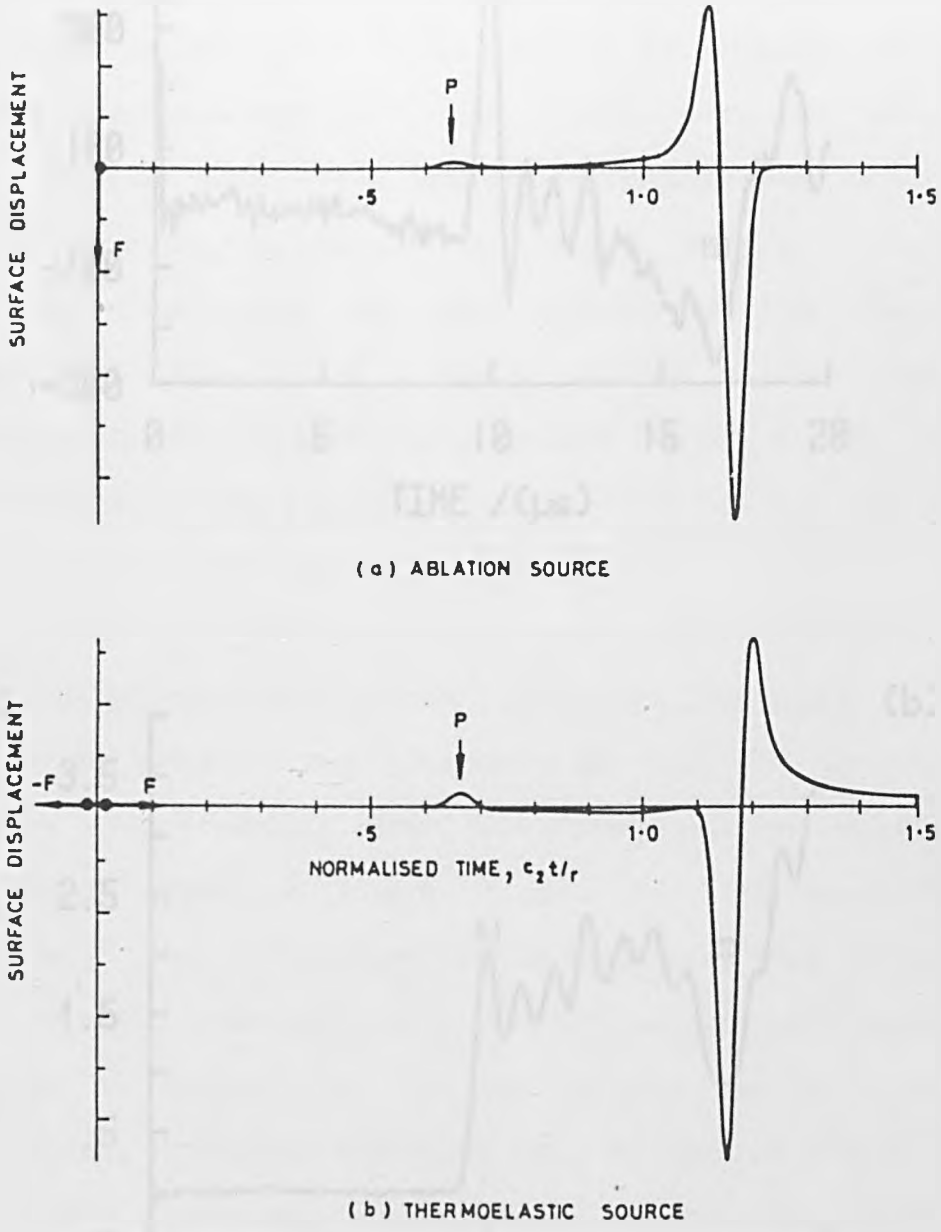

Fig. (4.11) Surface acoustic waveforms computed by Scruby et. al. (1982) for the
(a) ablation and
(b) thermoelastic sources.

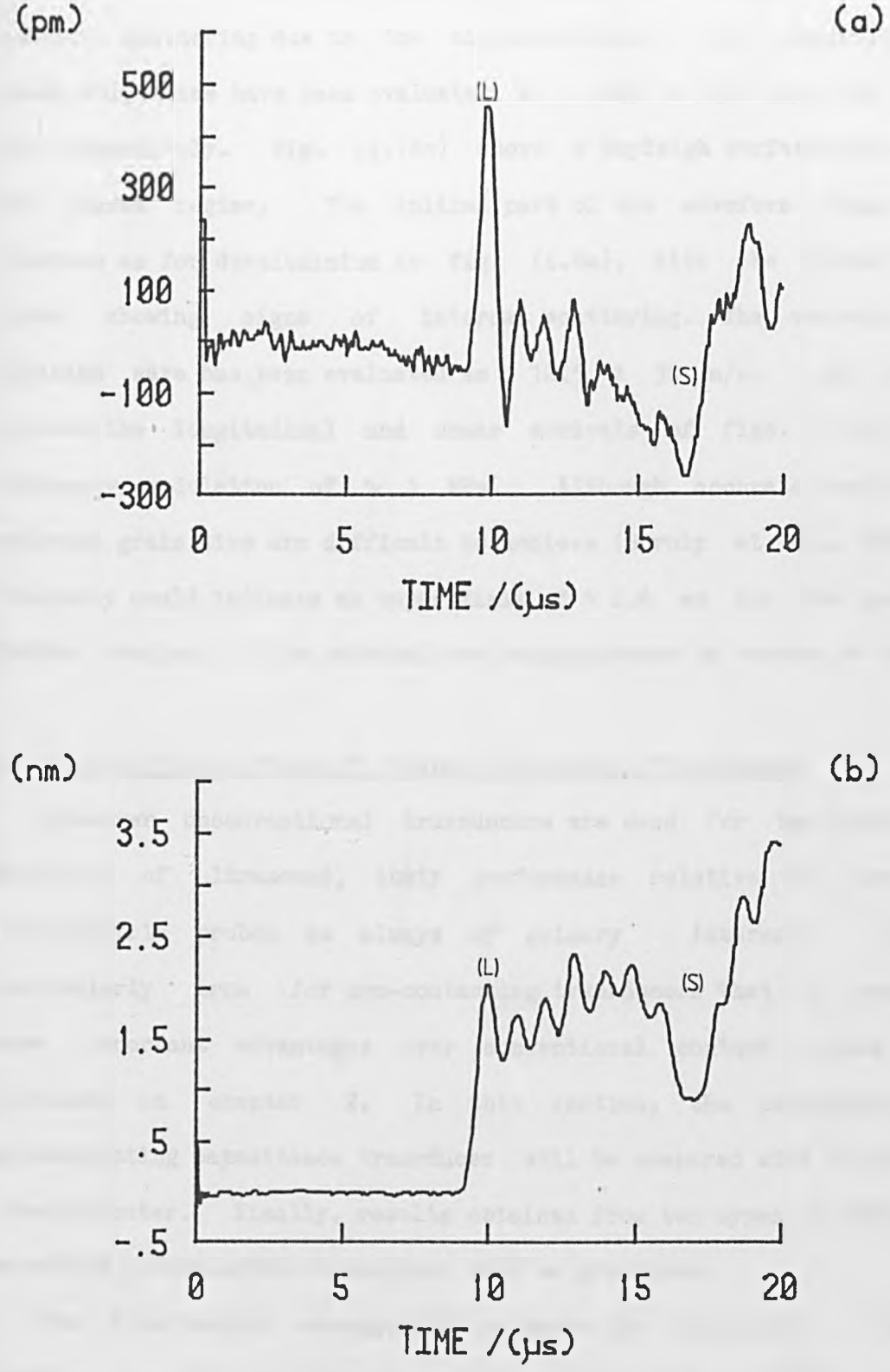

Fig. (4.12) Bulk acoustic waveforms detected in graphite in the
(a) thermoelastic regime and
(b) the plasma regime.

both figures, and is therefore thought to arise from forward acoustic scattering due to the microstructure. The longitudinal and shear velocities have been evaluated as 2670 ± 50 m/s and 1400 ± 30 m/s respectively. Fig. (4.12c) shows a Rayleigh surface wave taken in the plasma regime. The initial part of the waveform shows similar features as for duraluminium in fig. (4.8a), with the latter portion again showing signs of internal scattering. The velocity of the Rayleigh wave has been evaluated as 1245 ± 30 m/s. The structure between the longitudinal and shear arrivals of figs. (4.12) has a frequency modulation of ∿ 1 MHz. Although accurate predictions of material grain size are difficult to achieve (Scruby et. al., 1986), this frequency would indicate an upper limit of ∿ 2.6 mm for the grain size. Further studies in this material are being pursued by workers at the CEGB.

4.7 A Quantitative Study of Wideband Ultrasonic Transducers

Whenever unconventional transducers are used for the generation or detection of ultrasound, their performance relative to conventional piezoelectric probes is always of primary interest. This is particularly true for non-contacting transducers that in some cases have important advantages over conventional contact probes as was discussed in chapter 2. In this section, the performance of a non-contacting capacitance transducer will be compared with the Michelson interferometer. Finally, results obtained from two types of EMATs, and a broadband piezoelectric transducer will be presented.

The experimental arrangement is shown in fig.(4.13). The test specimen was a 50 mm diameter, 25.4 mm thick, duraluminium alloy disc which was mounted on a micrometer adjustable mount to allow easy alignment of the interferometer. As in previous sections, to

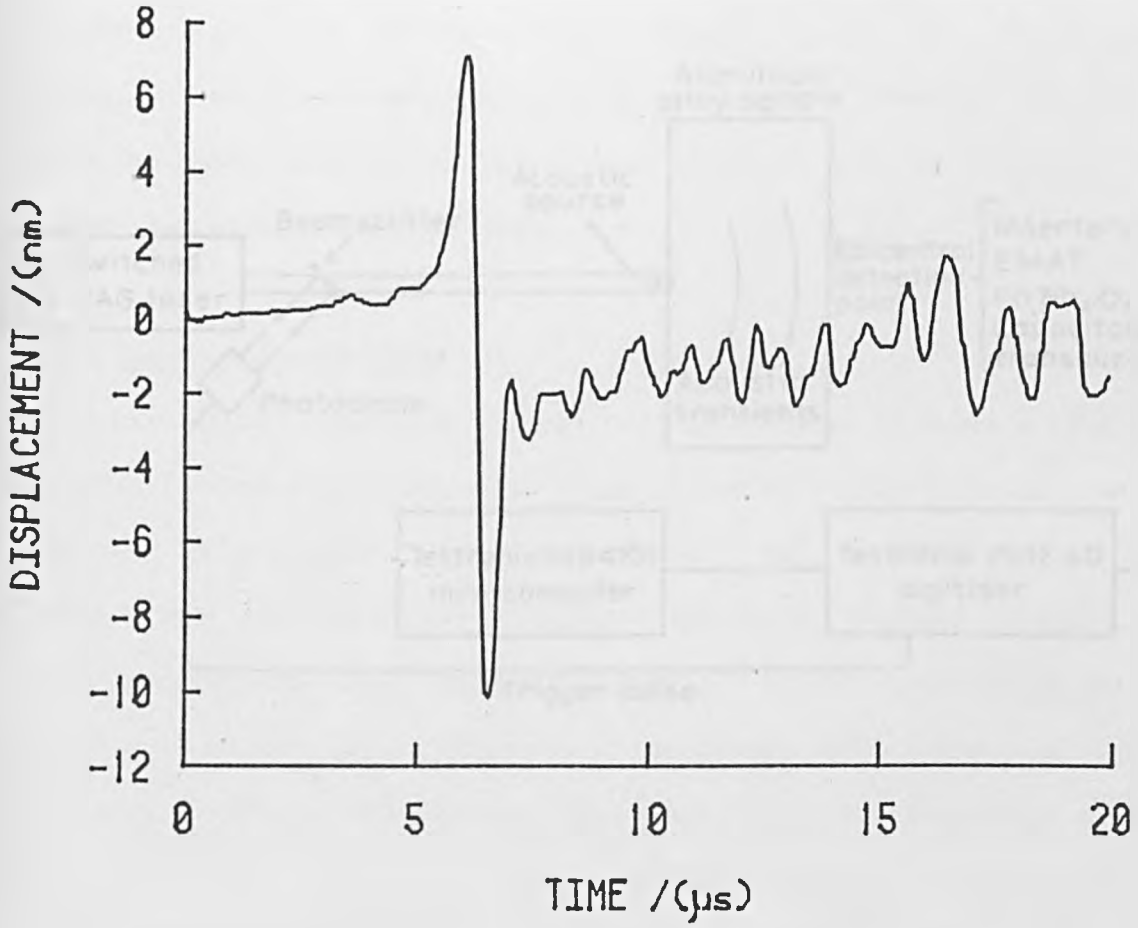

Fig. (4.12c) Rayleigh surface wave detected on graphite. Features after the Rayleigh pulse are thought to arise from scattering from the microstructure.

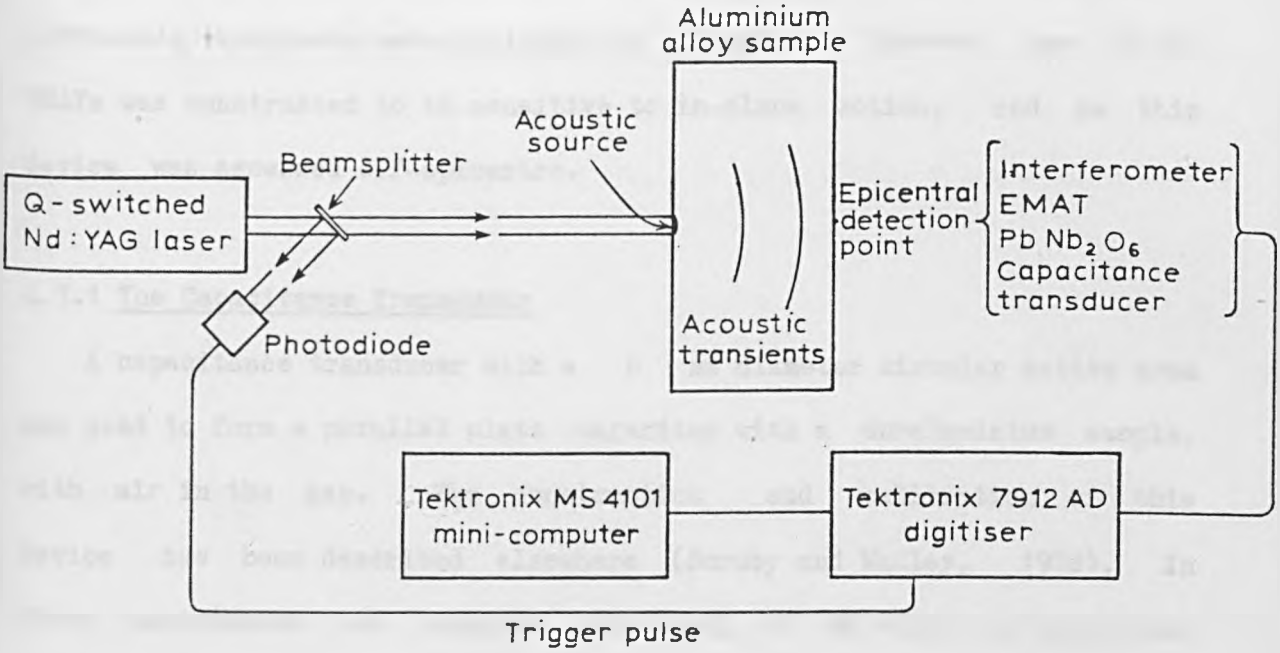

Fig. (4.13) Schematic diagram of the experimental arrangement. Transducers detecting on epicentre were either an interferometer, an EMAT, a piezoelectric or a capacitance transducer.

facilitate the operation of both the capacitance probe and interferometer, the sample surface was polished on the detection side. A 4 mm diameter spot at the centre of the generation side of the sample was irradiated with 20 ns risetime, 50 mJ energy, laser pulses.

The laser power density at the sample surface was below the threshold for material ablation so that ultrasonic generation occurred in the thermoelastic regime. Most of the generated ultrasonic transients were monitored on epicentre. However, one of the EMATs was constructed to be sensitive to in-plane motion, and so this device was assessed off-epicentre.

4.7.1 The Capacitance Transducer

A capacitance transducer with a 6 mm diameter circular active area was used to form a parallel plate capacitor with a duraluminium sample, with air in the gap. The construction and calibration of this device has been described elsewhere (Scruby and Wadley, 1978). In these experiments an applied potential of 80 volts was maintained across a 10 μm air gap. Ultrasonic transients that travelled across the sample surface and between the face of the transducer altered the width of the gap, and hence the capacitance. By maintaining a fixed voltage across the gap, the charge altered linearly with the gap width and was monitored using a charge amplifier, which had a 0 to $\wedge$ 7 MHz bandwidth and a sensitivity of 250 mV/pC.

4.8 Cross-calibration of the Interferometer with the Capacitance Transducer

Figs. (4.14a) and (4.14b) show the normal epicentral response to the ultrasonic transients, as detected with the interferometer and capacitance probe respectively on the same polished duraluminium sample. The features of these waveforms have already been described in section 4.3.1.

4.8.1 Calibration of the Capacitance Transducer

For a transducer with an active plate area A, forming a parallel plate capacitor with the sample surface, the capacitance C_g of the air gap is given by,

$$C_g = \frac{\varepsilon_0 A}{x} \tag{4.1}$$

where ε_0 is the permittivity of free space.

$$dC_g = -\frac{\varepsilon_0 A}{x^2}\, dx$$

or $$dC_g = -\frac{C_g}{x}\, dx \tag{4.2}$$

But $dq = V dC_g$ and from equation (4.2),

$$\frac{dq}{dx} = -\frac{C_g V}{x} \tag{4.3}$$

The absolute displacement sensitivity of the capacitance transducer can be represented as,

$$\frac{dV}{dx} = \frac{dV}{dq} \cdot \frac{dq}{dx} = -\frac{dV}{dq} \cdot \frac{C_g V}{x} \tag{4.4}$$

where dV/dq is the sensitivity of the charge amplifier.

$$\frac{dV}{dx} = -\frac{dV}{dq} \cdot \frac{V C_g^2}{\varepsilon_0 A} \tag{4.5}$$

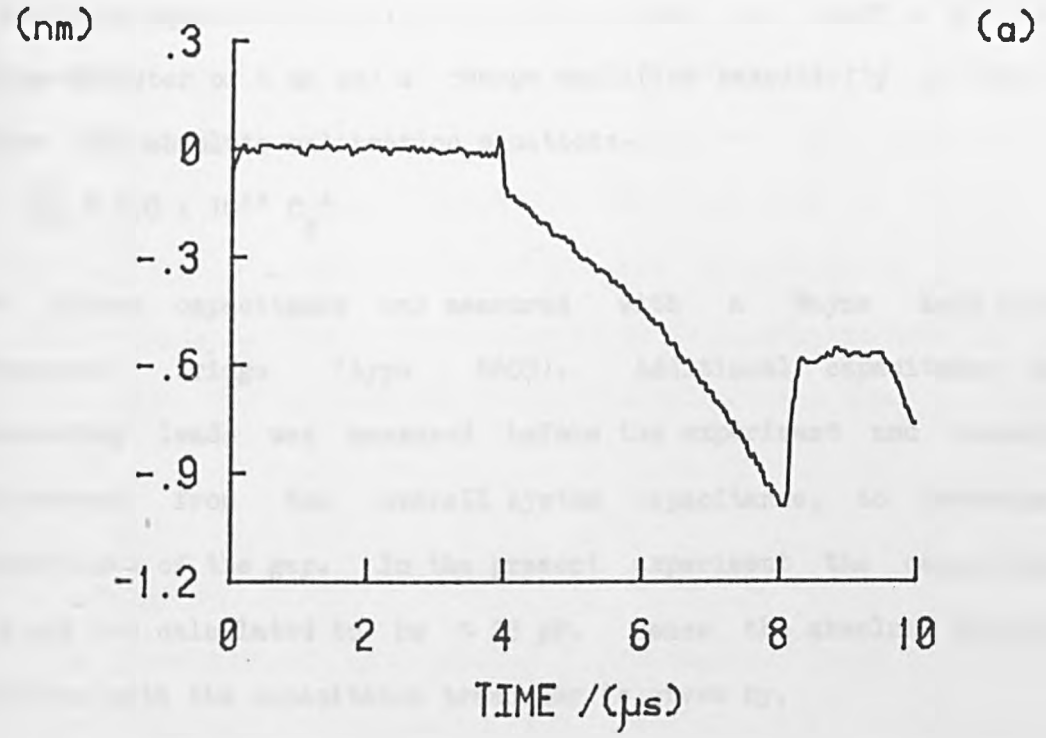

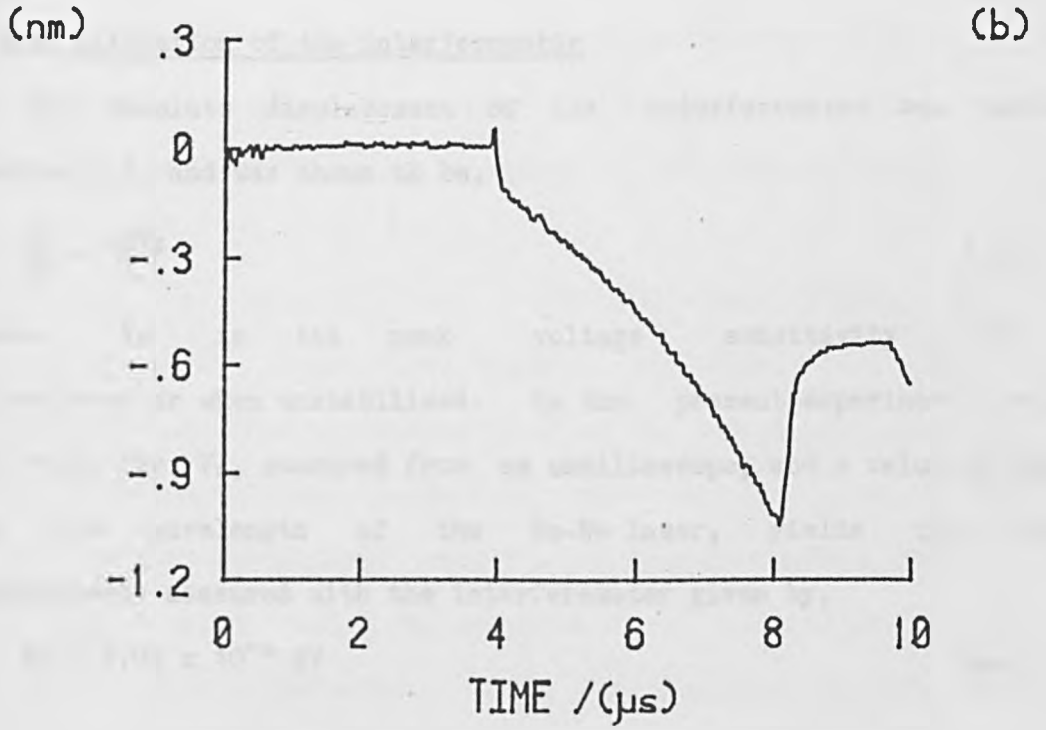

Fig. (4.14) Epicentral waveforms detected in the thermoelastic regime with
(a) the interferometer and
(b) the capacitance transducer.

Evaluating equation (4.5) for V = 80 volts, $\varepsilon_0 = 8.85 \times 10^{-12}$ F/m, a plate diameter of 6 mm and a charge amplifier sensitivity of 250 mV/pC gives the absolute calibration equation:-

$$\frac{dV}{dx} \sim 8.0 \times 10^{28} C_g^{\,2}$$

The system capacitance was measured with a Wayne Kerr automatic component bridge (type B605). Additional capacitance due to connecting leads was measured before the experiment and subsequently subtracted from the overall system capacitance, to determine the capacitance of the gap. In the present experiment the capacitance of the gap was calculated to be $\sim$ 25 pF. Hence the absolute displacement measured with the capacitance tranducer is given by,

$$dx \sim \frac{dV}{4.88 \times 10^7} \qquad (4.6)$$

4.8.2 Calibration of the Interferometer

The absolute displacement of the interferometer was derived in section 3.2, and was shown to be,

$$\frac{dV}{dx} = \frac{4\pi V_0}{\lambda} \qquad (4.7)$$

where V_0 is the peak voltage sensitivity of the interferometer when unstabilised. In the present experiment a value of 1.0 volts for V_0, measured from an oscilloscope, and a value of 632.8 nm for the wavelength of the He-Ne laser, yields the absolute displacement measured with the interferometer given by,

$$dx \sim 5.04 \times 10^{-8}\ dV \qquad (4.8)$$

4.8.3 Results

The amplitudes of the thermoelastic waveforms of fig. (4.14) have been measured from the zero base line down to the minimum of the waveform at the shear arrival. The amplitudes for the capacitance transducer and interferometer waveforms were approximately 51 mV and 20 mV respectively, giving corresponding absolute displacements of 1.05 ± 0.08 nm and 1.0 ± 0.07 nm using the calibration equations (4.6) and (4.8).

4.8.4 Discussion

The risetimes of the initial longitudinal step is affected by the spatial extent of both source and detector, the bandwidth of the amplifier and physical properties of the material under test. It can readily be shown that, if an acoustic point source is a depth h vertically below a detecting transducer plate of radius r, then the geometric time delay t, due to differing path lengths between the central and edge regions of the detector can be written as,

$$t = [(r^2 + h^2)^{1/2} - h]/V$$

where V is the velocity of the ultrasonic pulse. For a source 25.4 mm deep and a longitudinal velocity of 6300 m/s, the geometric time delay would be approximately 28 ns for the 6 mm diameter active area of the capacitance transducer, even for an ideal point source. It is therefore incapable of resolving an acoustic source with a risetime of 20 ns which might be expected from the Nd:YAG laser. In contrast, the interferometer can be focussed to produce a small detection spot (∿ 0.1 mm) making it almost immune to geometric bandwidth limitations.

To examine the risetimes of the two transducers, longitudinal

acoustic arrivals were examined by focusing the incident laser pulse to create a brief plasma on the sample surface, resulting in a normal force with a delta-like time dependence. Consequently a brief longitudinal pulse was generated on epicentre, so that both rise and fall times of the transducers could be examined. Figs. (4.15a) and (4.15b) show, on an expanded timescale, the longitudinal pulse obtained with the focused interferometer (f = 15 cm) and capacitance transducer respectively as detectors. The interferometer waveform has a slightly faster risetime (23 ± 2 ns) than the capacitance transducer waveform (26 ± 2 ns) and both are of the same order as the laser risetime of ∿ 20 ns. It should be noted that an acoustic risetime of ∿ 7 ns has been recorded with the interferometer, from waveforms generated by a 25 ps laser excitation source, demonstrating that the risetime of 23 ns in these experiments was limited purely by the laser source. From the two figures it is evident that the interferometer fall time is much shorter than that of the capacitance probe.

The small spatial extent of the interferometer laser beam has a further advantage of additional resolution. Acoustic signals immediately after the primary longitudinal arrival can be seen in the interferometer waveform of fig. (4.15a), which are undetected in fig. (4.15b) due to spatial integration over the active area of the capacitance transducer. These signals can be discerned more clearly in the average of eight waveforms shown in fig. (4.15c), demonstrating that they are not due to random noise. As in the case of acoustic waveforms obtained in graphite, these signals in duraluminium are thought to arise from forward scattering from the microstructure. Similar features have been reported by Scruby et. al. (1986) in steel samples.

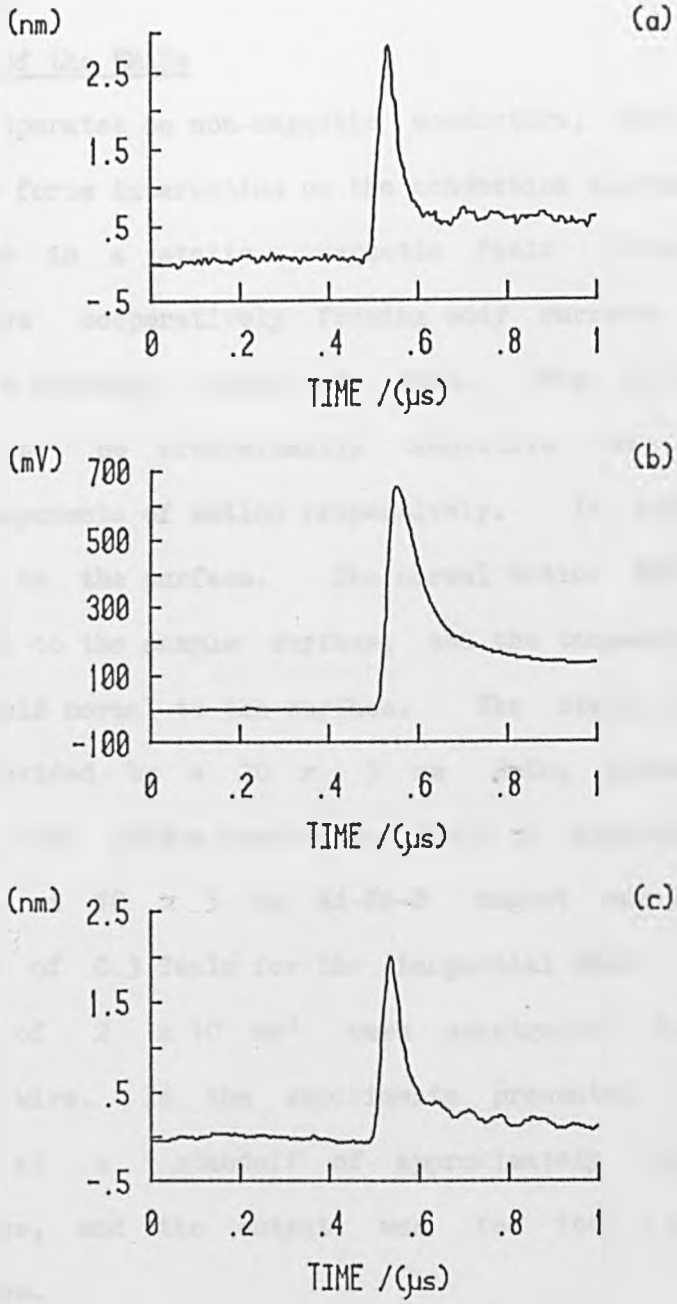

Fig. (4.15) The longitudinal pulse on an expanded timescale from a focussed laser source detected using
(a,c) the interferometer
(b) the capacitance transducer.

The interferometer has a small detection area and can resolve features which occur just after the longitudinal pulse, which are caused by scattering from the sample microstructure. These are seen more clearly in (c) which was averaged over 8 laser shots.

4.9 A Comparison of the Interferometer with EMATs and a Piezoelectric Transducer

4.9.1 Design of the EMATs

An EMAT operates on non-magnetic conductors, such as duraluminium, via a Lorentz force interaction on the conduction electrons moved by the acoustic wave in a static magnetic field (Frost, 1979). The electrons move cooperatively forming eddy currents which can be detected by a suitably orientated coil. Fig. (4.16) shows two EMATs constructed to be predominantly sensitive to the normal and tangential components of motion respectively. In both cases the coil was parallel to the surface. The normal motion EMAT had the static field parallel to the sample surface, and the tangential motion EMAT had the static field normal to the surface. The static field in the normal EMAT was provided by a 20 x 5 mm $SmCo_5$ permanent magnet with mild steel flux guides producing a field of approximately 0.9 Tesla in the gap. A 10 x 5 mm Nd-Fe-B magnet was used to produce a static field of 0.3 Tesla for the tangential EMAT. The coils, with active areas of 2 x 10 mm^2 were constructed from 20 turns of 48 gauge copper wire. In the experiments presented here both EMATs were used at a standoff of approximately 0.5 mm from the sample surface, and the output was fed into a charge amplifier described above.

4.9.2 The Piezoelectric Transducer

A commercial lead metaniobate ($Pb\ Nb_2\ O_6$) transducer (Panametrics model no. V109) with a centre frequency of 5 MHz and a quoted bandwidth of 1 MHz, has also been examined. It was designed to be sensitive to longitudinal displacements and did not require any

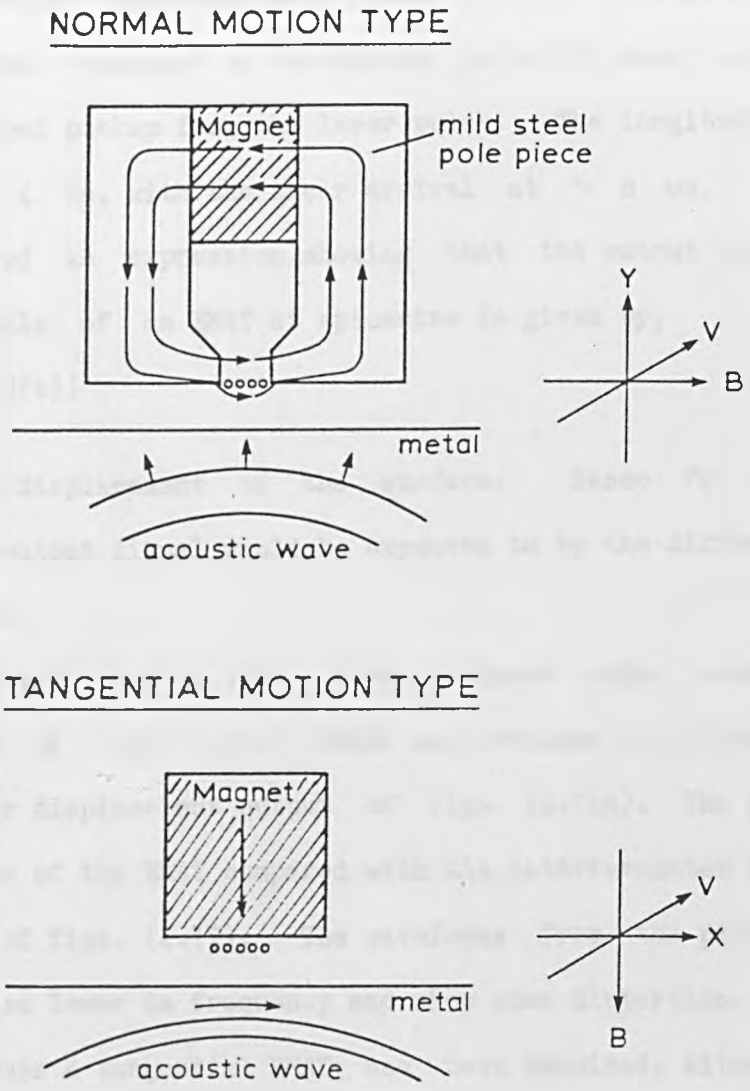

Fig. (4.16) Schematic diagram of the normal and tangential motion sensing electro-magnetic acoustic transducers (EMATs).

additional amplification. This contact transducer was bonded to the sample surface with a thin layer of vacuum grease.

The thermoelastic waveforms detected with the normal sensing EMAT, and the Panametrics transducer are shown in fig. (4.17a) and (4.17b) respectively. The "ringing" in the initial parts of each waveform was due to electrical pickup from the laser pulse. The longitudinal pulse is evident at $\sim$ 4 μs, with the shear arrival at $\sim$ 8 μs. Kawashima (1984) has derived an expression showing that the output voltage V(t) across the terminals of an EMAT at epicentre is given by,

$$V(t) = -\frac{d}{dt}[2S(t)]$$

where S(t) is the displacement of the surface. Hence for the normal motion EMAT, the output signal would be expected to be the differential of the interferometer.

Both figs. (4.17a) and (4.17b) have features which resemble the velocity waveform of fig. (4.17c), which was obtained by differentiating the interferometer displacement output of fig. (4.14a). The much lower frequency response of the EMAT compared with the interferometer is evident from examination of figs. (4.17). The waveforms from the piezoelectric transducer are also lower in frequency and show some distortion.

For completeness a tangential EMAT has been examined, situated at $\sim 40^0$ off epicentre with respect to the thermoelastic source, for the maximum directivity of shear waves (Hutchins et. al., 1982). Fig. (4.18a) shows the waveform obtained using the EMAT, and fig. (4.18b) shows a corresponding interferometer waveform. As expected the EMAT is more sensitive to the acoustic energy associated with the shear arrival. The sensitivities, risetimes and signal to noise ratios of the interferometer, capacitance transducer, longitudinal EMAT and piezoelectric transducer are

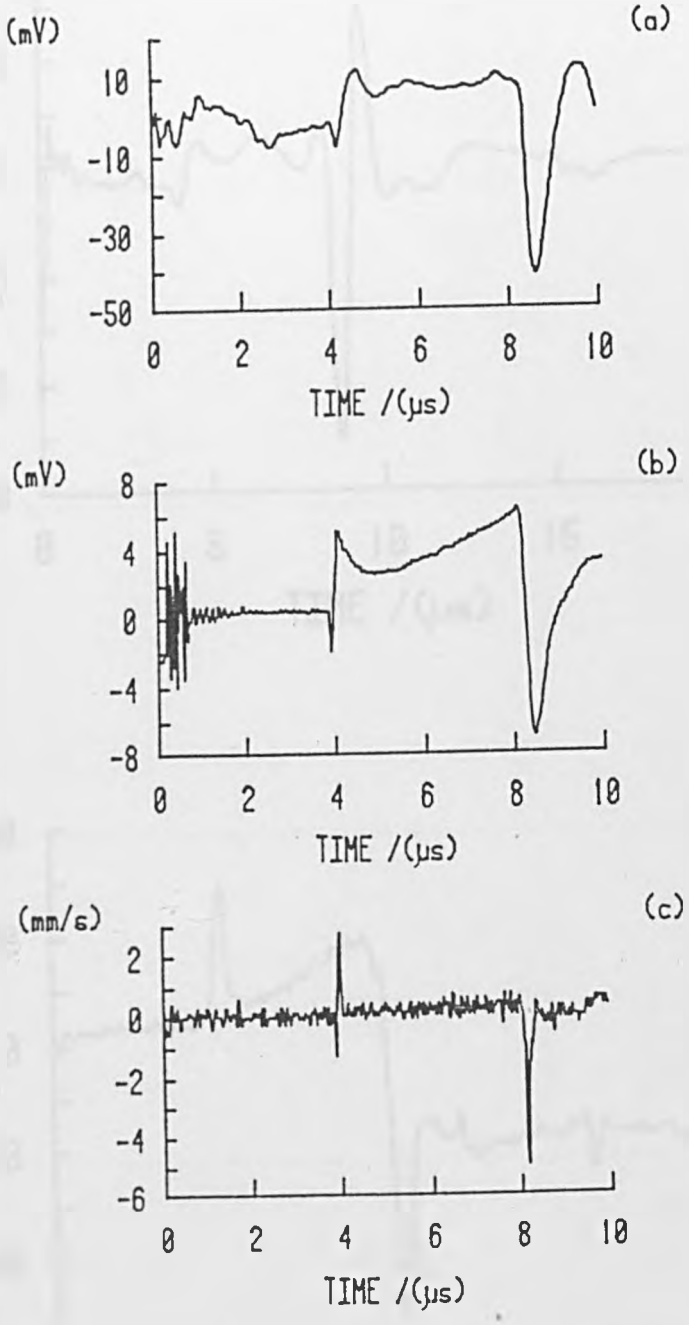

Fig. (4.17) Epicentral waveforms detected in the thermoelastic regime using
(a) the normal sensing EMAT and
(b) the panametrics broadband piezoelectric transducer.

(c) is the differential of the waveform detected with the interferometer, shown in fig. (4.14a).

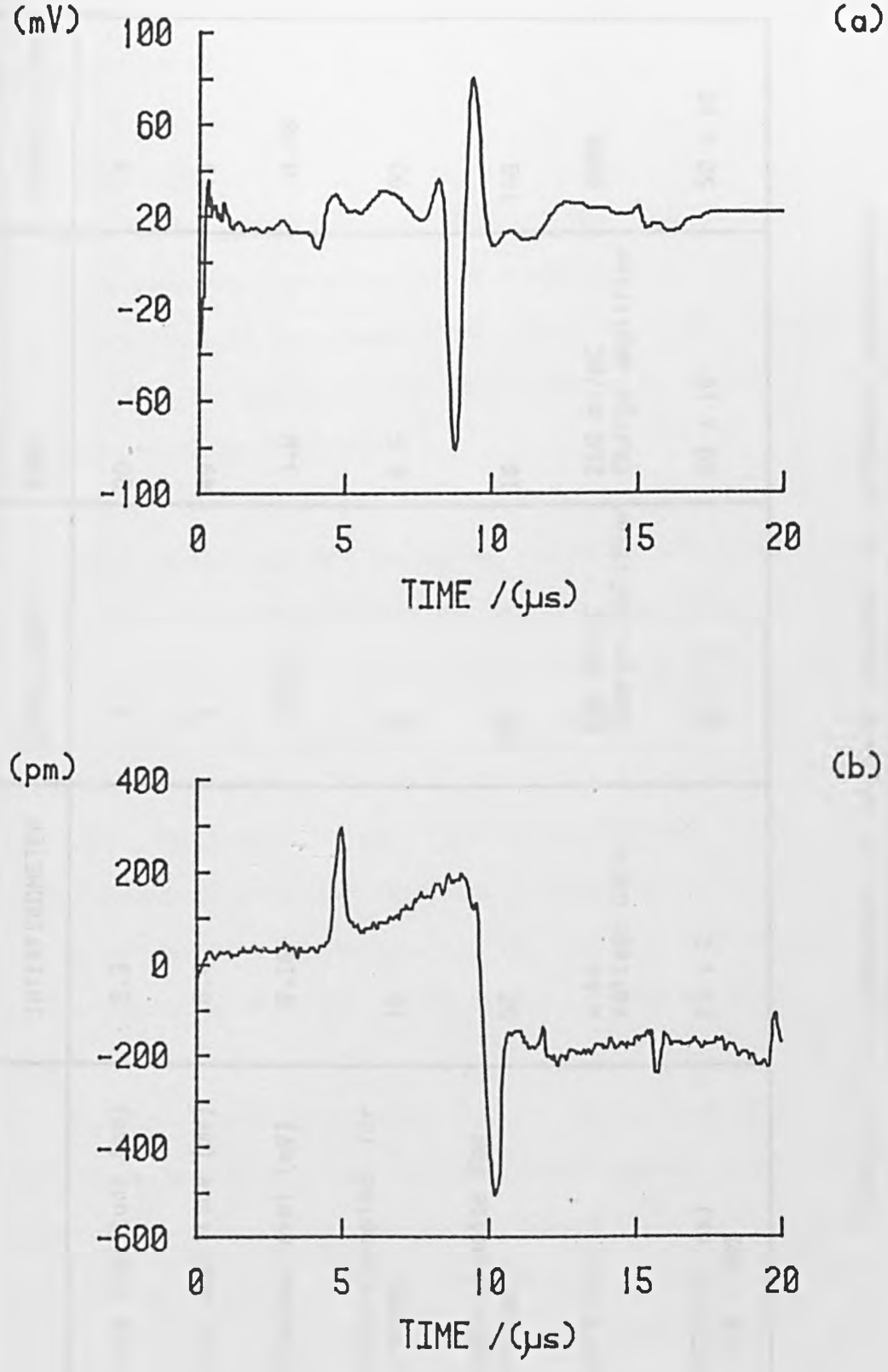

Fig. (4.18) Off epicentral waveforms detected in the thermoelastic regime using
(a) the tangential sensing EMAT and
(b) the interferometer.

	INTERFEROMETER	CAPACITANCE	EMAT	PIEZOELECTRIC
L-step amplitude (mV)	2.3	5	20	7
S-step amplitude (mV)	8.4	23	49	13
RMS noise level (mV)	0.16	0.10	3.0	0.08
Signal-to-noise for L-step	16	50	6.6	90
Signal-to-noise for S-step	52	230	16	168
Amplifiers	x 40 Voltage Gain	250 mV/pC Charge Amplifier	250 mV/pC Charge amplifier	NONE
RISETIMES (ns) 10% → 90%	23 ± 2	26 ± 2	80 ± 10	50 ± 10

Table (4.1) A comparison of signals recorded by different transducers when detecting acoustic waveforms from a thermoelastic laser source. For an absolute comparison, the interferometer waveform of fig. (4.14a) shows that the L-step displacement was 115 pm, and the S-step displacement was 420 pm. In all cases the incident laser pulse energy was 50 mJ.

summarised in table (4.1).

4.9.3 Discussion

A complete comparison of the various transducers as ultrasonic detectors would include measurements of their sensitivity as a function of frequency, for both longitudinal and shear arrivals. However, in view of the fact that the laser acoustic source was in the nature of a pulse, this was impractical in this work.

Neither the EMATs nor the Panametrics transducer are absolute devices. In the case of the EMATs, calibration is possible but requires an accurate knowledge of the electrical properties of the sample, magnetic field distributions and transducer standoff distance. This data is difficult to ascertain in practice. In the case of the Panametrics transducer, the existence of a coupling layer prevents absolute calibration, and its limited bandwidth results in distortion of the measured acoustic waveform. However, the risetime of 50 ns is in keeping with the devices' quoted centre frequency of 5 MHz. A similar estimate for the EMATS would indicate a centre frequency of 3 MHz.

The signal to noise figures for the longitudinal arrival were much as would be expected, with the high efficiency contact probe performing best. Although the capacitance probe's performance is better than that of the interferometer, the capacitance probe is only just non-contacting. The matter of surface preparation should not be overlooked in any comparison of different types of detectors. The interferometer operates best on polished surfaces. The capacitance probe has more stringent requirements for surface preparation, and for absolute calibration the surface must be optically flat, and free from dirt.

The EMATs in these experiments performed the worst. However it should be noted that from an applications point of view, EMATs are the most adaptable, being able to work off rough surfaces and tolerating variations within the $\sim$ 0.5 mm standoff and contamination in the gap, although these effects do decrease the device sensitivity.

The tangential EMAT is an efficient detector of shear waves from a thermoelastic source, and may prove to be the most suitable detector for nondestructive practical applications of laser generated ultrasound. It has already been successfully used for the non-contacting detection of surface breaking cracks in fillet welds (Dewhurst et. al., 1986).

4.10 Conclusion

The interferometer has proved to be an excellent quantitative device for the measurement of both bulk and surface waves. In the thermoelastic regime, on epicentre, it has been shown by comparison with theory that horizontal forces predominate within the acoustic source. In the plasma regime, the source includes both normal and horizontal forces, the former causing a significant increase in longitudinal pulse amplitude. At sufficiently high laser power densities the time dependence of the laser source approaches that of the Heaviside function. For one-sided generation and detection the Rayleigh surface wave predominated, with its polarity inverting between the thermoelastic and plasma regimes. Laser generation and detection of ultrasound has been successfully demonstrated in a graphite sample, even though the interferometer described is not ideally suited to poorly reflecting materials.

Calibration of the interferometer and capacitance probe was achieved independently, and are in excellent agreement for the overall absolute displacement amplitude measured in the thermoelastic regime. It has been

shown that greater resolution can be obtained with the interferometer due to its small detection spot, whereas the other wideband transducers studied significantly integrate the ultrasonic signals over their active areas.

4.11 References

R. J. Dewhurst, D. A. Hutchins, S. B. Palmer and C. B. Scruby, J. Appl. Phys. 53 4064 (1982).

R. J. Dewhurst, C. Edwards and S. B. Palmer, Appl. Phys. Lett. 49 374 (1986).

P. A. Doyle, J. Phys. D. 19 1613 (1986).

H. M. Frost, in "Physical Acoustics" (Edited by W. P. Mason and R. N. Thurston, Academic Press, New York) vol. 14, p. 179 (1979).

D. A. Hutchins, R. J. Dewhurst, and S. B. Palmer, J. Acoust. Soc. Am. 70 1369 (1982).

H. Lamb, Phil. Trans. Roy. Soc. Lond. A203 1 (1904).

K. Kawashima, IEEE Trans. Son. Ultrason. SU-31 83 (1984).

L. Knopoff, J. Appl. Phys. 29 661 (1958).

C. L. Pekeris, Geophysics 41 469 (1955).

L. R. F. Rose, J. Acoust. Soc. Amer. 75 723 (1984).

C. B. Scruby and H. N. G. Wadley, J. Phys. D: Appl. Phys. 11 1487 (1978).

C. B. Scruby, R. L. Smith, and B. C. Moss, NDT International, 19 307 (1986).

C. B. Scruby, R. J. Dewhurst, D. A. Hutchins, and S. B. Palmer, in "Research Techniques in Nondestructive Testing" (Edited by R. S. Sharpe, Academic Press, London) Vol. 5, p. 281 (1982).

C. B. Scruby, R. J. Dewhurst, D. A. Hutchins and S. B. Palmer, J. Appl. Phys. 51 6210 (1980).

CHAPTER 5

Rayleigh Wave Interactions with Surface Breaking Defects

5.0 Introduction

Ultrasonic methods have been widely used, for many years, in the detection of both internal and surface discontinuities. In terms of civil engineering, the effectiveness of trenches for screening structural foundations from vibratory surface wave energy has been studied by Woods (1968). More recently, at ultrasonic frequencies, the detection and subsequent monitoring of shallow surface breaking cracks in industrial components, has become a subject of great interest, since it represents an important indication of predicting imminent fatigue failures. With increasingly more complex and expensive manufacturing processes, there is a special interest to develop quantitative techniques for nondestructive evaluation.

There is a growing awareness that laser devices offer new possibilities in ultrasonic nondestructive testing. In the case of the generation of ultrasound, the short duration of the excitation laser pulse, depending on the type of laser used, is typically in the range 70 ps to 40 ns. Provided the laser spot diameter is small, this leads to the generation of short duration surface acoustic pulses. These pulses contain a substantial amount of the total acoustic energy generated by the laser, and are therefore expected to play an important role in newly developed laser-based nondestructive testing techniques.

In this chapter, the interaction of Rayleigh waves with surface breaking slots will be examined, with a view to quantitative analysis of the slot depths. In order to fully understand the interaction process,

discontinuities which essentially make up a slot, in the form of 90^0 and 270^0 corners, will be examined. Also, in collaboration with Bond and Saffari at University College London , the time dependent behaviour of the surface displacements has been predicted numerically. The computer predictions will be compared with corresponding experimental results.

The existence of Rayleigh waves travelling along the surface of an elastic half space was predicted by Lord Rayleigh in 1885. The particle motion of these waves is confined to a layer approximately one wavelength thick at the surface of the elastic solid, and their amplitudes decay exponentially with penetration depth. Thus at frequencies of about 3 MHz in aluminium, the wavelength and hence penetration depth of the Rayleigh waves is of the order of 1 mm. This makes Rayleigh waves an obvious choice for nondestructive evaluation of surface breaking defects. Additionally since Rayleigh waves only propagate in two dimensions, their energy decays more slowly with increasing distance from their point of origin, compared with that of bulk waves.

5.1 Ultrasonic Detection of Surface Breaking Defects: A Review

When a Rayleigh wave is incident on a surface breaking defect, such as a slot, a proportion of the Rayleigh pulse is mode converted into shear and longitudinal pulses, which may then be reflected along the material surface, scattered into the bulk of the material, or transmitted beyond the slot. The interaction is complex, with surface waveforms being generated which not only show the presence of the slot, but also contain information about its depth. Such information can in principle be collected from surface waveform measurements using either pulse-echo or pulse-transmission methods. Previously, one method of obtaining information about the slot depth has been through the use of spectral

analysis techniques, on Rayleigh waves which have been transmitted through (Burger and Testa, 1981) or reflected from (Singh and Singh, 1981) the slot. For the case of a broadband Rayleigh pulse incident on a surface breaking slot, these authors have shown that the high frequency components are selectively reflected by the slot, whilst the lower frequency components are transmitted. Thus Fourier transforming the reflected or transmitted pulses, and comparison with a reference, will reveal the frequency components that have been selectively filtered by the slot, and thus related to the slot depth. Slot depths of $\sim$ 1 mm were successfully estimated from measurements with a 5 MHz Rayleigh wave transducer. Cooper (1985) has also used this spectroscopic approach to detect slots of 1 mm depth using a ball-capacitance transducer, with the experimental results agreeing with the numerical finite difference calculations of Hirao et. al. (1982).

Analytical methods in the time domain were originally suggested by Cooke (1972), who estimated the depth of surface breaking cracks by monitoring the time-of-flight from the source to receiver. Any intervening crack lengthened the path since the Rayleigh waves had to travel around the face of the crack and up the other side. However, this technique fails when the Rayleigh wavelength becomes much larger than the crack depth, and the Rayleigh waves pass under the crack with little interaction. The method requires a knowledge of the time delay of a Rayleigh pulse from the source to receiver in a region where no crack exists. This delay is usually evaluated from the distance between source and receiver and using the Rayleigh wave velocity for the material concerned. Morgan (1974) attempted to relate time dependent features, occurring in the reflected surface pulse, to the corner discontinuities at the top and bottom of the slot. However, the limited frequency bandwidth

of the Rayleigh wave wedge transducer did not provide sufficiently brief transients to separate out the expected echoes from a 1.4 mm deep slot in aluminium. Further work (Lidington and Silk, 1975) used a short pulse surface wave probe, operating at a frequency of 2.5 MHz, to investigate the echoes from the slot top and base, and estimated depths from 2 mm to 30 mm in steel.

Ideally the detection of Rayleigh surface waves should be carried out using a non-contacting device, so as not to perturb the surface motion. The device should also be broadband, and have a sufficiently small detection area, such that the bandwidth reduction caused by the finite transit time of a surface wave across the transducer is minimised. Interferometric detectors fulfil all of these requirements. Previous workers have used a variety of interferometric techniques for the detection of ultrasound, as decribed in chapter 2. Bondarenko et. al. (1976), Calder and Wilcox (1980) and Wellman (1980), demonstrated the feasibility of a remote flaw detection system using laser generation and detection of ultrasound, although surface damage inevitably occured due to the high pulsed laser powers used. Nadeau and Hutchins (1984) have reported studies of acoustic pulse interactions with slots in aluminium using a Nd:YAG laser as an acoustic generator, and a Michelson interferometer as detector. They studied slots in the region of 1 to 5 mm deep and 1 mm wide, but were only able to resolve one reflected pulse from the slot, which was insufficient to estimate its depth. Since mode conversion of Rayleigh waves into bulk waves occurs in slot interactions, then equally possible is the mode conversion of a bulk wave, incident on the base of a slot, into a Rayleigh pulse. Thus the presence of an "unexpected" surface wave would be indicative of a surface discontinuity. Further invesigations with the source and

detector on opposite sides of a slot and equidisatant from it, showed that acoustic mode conversion of the transmitted Rayleigh pulse, offered promise as a sensitive means for surface breaking defect detection, although reciprocity was not easily observed in this case. Recently Hutchins et. al. (1986) extended these findings to the case of bulk wave generation on the opposite side to the slot, and laterally displaced. Interferometric detection, both on and off epicentre, showed Rayleigh waves, which have been determined from time of flight measurements to arise from shear wave to Rayleigh wave mode converison, demonstrating that the presence of a surface breaking defect could be accurately inferred.

Cooper et. al. (1986) have shown that in the case of laser generated Rayleigh pulses, slot depth measurements could conveniently be evaluated in the time domain. Using duraluminium samples, slot depths in the range 0.5 mm to 5.0 mm were measured, with resolution limited by the frequency bandwidth ($\sim$ 5 MHz) of the ball-capacitance transducer used.

Other experimental techniques using scattering amplitude and diffraction techniques to measure crack depth have been reviewed by Silk (1979) and Doyle and Scala (1978).

With the ever present increase in computer power, a useful insight into the complex interaction mechanisms of ultrasound with slots can be gained from the field of computer modelling. On the computational analysis of this problem, models for describing the interaction of acoustic waves with discontinuities have been developed extensively by Bond and his co-workers (1979), and more recently by Hirao and Fukuoka (1982), based on a finite difference computational algorithm. The techniques of computer modelling have been reviewed by Bond (1982).

5.2 Interferometric Detection of Surface Breaking Slots in the Plasma Regime

5.2.1 Experimental Arrangement

A typical experimental arrangement used to study the interaction of laser generated Rayleigh pulses with machined slots, in the surface of a duraluminium block, is shown in fig. (5.1). Laser pulses from a Q-switched Nd:YAG laser (JK Lasers Ltd.), having typically 15 mJ of energy in a 30 ns duration, were focussed using a 15 cm focal length convex lens to form a plasma on the sample surface, on one side of the slot. The resultant surface displacements were monitored with the interferometer situated on the same side of the slot as the laser source. The interferometer was focussed onto the sample surface with a 20 cm convex lens to produce a small detection spot, and maintain high resolution. The source to receiver distance was set at 9 mm, with a receiver to slot distance of 6 mm. All sample surfaces were polished to obtain maximum interferometer sensitivity.

5.2.2 Results and Discussion

5.2.3 Rayleigh Pulse Interaction With Slots Having Equal Widths and Different Depths

One set of experiments were performed on duraluminium samples having typical dimensions of 150 x 80 x 40 mm. Each sample had a slot cut into the surface with a slitting wheel. The slot widths were 0.1 mm for each sample, with slot depths varying from 0.10 mm to 1.0 mm. Fig. (5.2) shows a waveform detected on a sample that was free from flaws. The waveform shows a short duration, large amplitude, Rayleigh pulse (R) which travelled along the material surface, in addition to a surface skimming longitudinal pulse (P). The arrival at $\sim$ 9 μs (PP) corresponds to a

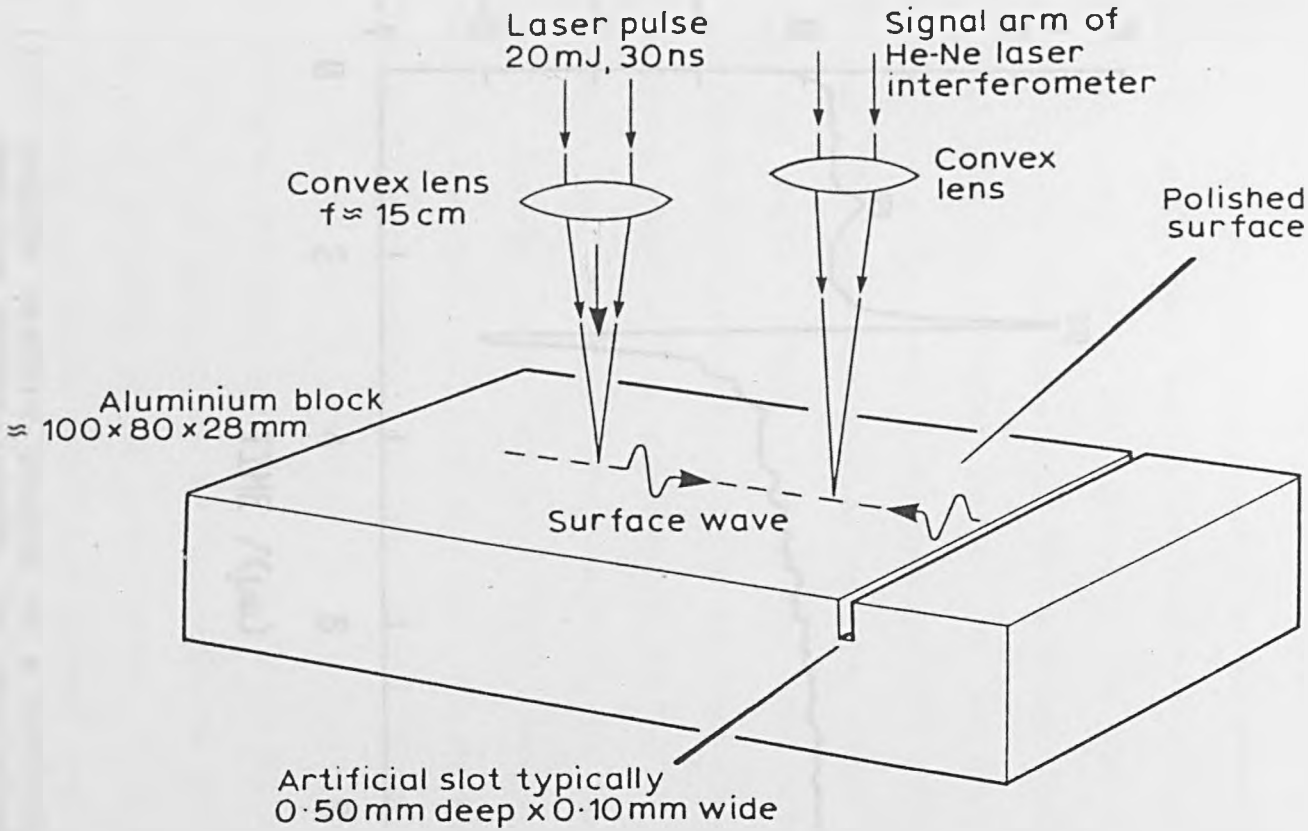

Fig. (5.1) Schematic diagram of the experimental arrangement used for studying Rayleigh pulse interactions with surface breaking slots.

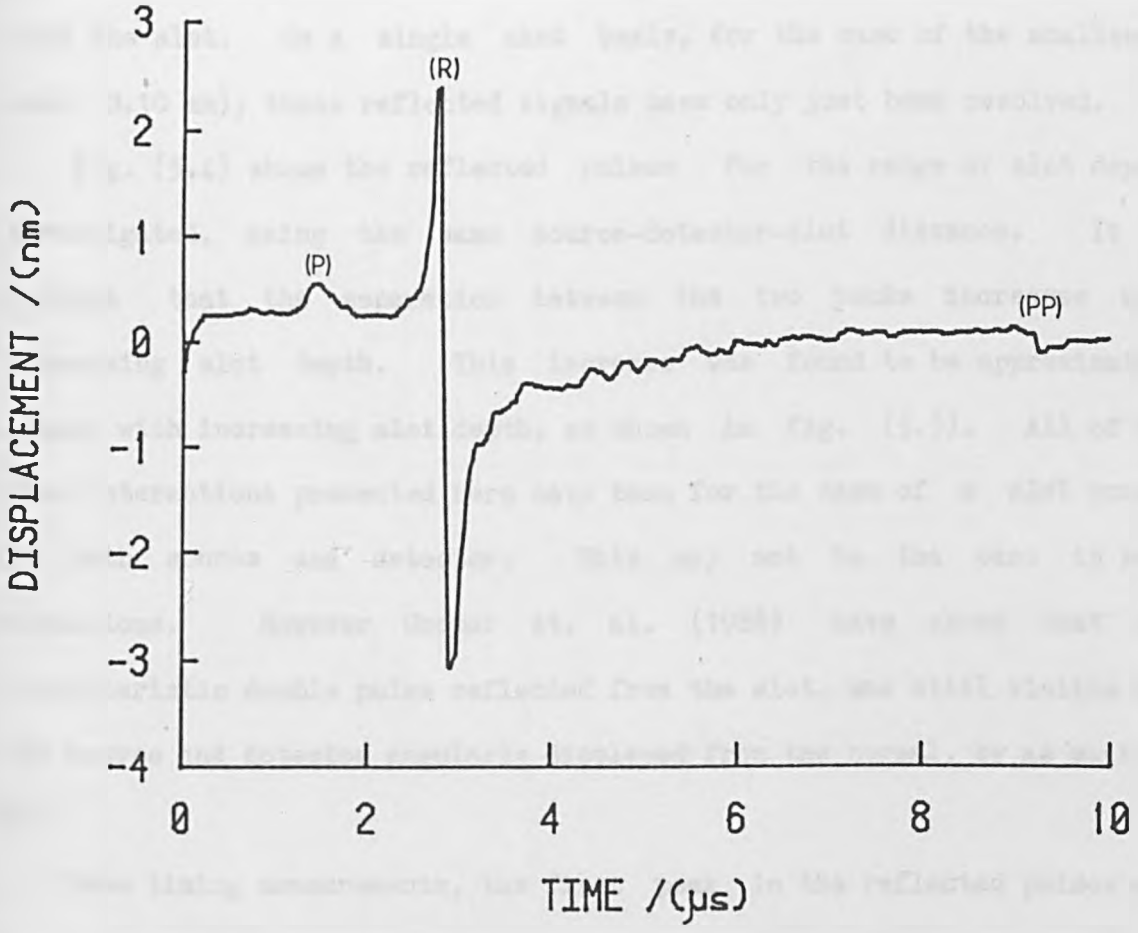

Fig. (5.2) Acoustic waveform detected on a duraluminium block free from surface defects. The longitudinal (P), and Rayleigh (R) pulses are marked. (PP) arises from a longitudinal pulse reflected from the back wall of the sample.

longitudinal pulse reflected from the back wall of the sample. Notice, however, that there are no significant arrivals visible between the Rayleigh pulse and back wall echo. Fig. (5.3) shows three typical waveforms obtained from pulse-echo measurements on 0.10, 0.50, and 1.0 mm deep slots. The initial portions of the waveforms are similar to that of fig. (5.2). However, the latter portion of the waveforms consisted of two additional signals, that have arisen from some ultrasonic interaction with the slot. On a single shot basis, for the case of the shallowest slot (0.10 mm), these reflected signals have only just been resolved.

Fig. (5.4) shows the reflected pulses for the range of slot depths investigated, using the same source-detector-slot distance. It is evident that the separation between the two peaks increases with increasing slot depth. This increase was found to be approximately linear with increasing slot depth, as shown in fig. (5.5). All of the slot interactions presented here have been for the case of a slot normal to both source and detector. This may not be the case in real situations. However Cooper et. al. (1986) have shown that the characteristic double pulse reflected from the slot, was still visible for the source and detector angularly displaced from the normal, by as much as 80^0.

From timing measurements, the first peak in the reflected pulses was found to be a Rayleigh pulse which was back reflected from the top of the slot. The nature and origin of the second pulse, however, was not so obvious. Pekeris and Lifson (1957) have demonstrated, that for angles greater than some onset angle, a Rayleigh pulse appears from a buried source. Such a result would not be expected for a planar continuous wave incident on a plane boundary, and may have its origin in the transient nature of the ultrasonic pulses. Based on this result, Cooper et. al.

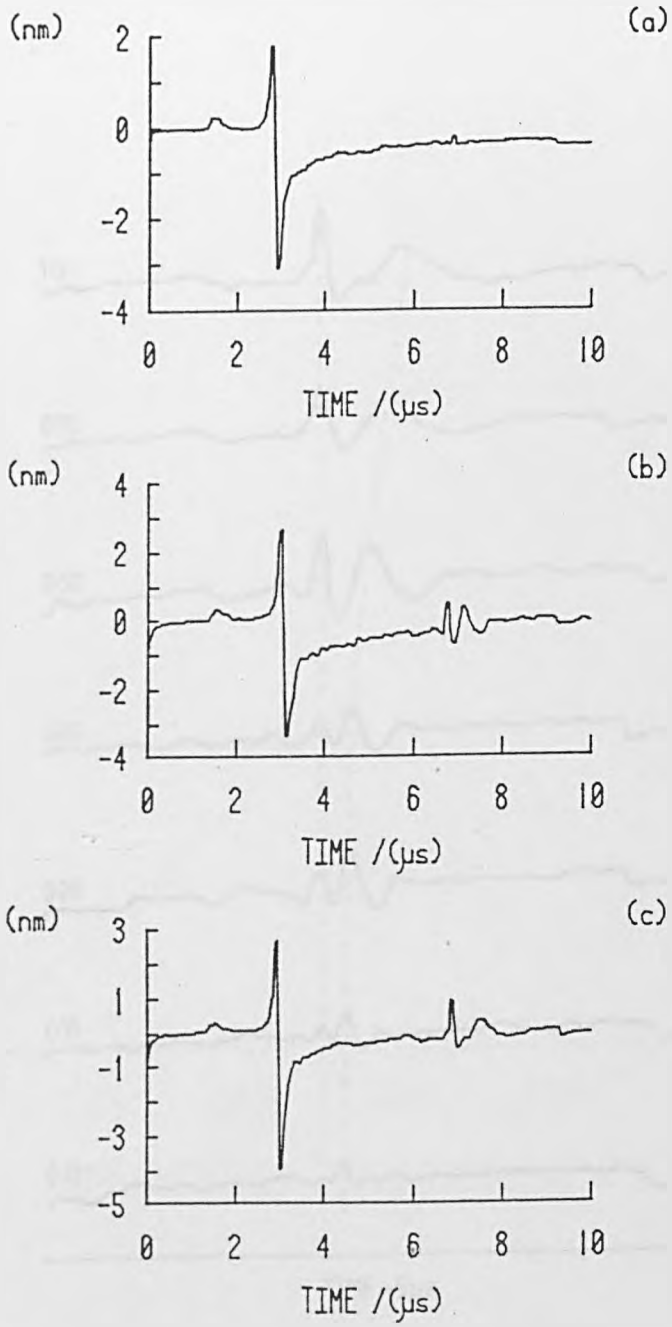

Fig. (5.3) Acoustic waveforms containing reflections from machined slots in duraluminium. Slot dimensions were 0.10 mm wide with depths of

(a) 0.10 mm
(b) 0.50 mm
(c) 1.0 mm

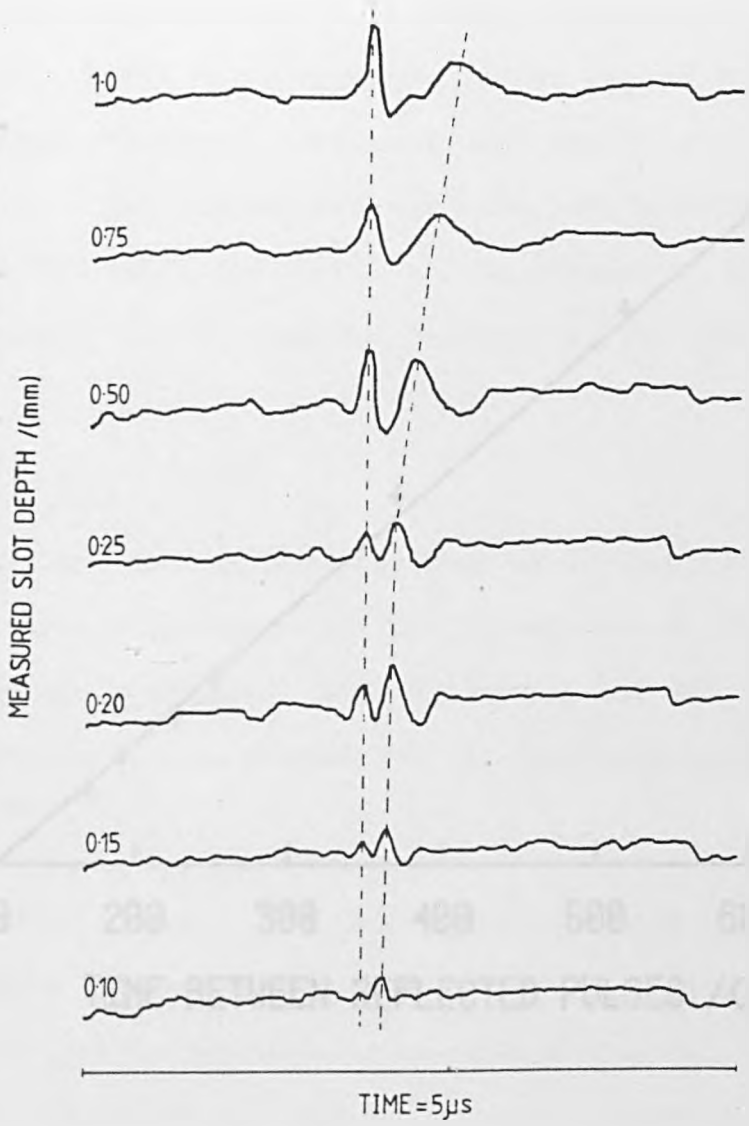

Fig. (5.4) Reflected surface acoustic pulses in duraluminium as a function of machined slot depth. The slot width was 0.10 mm in all cases.

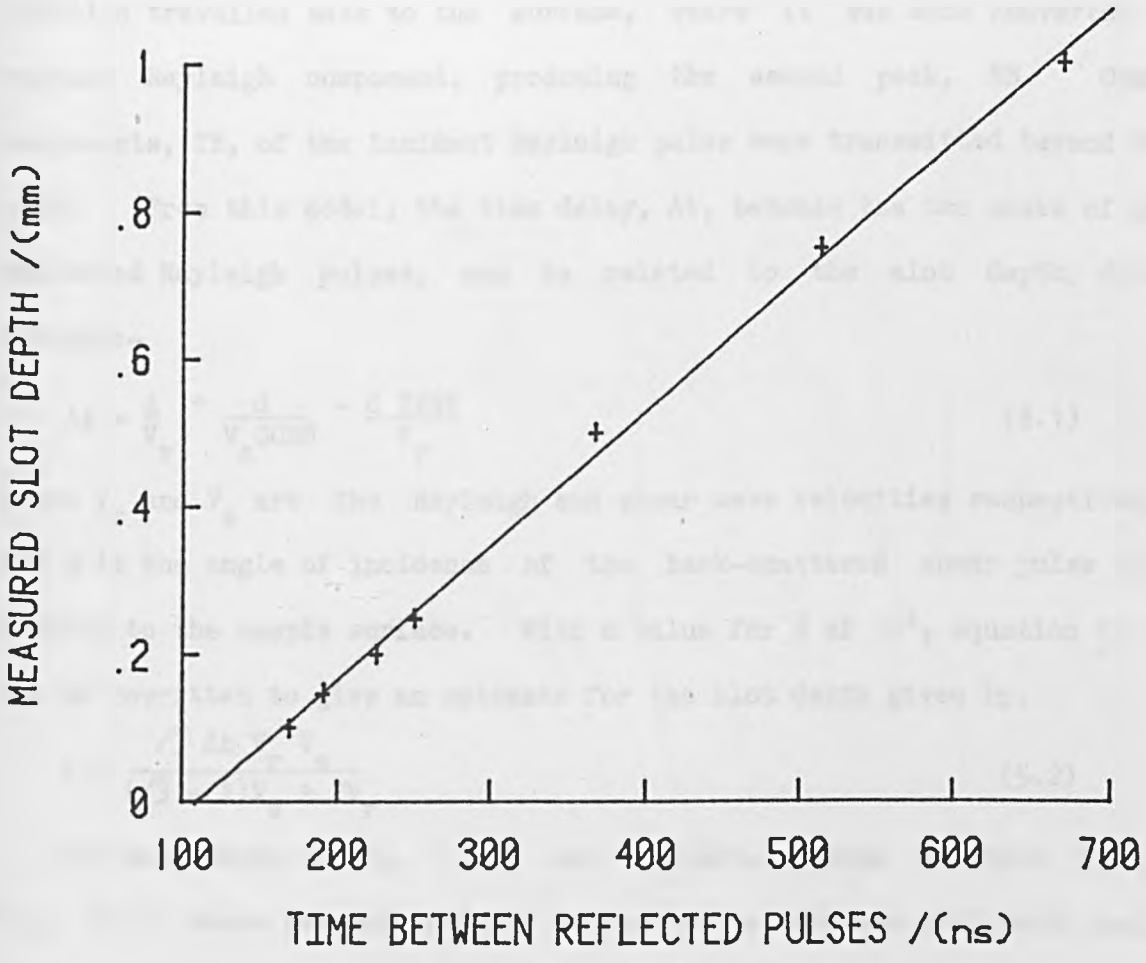

Fig. (5.5) Experimental results of the reflected pulse separation as a function of slot depth. The relationship is approximately linear.

(1986) proposed a model for the appearance of the second reflected pulse. The proposed interaction mechanism is shown schematically in fig. (5.6). The first peak is clearly the reflected Rayleigh pulse, RR, arising from an interaction with the top corner of the slot. A transmitted component, RT, travels down the side wall of the slot, and is partially mode converted, at the slot tip, into shear energy. It was proposed that some fraction travelled back to the surface, where it was mode converted to another Rayleigh component, producing the second peak, RS. Other components, TR, of the incident Rayleigh pulse were transmitted beyond the slot. From this model, the time delay, Δt, betweem the two peaks of the reflected Rayleigh pulses, can be related to the slot depth, d, as follows:-

$$\Delta t = \frac{d}{V_r} + \frac{d}{V_s \cos\theta} - \frac{d \tan\theta}{V_r} \qquad (5.1)$$

where V_r and V_s are the Rayleigh and shear wave velocities respectively, and θ is the angle of incidence of the back-scattered shear pulse with respect to the sample surface. With a value for θ of 30^0, equation (5.1) can be rewritten to give an estimate for the slot depth given by,

$$d = \frac{\sqrt{3}\,\Delta t\, V_r\, V_s}{(\sqrt{3} - 1)V_s + 2V_r} \qquad (5.2)$$

The data shown in fig. (5.5) was evaluated using equation (5.2). Fig. (5.7) shows the relationship between the calculated slot depth using equation (5.2), and the mechanically measured slot depth. The resulting slope is again linear, with a gradient of ~ 1 as expected. However, the experimental points are consistently on one side of the expected 45^0 slope, resulting in an over estimation of the slot depth by ~ 0.2 mm. It was noted that this discrepancy corresponded to the round trip distance of a Rayleigh pulse traversing the base of the slot twice. A modification to equation (5.2) can then be used to adequately describe the data:-

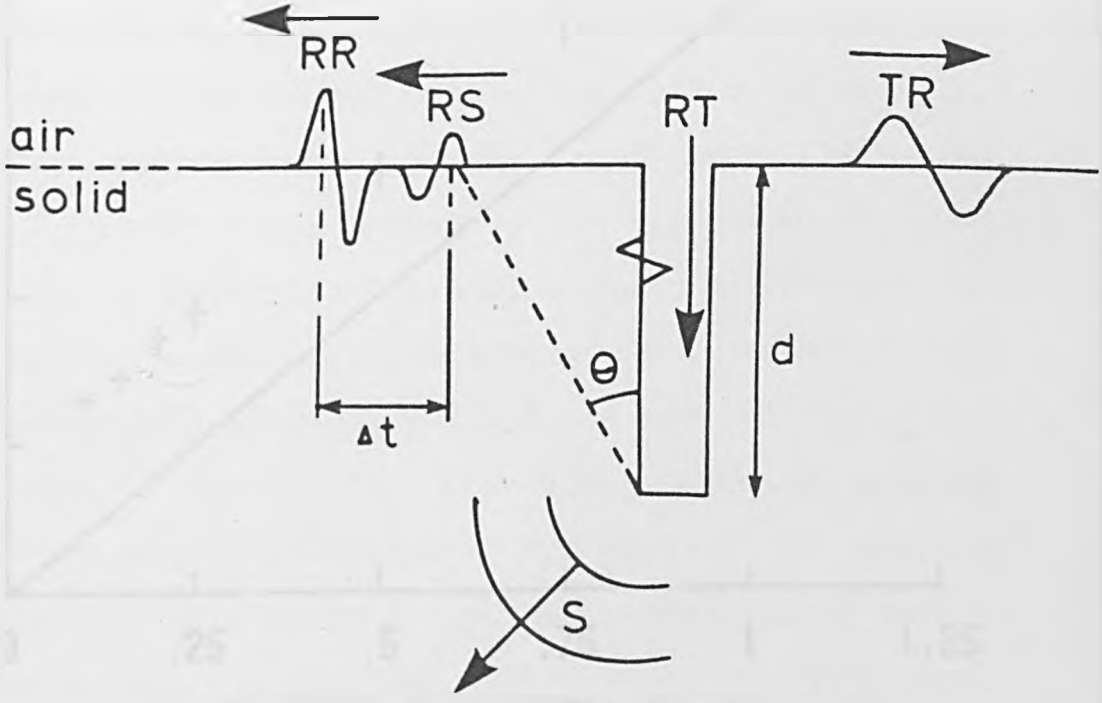

Fig. (5.6) Proposed model of Cooper et. al. (1986) for the interaction of a Rayleigh pulse with a machined slot.
RR: reflected Rayleigh pulse
RT: Rayleigh pulse transmitted around the first corner
RS: Rayleigh pulse resulting from a mode converted shear wave ,S, at the slot base
TR: transmitted Rayleigh pulse

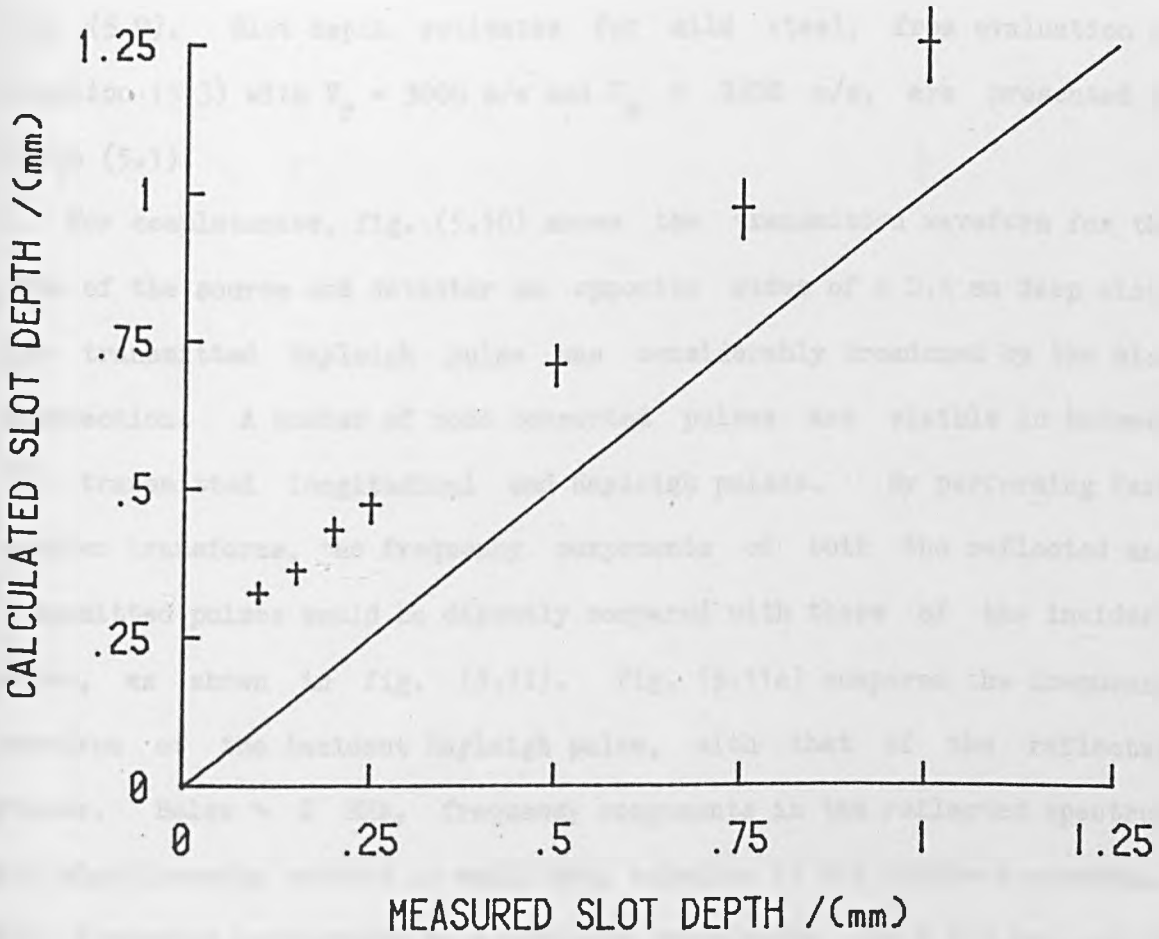

Fig. (5.7) Experimental results of slot depth estimation, evaluated from equation (5.2), and their comparison with expected behaviour (solid line). The discrepancy corresponds to the round-trip distance of a Rayleigh pulse traversing the base of the slot twice.

$$d = \frac{\sqrt{3}\,\Delta t\, V_r\, V_s}{(\sqrt{3}-1)V_s + 2V_r} - 2w \qquad (5.3)$$

where w is the width of the slot. Reanalysing the data of fig. (5.5), using equation (5.3) with V_r = 2900 m/s and V_s = 3100 m/s, produces excellent agreement as shown in fig. (5.8).

Waveforms, similar to those detected in duraluminium, were also detected from 0.25, 0.50, and 1.0 mm deep slots in mild steel, as shown in fig. (5.9). Slot depth estimates for mild steel, from evaluation of equation (5.3) with V_r = 3000 m/s and V_s = 3300 m/s, are presented in table (5.1).

For completeness, fig. (5.10) shows the transmitted waveform for the case of the source and detector on opposite sides of a 0.5 mm deep slot. The transmitted Rayleigh pulse was considerably broadened by the slot interaction. A number of mode converted pulses are visible in between the transmitted longitudinal and Rayleigh pulses. By performing fast fourier transforms, the frequency components of both the reflected and transmitted pulses could be directly compared with those of the incident pulse, as shown in fig. (5.11). Fig. (5.11a) compares the frequency spectrum of the incident Rayleigh pulse, with that of the reflected pulses. Below $\sim$ 2 MHz, frequency components in the reflected spectrum are significantly reduced in amplitude, relative to the incident spectrum. This frequency corresponds to a Rayleigh wavelength of $\sim$ 1.5 mm, and is consistent with the fact that Rayleigh waves, of wavelength less than the slot depth should be substantially reflected by the side wall of the slot (Burger and Testa, 1981). Conversely, fig. (5.11b) compares the incident and transmitted Rayleigh pulse spectra. In this case, high frequency components are attenuated relative to the incident pulse spectrum with the attenuation becoming rapid above $\sim$ 1 MHz. This frequency corresponds to a Rayleigh wavelength of $\sim$ 3 mm, and confirms that long wavelength

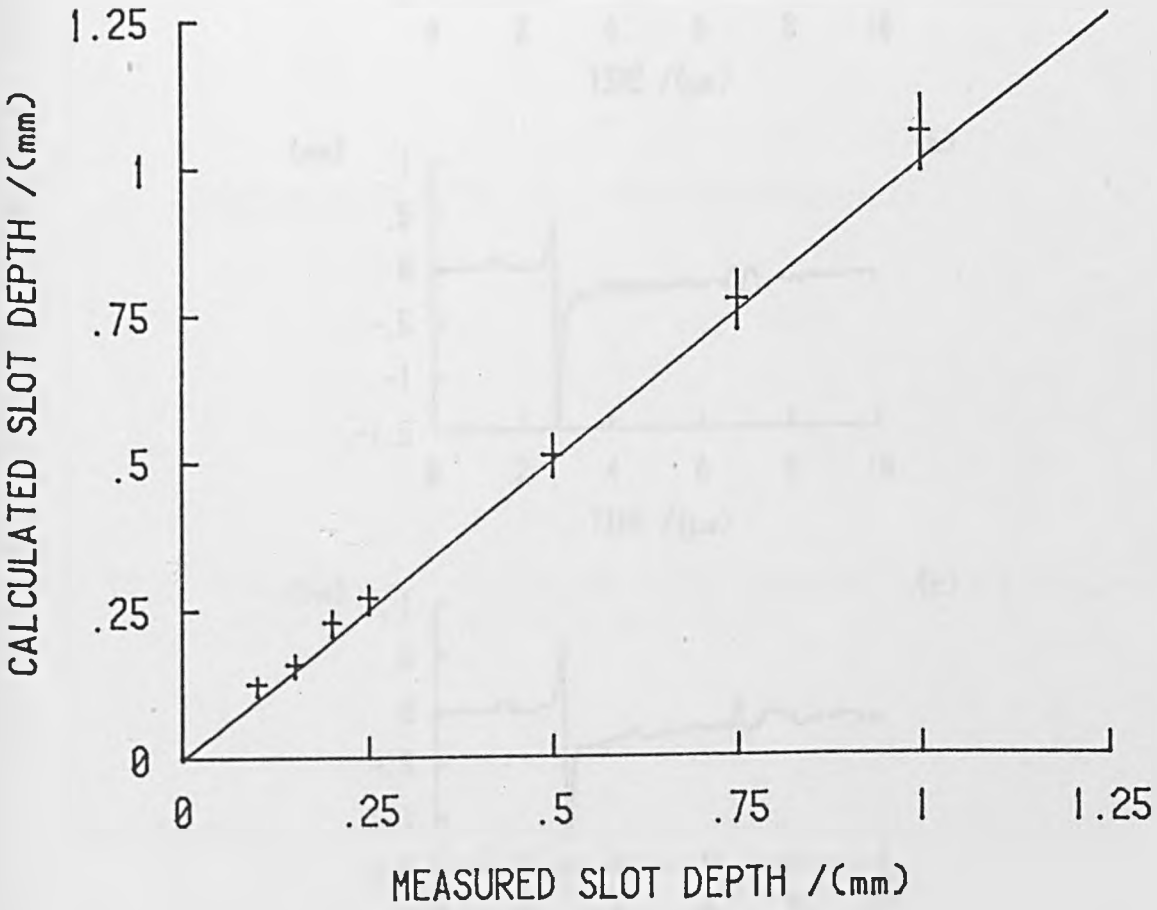

Fig. (5.8) Experimental results of slot depth estimation, evaluated from equation (5.3), and their comparison with expected behaviour (solid line). There is good agreement when the slot width is taken into account.

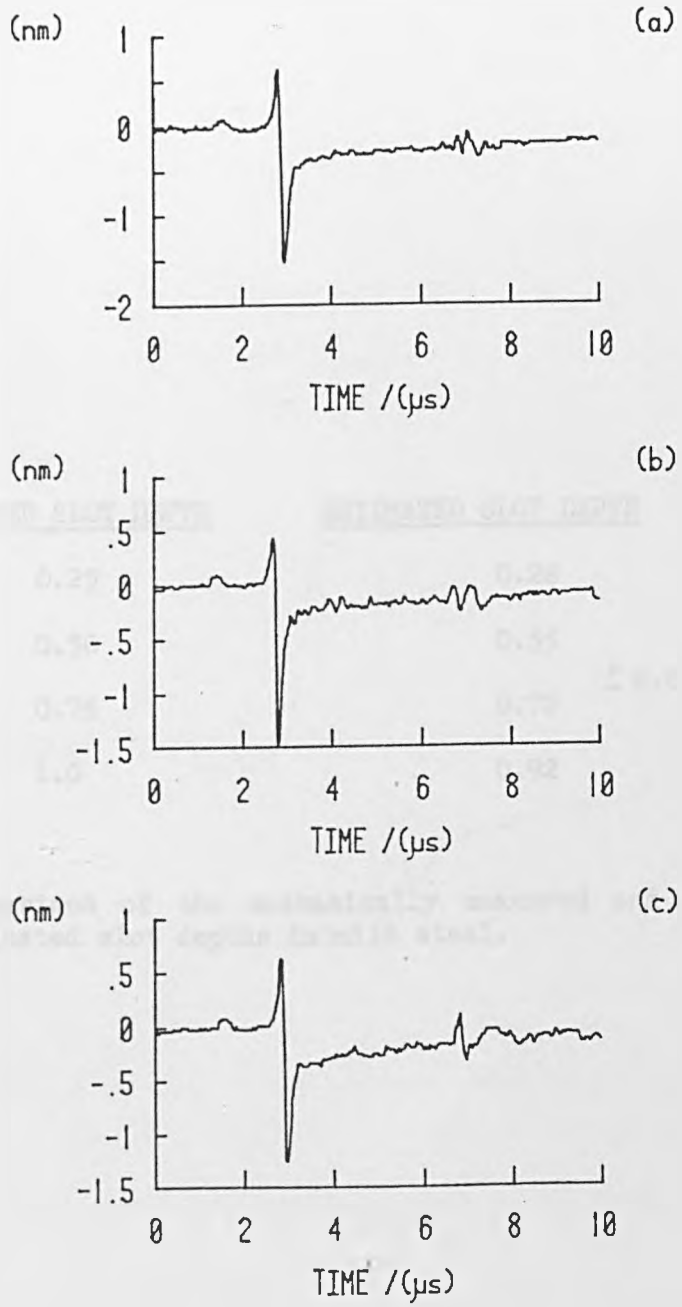

Fig. (5.9) Acoustic waveforms containing reflections from machined slots in mild steel. Slot dimensions were 0.10 mm wide with depths of

(a) 0.25 mm
(b) 0.50 mm
(c) 1.0 mm

MEASURED SLOT DEPTH	ESTIMATED SLOT DEPTH	
0.25	0.28	
0.50	0.55	± 0.01
0.75	0.72	
1.0	0.92	

Table (5.1) Comparison of the mechanically measured and ultrasonically estimated slot depths in mild steel.

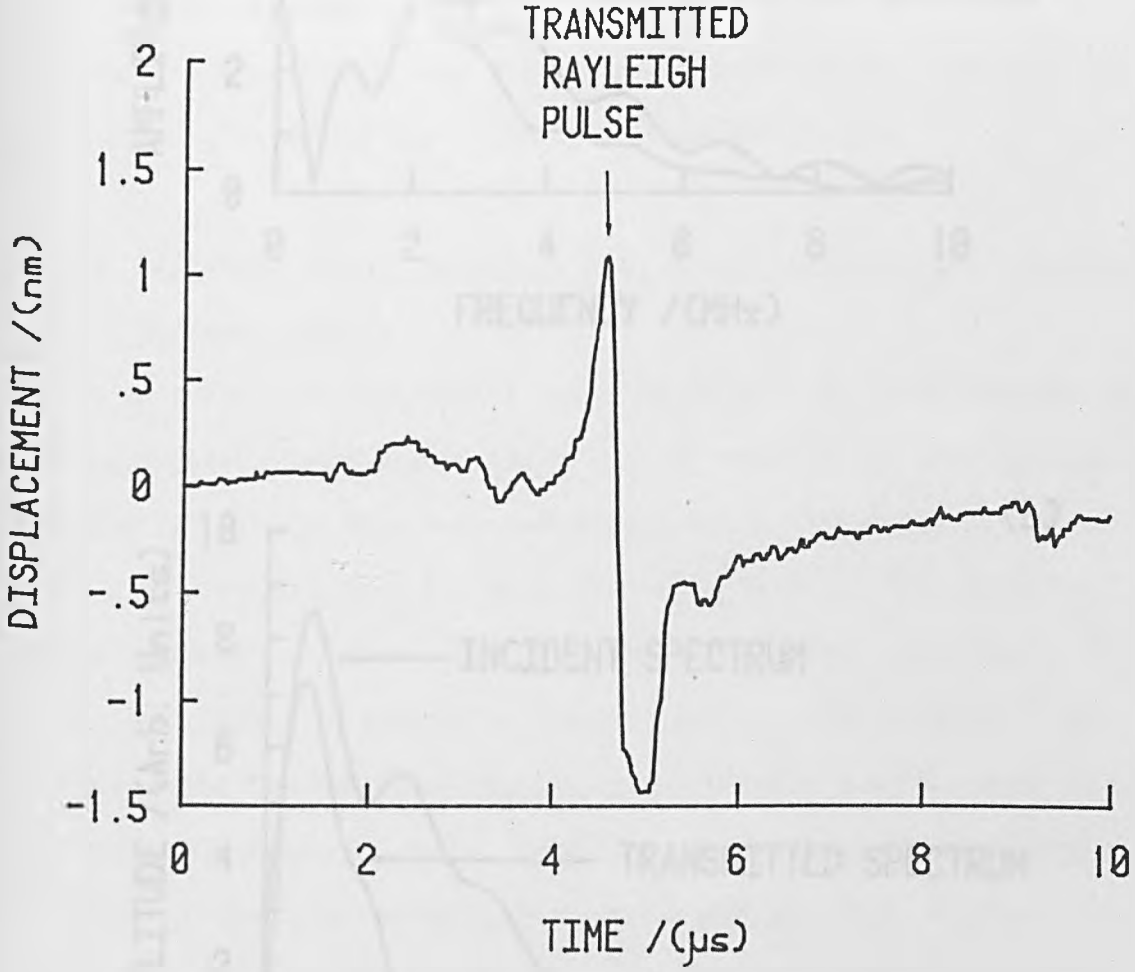

Fig. (5.10) Acoustic waveform transmitted through a machined slot in duraluminium. The size of the slot was 0.50 mm deep and 0.10 mm wide.

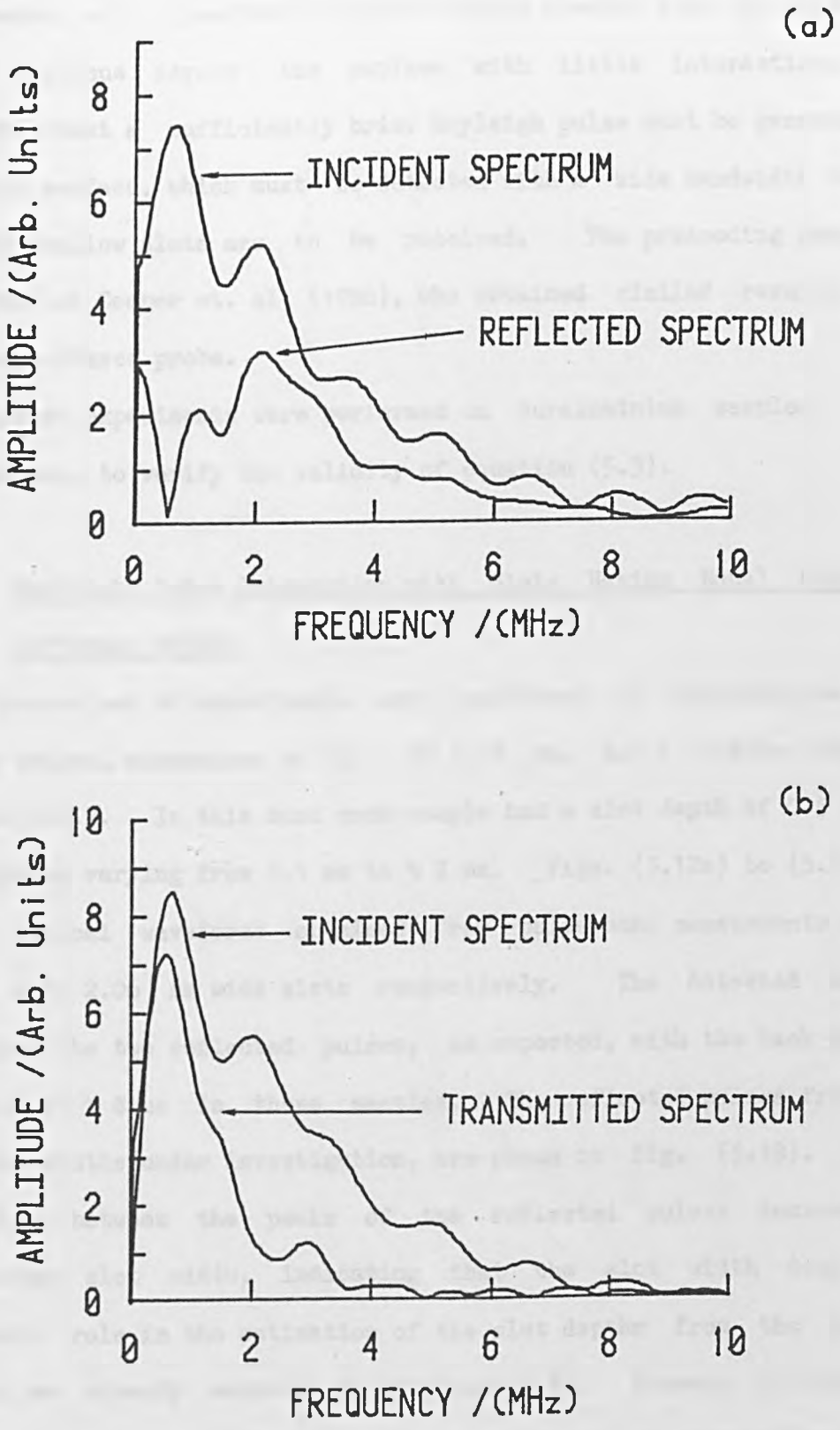

Fig. (5.11) (a) Comparison of the FFT's computed for the incident and reflected Rayleigh pulses from a 0.50 mm deep, 0.10 mm wide slot in duraluminium.
(b) Comparison of the FFT's computed for the incident and transmitted Rayleigh pulses for the same slot.

components, with a penetration significantly greater than the depth of the slot, continue across the surface with little interaction. This indicates that a sufficiently brief Rayleigh pulse must be generated on a material surface, which must be detected with a wide bandwidth detector, if very shallow slots are to be resolved. The preceeding data agrees with that of Cooper et. al. (1986), who obtained similar results using a ball-capacitance probe.

Further experiments were performed on duraluminium samples, in the time domain, to verify the validity of equation (5.3).

5.2.4 Rayleigh Pulse Interaction with Slots Having Equal Depths and Different Widths

A second set of experiments were performed on duraluminium samples having typical dimensions of 150 x 80 x 28 mm, in a similar fashion to section 5.2.3. In this case each sample had a slot depth of 0.5 mm, with slot widths varying from 0.1 mm to $\sim$ 2 mm. Figs. (5.12a) to (5.12c) show three typical waveforms obtained from pulse-echo measurments on 0.28, 0.87, and 2.06 mm wide slots respectively. The detected waveforms contained the two reflected pulses, as expected, with the back wall echo arriving at $\sim$ 8 μs in these samples. The reflected pulses from all of the slot widths under investigation, are shown in fig. (5.13). Clearly the time between the peaks of the reflected pulses increases with increasing slot width, indicating that the slot width does play an important role in the estimation of the slot depths from the reflected pulses, as already assumed in equation (5.3). However, in contrast to the results of fig. (5.5), this increase in pulse separation does not appear to be a linear function of slot width, as shown in fig. (5.14). Fig. (5.15) shows a graph of calculated slot depth, evaluated with

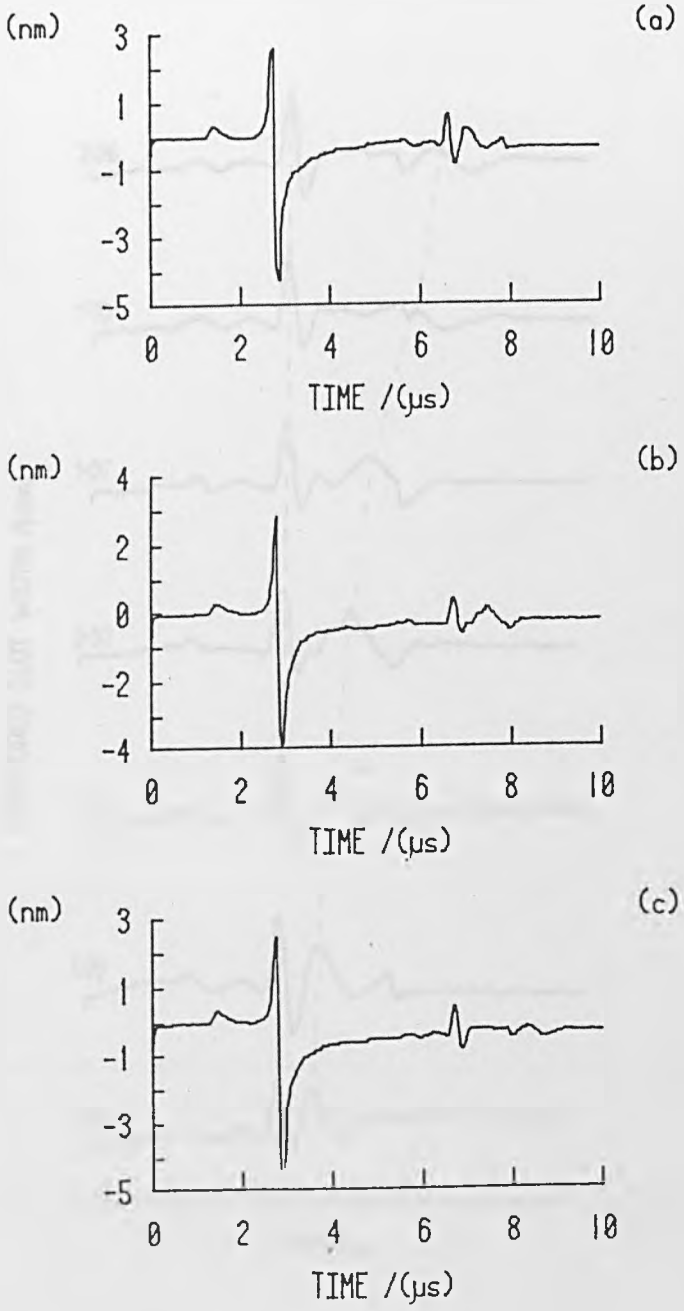

Fig. (5.12) Acoustic waveforms containing reflections from machined slots in duraluminium. Slot dimensions were 0.50 mm deep with widths of

(a) 0.28 mm
(b) 0.87 mm
(c) 2.06 mm

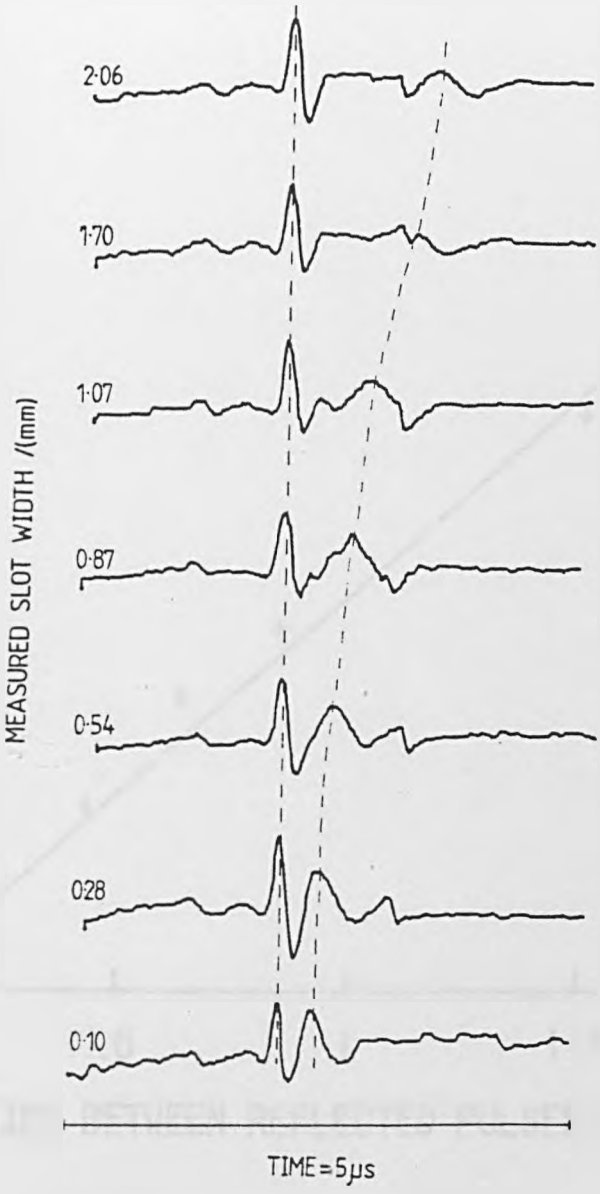

Fig. (5.13) Reflected surface acoustic waveform in duraluminium as a function of machined slot width. The slot depth was 0.50 mm in all cases.

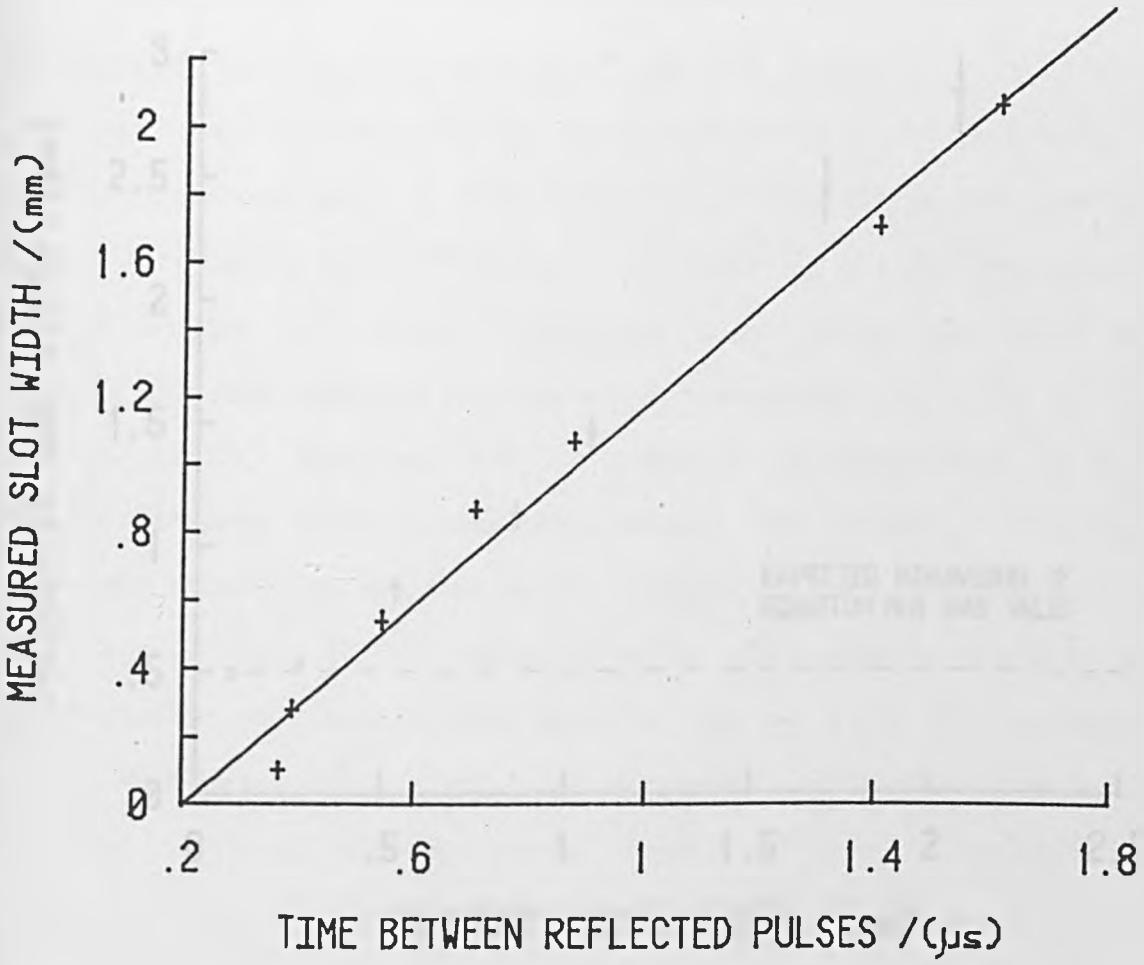

Fig. (5.14) Experimental results of the reflected pulse separation as a function of slot width. The relationship does not appear to be linear.

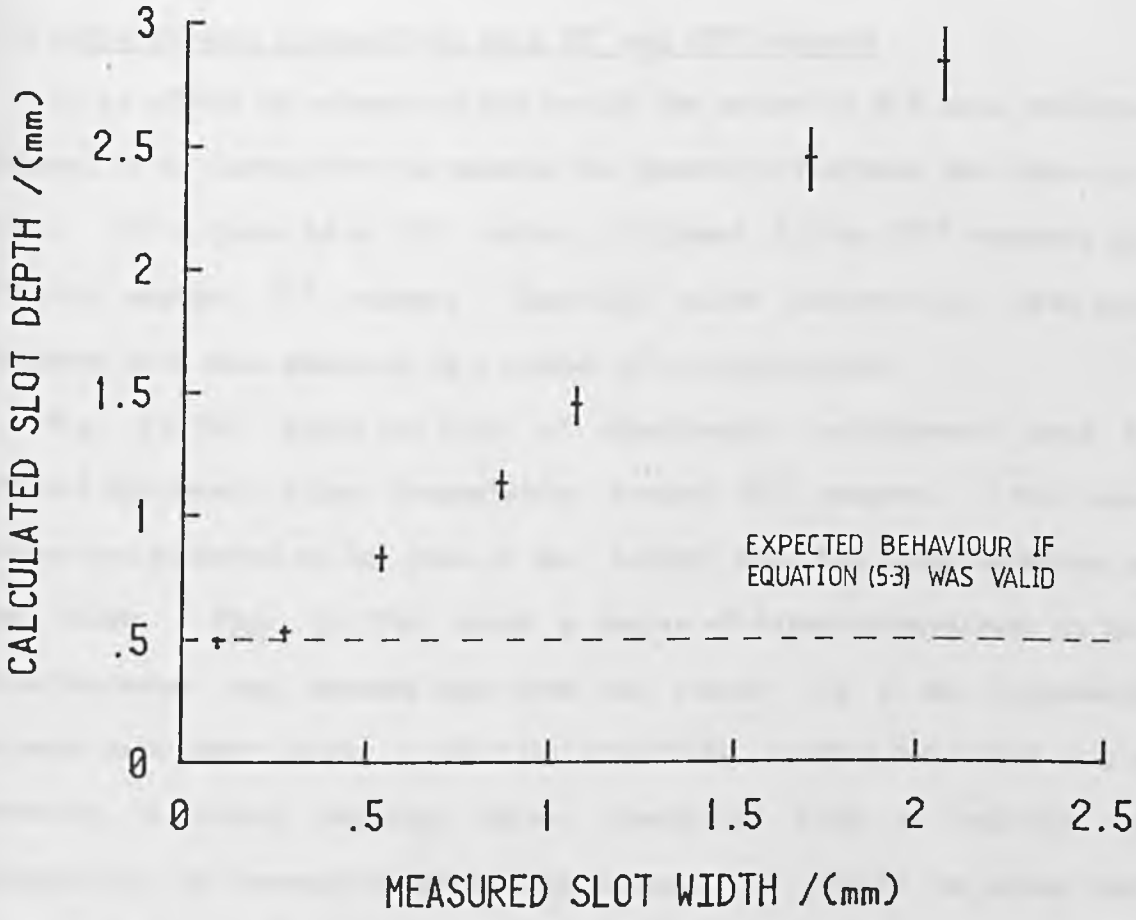

Fig. (5.15) Experimental results of slot depth estimation as a function of measured slot width. Equation (5.3) is only valid for slot widths of $\sim$ 0.3 mm and less.

equation (5.3), against measured slot width. Clearly the slot depth estimation formula is only valid for slot widths less than $\sim$ 0.3 mm.

From the preceeding results and discussion, it would be expected that when the slot becomes infinitely wide, as for the case of a downstep, no second peak should exist. This is borne out by the waveforms of fig. (5.16) obtained on 0.5 mm and 1.0 mm down steps.

5.3 Rayleigh wave interactions with 90^0 and 270^0 corners

In an effort to understand and verify the nature of the back reflected pulses, it is instructive to examine the geometric features that make up a slot. First there is a 90^0 corner, followed by two 270^0 corners, and finally another 90^0 corner. Rayleigh pulse interactions with such features have been examined in a number of configurations.

Fig. (5.17a) shows one form of experimental arrangement used to explore ultrasonic pulse transmission around 90^0 corners. The laser source was situated on one side of the corner and the interferometer on the other. Fig. (5.17b) shows a series of detected waveforms as the interferometer was scanned away from the corner, in 3 mm increments between each laser shot. All the waveforms confirm that from such a geometry, a strong Rayleigh pulse, identified from its velocity of propagation, is transmitted around the corner. It should be noted that the Rayleigh pulse has significantly changed shape, to a predominantly unipolar pulse. There is also evidence of both longitudinal and shear pulses arriving at the detector travelling directly from the laser source. The directivity pattern for the longitudinal and shear pulses have maxima at $\sim 30^0$ and 60^0 respectively (Scruby et. al., 1982) with corresponding maxima in the waveforms for detector distances of 9 mm and 18 mm.

An experiment with the interferometer on the same surface of the laser

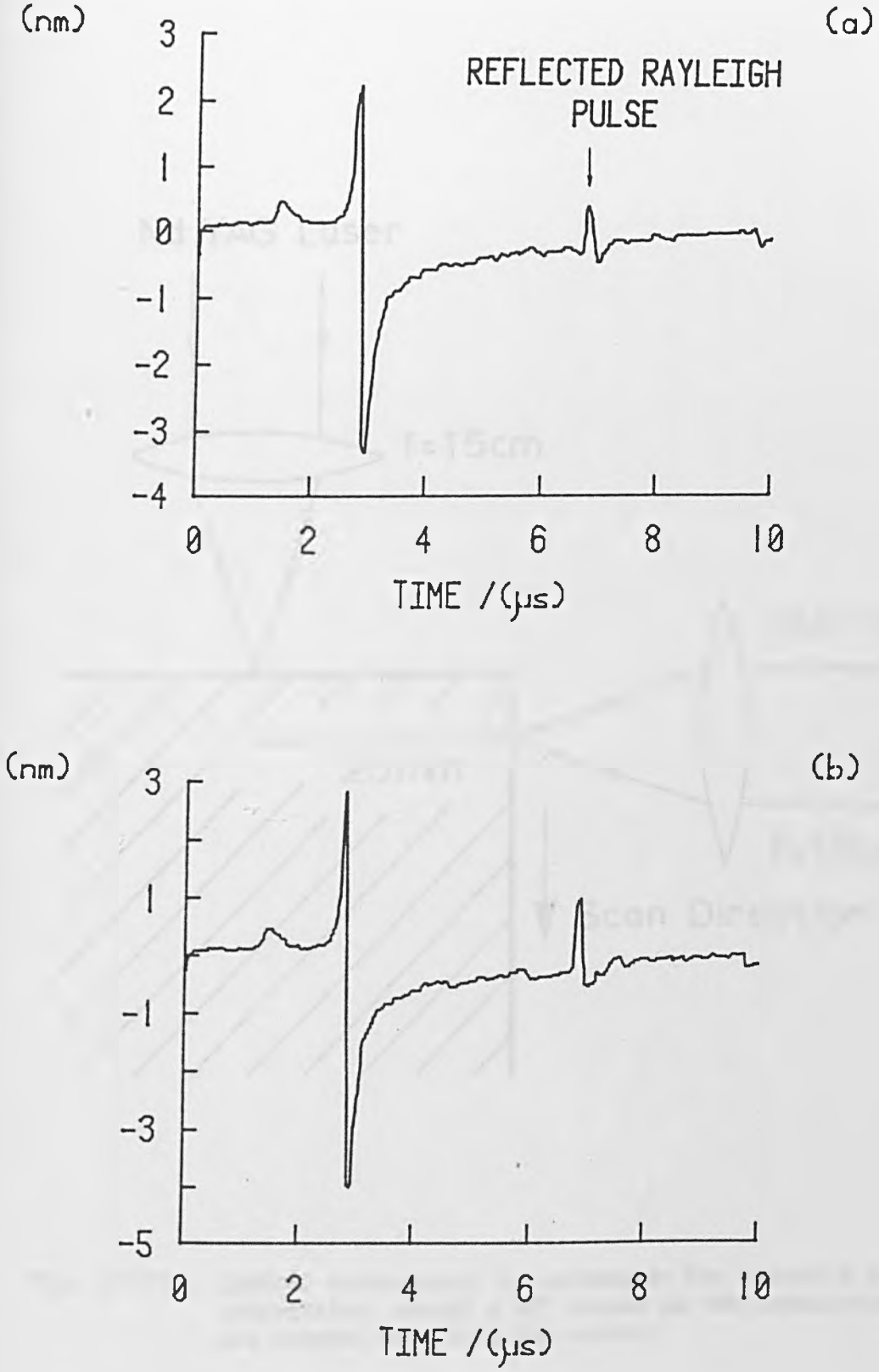

Fig. (5.16) Acoustic surface waveforms showing the predominantly unipolar nature of a reflection from a downstep of depth
(a) 0.50 mm
(b) 1.0 mm

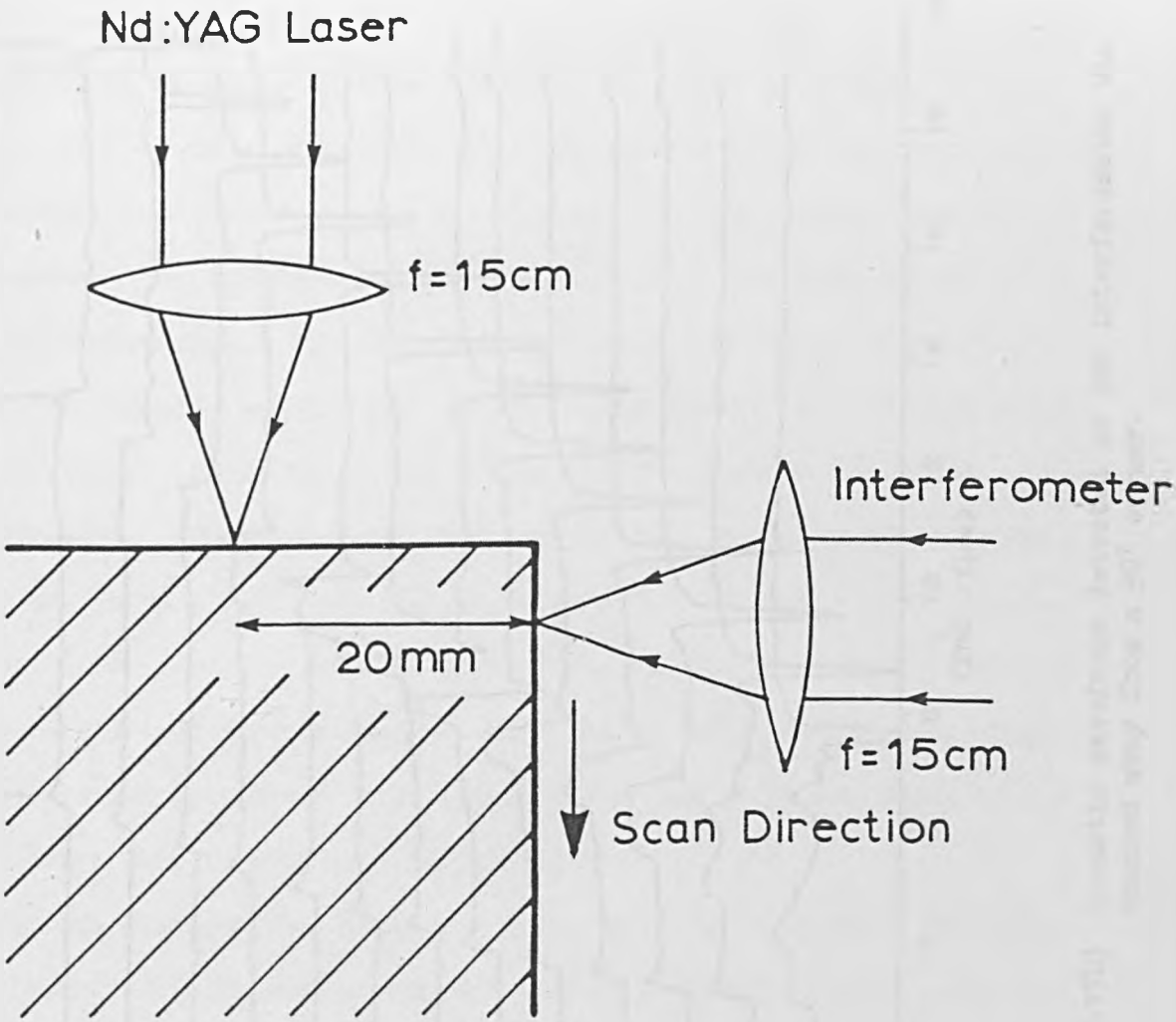

Fig. (5.17a) Optical arrangement to determine the acoustic pulses propagating around a 90^0 corner as the interferometer was scanned away from the corner.

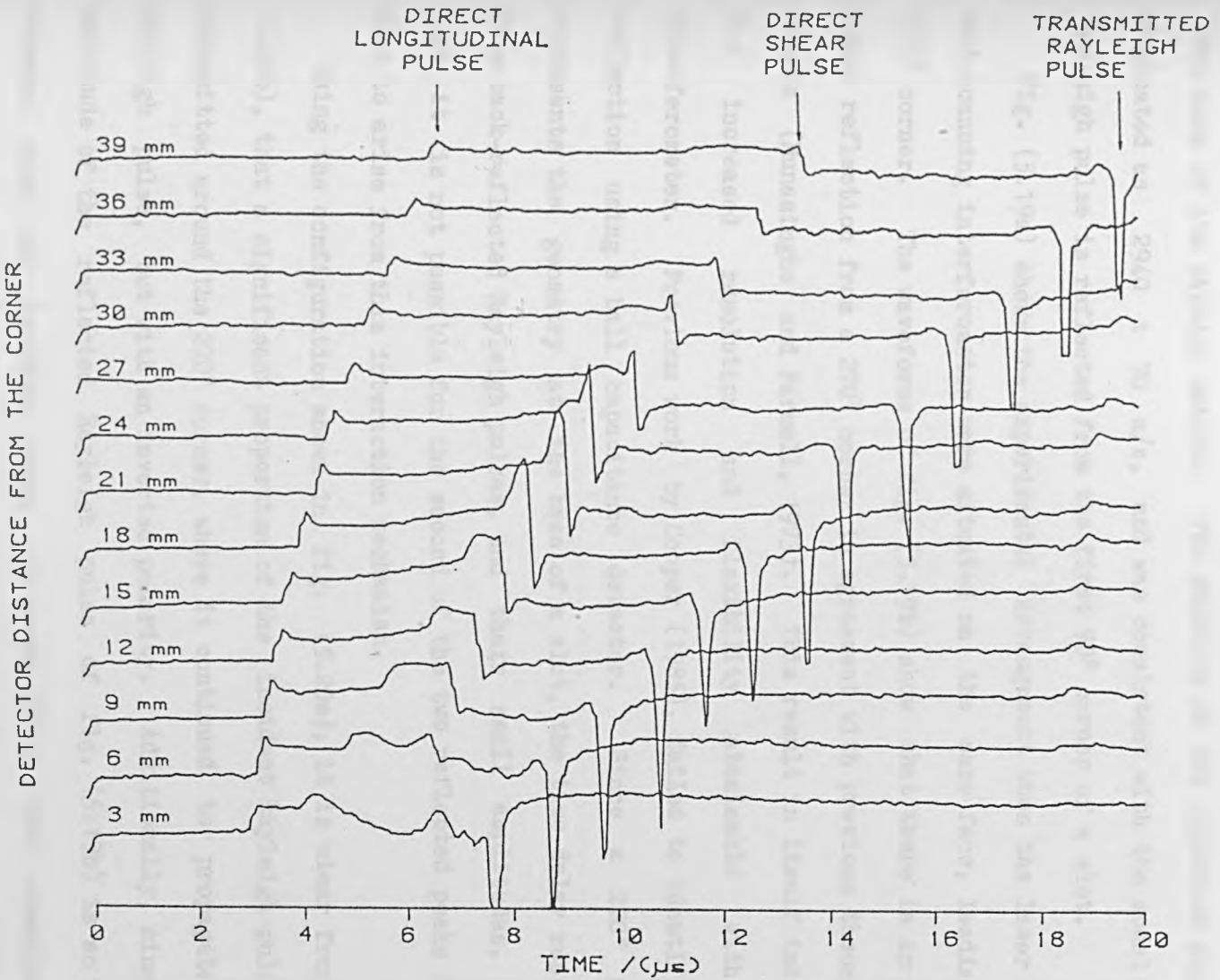

Fig. (5.17b) Acoustic waveforms detected as the interferometer was scanned away from a 90^0 corner.

source, as in fig. (5.18a), shows that the reflected Rayleigh pulse from a 90^0 corner consists of just one peak, shown in fig. (5.18b). The reflected pulse had the same polarity as the incident pulse, and had again lost much of its bipolar nature. The velocity of the reflected pulse was evaluated as 2940 ± 70 m/s, and was consistent with the model that a Rayleigh pulse is reflected from the first 90^0 corner of a slot.

Fig. (5.19a) shows the experimental arrangement when the laser source and scanning interferometer were situated on the same face, leading to a 270^0 corner. The waveforms of fig. (5.19b) show that there is in fact a small reflection from a 270^0 corner in agreement with previous theoretical models (Munasinghe and Farnell, 1973). This result in itself indicates the increased resolution and flexibility attainable with the interferometer. Previous work by Cooper (1985), failed to identify this reflection using a ball capacitance detector. Since a 270^0 corner represents the geometry at the base of a slot, the time delay resulting from back-reflected Rayleigh pulses, and their small amplitudes, shows that it is not possible for the second of the two reflected peaks from a slot to arise from this interaction mechanism.

Using the configuration shown in fig. (5.20a), it is clear from fig. (5.20b), that a significant proportion of the incident Rayleigh pulse was transmitted around the 270^0 corner, where it continued to propagate as a Rayleigh pulse, but with an inverted polarity. Additionally, since the amplitude of the reflected Rayleigh pulse of fig. (5.19b) is so small compared with the incident pulse, it seems likely that considerable ultrasonic mode conversion occurs at the slot base.

To investigate this phenomena, computer simulations of acoustic surface waves interacting with surface discontinuities have been developed (Bond, 1979, Bond and Saffari, 1984, and Fuyuki and Nakano, 1984), based

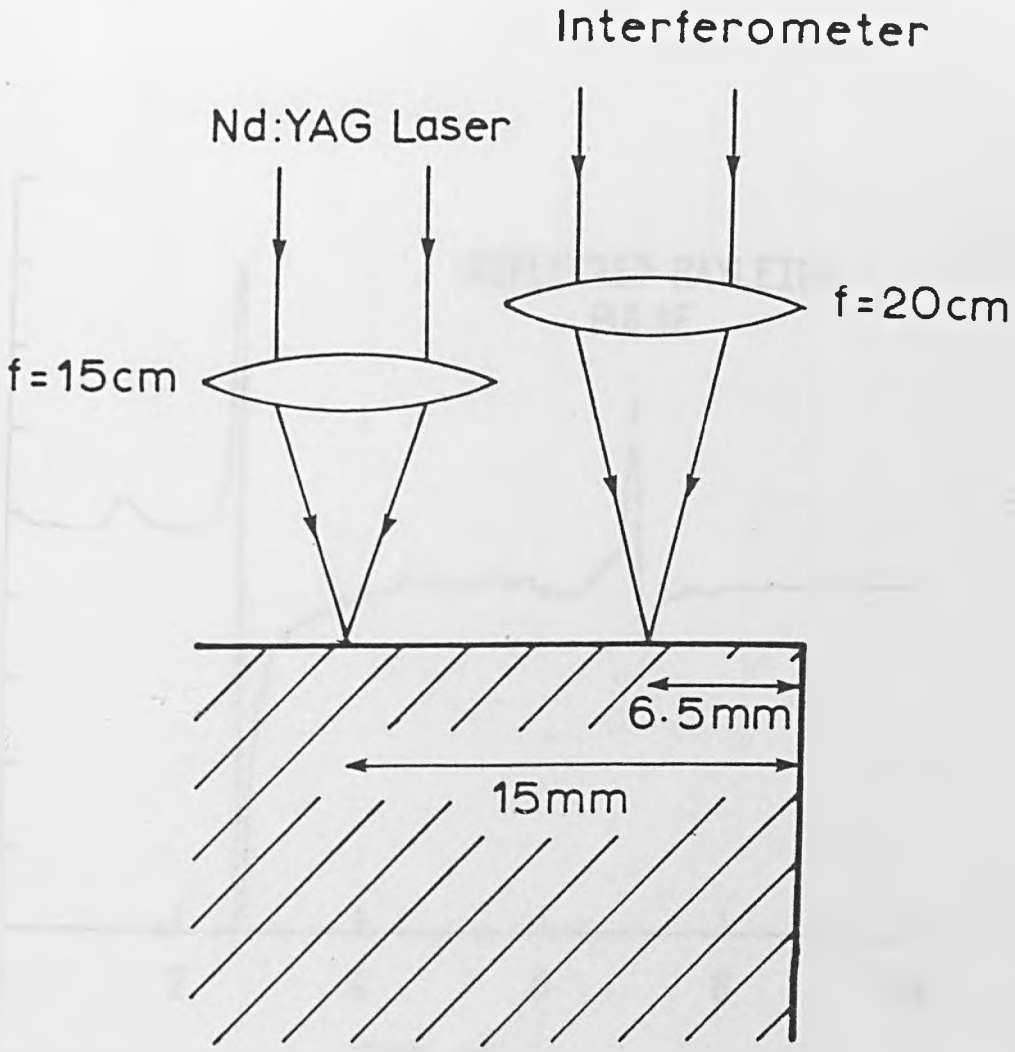

Fig. (5.18a) Optical arrangement for the detection of surface acoustic pulses reflected from a 90^0 corner.

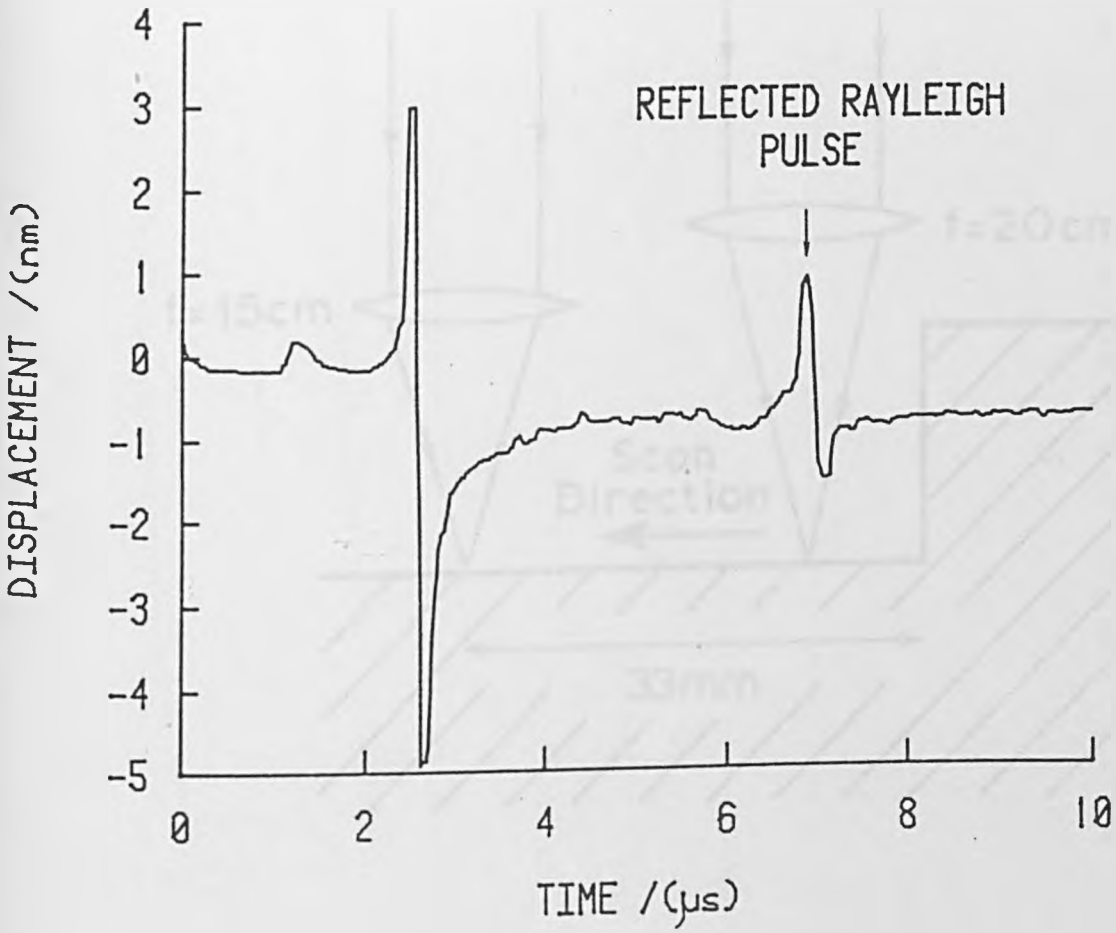

Fig. (5.18b) Acoustic waveform showing a typical reflected Rayleigh pulse from a 90^0 corner.

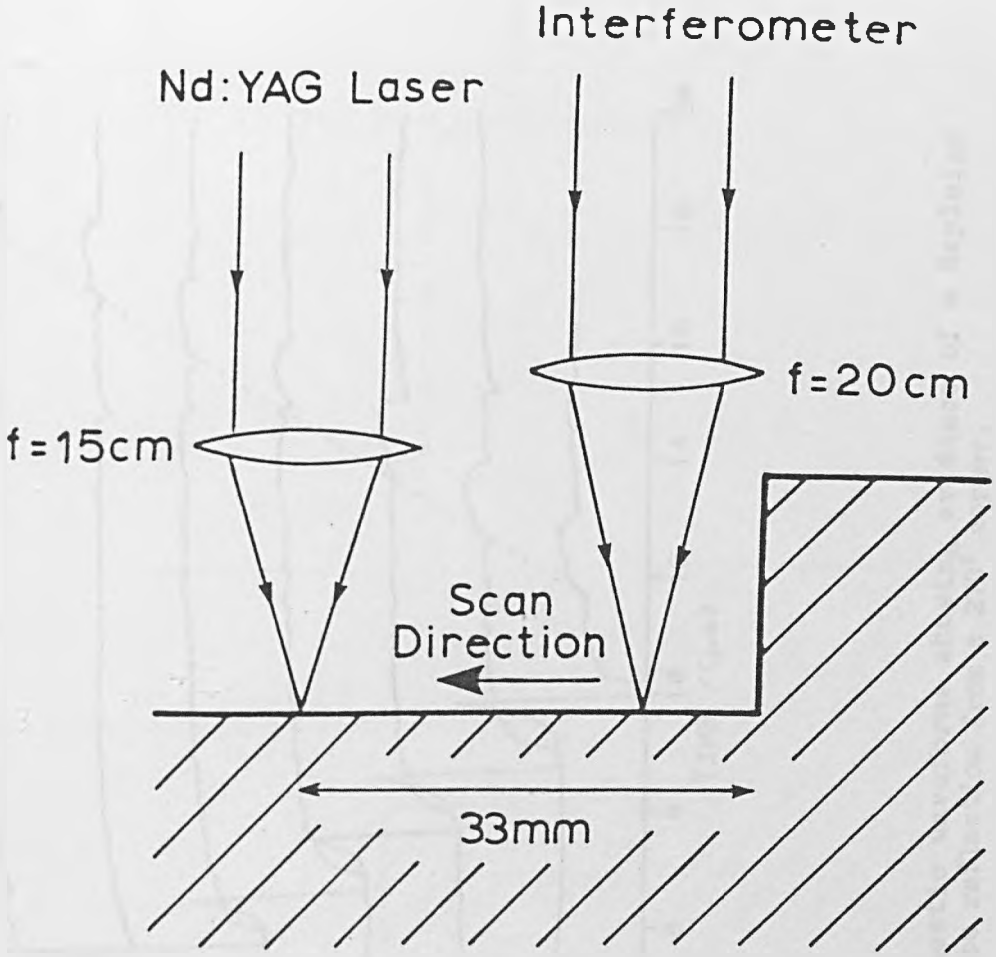

Fig. (5.19a) Optical arrangement to detect the surface acoustic pulses reflected from a 270^0 corner as the interferometer was scanned away from the corner.

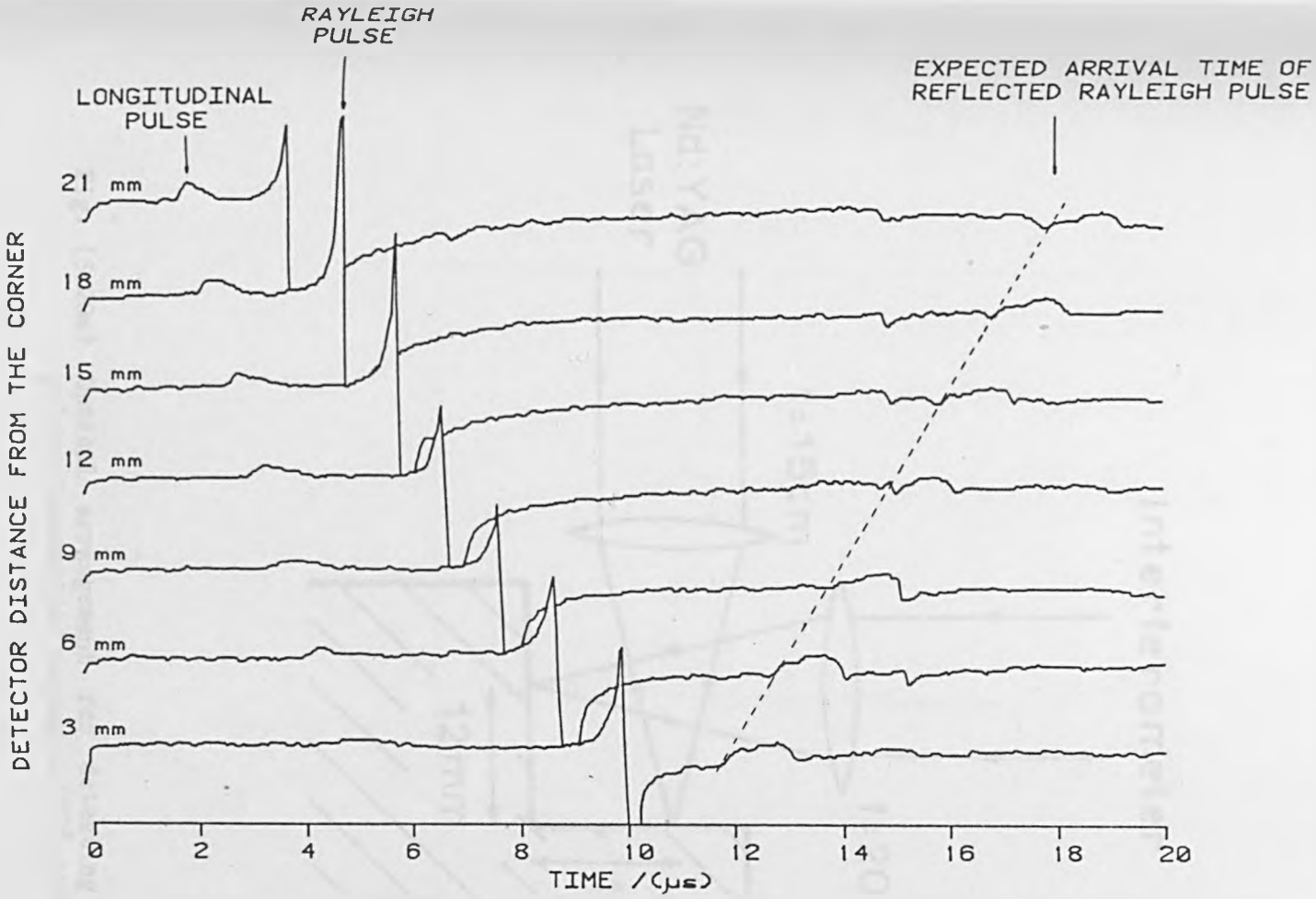

Fig. (5.19b) Acoustic waveforms showing evidence of a Rayleigh pulse reflection from a 270^0 corner.

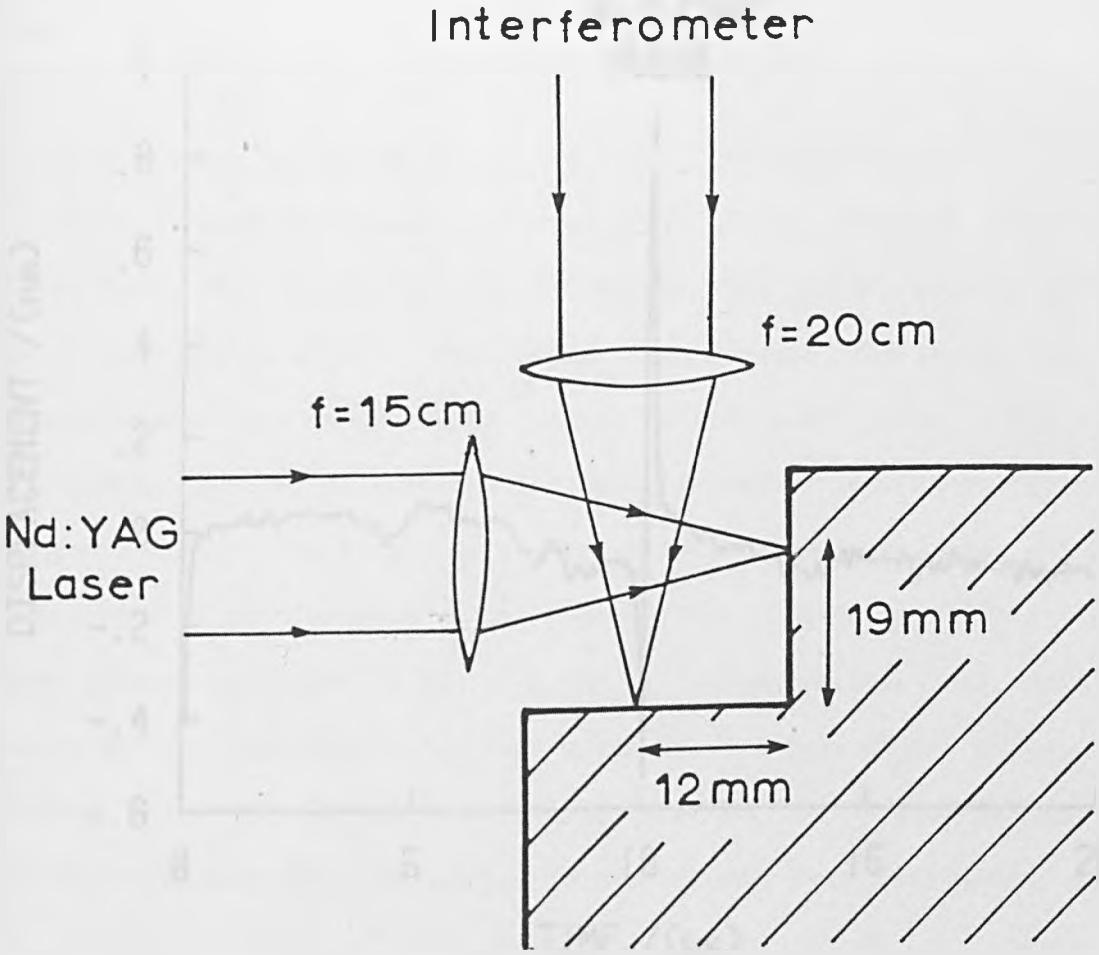

Fig. (5.20a) Optical arrangement for detecting surface acoustic pulses transmitted around a 270° corner.

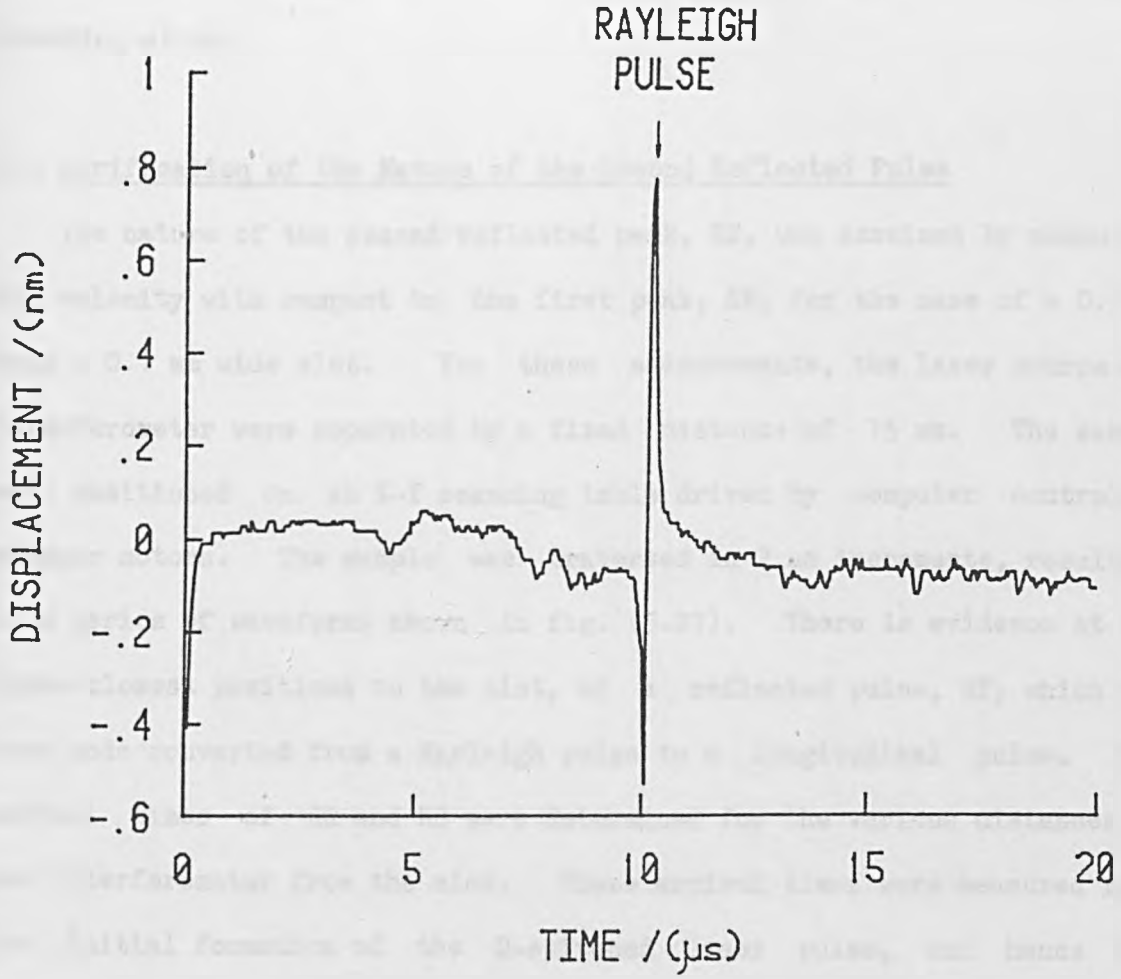

Fig. (5.20b) Acoustic waveform detected after Rayleigh pulse transmission around a 270° corner.

on the finite difference formulation of the wave equation for acoustic propagation in elastic solids. They have suggested that strong mode conversion takes place at a 270^0 corner, with surface wave energy being converted into bulk shear wave energy. This is in agreement with an experimental study in 1970 (Reinhardt and Daly) which used a photoelastic technique to investigate the interaction of Rayleigh wave with surface breaking slots.

5.4 Verification of the Nature of the Second Reflected Pulse

The nature of the second reflected peak, RS, was examined by measuring its velocity with respect to the first peak, RR, for the case of a 0.5 mm deep x 0.1 mm wide slot. For these measurements, the laser source and interferometer were separated by a fixed distance of 15 mm. The sample was positioned on an X-Y scanning table driven by computer controlled stepper motors. The sample was traversed in 2 mm increments, resulting in a series of waveforms shown in fig. (5.21). There is evidence at the three closest positions to the slot, of a reflected pulse, RP, which has been mode converted from a Rayleigh pulse to a longitudinal pulse. The arrival times of RR and RS were determined for the various distances of the interferometer from the slot. These arrival times were measured from the initial formation of the Q-switched laser pulse, and hence the acoustic source, to the peaks of the respective pulses. Fig. (5.22) shows the variation in arrival time for RR and RS, with the round trip distance from the interferometer detection point, to the slot. Although the absolute distance from the interferometer to the slot was not accurately known, the distance moved between each pair of measuring positions, was accurately derived from the calibration of the X scan on the stepper motor control. Thus the gradient of the lines in fig. (5.22)

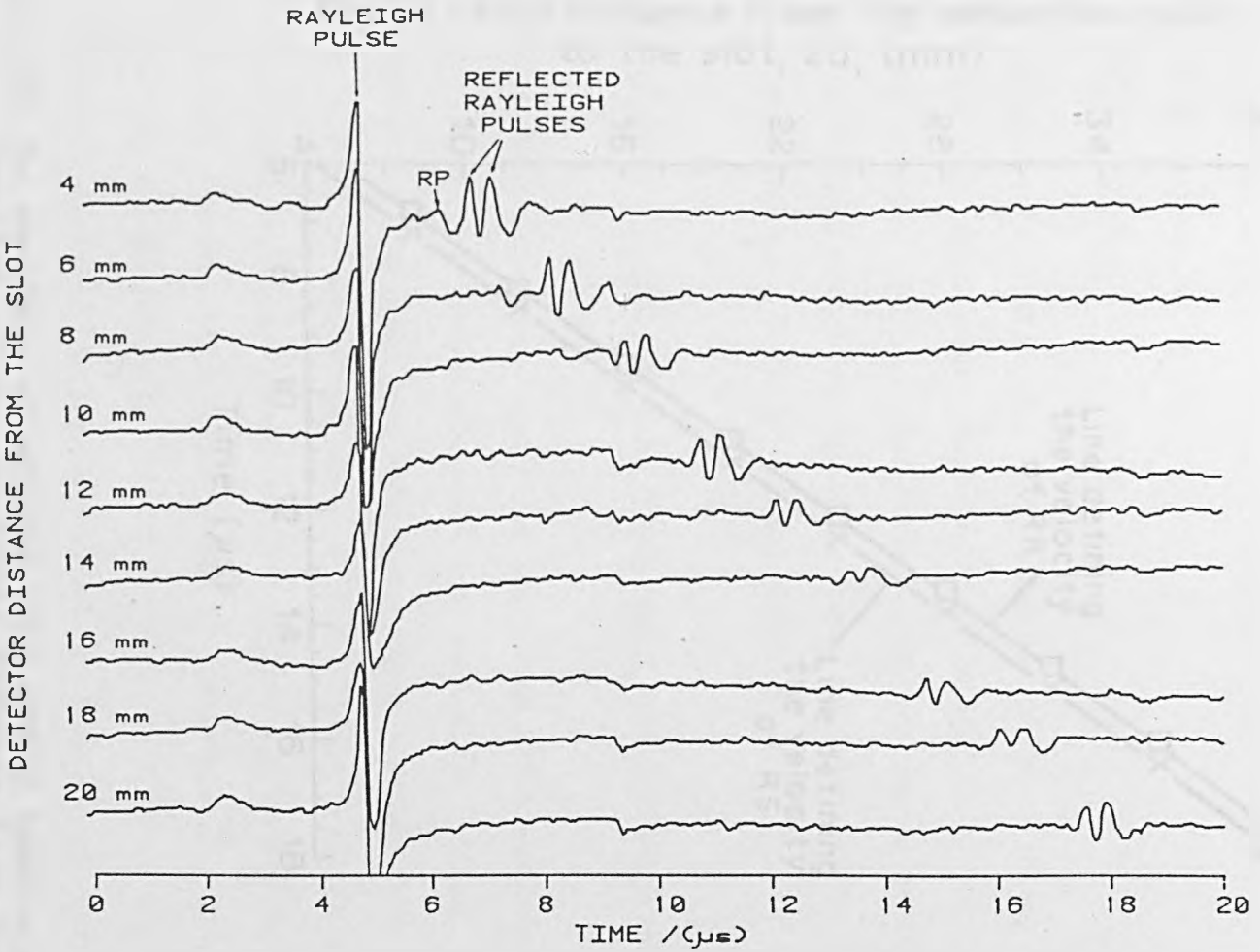

Fig. (5.21) Acoustic waveforms obtained to accurately determine the velocity of both reflected pulses.

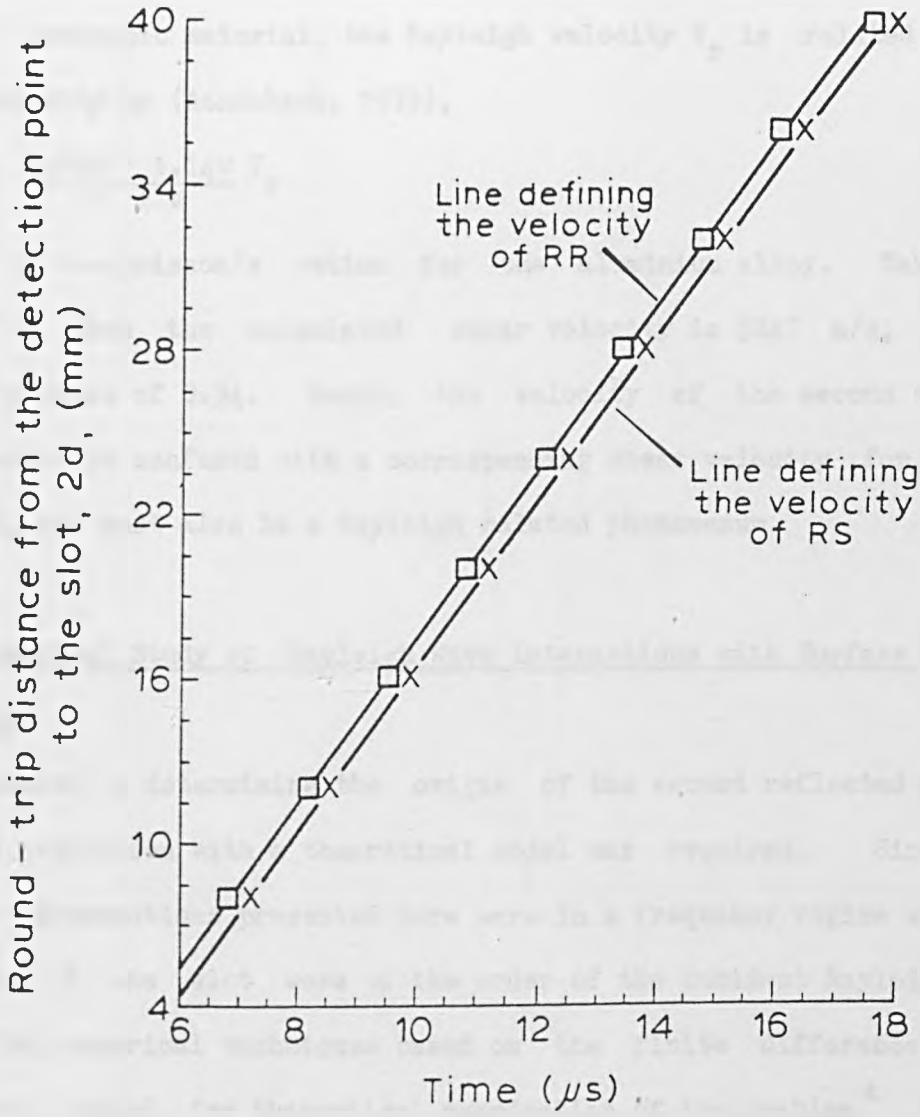

Fig. (5.22) The dependence of reflected pulse arrival times as a function of the round-trip distance from the interferometer to the slot. Time is measured relative to the formation of the Q-switched laser pulse.

gives an accurate determination of velocity for both RR and RS. The propagation velocity of the peak RR was evaluated as 3028 ± 19 m/s, and that of RS as 3022 ± 18 m/s. These two values can be considered equal within the limits of experimental error. Moreover, they may be compared with the value which can be expected for the shear velocity V_s. For an isotropic material, the Rayleigh velocity V_r is related to the shear velocity by (Achenbach, 1973),

$$V_r = \frac{0.862 + 1.14\nu}{1 + \nu} V_s$$

where ν is the poisson's ration for the aluminium alloy. Taking Vr = 3028 m/s, then the calculated shear velocity is 3247 m/s, using a poisson's ratio of 0.34. Hence, the velocity of the second reflected pulse cannot be confused with a corresponding shear velocity for the same material, and must also be a Rayleigh related phenomenum.

5.5 A Numerical Study of Rayleigh Wave Interactions with Surface Breaking Slots

To assist in determining the origin of the second reflected pulse, a detailed comparison with a theoretical model was required. Since the acoustic interactions presented here were in a frequency regime where the dimensions of the slot were of the order of the incident Rayleigh pulse wavelength, numerical techniques based on the finite difference method were best suited for theoretical examination of the problem.* This was examined by Saffari and Bond (1987).

The experimental incident Rayleigh pulse had a centre frequency of approximately 2 MHz. In the numerical study, this was approximated by a Ricker pulse (Ricker, 1945), depicted in fig. (5.23), which contained a smooth envelope of frequencies around a centre frequency. The form of

* Bond and Saffari (1984)

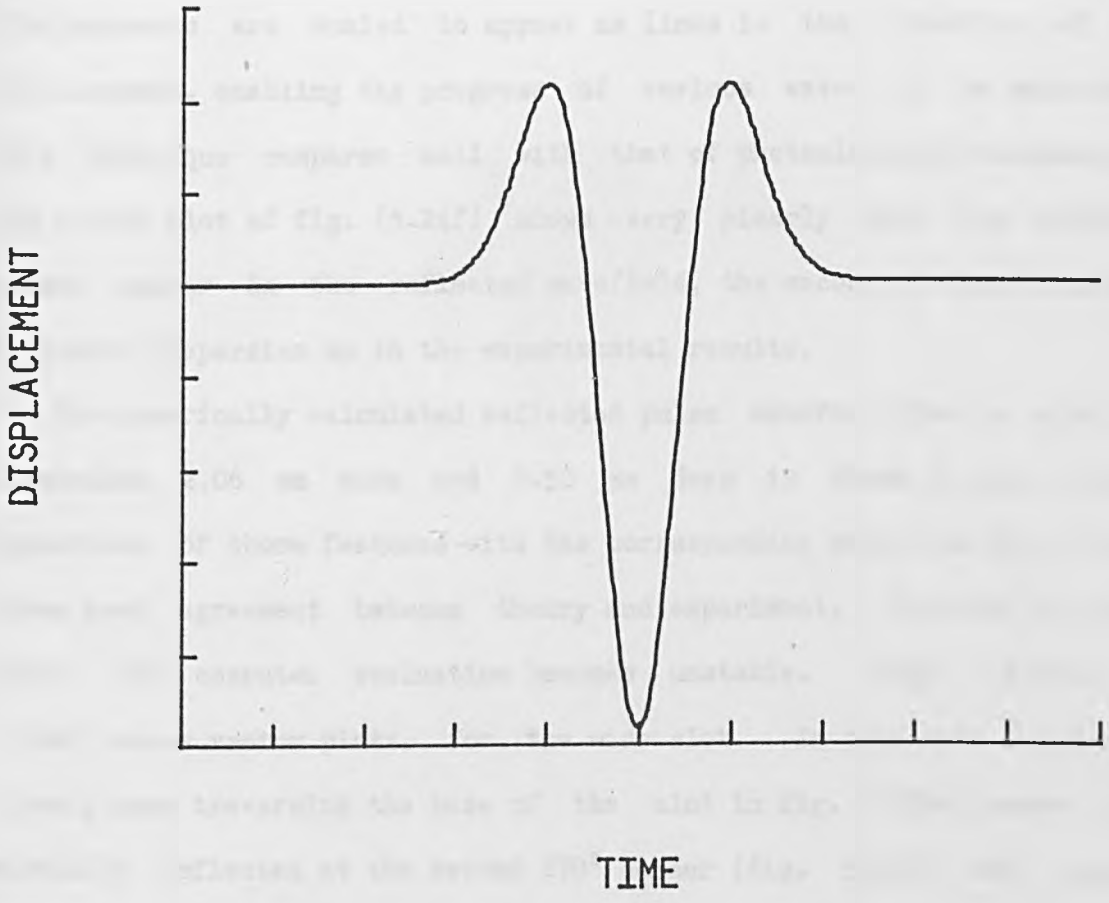

Fig. (5.23) The form of the Ricker pulse used for the numerical study of Rayleigh wave interactions with surface breaking slots.

the Ricker pulse is given by (Hirao et. al, 1982),

$$U = \sqrt{\pi}\ [{}^{1}/_{2} - (\pi t)^2]\ \exp[1 - (\pi t)^2]$$

where U is the displacement.

The time development of the complete displacement field has been iteratively calculated and is shown in figs. (5.24a) to (5.24f) for a Ricker pulse interaction with a 0.50 mm deep and 0.1 mm wide slot. This form of display is known as a vector plot in which the surface displacements are scaled to appear as lines in the direction of the displacement, enabling the progress of various waves to be monitored. This technique compares well with that of photoelastic visualisation. The vector plot of fig. (5.24f) shows very clearly that two distinct pulses appear in the reflected wavefield, the second of which exhibits frequency dispersion as in the experimental results.

The numerically calculated reflected pulse waveform for a slot of dimensions 2.06 mm wide and 0.50 mm deep is shown in fig. (5.25). Comparison of these features with the corresponding pulses in fig. (5.13) shows good agreement between theory and experiment. However, for long times, the computer evaluation becomes unstable. Figs. (5.26a) to (5.26f) shows vector plots, for the wide slot. In this case a pulse is clearly seen traversing the base of the slot in fig. (5.26a) where it is partially reflected at the second 270^0 corner (fig. 5.26b) and travels back along the slot base (fig. (5.26c). A transmitted component continues along the contours of the slot. When the reflected Rayleigh pulse reaches the first 270^0 corner again, a large proportion of the energy is converted to a shear wave, which has a near cylindrical wavefront. This curved shear wavefront is subsequently incident on the top stress-free surface near the slot top. Examination of the wave excited along the top surface by the shear wavefront reveals that its

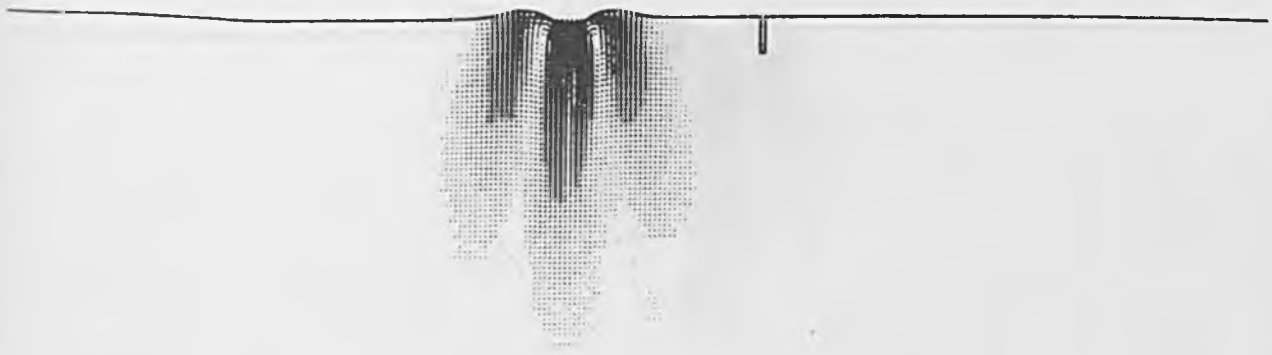

Fig. (5.24a) Time development of the complete displacement wavefield for the interaction of a Ricker pulse with a 0.50 mm deep, 0.10 mm wide slot.

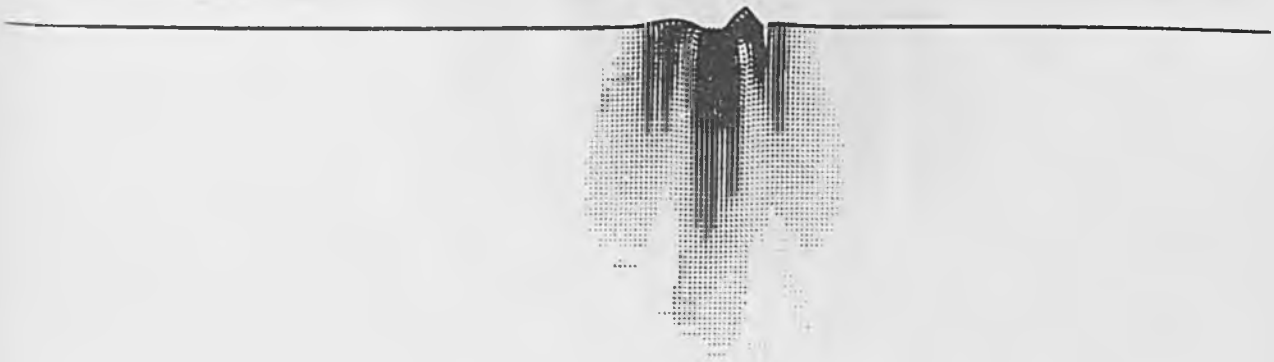

Fig. (5.24b)

Fig. (5.24c)

Fig. (5.24d)

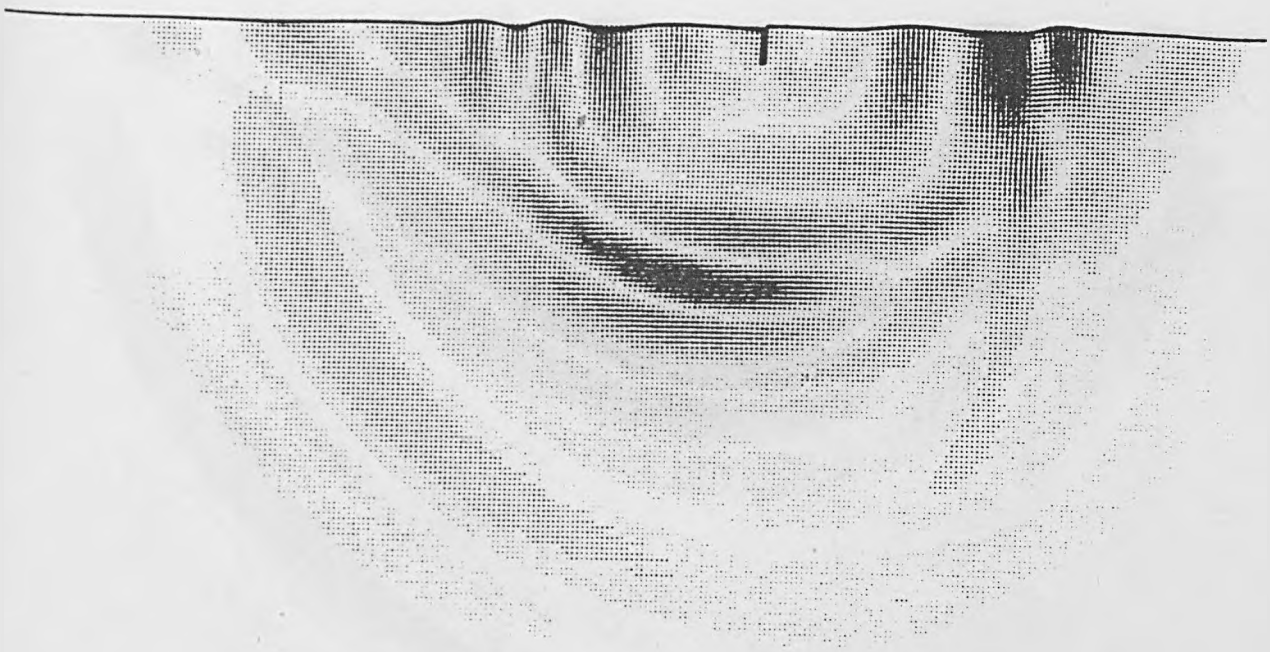

Fig. (5.24e)

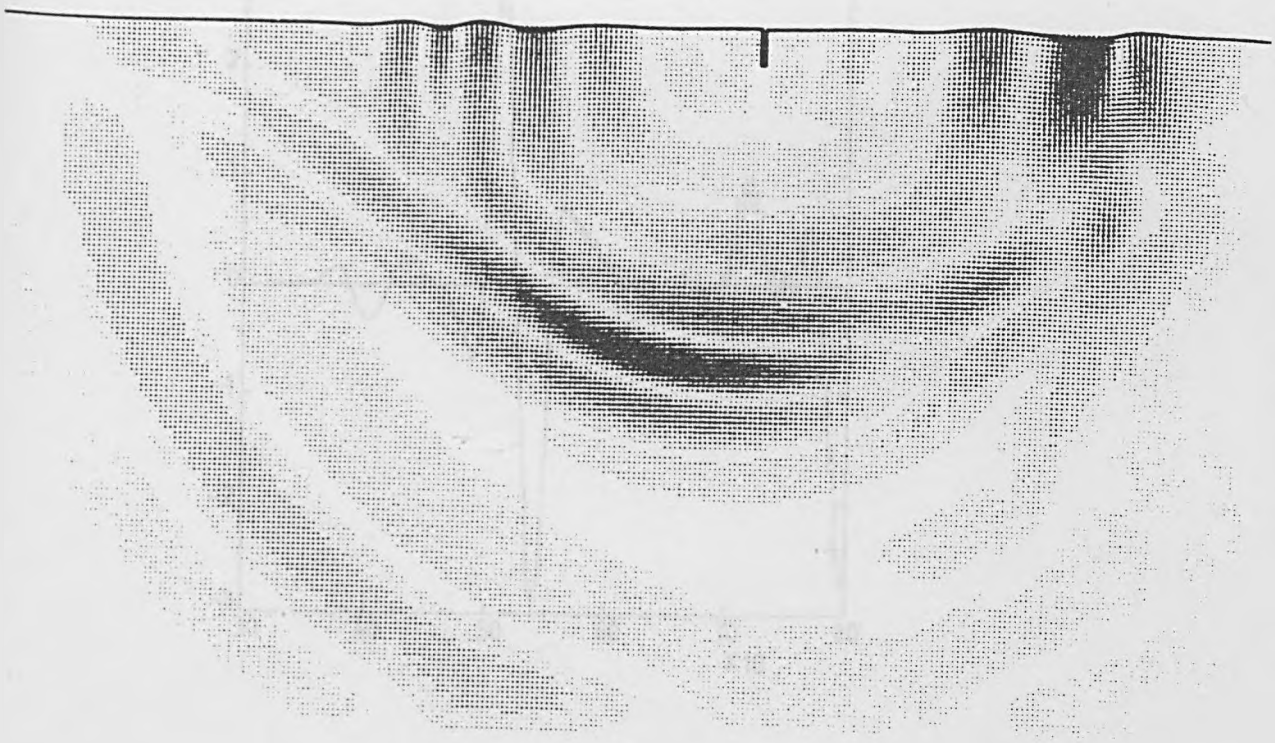

Fig. (5.24f)

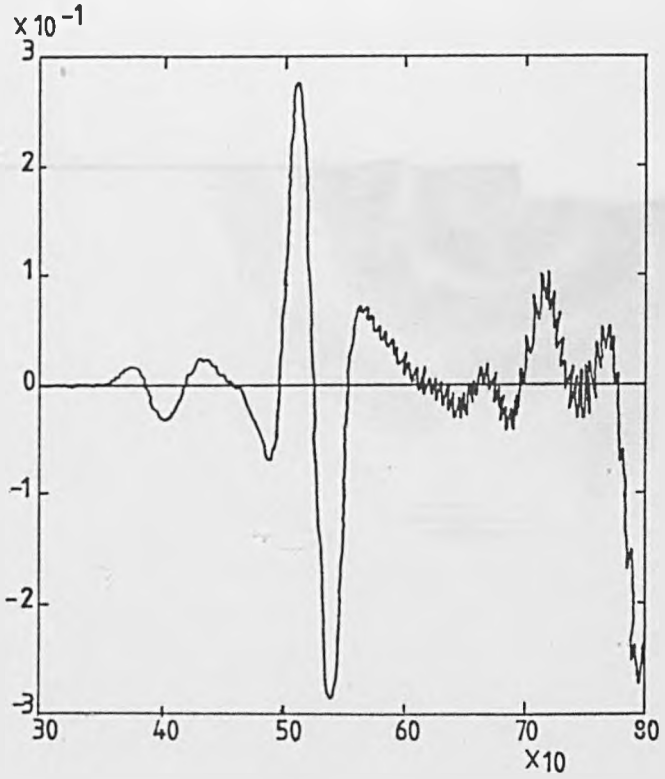

Fig. (5.25) The numerically calculated reflected waveform from a 2.06 mm wide, 0.50 mm deep slot.

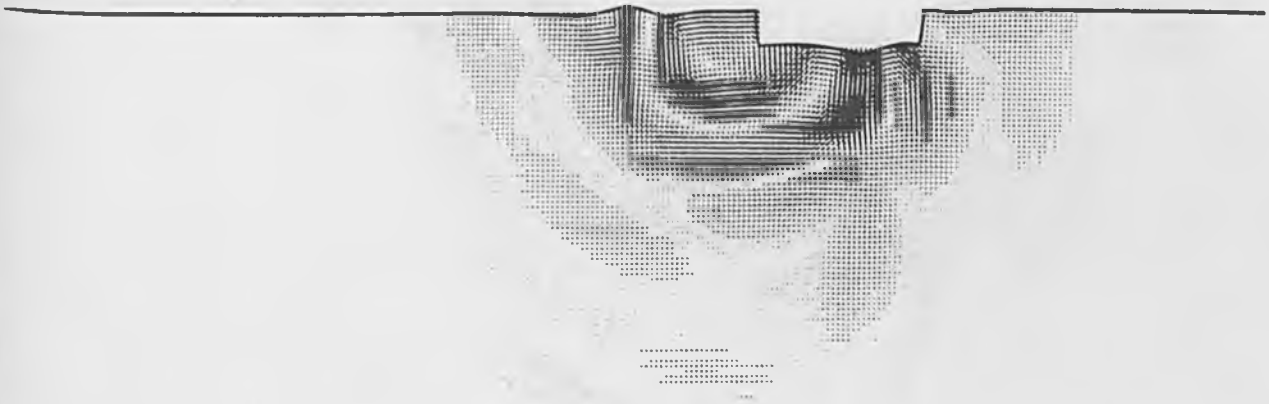

Fig. (5.26a) Time development of the complete displacement wavefield for the interaction of a Ricker pulse with a 2.06 mm wide, 0.50 mm deep slot.

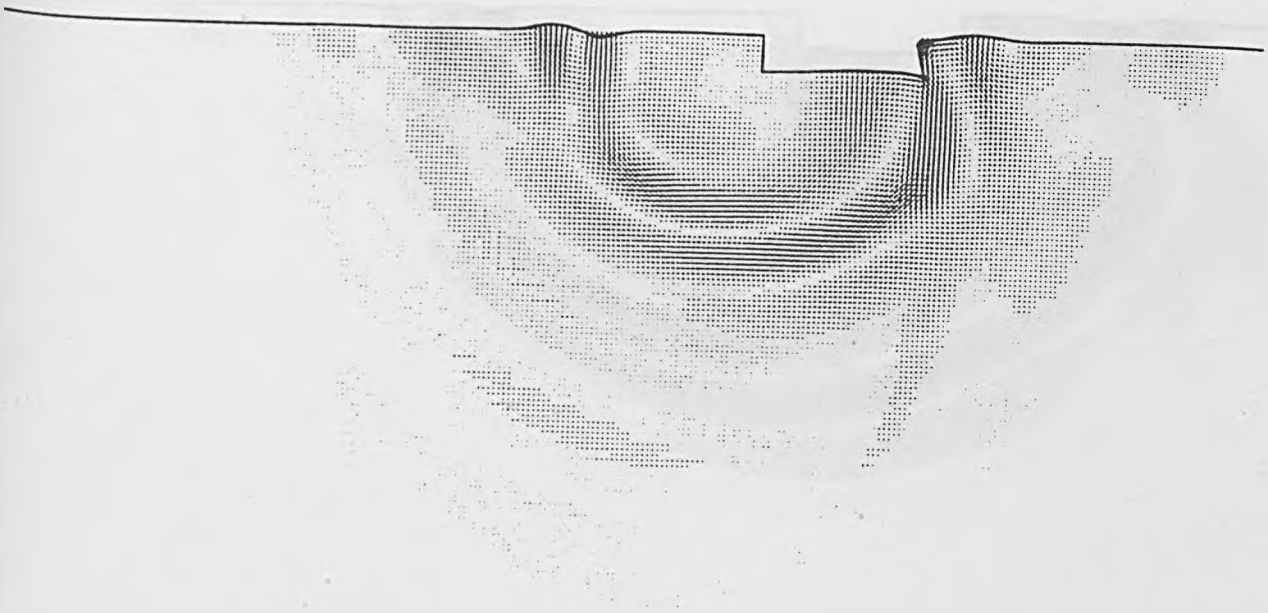

Fig. (5.26b)

Fig. (5.26c)

Fig. (5.26d)

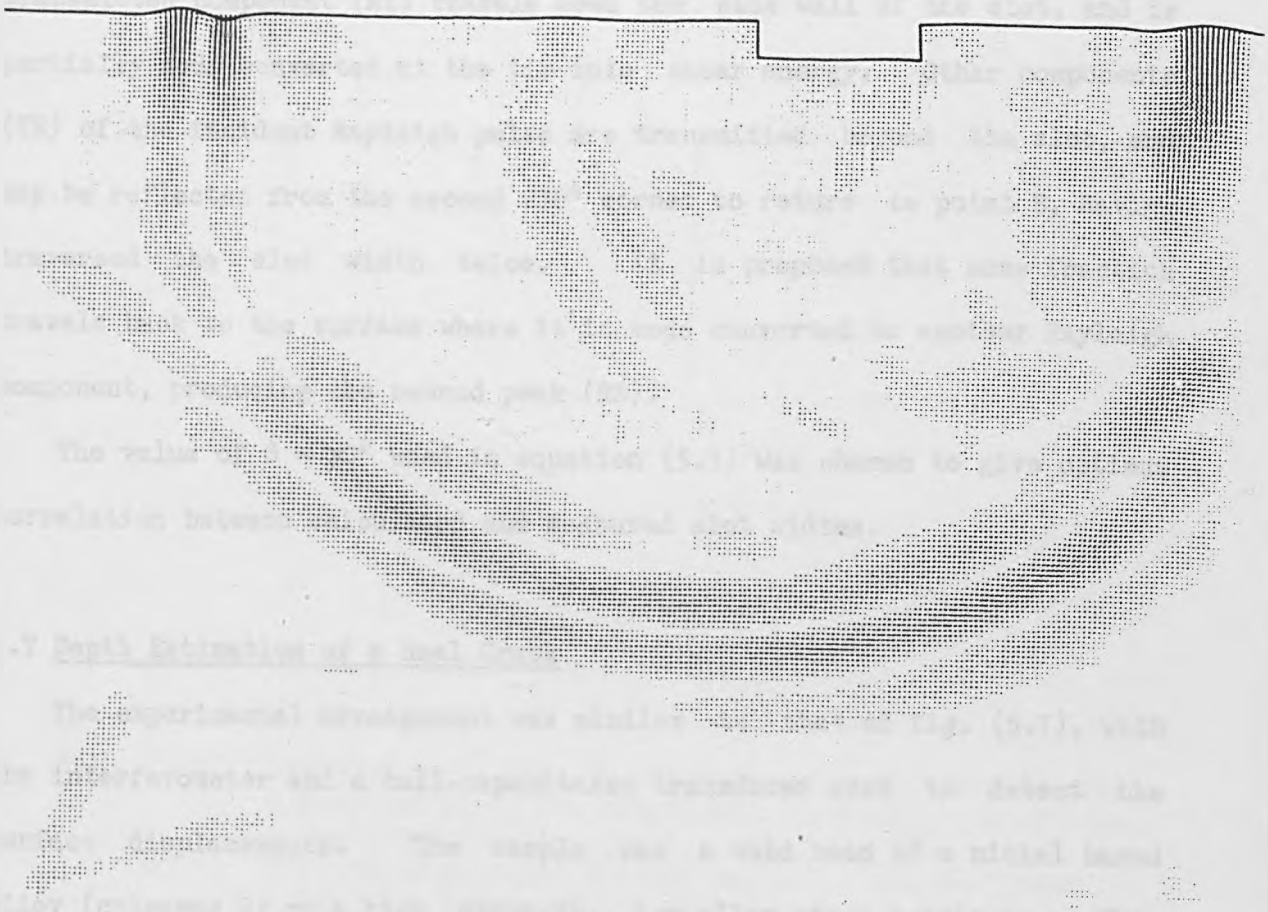

Fig. (5.26e)

motion is elliptical, characteristic of a Rayleigh wave.

5.6 Proposed Model of Rayleigh Pulse Interaction with a Slot

Based on the results presented in the previous sections, it is proposed that the observed waveforms can be understood in terms of the interaction mechanism depicted in fig. (5.27). The first peak is clearly the well known reflected Rayleigh pulse (RR), which arises from the incident Rayleigh pulse interaction with the top corner of the slot. A transmitted component (RT) travels down the side wall of the slot, and is partially mode converted at the tip into shear energy. Other components (TR) of the incident Rayleigh pulse are transmitted beyond the slot, and may be reflected from the second 270^0 corner to return to point B, having traversed the slot width twice. It is proposed that some fraction travels back to the surface where it is mode converted to another Rayleigh component, producing the second peak (RS).

The value of $\theta = 30^0$ used in equation (5.1) was chosen to give optimum correlation between calculated and measured slot widths.

5.7 Depth Estimation of a Real Crack

The experimental arrangement was similar to that of fig. (5.1), with the interferometer and a ball-capacitance transducer used to detect the surface displacements. The sample was a weld bead of a nickel based alloy (colmanoy 5) on a high strength, low alloy steel substrate. This had been quenched in water immediately after welding, so that the stresses produced due to rapid cooling caused fracture of the surface. The weld was composed of a double layer, sufficiently thick, ~ 6 mm, to support the propagation of Rayleigh waves, with frequencies above 1 MHz ($\lambda = 3$ mm), along the surface with only minor perturbations. The frequency spectrum

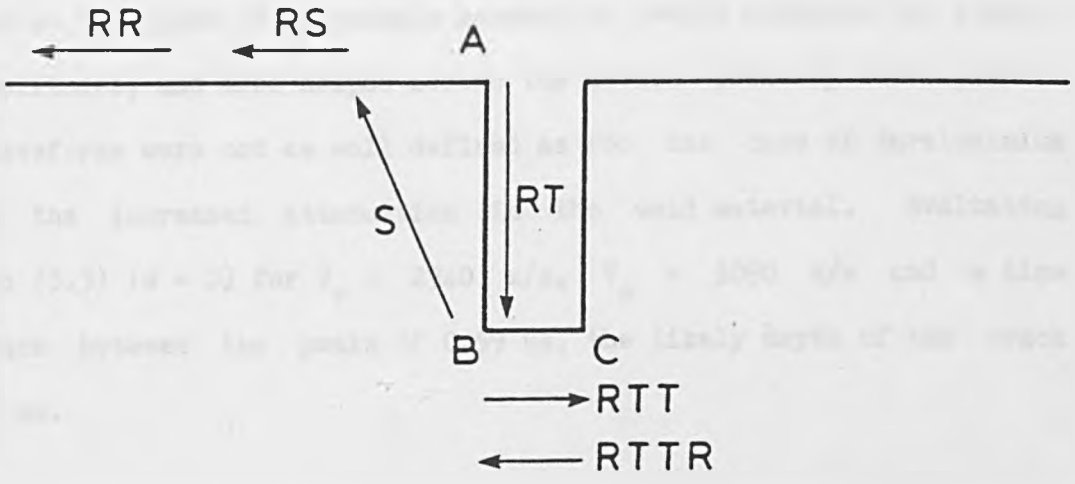

Fig. (5.27) Proposed model for the Rayleigh pulse interaction with a machined slot. Two additional components appear from comparison with fig. (5.6).
RTT: Rayleigh pulse transmitted along the slot base
RTTR: Rayleigh pulse reflected at C, and mode converted to shear energy at B.

of typical Rayleigh pulses used demonstrated that a significant portion of the Rayleigh energy was above 1 MHz. Figs. (5.28a) and (5.28b) show the resultant surface displacement observed in the pulse-echo configuration, detected with the interferometer and ball-capacitance probe respectively. As expected, the waveforms exhibit a small amplitude longitudinal pulse, a large amplitude Rayleigh pulse which originated from the source, followed by at least two reflected peaks. Such features were independent of the type of detector. However, it should be noted that for satisfactory operation of the ball-capacitance probe, a thin layer of grease was required at the point of ultrasonic generation, which enhanced the surface wave amplitudes, and also helped screen the device from any laser plasma. These waveforms were not as well defined as for the case of duraluminium due to the increased attenuation in the weld material. Evaluating equation (5.3) (w = 0) for V_r = 2940 m/s, V_s = 3090 m/s and a time difference between the peaks of 0.59 μs, the likely depth of the crack was 1.1 mm.

5.8 Interferometric Detection of Surface Breaking Slots in the Thermoelastic Regime

The ultrasonic generation conditions of section 5.2 led to slight surface pitting of the samples, on a single shot basis. In any "real" application this may be undesirable, hence slot depth estimation has been demonstrated in the purely thermoelastic regime, where no surface damage occurred, even after successive laser shots at the same point. The experimental arrangement was similar to that described in section 5.2.1, with incident laser energies of 3 mJ, focussed to a spot of 0.7 mm diameter.

Fig. (5.29) shows the waveform detected from a 0.5 mm down step. The

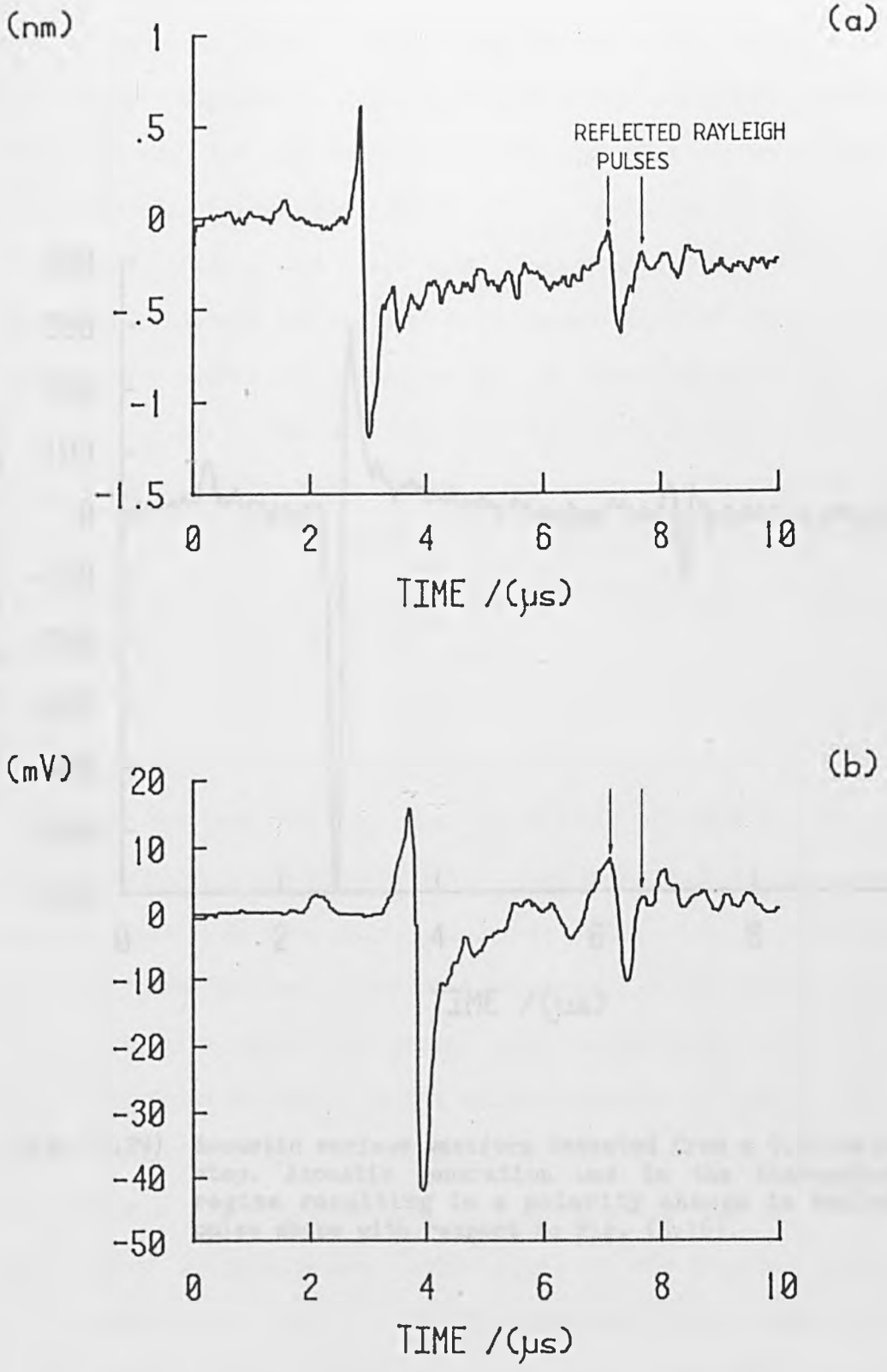

Fig. (5.28) Acoustic waveform detected on the surface of a nickel-based weld. Reflections from a crack were detected with
(a) the interferometer and
(b) a ball-capacitance transducer.

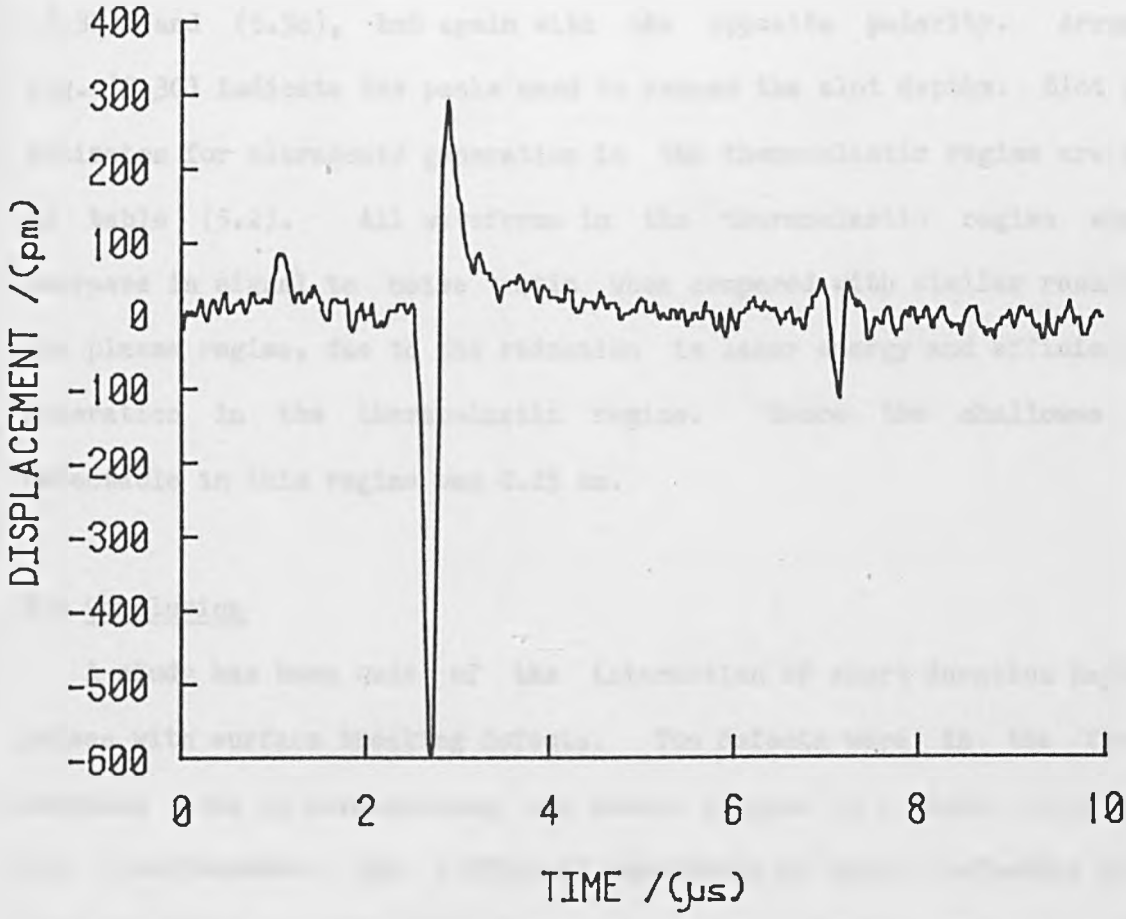

Fig. (5.29) Acoustic surface waveform detected from a 0.50 mm down step. Acoustic generation was in the thermoelastic regime resulting in a polarity change in Rayleigh pulse shape with respect to fig. (5.16).

polarity of both the incident and reflected Rayleigh pulses is inverted, with respect to fig. (5.16), with the reflected pulse again being essentially unipolar. Fig. (5.30) shows the waveforms detected from 0.50, 0.75 and 1.0 mm deep slots, with each slot having a width of 0.10 mm. Both fig. (5.30a) and (5.30c) bear remarkable resemblence to fig. (5.3b) and (5.3c), but again with the opposite polarity. Arrows on fig. (5.30) indicate the peaks used to assess the slot depths. Slot depth estimates for ultrasonic generation in the thermoelastic regime are shown in table (5.2). All waveforms in the thermoelastic regime show a decrease in signal to noise ratio when compared with similar results in the plasma regime, due to the reduction in laser energy and efficiency of generation in the thermoelastic regime. Hence the shallowest slot detectable in this regime was 0.25 mm.

5.9 Conclusion

A study has been made of the interaction of short duration Rayleigh pulses with surface breaking defects. The defects were in the form of machined slots in duraluminium, and cracks induced in a nickel alloy weld. The interferometer had sufficient resolution to detect reflected pulses from the slots in both the plasma and thermoelastic regimes. These pulses were found to relate to the characteristics of the surface defect. The interpretation of these results was developed from results obtained using Rayleigh pulse interactions with 90^0 and 270^0 corners. A computer simulation of the problem has lent support to the proposed model, and it has been demonstrated that the depth of a narrow surface breaking slot may be estimated, using an empirical relationship. However, equation (5.3) should be used with caution, since it represents a geometric approximation to what is really a complex interaction. From investigations involving

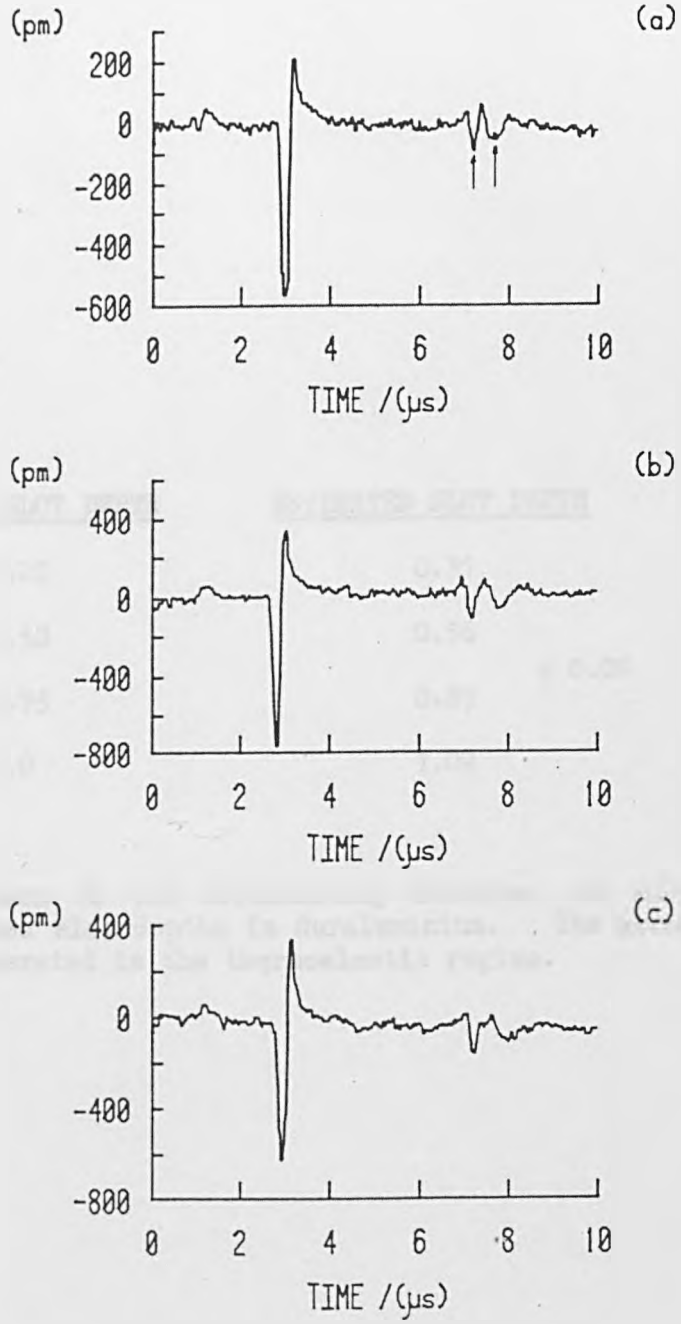

Fig. (5.30) Acoustic waveforms containing reflections from machined slots in duraluminium. Ultrasonic generation was performed in the thermoelastic regime. The slots had widths of 0.10 mm, and depths of

(a) 0.50 mm
(b) 0.75 mm
(c) 1.0 mm

MEASURED SLOT DEPTH	ESTIMATED SLOT DEPTH	
0.25	0.31	
0.50	0.56	
0.75	0.89	± 0.01
1.0	1.02	

Table (5.2) Comparison of the mechanically measured and ultrasonically estimated slot depths in duraluminium. The acoustic source was generated in the thermoelastic regime.

slots, the relationship is valid for slot depths in the range 0.10 to 1.0 mm, and is believed to be valid for slots with widths of $\sim$ 0.3 mm or less.

5.10 References

J. D. Achenbach, "Wave Propagation in Elastic Solids" (North-Holland, Amsterdam) p. 192 (1973).

L. J. Bond, Ultrasonics 17 71 (1979).

L. J. Bond, in "Research Techniques in Nondestructive Testing" (Edited by R. S. Sharpe, Academic Press, London) Vol. 6, p. 107 (1982).

L. J. Bond and N. Saffari, in "Research Techniques in Nondestructive Testing" (Edited by R. S. Sharpe, Academic Press, London) Vol. 7, p. 145 (1984).

A. N. Bondarenko, Yu. B. Drobot, and S. V. Kruglov, Sov. J. of NDT 12 655 (1976).

C. P. Burger and A. J. Testa, Proc. Ultrason. Int., London, p. 271 (1981).

C. A. Calder and W. W. Wilcox, Mater. Eval. 38 86 (1980).

D. Cooke, Proc. Brit. Aoustical. Soc. Spring Meeting, Loughborough (1972).

J. A. Cooper, in "Laser Generated Ultrasound with Applications to Nondestructive Evaluation" Ph.D. Thesis, Hull (1985).

J. A. Cooper, R. J. Dewhurst and S. B. Palmer, Phil. Trans. Roy. Soc. Lond. A 320 319 (1986).

P. A. Doyle and C. M. Scala, Ultrasonics 16 164 (1978).

M. Fuyuki and M. Nakano, Bull. Seismol. Soc. Am. 74 893 (1984).

M. Hirao, H. Fukuoka and Y. Miura, J. Acoust. Soc. Am. 72 602 (1982).

D. A. Hutchins, F. Nadeau and P. Cielo, Can. J. Appl. Phys. 64 No. 9 (1986).

B. H. Lidington and M. G. Silk, Brit. J. NDT 17 165 (1975).

L. L. Morgan, Acustica 30 222 (1974).

M. Munasinghe and G. W. Farnell, J. Appl. Phys. 44 2025 (1973).

F. Nadeau and D. Hutchins, Proc. IEEE Ultrasonics Symposium, p. 921 (1984).

C. L. Pekeris and H. Lifson, J. Acoust. Soc. Am. 29 1233 (1957).

Lord Rayleigh, Proc. London Math. Soc. 17 4 (1885).

H. W. Reinhardt and J. W. Daly, Mater. Eval. 28 213 (1970).

N. Ricker, Geophyics 10 207 (1945).

N. Saffari and L. J. Bond, private communication (1987).

C. B. Scruby, R. J. Dewhurst and S. B. Palmer, in "Research Techniques in Nondestructive Testing" (Edited by R. S. Sharpe, Academic, London) Vol. 5, p. 281 (1982).

M. G. Silk, in "Research Techniques in Nondestructive Testing" (Edited by R. S. Sharpe, Academic Press, London) Vol. 3, p. 51 (1979).

G. P. Singh and A. Singh, Mater. Eval. 39 1232 (1981).

R. J. Wellman, Harry Diamond Laboratories, report no. HDL-TR-1902 (1980).

R. D. Woods, J. Soil Mech. Founds Div. Am. Soc. Civ. Engrs. 94 951 (1968).

CHAPTER 6

Ultrasonic Material Monitoring at Elevated Temperatures

6.0 Introduction

With the use of more advanced materials fabrication techniques and the increasing requirement for quality control, non-invasive ultrasonic techniques such as optical sensing and electromagnetic acoustic transducers (EMATs)* are being considered for application on production lines. Techniques are needed to probe the interior of solid materials, such as metals, so as to characterise and monitor their microstructure, either during or after manufacture. In 1981, the American Iron and Steel Industry (AISI) identified the need for an internal temperature distribution sensor as a means to increase productivity, improve quality, and reduce energy consumption throughout the steel industry (Wadley et. al., 1986). A promising technique in determining the temperature is by the measurement of ultrasonic velocity. In this chapter previous high temperature testing techniques are reviewed. Following this is a description of a totally remote laser technique for high temperature material testing, and results are presented on the dependence of ultrasonic velocity with increasing temperature for a number of materials.

6.1 Techniques for Material Monitoring at High Temperatures

Most polycrystalline metals and alloys are found to behave in an approximately isotropic manner when subjected to elastic loading. Their elastic behaviour can thus be defined by just two independent elastic constants, for example, Young's modulus and the shear modulus. Techniques for the measurement of these elastic moduli can be separated

* (Whittington ,1978)

into two broad categories, namely static and dynamic testing methods. In the simplest static tests, Young's modulus can be determined from a uniaxial loading or bending test, and the shear modulus from a torsion test. In general, these tests require large samples, and the testing equipment can be expensive. Long test times are also required and the sample may be subjected to high stress levels. Under dynamic testing, elastic moduli are determined from measurements of the sample resonant frequency, or from the ultrasonic wave velocities in the sample. These methods are performed at extremely small strain amplitudes, and in very short times. Thus static methods of measurement of elasticity have now been largely superceded by dynamic methods.

One of the first dynamic methods that was widely used for measuring elastic moduli, made use of the fact that the resonant frequencies of samples vibrating in normal modes were governed by the moduli involved. Samples were often in the form of rods, bars or plates vibrating in longitudinal, torsional or flexural modes. This method has been adopted by Date et. al. (1971) on ferritic and austenitic steels. The specimen, a rectangular bar 10.2 cm long and 9.5 mm square, was mounted on three steel pins at the centre node. The amplified output of an oscillator was applied to two electrodes, and the frequency of the signal varied until sample resonance occurred. Although the resonance method has been used on austenitic steels, which do not change their crystal structure on heating up to 800 ^{0}C, it was found that measurements on ferritic steels, which start to transform at approximately 710 ^{0}C, could only be made to approximately 600 ^{0}C. This was due to the increase in damping as the transformation range was approached, and the driving method lacked the power required to achieve sample resonance.

Of the dynamic testing techniques available, the ultrasonic velocity

approach, utilising piezoelectric transducers for generating and detecting stress waves in the sample, has been one of the most widely studied for high temperature measurements. The main difficulty encountered at high temperatures is that many useful bonding materials are unstable, and fail to satisfactorily couple the transducer to the sample, either mechanically or ultrasonically (Butler et. al., 1979). In addition, if the Curie temperature of the transducer is exceeded, the piezoelectric properties are lost. As the Curie temperature is approached the amplitude of the ultrasound drops, and the pulse shape becomes distorted. This effect may become progressively worse if the transducer is operated close to the Curie temperature for any extended period. The purpose of the bond is to mechanically secure the transducer to the sample, and to couple acoustic energy into it. Thus difficulties will arise if the bond is not strong enough to withstand the large strains that will arise due to differential thermal expansion between the sample and transducer, and yet the bond must be of reasonably low attenuation so that usable non-distorted ultrasonic waves can be coupled into the sample. To this end work has been performed on bonding materials, particularly special ceramics, that will permit transducer operation at a high temperature. Butler et. al. (1979), have investigated various transducer-bond combinations, with some combinations working reliably for prolonged periods at temperatures of up to 400 ^{0}C.

Provided the sample is long, the transducer can be kept outside the oven and measurements made on only a portion of the rod, by reflecting waves from a shoulder or notch on the heated portion, in addition to the end surface, to obtain a differential delay (Frederick, 1948).

A momentary contact technique has been developed (Papadakis et. al., 1972) in an effort to test samples at substantially higher

temperatures. In this method, the ultrasound was transmitted to the sample by pressure coupling, with no bonding agent. The specimen was contacted momentarily ($\sim$ 100 ms) by one end of a cool buffer rod, about three times as long as the sample. A piezoelectric transducer mounted on the other end of the buffer rod transmitted an ultrasonic signal, and recieved ultrasonic echoes from the buffer/sample interface, and from the free end of the sample. Both longitudinal and shear waves were successfully used, with measurements performed on SAE 52100 steel in the temperature range 25 to 1200 ^{0}C.

6.1.1 Laser Techniques

In 1970, Brammer and Percival developed the first laser pulse technique for measuring the elastic constants of materials at elevated temperatures. The propagation velocities of longitudinal and shear waves were measured for a 2024 aluminium rod, over a temperature range of 22 to 500 ^{0}C. The elastic waves were generated by Q-switched ruby laser pulses, of 5 Joules in energy and 15 ns duration, incident at one end of the rod. The transit time of the elastic waves along the rod was measured with a piezoelectric transducer (tourmaline) at the opposite end of the rod. Thermocouples along the length of the rod ensured thermal equilibrium was attained prior to the laser firing. In contrast to earlier techniques, a single test of microseconds duration provided sufficient velocity information to evaluate the elastic constants of the material. Two consecutive longitudinal pulse arrivals were measured. The first arrival corresponded to the direct longitudinal pulse propagating through the length of the rod. However, since the wavefront originating at the input end of the rod is divergent rather than planar, the non-axial components of the longitudinal pulse will interact with the

lateral surfaces of the rod. The wave will then be reflected back towards the interior of the rod, with part of its energy mode-converted to shear waves. The shear wave travels at a slower velocity across the rod diameter, where it is mode-converted back to a longitudinal wave on reflection at the opposite surface, following one complete transit across the rod in the shear mode. Thus the second longitudinal pulse measured was delayed from the first by a time related to the rod diameter and the shear wave velocity in the material. Hence, although earlier ultrasonic methods of measuring elastic constants required two separate measurements to obtain the longitudinal and shear velocities, this alternative method, led to evaluations from a single measurement. However, resolving the separate pulses depended on both fast risetime ultrasonic pulses, and sufficiently long rods.

Calder and Wilcox (1978) also adopted a similar technique, but provided a totally remote system by using a Michelson interferometer to detect the elastic waves. The end of the sample under test became the moving mirror of the interferometer, requiring it to be polished to a reasonably reflective surface. Laser generation of the elastic waves was provided by Q-switched Nd:Glass laser pulses of up to 15 Joules in energy and typically 30 ns duration. A single frequency argon ion laser, operated at 514.5 nm and power levels of the order of 0.1 W, provided the light source for the Michelson interferometer. Measurements were made on 6061-T6 aluminium, AISI-304 stainless steel, copper, brass, tantalum, and molybdenum. The samples were situated inside a clamshell oven. The oven was open at both ends giving convenient optical access for both generating and detecting laser beams, and for sample loading. They had expected to reach temperatures of 600 ^{0}C for aluminium, 900 ^{0}C for brass, and the remaining metals heated to 1000 ^{0}C. However, degradation of the

polished specimen surface at high temperatures prevented the upper limits being reached in all cases, except for stainless steel. In anticipation of potential oxidation problems at high temperature, the mirrored end of one specimen of each metal was gold plated. These measures failed to obtain higher temperature data since although gold is corrosion resistant at these temperatures, it did not adhere well to the polished end of the sample. In other related experiments Calder et. al. (1981) also used the above technique to measure the elastic constants of plutonium at elevated temperatures. In this case they used a 50 mw helium-neon laser as the light source for the interferometer. To minimize the possibility of radiation reaching the laboratory environment, the test chamber was fabricated from stainless steel, and had two containment barriers. As an additional safety precaution, inert gas was circulated between the primary and secondary containment barriers, and filtered with a high efficiency particulate air filter. Windows at each end of the chamber provided laser access. The plutonium specimen was heated by a clamshell oven situated inside the chamber and the system evacuated to reduce the oxidation rate of the polished end of the plutonium rod. Both pure plutonium (Pu) and a Pu-1wt%Ga delta-stabilised alloy were tested. Interestingly, the sudden degradation of the specimen mirror at 119 ^{0}C for pure plutonium, prevented further results for higher temperatures. This effect has been attributed to the α to β phase change of Pu, and is apparently associated with the discontinuous change in density at the phase change temperature. There were no phase changes in the plutonium alloy until the δ to ε phase change above 500 ^{0}C, and in this case mirror degradation was reported to be gradual with increasing temperature. The results obtained using this technique were in very good agreement with the limited published data available, and showed linearly decreasing values of

the Young's and shear moduli with increasing temperature.

Wadley et. al. (1986) have presented the basic theory for reconstructing an internal temperature distribution from time of flight measurements. The accuracy of the reconstructed temperature distribution can never exceed that of the reference data that relates the ultrasonic velocity to temperature. It is therefore essential to provide reference data with uncertainties in temperature of 5 K or less. To measure the temperature dependence of ultrasonic velocity, they have used a modified version of the stepped bar or shoulder technique. The sample consisted of a cylindrical bar with a semicircular portion cut from one end. The stepped test section was placed in the hot zone of a furnace and brought to a uniform temperature along its length. A water cooled piezoelectric transducer was attached to the other end of the sample, which was situated outside the furnace. A laser beam was split into two pulses which were focused to generate a pair of ultrasonic pulses originating at both the end of the sample and the shoulder. The time difference between these two pulses was equivalent to the time of flight in the uniformly heated test section. One end of the furnace contained a window through which the sample was irradiated with Q-switched Nd:YAG laser pulses of 25 ns duration and up to 850 mJ in energy. Time of flight data was measured to within ± 50 ns. Data was presented for an austenitic steel (AISI-304 stainless steel) and a ferritic steel (AISI-1018 carbon steel) for temperatures up to approximately 1100 ^{0}C.

Wadley et. al. (1986) then used this reference data to experimentally determine the internal temperature distributions in austenitic steel samples of both cylindrical and square geometries. The samples were heated to approximately 700 ^{0}C in an induction heating unit, before being removed to the testing apparatus. An EMAT, with a sensing coil of 4 mm x

4 mm, was used to detect the ultrasonic pulses generated by an 850 mJ Nd:YAG laser pulse. The efficiency of EMATs decreases rapidly with distance from the sample, hence a standoff of 1 mm was used, making water cooling of the EMAT essential. Thermocouples mounted at various positions in the sample provided a continuous record of the internal temperature profile. The reconstructed temperature and the thermocouple values agreed to within ± 20 K for the cylindrical sample and ± 10 K for the square block. Discrepancies that have been discovered, appear to arise from temperature and frequency dependent ultrasonic attenuation that will depend on path length. The effect of this would be to slow the risetime of the recorded broadband signal used to reconstruct the profiles. With corrections to compensate for these effects, the extension of the method to higher temperatures is dependent only on the development of higher temperature EMATs, or the use of interferometers designed for rough surface operation.

Most recently Monchalin and Heon (1986) have determined both shear and longitudinal velocities in ceramics and metal/ceramic composites at temperatures up to 1000 ^{0}C. The samples were located inside a tubular oven, with vacuums of below 10^{-5} torr and continuous pumping found to be sufficient to prevent oxidation of all of the samples studied. Laser generation and detection of ultrasound was performed on opposite sides of the sample, on epicentre. The laser used for ultrasonic generation was a Q-switched Nd:YAG providing 8 ns pulses with a maximum energy of 750 mJ. The receiving probe was a heterodyne interferometer (Monchalin, 1985), which in this setup used a 1 W single mode argon ion laser, instead of the few mW He-Ne laser used previously. The use of the argon ion laser gave better sensitivity (more than an order of magnitude), and permitted samples with optically rough surfaces to be probed.

6.2 Non-contact Ultrasonic Velocity Measurement at High Temperatures

Since the Michelson interferometer had been designed to have a wide frequency bandwidth up to 130 MHz, a series of experiments were conducted on thin samples, to examine the possibility of making precise ultasonic velocity measurements, using a He-Ne laser of only 5 mW. The variation of longitudinal velocity with increasing sample temperature has been examined in five polycrystalline materials, namely dural, aluminium, AISI-310 stainless steel, iron and graphite, using a totally remote laser technique. Shear wave measurements have also been made for dural and iron. The metallic samples were obtained from Goodfellows Metals, and the graphite sample from the Central Electricity Generating Board (CEGB).

6.2.1 Experimental Arrangement

An illustration of the experimental arrangement is given in fig. (6.1). A Q-switched Nd:YAG laser pulse, of 25 ns duration and 65 mJ energy, was used as the acoustic source. A 50 cm lens partially focussed the incident pulse onto one face of the test sample, producing a weak plasma which generated brief longitudinal ultrasonic pulses (Dewhurst et. al., 1982). The other face of the sample was polished, and used to form one mirror of the modified Michelson interferometer. In the case of the graphite sample, even with poor surface reflectivity, interferometric detection was still possible, albeit at a reduced sensitivity. The samples, which were in the form of discs 19 mm in diameter and 8 mm thick, were located in the centre of a temperature controlled furnace, after the interferometer and Nd:YAG beams had been aligned. This ensured that the measurements were carried out through the true thickness of the sample.

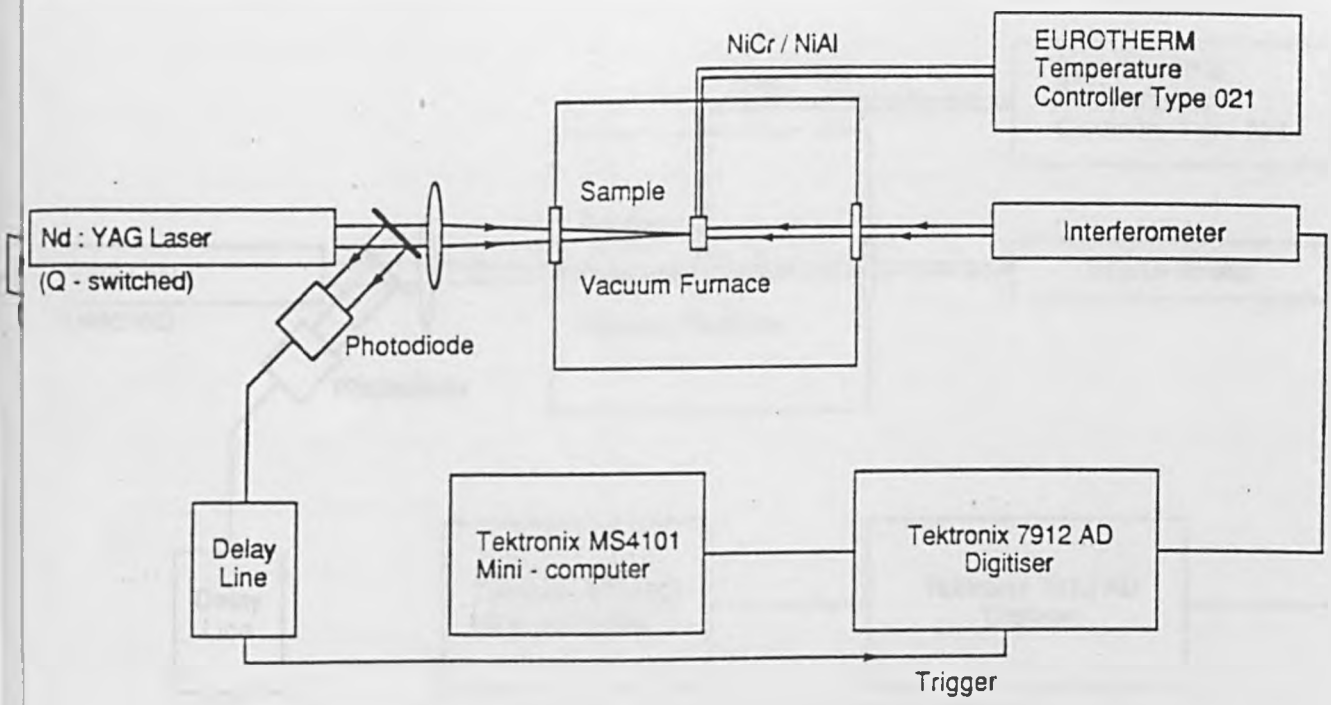

Fig. (6.1) Schematic diagram of the experimental arrangement used for high temperature ultrasonic velocity measurements.

Although single-sided generation and detection of ultrasound would generally be preferred for industrial inspection, operation on opposite sides avoids the perturbations caused by the heated air or the generated hot plasmas.

6.3 Description of the Furnace

A schematic diagram of the temperature controlled furnace is shown in fig. (6.2). Two chromel-alumel (Ni/Cr-Ni/Al) thermocouples were used in the furnace, with both exitting the sealed vessel via vacuum tight feedthroughs. One thermocouple, connected to a Eurotherm type-021 temperature controller, was used to regulate Lindberg 73-K5 heating units, designed to produce a uniform temperature distribution over a cylindrical volume 100 mm long and 30 mm in diameter. The second thermocouple, which was referenced to the melting point of ice, was attached to a digital voltmeter, from which the sample temperature could be determined. The samples fitted tightly into a stainless steel sample holder, with the measuring thermocouple located 1 mm from the sample edge, permitting the sample temperature to be measured with an absolute accuracy of ± 5 ^{0}C. The external casing of the furnace was water cooled, with a ceramic tube inside surrounded by heating elements, and insulated with glass fibre. For satisfactory operation of the interferometer, degradation of the polished sample surface should be avoided. For this reason the furnace was evacuated before any experiments using an Edwards (type ED100) rotary pump, of pumping speed 100 litres/min, which was left pumping during experiments in anticipation of any system outgassing at higher temperatures. The pressure inside the furnace was monitored with a Pirani gauge, and was kept below 10^{-2} torr. Laser access to the sample was provided by a quartz window at each end of the furnace. Accurate

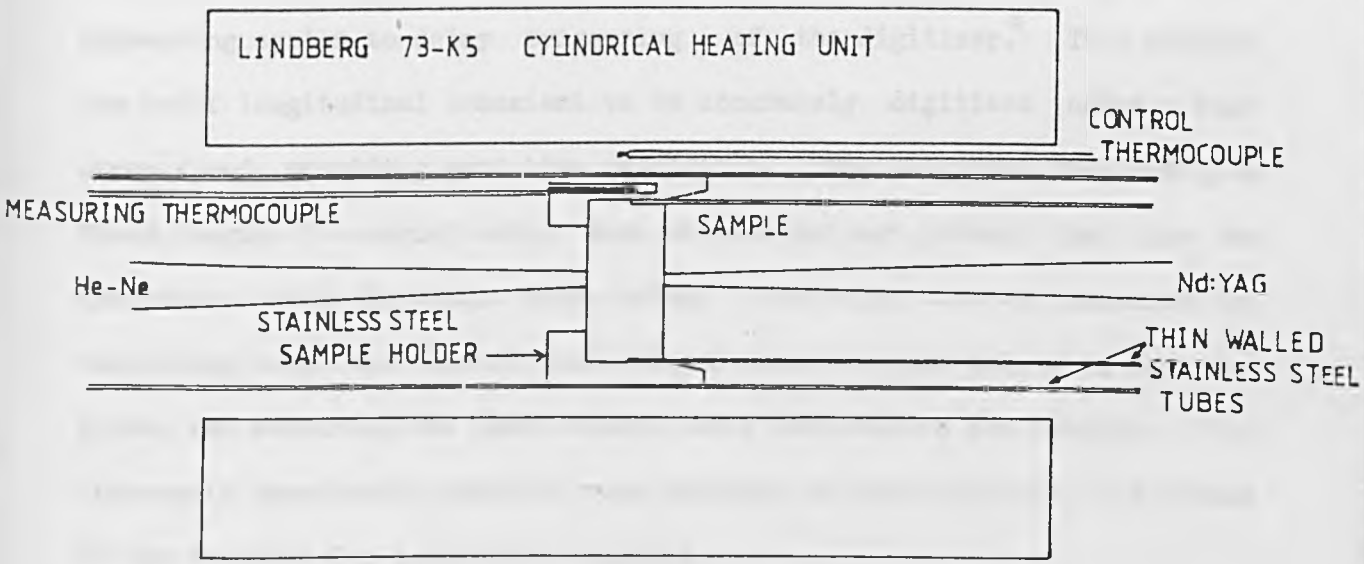

Fig. (6.2) Schematic diagram of the temperature controlled furnace.

alignment of the furnace with the interferometer was possible using translation adjustment mechanisms designed into the furnace support structure.

6.4 Experimental Technique

A delay, slightly less than the time between the laser trigger signal and the first longitudinal arrival, was introduced into the signal processing system to delay triggering of the digitiser.* This enabled the brief longitudinal transient to be accurately digitised using a fast sweep speed, providing good time resolution. The delay was provided by a fixed length of co-axial cable, thus eliminating any jitter that may be associated with electronic delay units. The delay time was measured by displaying both the direct and delayed laser trigger pulses on the same trace, and measuring the time between their arrivals on the display. The ultrasonic transients generated were captured on the digitiser, and stored on the computer for subsequent analysis.

When testing is performed at elevated temperatures, there is thermal expansion of the sample, and corrections must be made for the change in thickness. Although a single figure is often quoted for linear thermal expansion coefficients, this is an average value. The linear thermal expansion coefficients normally increase with increasing temperature. Linear expansion data was readily available for iron, aluminium (Goldsmith et. al., 1961), and stainless steel (Peckner and Bernstein, 1977), hence the longitudinal velocities in these materials have been calculated using corrected values of sample thickness at elevated temperatures. Data presented for dural has been corrected assuming the same thermal expansion as aluminium. Graphite has not been corrected due to scarcity of reliable data, and the many different graphite types that have been

* Each waveform was sampled over 512 points

reported. The method adopted for calculating the arrival time of the longitudinal pulse has been to measure the time corresponding to 10% of the peak arrival on the rising edge of the longitudinal pulse, to minimise the errors associated with pulse broadening at high temperatures.

Preliminary experiments on mild steel were initially performed in a sealed vacuum, and later in an argon atmosphere at a pressure of 80 Torr. Mirror degradation rapidly occurred in both cases. This degradation was reduced when the furnace was continuously evacuated. It was then found that the interferometer sensitivity remained almost constant up to temperatures of $\sim 500\ ^{0}C$. For samples that were tested to higher temperatures, gradual decreases in interferometer sensitivity occured with increasing temperature, until in some cases the experiment was stopped because of very poor signal to noise. This was accompanied by a gradual increase in furnace pressure with temperature. The small rotary pump could not cope with the amount of system outgassing at the higher temperatures, with gradual surface oxidation being the cause of signal loss.

All the data presented has been obtained for increasing temperatures. Data has also been obtained for dural and aluminium as the sample was cooled, with the results being the same within experimental error. It was not possible to take measurements for iron and stainless steel with decreasing temperature due to the problems of surface oxidation as already discussed.

6.5 Results and Discussion

6.5.1 Dural

Fig. (6.3) shows typical waveforms obtained for dural at room temperature and at 509 °C on 5 μs and 500 ns timescales. In all cases the digitiser was triggered after the same fixed delay. The change in arrival time, associated with a decrease in velocity with increasing temperature, can be seen for both longitudinal (L) and shear (S) waves. The longitudinal arrival was also studied with greater precision as illustrated by the shorter timescale traces. The 5 μs traces show the direct longitudinal pulse and a downstep associated with the direct shear wave, followed by the first longitudinal echo and sidewall reflections.

It is interesting to note that the gradient of the waveform between the direct longitudinal and shear pulses increases with temperature, this being indicative of an enhanced normal force at the sample surface arising from the acoustic source (Dewhurst et. al. 1982). Two explanations for this phenomena exist. Firstly, as the sample temperature increases, less laser energy is required to achieve the sample melting point, and hence plasma formation, with more of the laser energy being available to prolong the duration of the plasma. Secondly, any oxide layers that may form on the sample will act as constraining layers, which will enhance the normal impulse into the sample.

Fig. (6.4) indicates the variation of longitudinal velocity with increasing temperature for dural. Both the absolute value of longitudinal velocity at room temperature (6490 ± 65 m/s) and the gradient are in agreement with values measured at room temperature and below using a pulse echo overlap technique with a 15 MHz X-cut quartz transducer bonded to a similar sample. Above the Debye temperature of ∿ 145 °C (Yates, 1972), the dependence of the longitudinal velocity on temperature

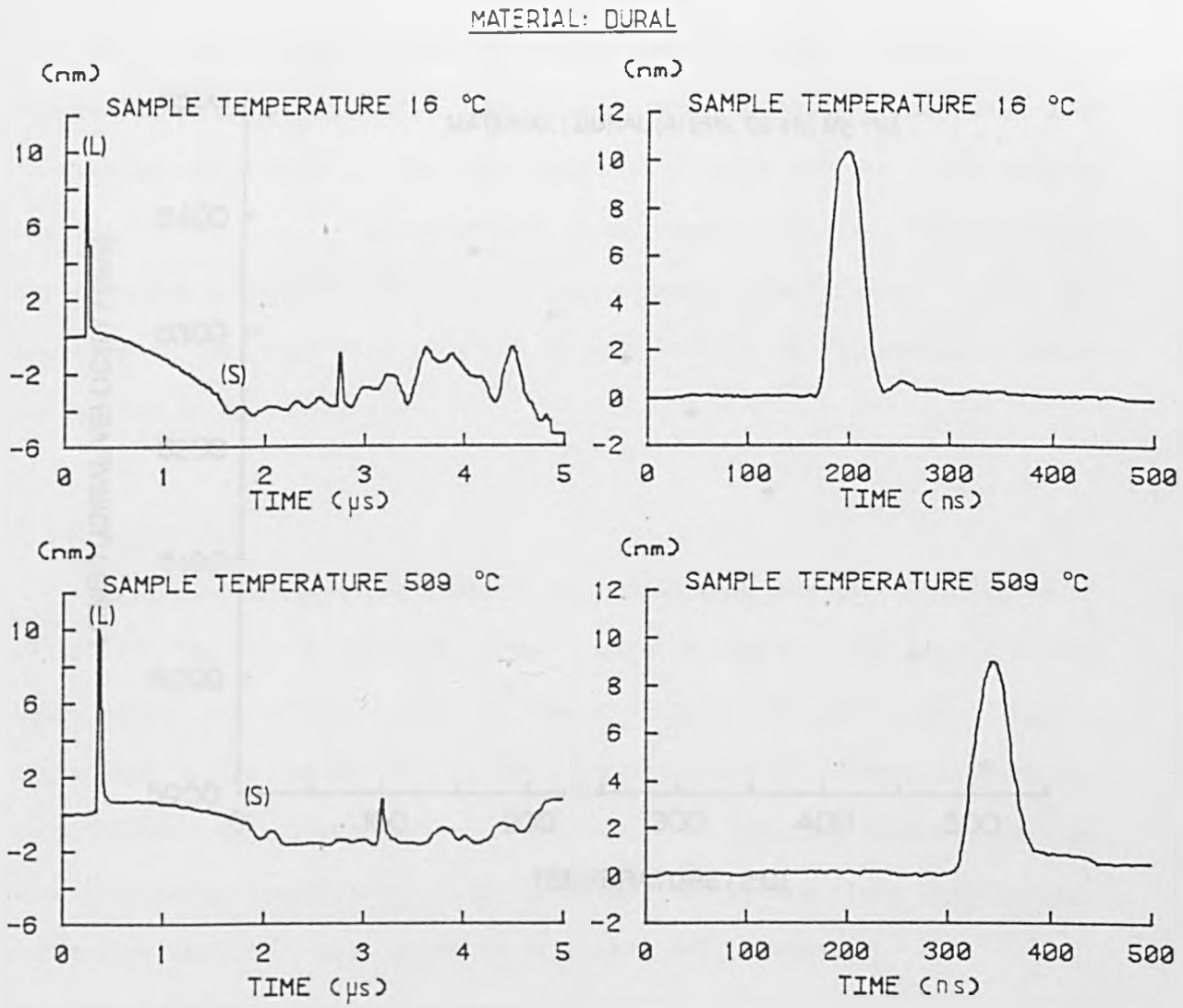

Fig. (6.3) Waveforms obtained at room and elevated temperatures in Dural. The 500 ns timescale waveforms depict the initial longitudinal pulse expanded out. Both longitudinal (L) and shear (S) velocities decrease with increasing temperature.

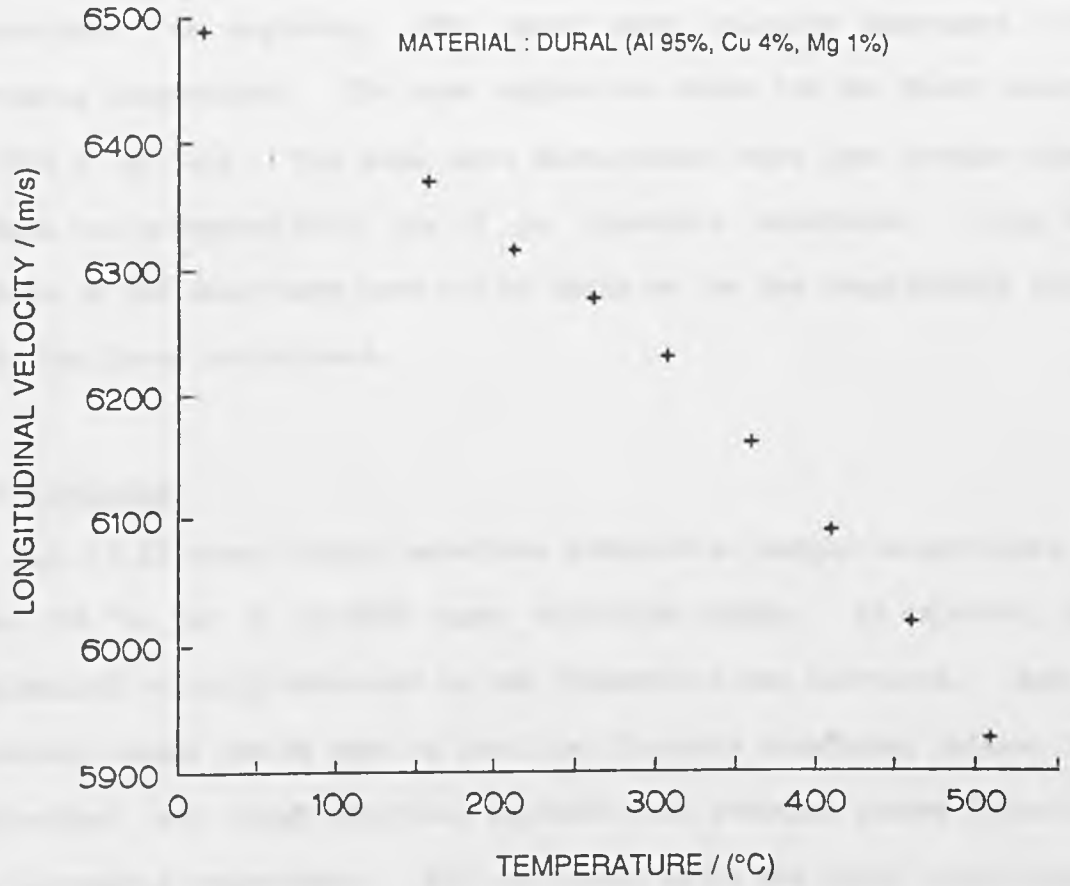

Fig. (6.4) Variation of longitudinal velocity with increasing temperature in Dural.

would be expected to be linear, provided that no magnetic or crystallographic phase transitions occur. However above $\sim$ 350 ^{0}C the gradient steepens as the temperature approaches the sample melting point of $\sim$ 560 ^{0}C.

Fig. (6.5) shows a plot of shear wave velocity against sample temperature. As expected, the shear wave velocity decreased with increasing temperature. The room temperature value for the shear velocty was 3065 ± 80 m/s. The shear wave measurements were less precise since the data was extracted from the 5 μs timescale waveforms. Also the features of the shear wave were not as sharp as for the longitudinal pulse due to the laser source used.

6.5.2 Aluminium

Fig. (6.6) shows typical waveforms obtained at sample temperatures of 17 and 556 ^{0}C, for a 99.999% pure aluminium sample. As expected, the longitudinal velocity decreased as the temperature was increased. Again, a gradient change can be seen on the 5 μs timescale waveforms, between the longitudinal and shear arrivals, indicative of stronger plasma formation with increasing temperature. The arrivals after the first longitudinal reflection have been attributed to side-wall reflections.

It should be noted that when elements dissolve in a metal to form a solid solution, they make the metal harder. Thus the longitudinal velocity should be slower in the soft pure aluminium, than in the aluminium alloy, dural. This is borne out by the results of longitudinal velocity versus temperature in figs. (6.4) and (6.7), where the room temperature longitudinal velocity was 6490 ± 65 m/s for dural and 6400 ± 65 m/s for aluminium. Again, the gradient of fig. (6.7) steepens as the melting point of aluminium ($\sim$ 660 ^{0}C) is approached. A similar

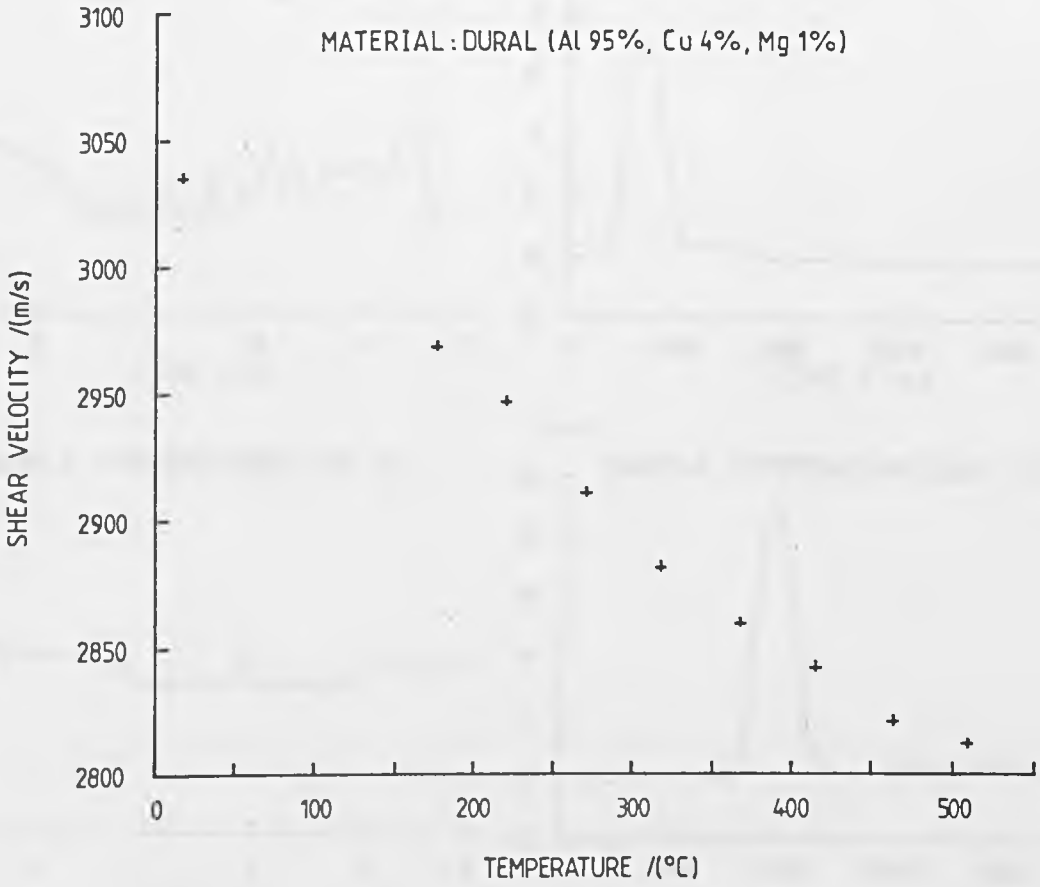

Fig. (6.5) Variation of shear wave velocity with increasing temperature in Dural.

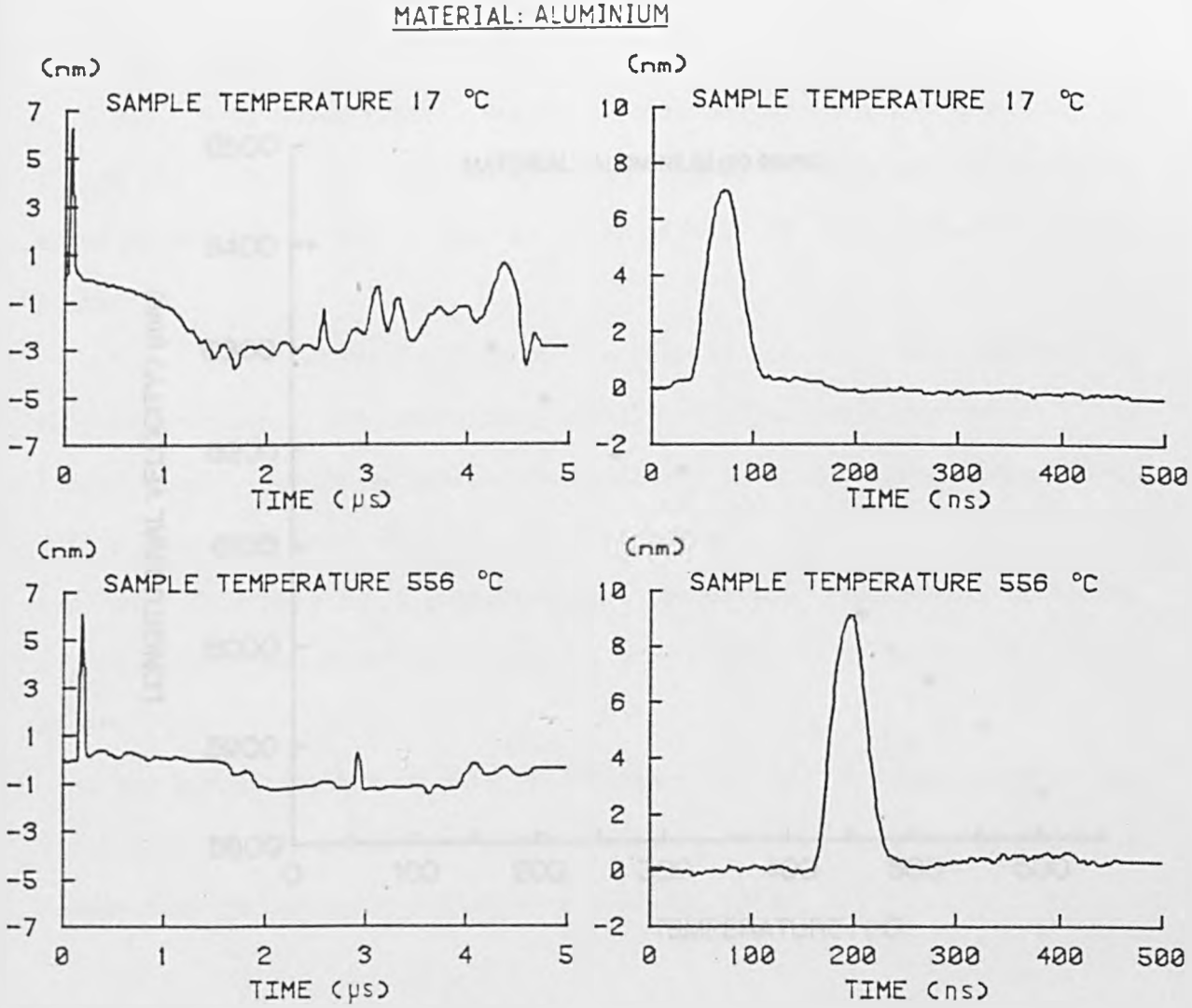

Fig. (6.6) Waveforms obtained at room and elevated temperatures in aluminium.

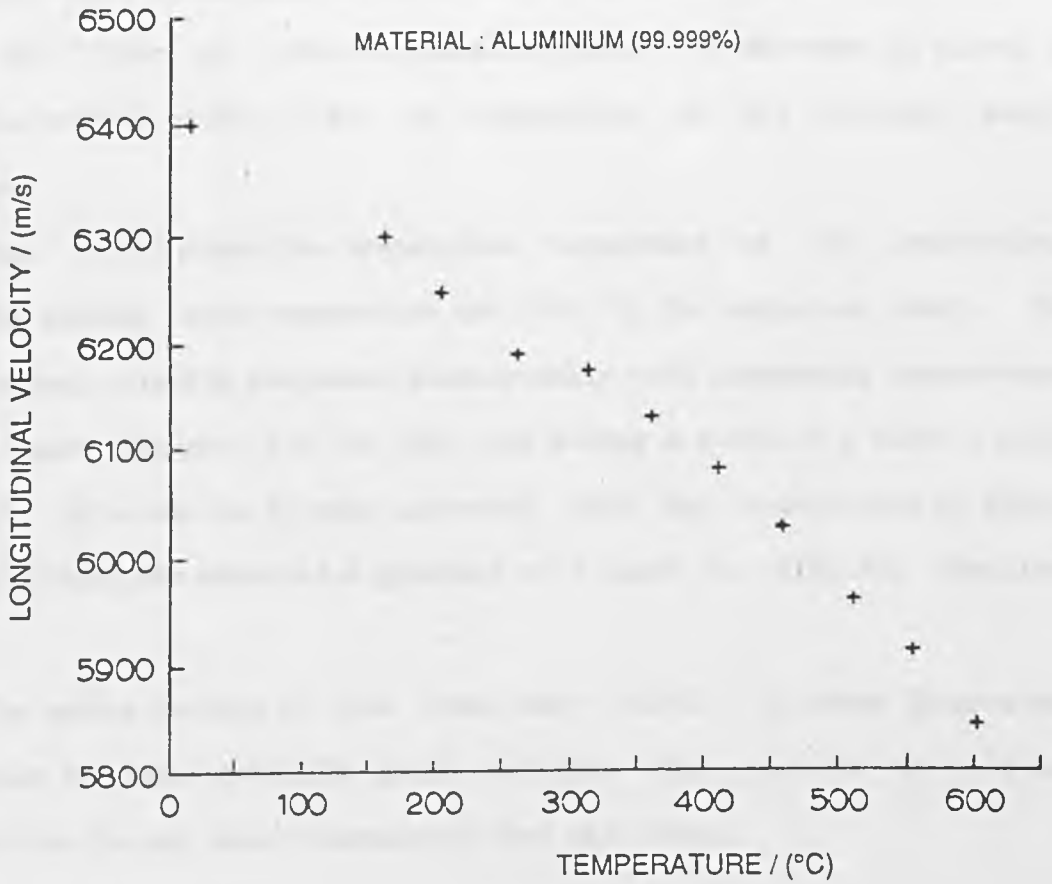

Fig. (6.7) Variation of longitudinal velocity with increasing temperature in aluminium.

curvature of data was reported by Brammer and Percival (1972) for their measurements on 2024 aluminium (see fig. (6.8)).

6.5.3 Stainless steel

Fig. (6.9) shows typical waveforms obtained at sample temperatures of 19 and 954 ^{0}C for an AISI-310 stainless steel. A decrease in signal to noise is evident at 954 ^{0}C due to degradation of the polished sample surface.

Fig. (6.10) shows the temperature dependence of the longitudinal velocity between room temperature and 1000 ^{0}C, for stainless steel. The longitudinal velocity decreases monotonically with increasing temperature, with a least squares fit of the data having a slope of - 0.625 ± 0.007 m/s/^{0}C. This data is in good agreement with the recent work of Wadley et. al. (1986) who observed a gradient of - 0.685 in AISI-304 stainless steel.

The carbon content of this steel was < 0.25%. No phase diagram was available for this particular grade stainless steel, however the data was insensitive to any phase transitions that may occur.

6.5.4 Iron

Fig. (6.11) shows longitudinal velocity versus temperature for the iron sample. The room temperature value of 5990 ± 60 m/s for the longitudinal velocity, agrees with the value given by Kaye and Laby (1986) for soft iron of 5957 m/s, within experimental error. A portion of the iron-carbon phase diagram is shown in fig. (6.12). The Debye temperature for iron is $\sim$ 194 ^{0}C (Yates, 1972) so that one might expect linearity up to the Curie temperature, which for iron is $\sim$ 768 ^{0}C. However, iron is ferromagnetic below its Curie temperature and the elastic constants will

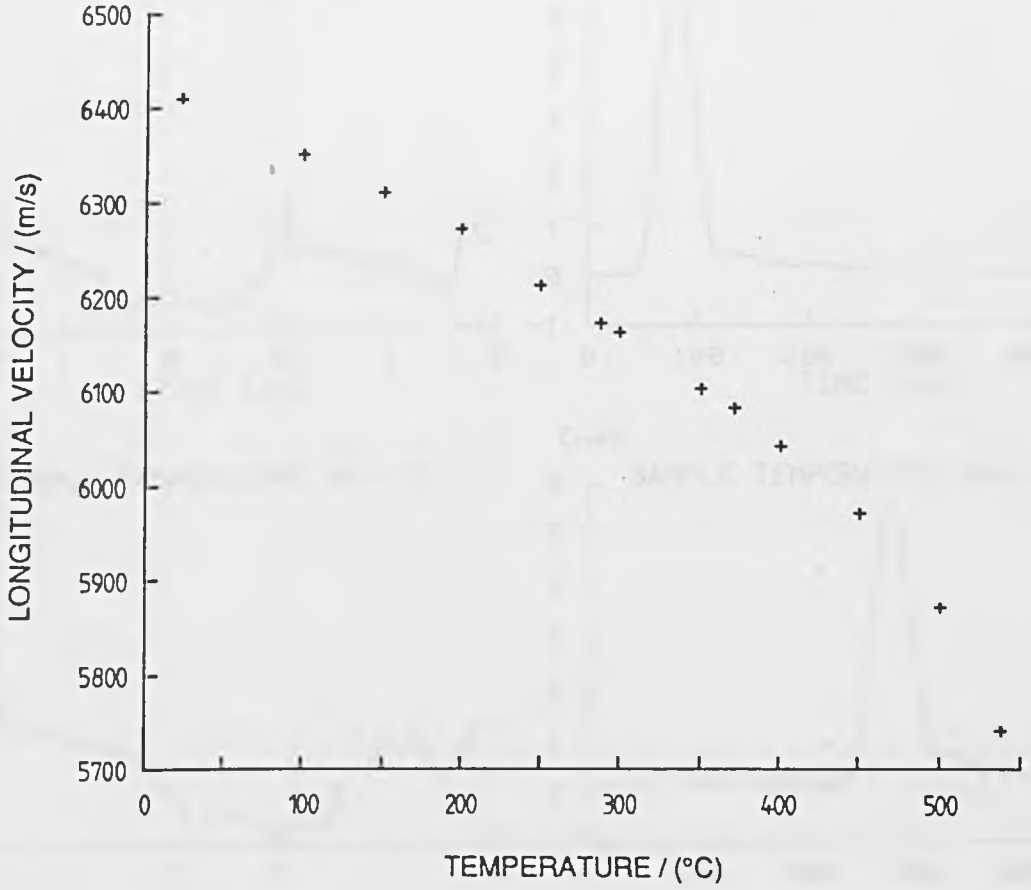

Fig. (6.8) Data obtained in 2024 aluminium by Brammer and Percival (1970).

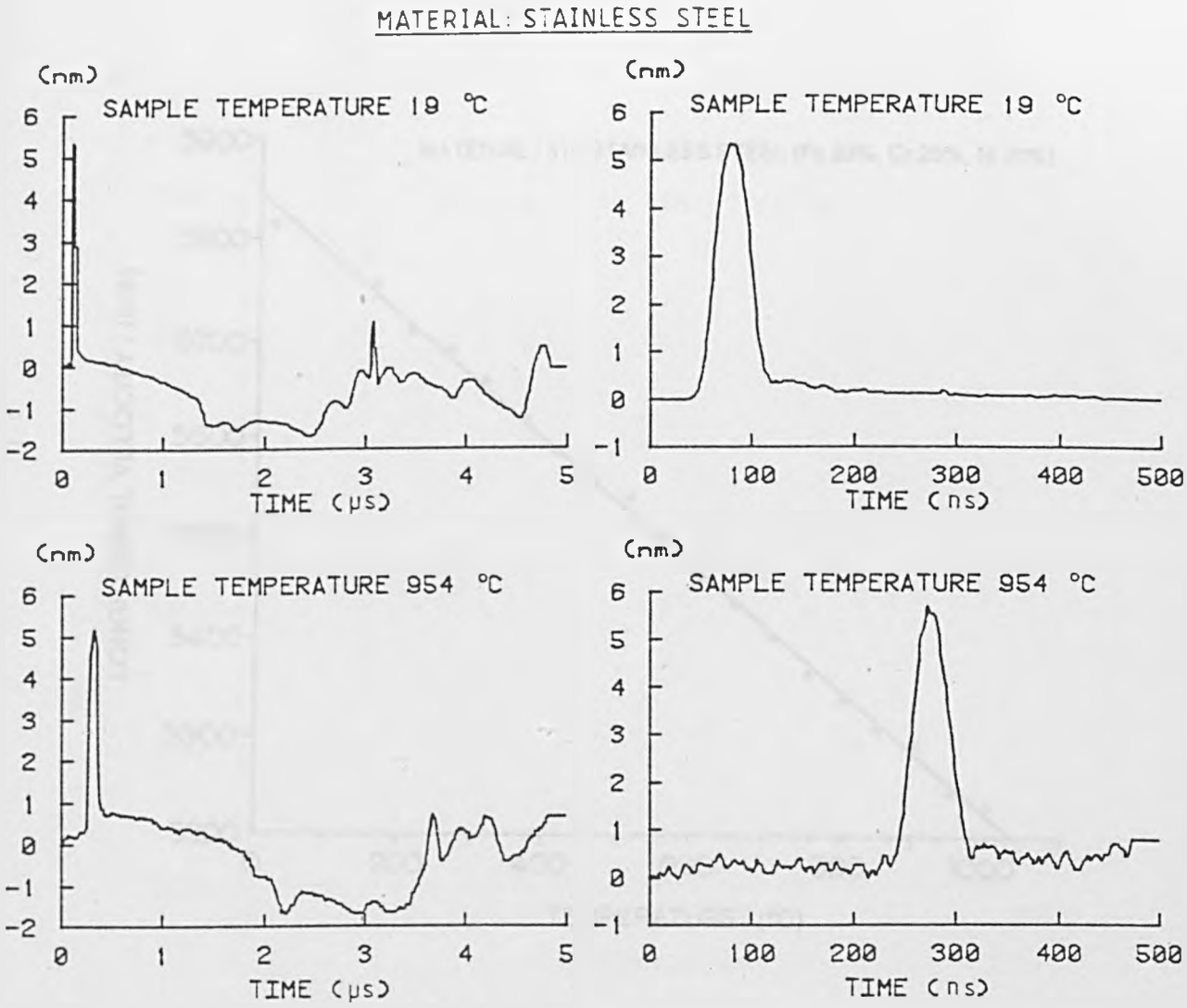

Fig. (6.9) Waveforms obtained at room and elevated temperatures in AISI-310 stainless steel.

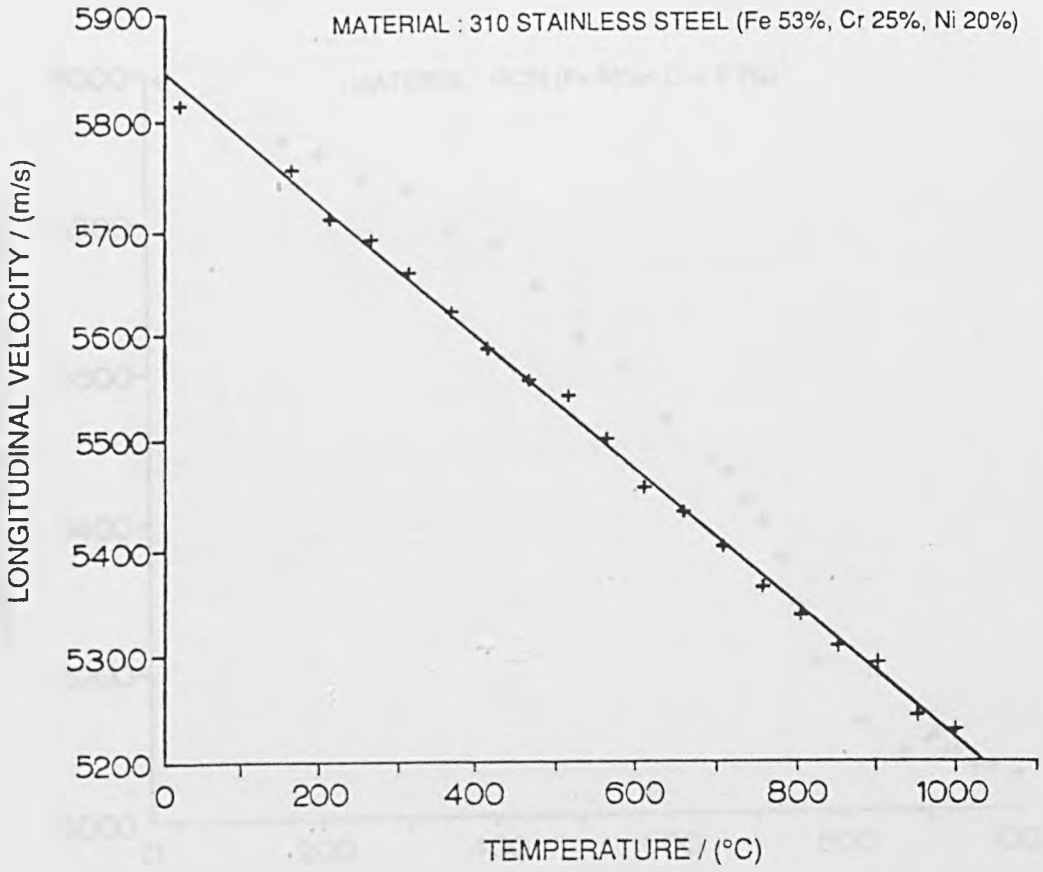

Fig. (6.10) Variation of longitudinal velocity with increasing temperature in AISI-310 stainless steel.

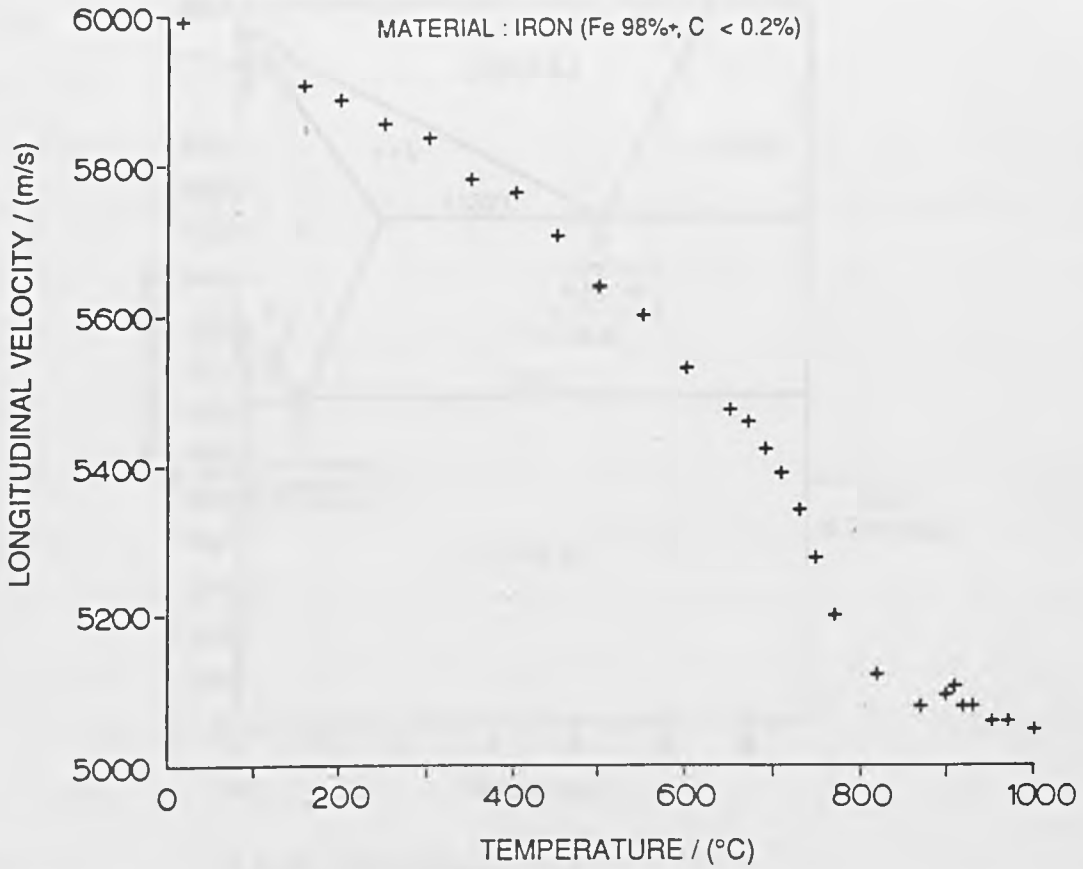

Fig. (6.11) Variation of longitudinal velocity with increasing temperature in iron.

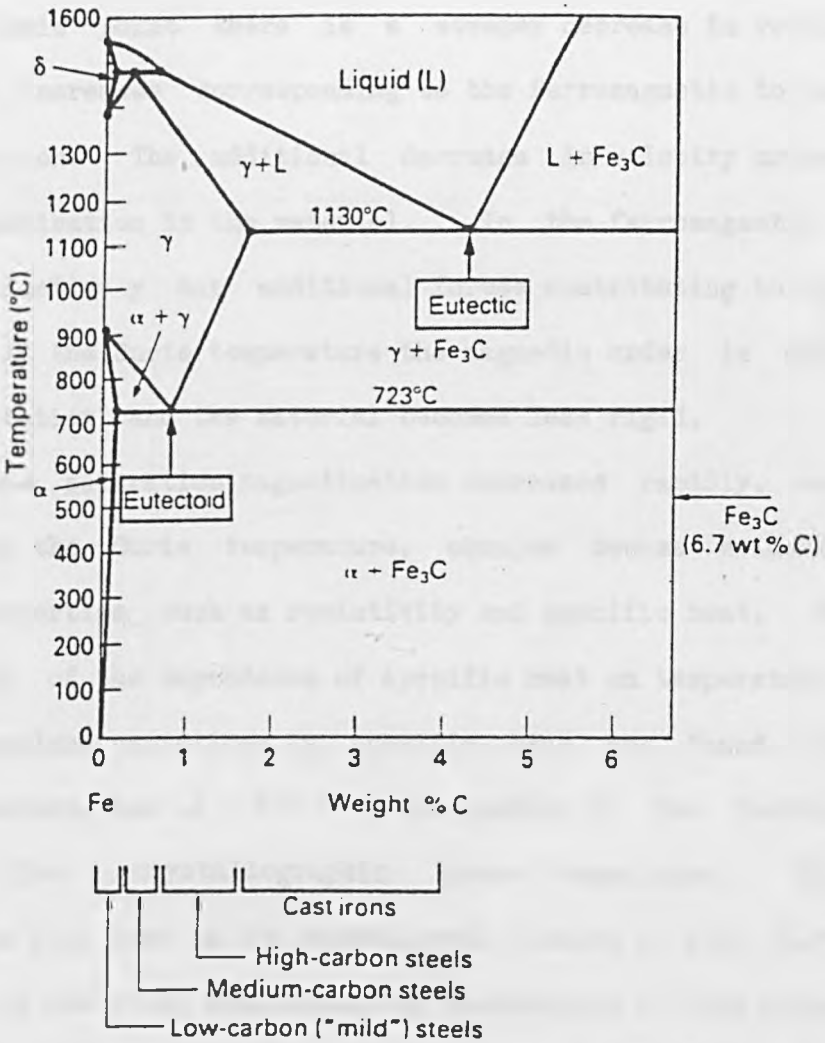

Fig. (6.12) The left hand part of the iron-carbon phase diagram (after Ashby and Jones, 1986).

gradually decrease as the spontaneous magnetism decreases on heating. The data does in fact curve towards the Curie point, a feature which was also seen by Wadley et. al. (1986) on an AISI-1018 ferritic steel. These authors offered a number of explanations for this phenomena, of which the phase change model is in agreement with the results presented here. Around the Curie point there is a steeper decrease in velocity as the temperature increases corresponding to the ferromagnetic to paramagnetic phase transition. The additional decrease in velocity arises from the loss of magnetisation in the material. In the ferromagnetic state, the material effectively has additional forces contributing to the material rigidity. At the Curie temperature the magnetic order is destroyed by thermal agitation and the material becomes less rigid.

When the saturation magnetisation decreases rapidly, and finally disappears at the Curie temperature, changes become evident in other physical properties such as resistivity and specific heat. Fig. (6.13) shows a graph of the dependence of specific heat on temperature (Bozorth, 1951). Anomalous variations in specific heat are found close to the Curie temperature, and at $\sim$ 910 ^{0}C corresponding to the ferrite (bcc) to austenite (fcc) crystallographic phase transition. This latter transition is also seen in the experimental results of fig. (6.11), and is believed to be the first non-contacting measurement of this parameter.

Dever (1972) has measured the temperature dependence of the elastic constants of single-crystal iron from 25 to 900 ^{0}C. Relationships can be derived for the average elastic constants, which take into account the random orientation of grains in a polycrystalline material, and expressed in terms of the true elastic constants (Musgrave, 1970). It follows

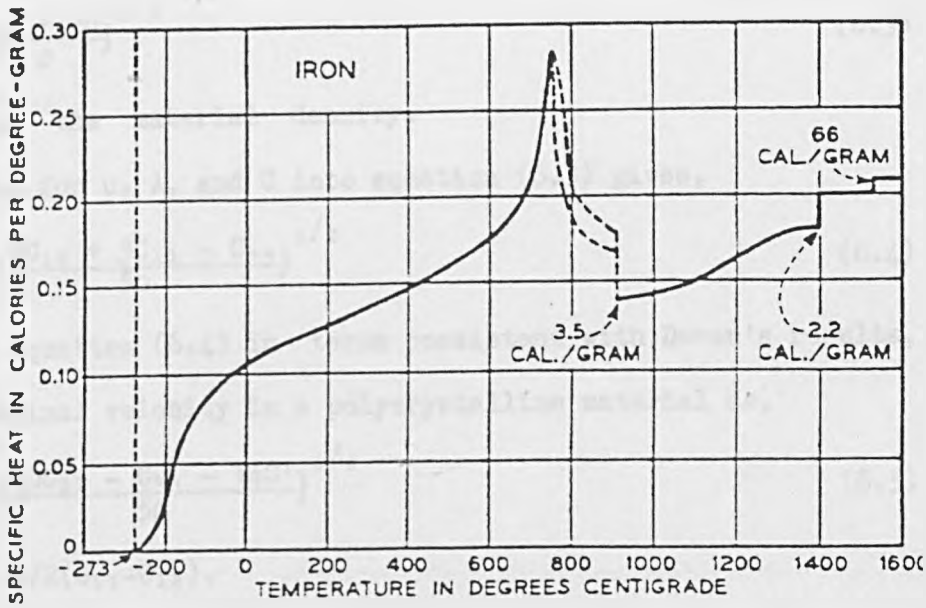

Fig. (6.13) Specific heat and heats of transition of iron as dependent on temperature (after Bozorth, 1951).

that the Lamé constants, μ and λ, can be expressed as,

$$\mu = \bar{C}_{12} = C_{12} + \frac{C}{5} \tag{6.1}$$

$$\lambda = \bar{C}_{44} = C_{44} + \frac{C}{5} \tag{6.2}$$

where $C = C_{11} - C_{12} - 2C_{44}$ and C_{11}, C_{44} and C_{12} are the three independent single crystal elastic constants for a cubic material.

The longitudinal velocity, V_L, is given by,

$$V_L = \left(\frac{\lambda + 2\mu}{\rho}\right)^{1/2} \tag{6.3}$$

where ρ is the material density.

Substituting for μ, λ, and C into equation (6.3) gives,

$$V_L = \left(\frac{7C_{12} + 3C_{11} - C_{44}}{5\rho}\right)^{1/2} \tag{6.4}$$

Expressing equation (6.4) in terms consistent with Dever's results, gives the longitudinal velocity in a polycrystalline material as,

$$V_L = \left(\frac{10C_{11} - C_{44} - 14C'}{5\rho}\right)^{1/2} \tag{6.5}$$

where $C' = 1/2(C_{11}-C_{12})$.

Equation (6.5) has been evaluated to simulate the case of a polycrystalline sample of pure iron, with a density of 7870 Kg/m^3 (Tennent, 1971), using Dever's single crystal data. The results are given in fig. (6.14). It can be seen that the data curves towards the Curie temperature, where there is a discontinuity, and the remaining points show a faster decrease in velocity. The characteristics of Dever's modified data are in good agreement with that of fig. (6.11) (up to 900 ^0C) except for the discontinuity, which could have been missed out due to too few data points around the transition region.

Fig. (6.15) shows the variation of the shear wave velocity up to temperatures of 900 ^0C for the iron sample. The characteristics of this

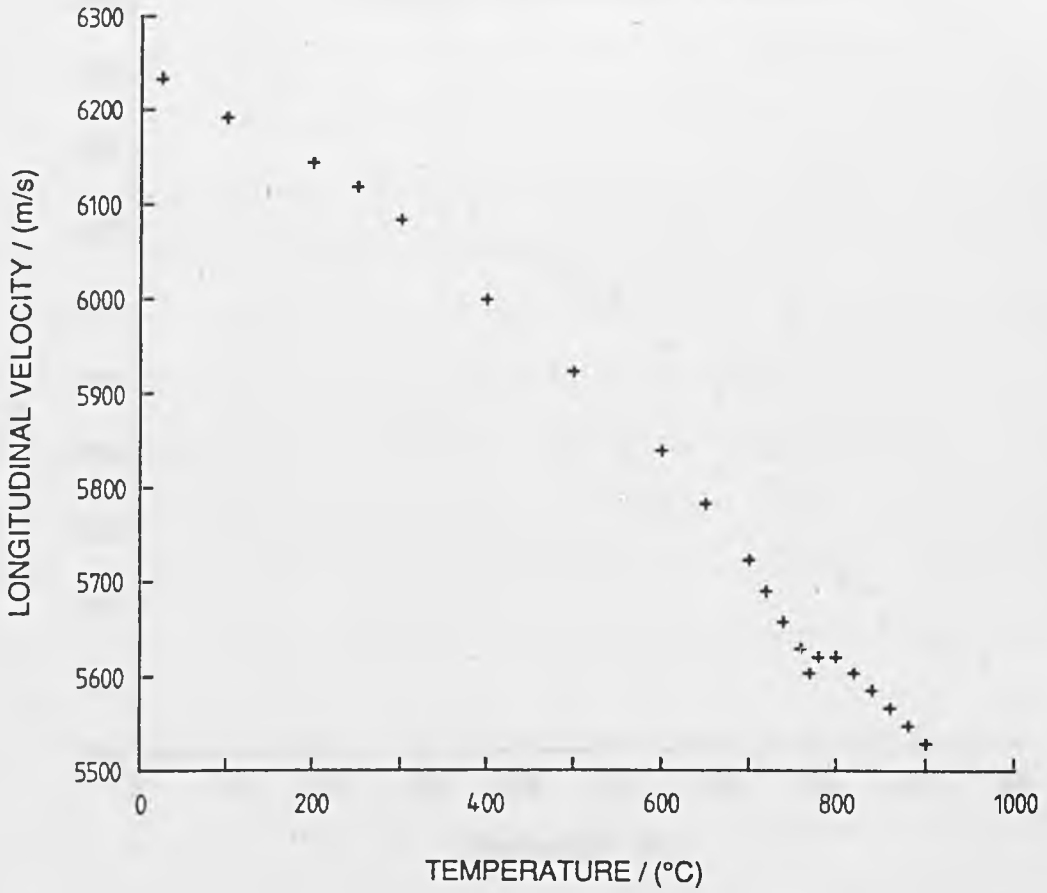

Fig. (6.14) Variation of longitudinal velocity with increasing temperature for iron. Dever's single crystal data (1972) has been evaluated in terms of a polycrystalline material.

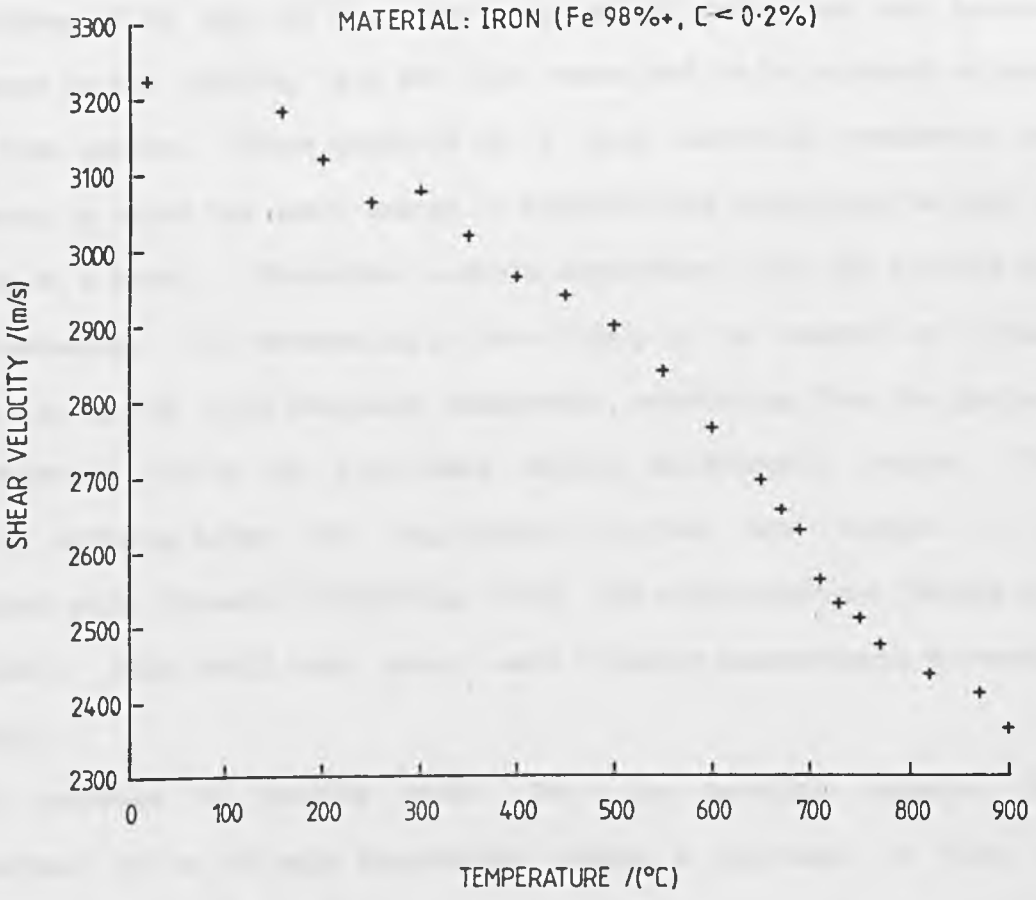

Fig. (6.15) Variation of shear wave velocity with increasing temperature in iron.

figure are similar to that of fig. (6.11) for the longitudinal velocity.

6.5.5 Graphite

Fig. (6.16) shows typical waveforms for the graphite sample at temperatures of 18 and 702 °C. The longitudinal pulses are much broader than those in the metals, and for this reason had to be captured on much longer time scales. Since graphite is a good electrical conductor, the skin depth in which the laser energy is absorbed was comparable to that in the case of a metal. Therefore in-depth absorption does not account for the broadening. The broadening is more likely to be caused by either attenuation of the high frequency components, scattering from the grains, or dispersion within the individual highly anisotropic grains. The features arriving after the longitudinal arrival are thought to to associated with forward scattering from the microstructure (Scruby et. al., 1986). This would make shear wave velocity measurements extremely difficult.

In contrast to results given for the metallic samples, the longitudinal pulse at high temperature shows a decrease in time of arrival, corresponding to an increase in longitudinal velocity. The longitudinal velocity-temperature results are shown plotted in fig. (6.17). The velocity appears to increase by approximately 2% over a temperature range of 700 °C. Faris et. al. (1952) found similar behaviour for their Young's modulus measurements on SA-25 graphite, and also did not correct for thermal expansion of their sample. In solids which do not possess cubic symmetry (graphite is a hexagonal structure), it is known that expansion in one particular crystalline direction exceeds that in the perpendicular plane (Yates, p.69, 1972). Additionally, expansion in this preferential direction will give rise to a contraction

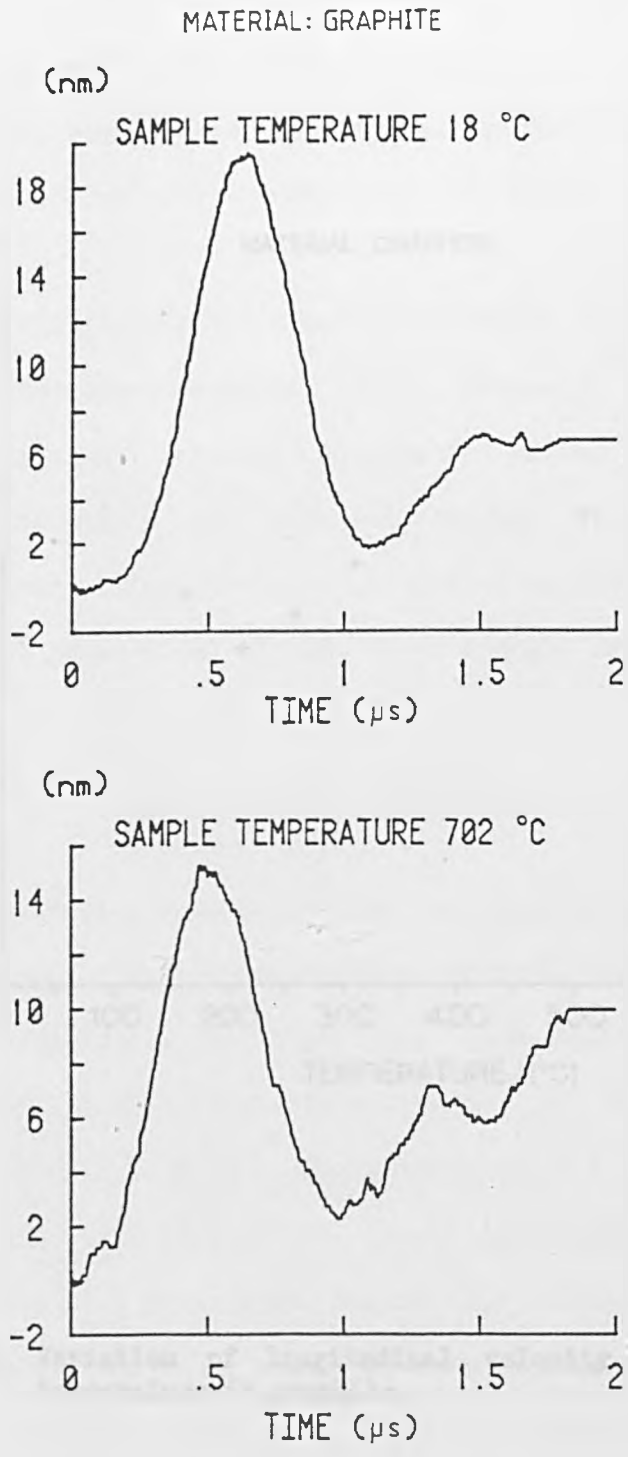

Fig. (6.16) Waveforms obtained at room and elevated temperatures in graphite.

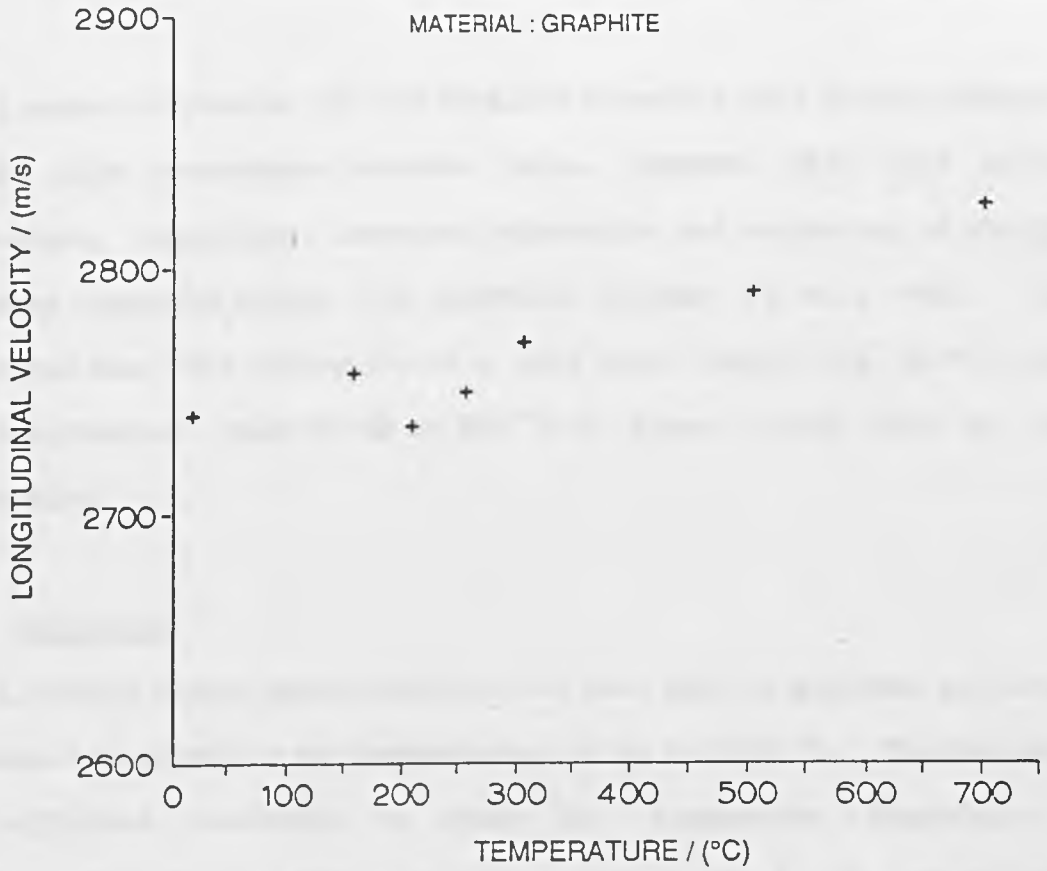

Fig. (6.17) Variation of longitudinal velocity with increasing temperature in graphite.

in the perpendicular plane, the effect of which may be to predominate over the small contribution to the expansion, resulting in a net contraction. This anisotropy has been studied in pyrolytic graphite by Bailey and Yates (1969), and may account for the anomalous velocity behaviour reported here.

A number of results for the metallic materials show slight broadening of the high temperature acoustic pulse, compared with that at room temperature, indicating increased attenuation and scattering of the high frequency compnents within the material (Scruby et. al., 1986). This effect has been most noticeable in a mild steel sample (fig. 6.18), where the longitudinal pulse width at 800 ^{0}C is almost twice that at room temperature.

6.6 Conclusion

A totally remote laser technique has been used to generate and detect ultrasound in materials at temperatures of up to 1000 ^{0}C. The technique has sufficient resolution to study the temperature dependence of longitudinal velocity with an absolute accuracy of ± 1% and relative accuracies of better than 0.1%. Preliminary studies of shear waves have shown similar characteristics as for longitudinal waves. However, the experiments to date have been more suited for accurate measurement of longitudinal waves, and the shear wave measurements were much less precise. The accuracy could be improved by inserting the appropriate delay so as to obtain better time resolution. Additionally a shear step or pulse could be generated by using either a thermoelastic source on epicentre, or if sample dimensions permit, at the onset of ablation off epicentre.

While major advances in predictive process modelling and process

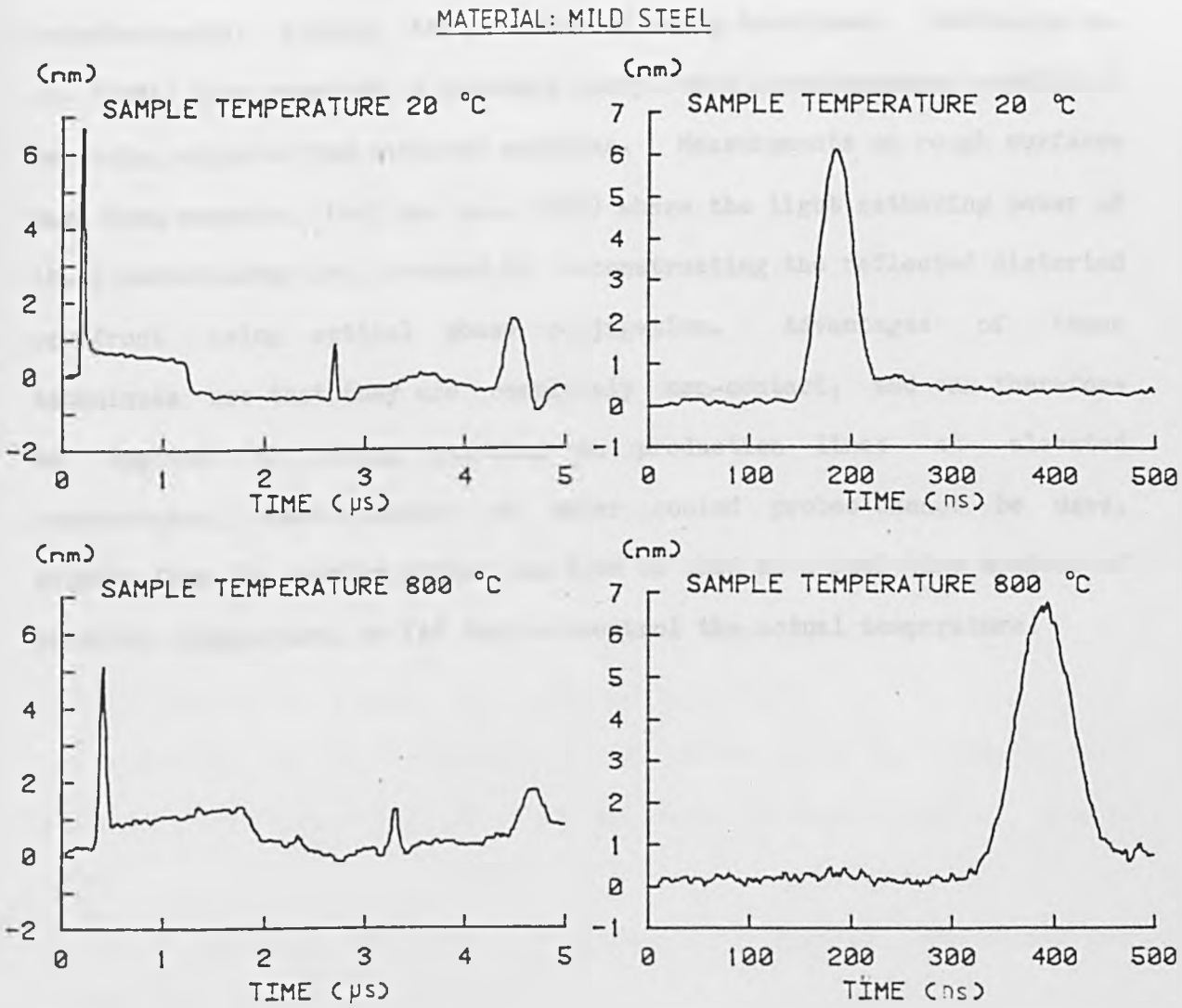

Fig. (6.18) Waveforms obtained at room and elevated temperatures in mild steel.

control have been made, the development of material processing sensors is presently the limiting factor for many potential applications of automated process control. The technology described above will only have real applications on samples that have a reasonably reflecting surface available for interferometer access. However, more sensitive interferometric sensors are constantly being developed. Monchalin et. al. (1985) have reported a confocal Fabry-Perot interferometer capable of receiving signals from machined surfaces. Measurements on rough surfaces have been reported (Paul et. al., 1987) where the light gathering power of the interferometer is increased by reconstructing the reflected distorted wavefront using optical phase conjugation. Advantages of these techniques are that they are completely non-contact, and can therefore be applied to moving material on production lines at elevated temperatures, where contact or water cooled probes cannot be used. Signals from the sensing system can then be used as a real time monitor of material temperature, or fed back to control the actual temperature.

6.7 References

M. F. Ashby, D. R. H. Jones, in "Engineering Materials 2: An Introduction to Microstructures, Processing and Design" (Pergamon Press, Oxford, 1986).

A. C. Bailey, B. Yates, UKAEA TRG Report 1874 (C/X), 1969.

R. M. Bozorth ,in "Ferromagnetism" (D. Van Nostrand Company Inc., Canada) p. 738, (1951).

J. A. Brammer, C. M. Percival, Exper. Mech. 10 245 (1970).

B. Butler, S. B. Palmer, G. J. Primavesi, Ultrasonics 17 249 (1979).

C. A. Calder, W. W. Wilcox, in "Characterisation of Materials for Service at Elevated Temperatures" (Edited by G. V. Smith, ASME) p.169, (1978).

C. A. Calder, E. C. Draney, W. W. Wilcox, J. Nucl. Mater. 97 126 (1981).

E. H. F. Date, M. Atkins, G. V. Beaton, Ultrasonics 9 209 (1971).

D. J. Dever, J. Appl. Phys. 43 3293 (1972).

R. J. Dewhurst, D. A. Hutchins, S. B. Palmer, C. B. Scruby, J. Appl. Phys. 53 4064 (1982).

F. E. Faris, L. Green, C. A. Smith, J. Appl. Phys. 23 89 (1952).

J. P. Frederick, J. Acoust. Soc. Amer. 20 568 (1948).

A. Goldsmith, T. E. Waterman, H. J. Hirschhorn, in "Handbook of Thermophysical Properties of Solid Materials" (Pergamon Press, London ,1961).

G. W. C. Kaye, T. H. Laby, in "Tables of Physical and Mechanical Constants" (Longman, London, 1986).

J. P. Monchalin, Appl. Phys. Lett. 47 14 (1985).

J. P. Monchalin, and R. Heon, Mater. Eval. 44 1237 (1986).

M. J. P. Musgrave, in "Crystal Acoustics" (Holden-Day Inc., London, 1970).

E. P. Papadakis, L. C. Lynnworth, K. A. Fowler, E. H. Carnevale, J. Acoust. Soc. Amer. 52 850 (1972).

M. Paul, B. Betz, W. Arnold, submitted to Appl. Phys. Lett. (1987).

D. Peckner, I. M. Bernstein, in "Handbook of Stainless Steels" (McGraw Hill, New York) p.19-8, (1977).

C. B. Scruby, R. L. Smith, B. C. Moss, NDT Inter. 19 307 (1986).

R. M. Tennent, in "Science Data Book" (Oliver and Boyd, Edinburgh, 1971).

H. N. G. Wadley, S. J. Norton, F. Mauer, B. Droney, Phil. Trans. Roy. Soc. Lond. A 320 341 (1986).

B. Yates, in "Thermal Expansion" (Plenum Press, New York) p. 6 (1972).

K. R. Whittington, Brit. J. of N.D.T. p. 242 (September, 1978)

Chapter 7

Ultrasonic Thickness Measurements in Thin Plates Using Lasers

7.0 Introduction

Pulsed ultrasound has long been used to measure the thickness of components, where there is access to only one of the faces. Industrial ultrasonic thickness measurements are most commonly made by timing the round trip transit time for a longitudinal pulse to traverse a sheet or plate. The measured time can then be converted into a thickness measurement, provided the ultrasonic velocity in the material is known. Many commercial ultrasonic thickness gauges are now in use, based on this principle (Krautkramer, 1983). However, they rely on a piezoelectric ultrasonic transducer that is in mechanical contact with the component, and acts as both transmitter and receiver of ultrasound. This is a limitation where the surface is curved, hot or rough. A further limitation of the standard approach is the inherent dead time of the transducer associated with the transfer from transmitting to receiving mode. This limitation has been partially overcome by the use of "double crystal" probes, but the minimum thickness that can reliably be gauged is only of the order of 0.5 mm. Dead time is, to a certain extent, a limiting factor, but discrimination between separate echoes at typical ultrasonic frequencies of 10 KHz to 20 MHz provides an insurmountable restriction.

There has been considerable interest recently in the use of laser based techniques to overcome these problems. In this chapter, two different techniques will be examined using a pulse-echo configuration to measure the thickness of aluminium shims in the range 0.1 to 2 mm. The

measurement of aluminium sheet thicknesses of the order of 0.5 mm and less will be examined using Lamb waves.

7.1 The Pulse-Echo Technique

The most common technique for ultrasonic thickness measurements is to monitor the time dependent surface displacements caused by multiple longitudinal pulse reflections in a sample. The thickness, d, of a sample may be evaluated from the simple relationship,

$$d = \frac{tV}{2} \qquad (7.1)$$

where t is the time interval between two consecutively reflected pulses and V is the velocity of the ultrasonic pulse in the material. If the ultrasonic pulse has a width of the order of the laser pulse duration, then the pulse separation must be greater than the laser pulse width in order that the reflected pulses do not combine additively. Thus a minimum measurable thickness with any laser technique is given by,

$$d_{min} = \frac{\tau V}{2} \qquad (7.2)$$

where τ is the laser pulse duration. For a laser pulse width of 50 ns and a longitudinal velocity of 6320 m/s for aluminium, the minimum measurable thickness is of the order of 0.16 mm. It follows from this simple expression that it is advantageous to use lasers of short pulse duration. In order to be able to detect and resolve the sharp acoustic pulses generated, detectors are required that are fast and free from "ringing". Conventional piezoelectric transducers are not suitable for this purpose. The fast risetime and short duration of laser-acoustic pulses, allows measurement to be made on a wide range of thickness of materials, with advantages of a non-contact technique. Tam (1984) has used a nitrogen laser of energy $\sim$ 1 mJ, and pulse duration $\sim$ 0.5 ns full width half

maximum, for generation of acoustic pulses of the order of 1 ns duration. These repetitive longitudinal pulses were satisfactorily detected, on epicentre, with a contacting thin film zinc oxide transducer, enabling the thickness of stainless steel sheet in the range 12 to 260 μm to be accurately determined. This work was extended by Sontag and Tam (1985) who used a He-Ne laser probe beam deflection technique for ultrasonic detection. The low laser energies employed ensured that no surface damage occurred. Multiple longitudinal reflections were clearly visible in thin silicon wafers of known thicknesses (0.26 to 0.6 mm) and with different orientations and doping levels, which enabled accurate measurements of the longitudinal velocities using a Fourier transform analysis. However, it should be noted that factors such as high attenuation, and surface roughness may make the detection of very narrow acoustic pulses (< 10 ns) difficult.

7.2 Experimental arrangement

A convex lens of 10 cm focal length, was used to focus laser pulses, of energy $\sim$ 5 mJ, onto one surface of a parallel sided 99% pure aluminium sample. Plate thicknesses in the range 0.1 to 2 mm have been examined. The dimensions of the plates were such that side wall reflections did not obscure the desired signals. The resulting ultrasonic transients were monitored on the opposite face, on epicentre, with the interferometer which was focussed to a spot with a 15 cm focal length convex lens.

7.2.1 Results

Fig. (7.1) shows waveforms detected on a 1.98 mm thick sample on 2 and 5 μs timescales. Multiple longitudinal echoes are clearly visible in both traces. It is clear from fig. (7.1a) that the longitudinal echo

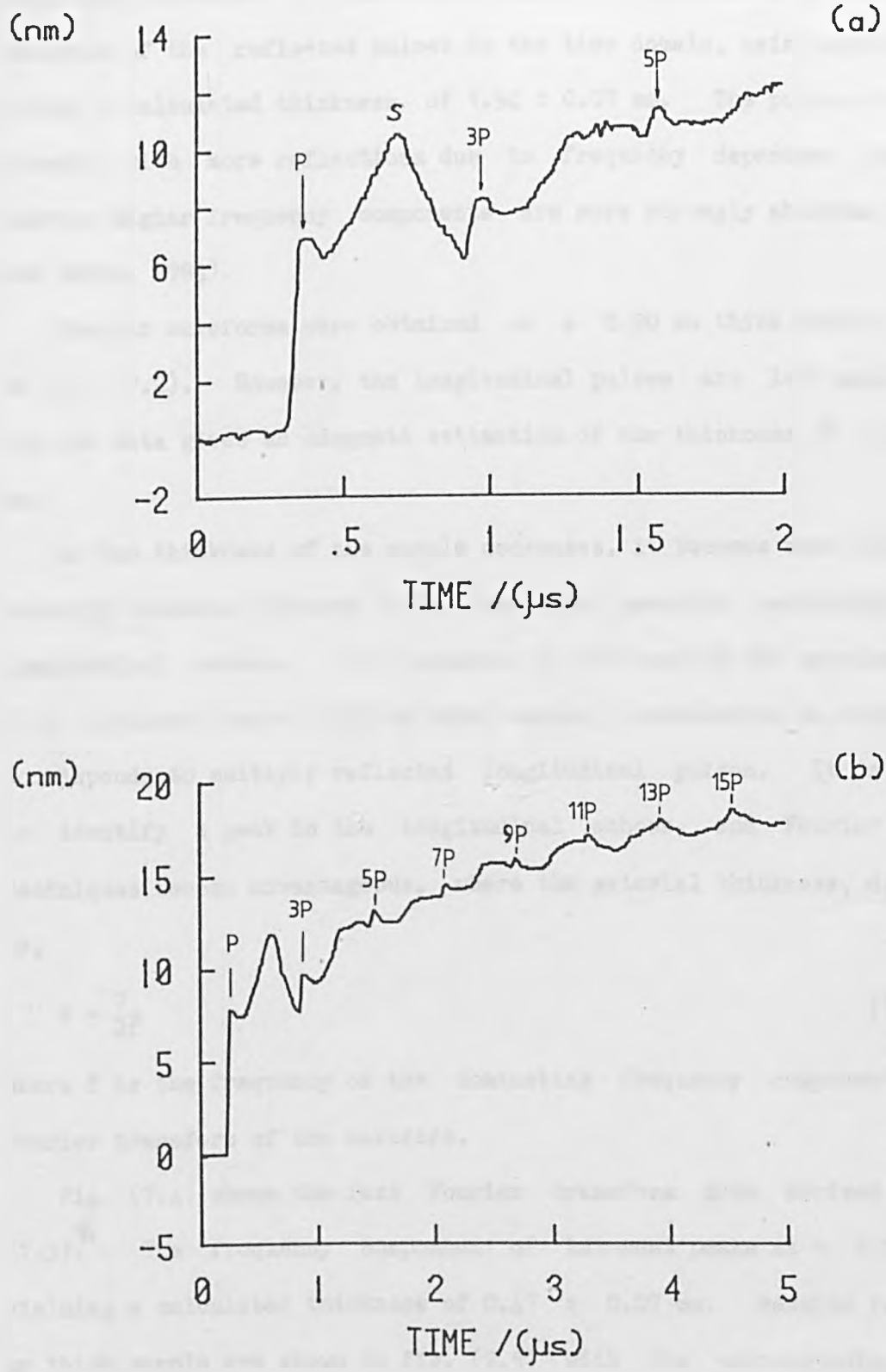

Fig. (7.1) Experimental results showing repetitive longitudinal pulse reflections in a 1.98 mm thick aluminium sample, on different timescales.

amplitude decreases in time corresponding to attenuation in the material. Analysis of the reflected pulses in the time domain, using equation (7.1) yields a calculated thickness of 1.94 ± 0.07 mm. The pulses also become broader with more reflections due to frequency dependent absorption, whereby higher frequency components are more strongly absorbed (Reynolds and Smith, 1984).

Similar waveforms were obtained on a 0.90 mm thick sample, as shown in fig. (7.2). However, the longitudinal pulses are less well defined, but the data gives an adequate estimation of the thickness of 0.97 ± 0.07 mm.

As the thickness of the sample decreases, it becomes more difficult to identify discrete features in the acoustic waveform pertaining to the longitudinal echoes. For example, in the case of the waveform of fig. (7.3) obtained from a 0.425 mm thick sample, a modulation is visible which corresponds to multiply reflected longitudinal pulses. It is difficult to identify a peak in the longitudinal echoes, and Fourier analysis techniques become advantageous, where the material thickness, d, is given by,

$$d = \frac{V}{2f} \qquad (7.3)$$

where f is the frequency of the dominating frequency component in the Fourier transform of the waveform.

Fig. (7.4) shows the fast Fourier transform data derived from fig. (7.3).* The frequency component of interest peaks at ∿ 6.75 MHz, yielding a calculated thickness of 0.47 ± 0.07 mm. Results for a 102 μm thick sample are shown in fig. (7.5) with the corresponding Fourier transform in fig. (7.6). As expected from the result derived from equation (7.2) for the minimum measurable thickness, the waveform of fig. (7.5) is not understood, and the dominant frequency component of fig.

* The FFT routine splits the target array into real and imaginary parts, with each array containing 256 points.

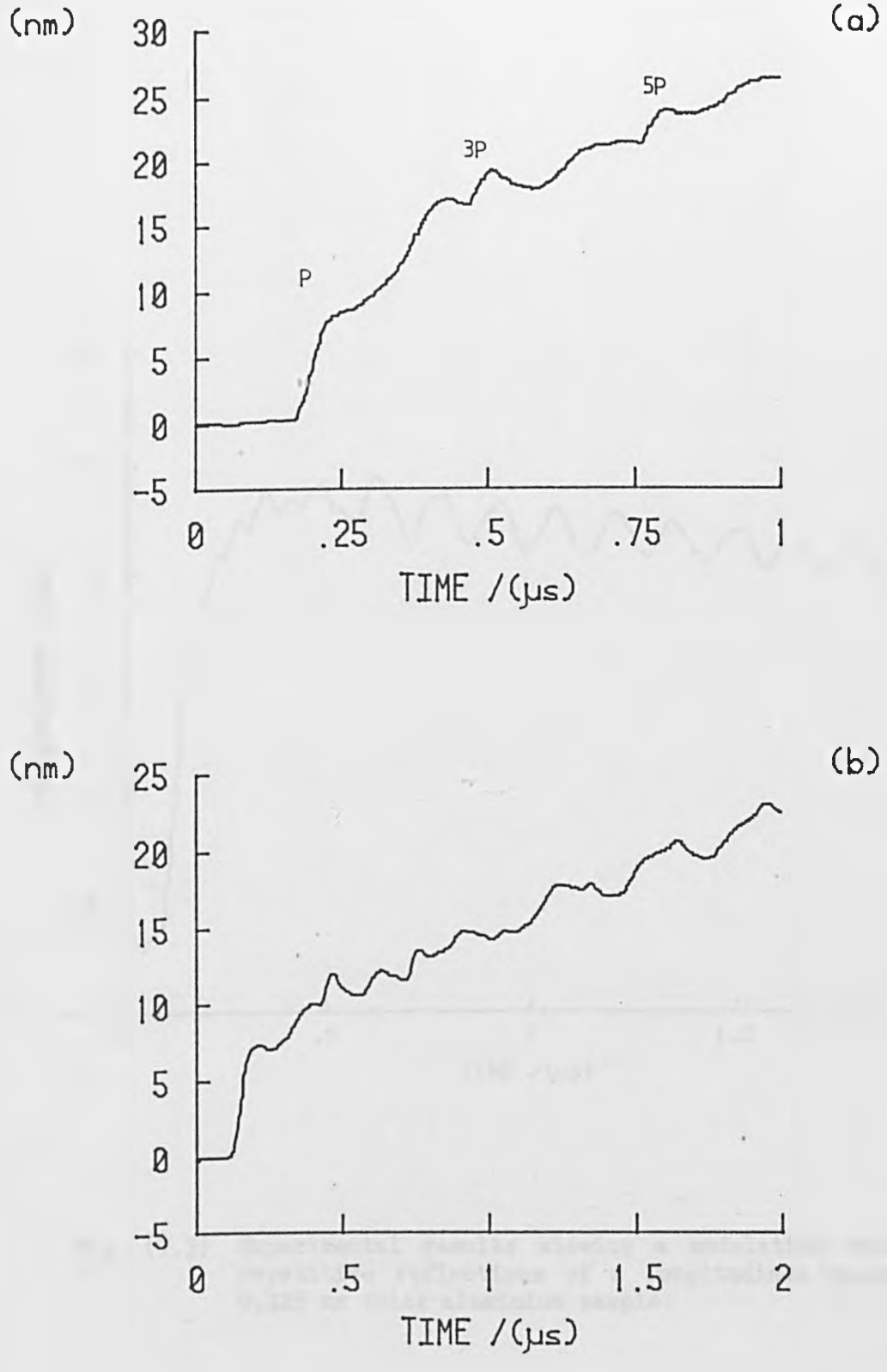

Fig. (7.2) Experimental results showing repetitive longitudinal pulse reflections in a 0.9 mm thick aluminium sample, on different timescales.

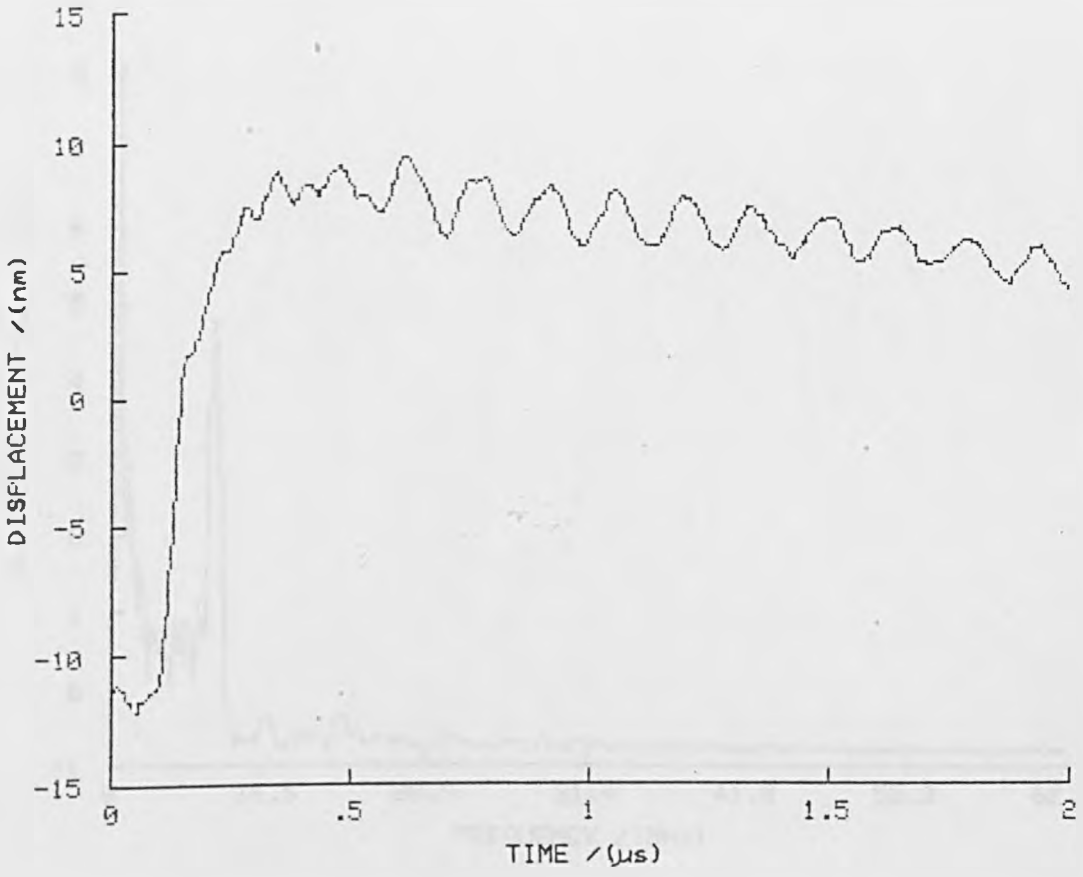

Fig. (7.3) Experimental results showing a modulation caused by repetitive reflections of a longitudinal pulse in a 0.425 mm thick aluminium sample.

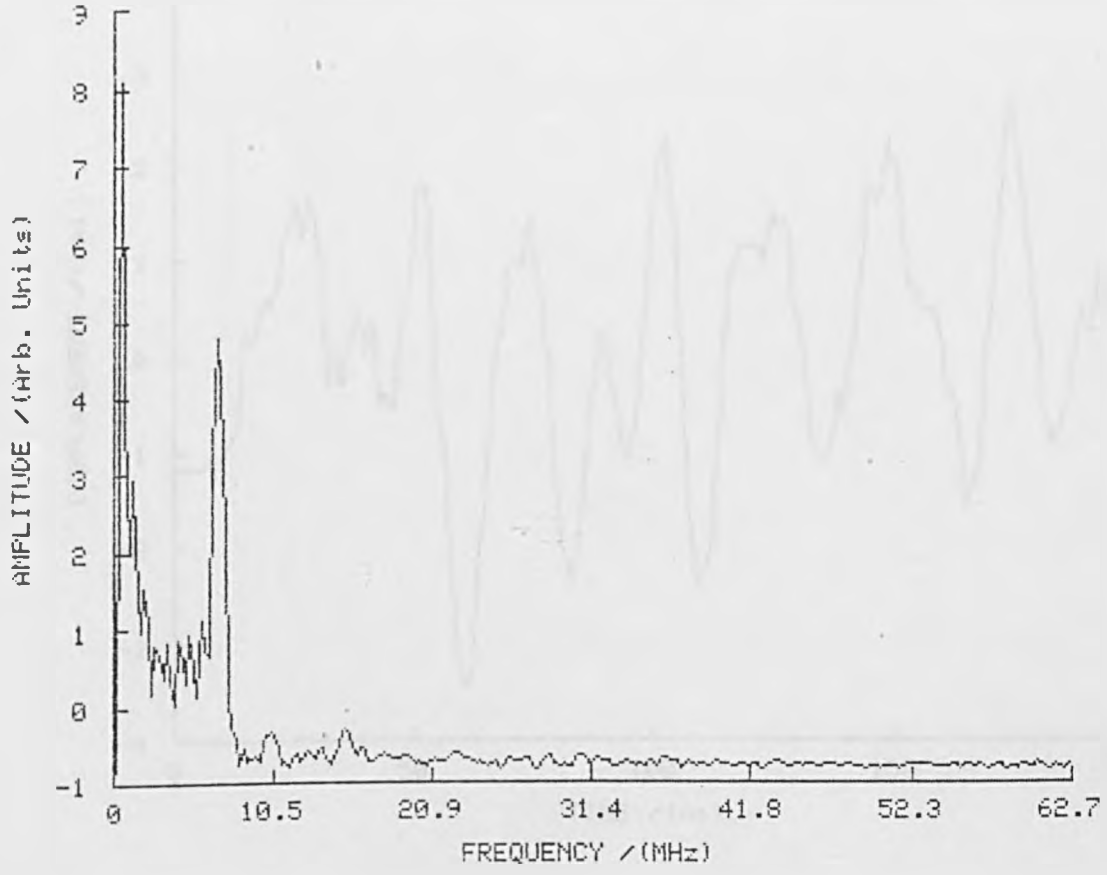

Fig. (7.4) Fourier transform of fig. (7.3). The frequency component at 6.75 MHz can be related to the plate thickness.

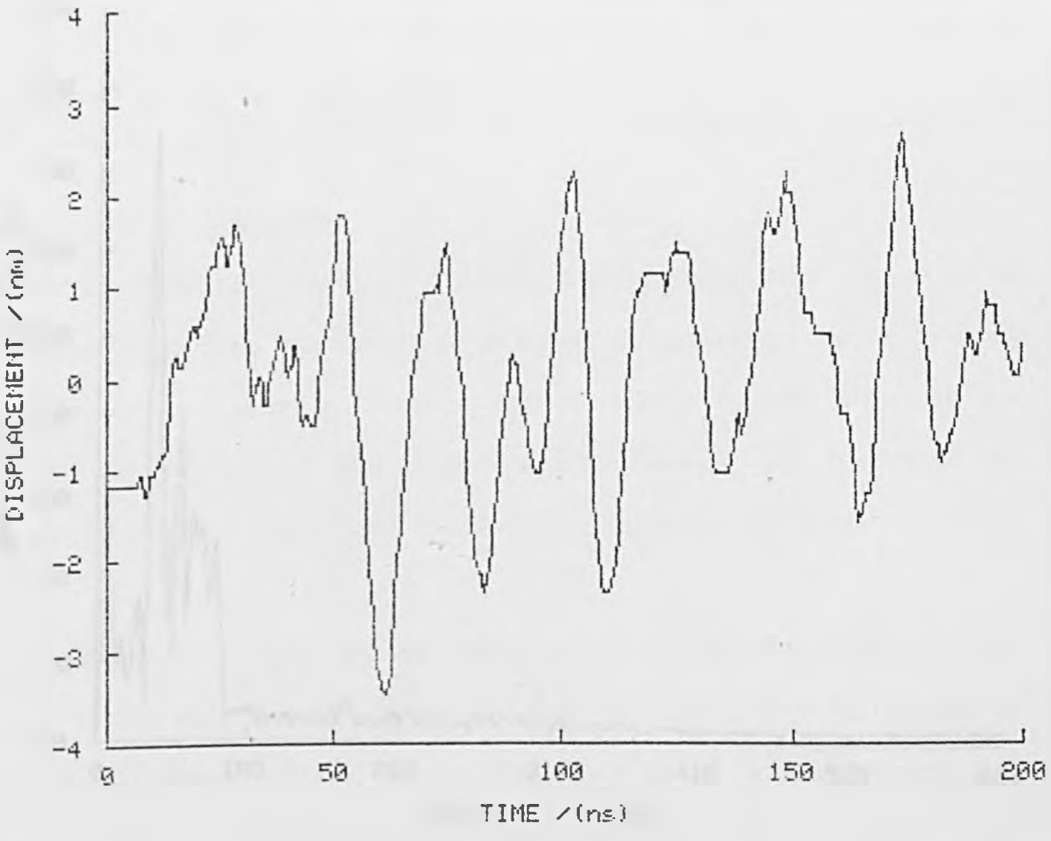

Fig. (7.5) Experimental results obtained from a 102 μm thick sample. The features of the waveform are not understood.

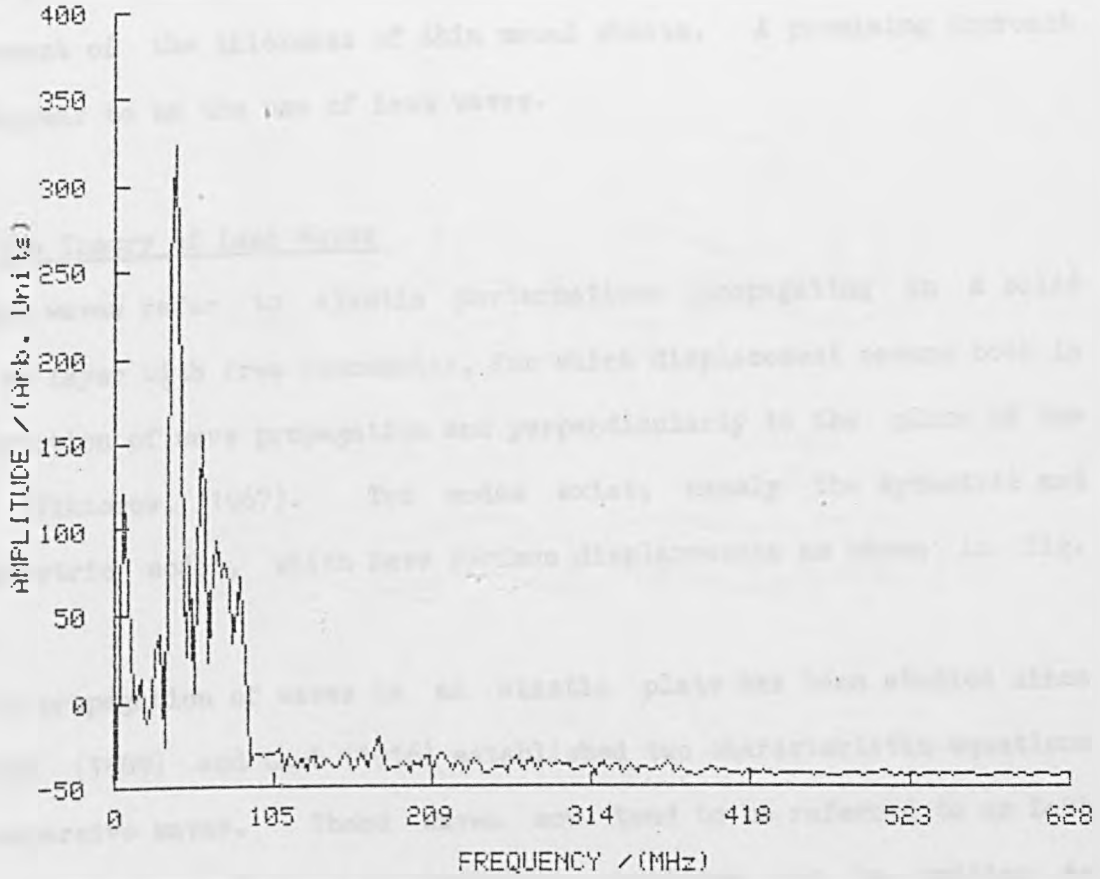

Fig. (7.6) Fourier transform of fig. (7.5).

(7.6) yields a poor thickness estimation of 80 ± 9 μm.

7.3 Thickness Measurements using Lamb Waves

The rapid growth of industrial ultrasonic testing applications in recent years has stimulated increasing interest in the accurate measurement of the thickness of thin metal sheets. A promising approach would appear to be the use of Lamb waves.

7.3.1 The Theory of Lamb Waves

Lamb waves refer to elastic perturbations propagating in a solid plate or layer with free boundaries, for which displacement occurs both in the direction of wave propagation and perpendicularly to the plane of the plate (Viktorov, 1967). Two modes exist, namely the symmetric and antisymmetric modes, which have surface displacements as shown in fig. (7.7).

The propagation of waves in an elastic plate has been studied since Rayleigh (1889) and Lamb (1916) established two characteristic equations for dispersive waves. These waves now tend to be referred to as Lamb waves. The first of these characteristic equations can be written as (Lamb, 1916),

$$\frac{\tanh(\beta d/2)}{\tanh(\alpha d/2)} = \frac{4\varepsilon^2\alpha\beta}{(\varepsilon^2+\beta^2)^2} \qquad (7.4)$$

which is satisfied by symmetric Lamb waves, and the second is given by,

$$\frac{\tanh(\beta d/2)}{\tanh(\alpha d/2)} = \frac{(\varepsilon^2+\beta^2)^2}{4\varepsilon^2\alpha\beta} \qquad (7.5)$$

which is satisfied by antisymmetric Lamb waves, where d is the plate thickness, and α and β are related to the plate material elastic properties by $\alpha^2 = \varepsilon^2 - h^2$, and $\beta^2 = \varepsilon^2 - k^2$, where $h^2 = \rho\omega^2/(\lambda + 2\mu)$, and

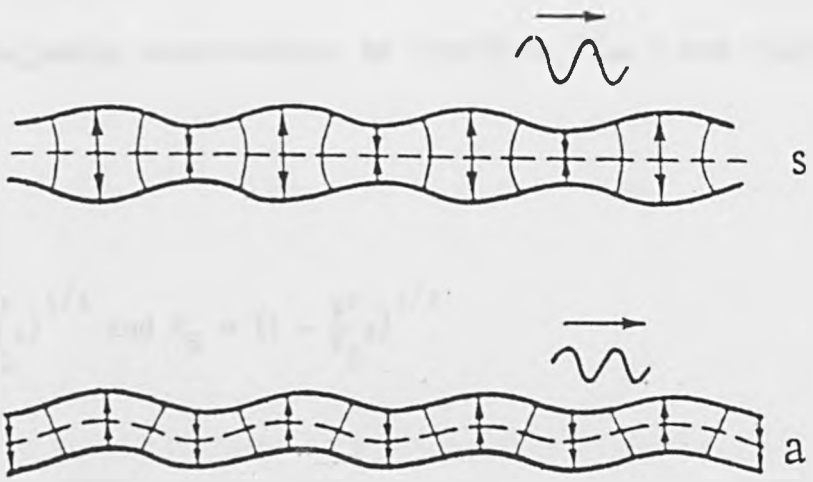

Fig. (7.7) Schematic diagram of the deformation of a plate during the propagation of symmetric (s) and antisymmetric (a) Lamb waves (after Viktorov, 1967).

$k^2 = \rho\omega^2/\mu$. λ and μ are the Lame constants, ε is the wavenumber and ρ is the density. These equations may be put into a form more suitable for evaluation by noting that the longitudinal and shear velocities may be written as,

$$V_L = \left(\frac{\lambda + 2\mu}{\rho}\right)^{1/2}$$

and

$$V_S = \left(\frac{\mu}{\rho}\right)^{1/2}$$

Thus making the following substitutions in equations (7.4) and (7.5),

$$\alpha = \frac{2\pi f R_L}{V}$$

$$\beta = \frac{2\pi f R_S}{V}$$

where $R_L = \left(1 - \frac{V^2}{V_L{}^2}\right)^{1/2}$ and $R_S = \left(1 - \frac{V^2}{V_S{}^2}\right)^{1/2}$

it follows that,

$$\frac{\tanh\left(\frac{\pi f d R_S}{V}\right)}{\tanh\left(\frac{\pi f d R_L}{V}\right)} = \frac{4R_L R_S}{(1 + R_S{}^2)^2} \qquad (7.6)$$

for symmetric Lamb modes and,

$$\frac{\tanh\left(\frac{\pi f d R_S}{V}\right)}{\tanh\left(\frac{\pi f d R_L}{V}\right)} = \frac{(1 + R_S{}^2)^2}{4R_L R_S} \qquad (7.7)$$

for the antisymmetric Lamb modes.

It is convenient to look upon these equations as expressions relating the Lamb wave phase velocity, V, to the product of frequency and plate thickness, fd. Since the longitudinal and shear velocities are well known for most materials, it is convenient in practice to arbitrarily select values for the Lamb wave phase velocity, and solve equations (7.6) and (7.7) for the corresponding values of fd. Numerical solutions of equations (7.6) and (7.7), in the form of dispersion curves relating the

phase velocity of a number of symmetric and antisymmetric Lamb modes to the frequency-plate thickness product are presented in fig. (7.8) (Farnell, 1978) for a typical isotropic plate. These curves were verified experimentally by Worlton (1961).

For small values of fd, where the wavelength of the Lamb waves is large compared with the plate thickness, the hyperbolic functions of equations (7.6) and (7.7) may be replaced by their arguments, such that for the symmetric mode, equation (7.6) reduces to,

$$(1 + R_S^2)^2 = 4R_L^2 \tag{7.8}$$

which on substituting for R_L and R_S gives,

$$V_{sheet} = 2V_S\left[\frac{V_L^2 - V_S^2}{V_L^2}\right]^{1/2} \tag{7.9}$$

or alternatively

$$V_{sheet} = \left[4\left(\frac{\lambda + \mu}{\lambda + 2\mu}\right)\frac{\mu}{\rho}\right]^{1/2} \tag{7.10}$$

Hence the symmetric modes tend towards a single well defined velocity, the sheet velocity.

For waves of short wavelength compared with the plate thickness, equations (7.6) and (7.7) can be written as,

$$(1 + R_S^2)^2 - 4R_L R_S = 0 \tag{7.11}$$

of more familiarly as,

$$\left[\frac{V}{V_S}\right]^6 - 8\left[\frac{V}{V_S}\right]^4 + 24\left[\frac{V}{V_S}\right]^2 - 16\left[\frac{V}{V_L}\right]^2 + 16\left[\frac{V_S}{V_L}\right]^2 - 16 = 0 \tag{7.12}$$

Equation (7.12) is recognised as Rayleighs equation, which describes wave motions travelling on the surface of an elastic solid (Viktorov, 1967, p.3). The Rayleigh result appears since for such small wavelengths the finite thickness of the plate appears as a semi-infinite media. Thus from observation of the dispersion curves of fig. (7.8) and equations (7.6) and (7.7) it becomes clear that the phase velocities of the lowest order symmetric and antisymmetric modes, become assymptotic to the

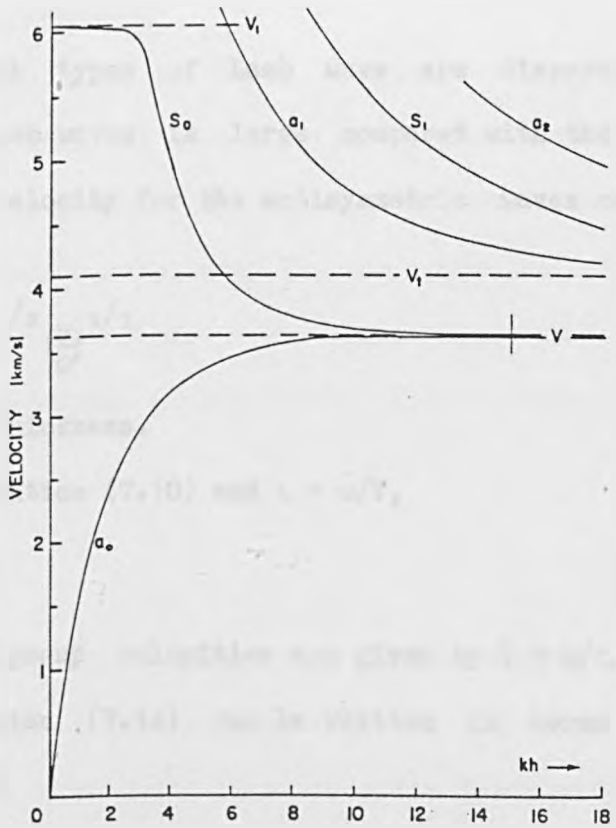

Fig. (7.8) Dispersion curves for symmetric (s) and antisymmetric (a) Lamb modes propagating in an isotropic plate of thickness h (after Farnell, 1978). The Rayleigh, shear and longitudinal velocities are shown as V, V_t and V_l respectively.

velocity of a Rayleigh wave, for increasing plate thickness. In contrast, as the plate thickness decreases, the phase velocity of the lowest order antisymmetric mode tends to zero, while that of the lowest order symmetric mode tends to the longitudinal or sheet velocity.

7.4 Estimation of the Thickness of Metal Sheet using Lamb Waves

7.4.1 Introduction

In general both types of Lamb wave are dispersive. When the wavelength of the Lamb waves is large compared with the thickness ($\lambda >> d$), then the phase velocity for the antisymmetric waves can be written as (Lamb, 1916),

$$V = \frac{2\varepsilon h}{\sqrt{3}}\left(\frac{\lambda + \mu}{\lambda + 2\mu}\right)^{1/2}\left(\frac{\mu}{\rho}\right)^{1/2} \qquad (7.13)$$

were h is the half thickness.

Substituting for equation (7.10) and $\varepsilon = \omega/V$,

$$V^2 = \frac{\omega d}{2\sqrt{3}}\, V_{sheet} \qquad (7.14)$$

Since the phase and group velocities are given by $V = \omega/\varepsilon$, and $V_g = d\omega/d\varepsilon$ respectively, equation (7.14) can be written in terms of the group velocity as follows,

$$V_g^{\,2} = \frac{4\pi f d}{\sqrt{3}}\, V_{sheet} \qquad (7.15)$$

Equation (7.15) indicates that plotting $V_g^{\,2}$ versus $4\pi f V_{sheet}/\sqrt{3}$ should result in a straight line, the gradient of which will yield the plate thickness, d, provided that the assumption of the wavelength being much greater than the plate thickness is valid. Thus it was necessary to evaluate the dominant frequency component and corresponding group velocities at different points along the antisymmetric wave train. The technique which was adopted evaluated the frequency from the inverse of the time difference between successive maxima (and successive minima), and

associating it with a velocity determined from the source to detector distance, and the mean arrival time. Fig. (7.9) illustrates this technique. Other variations of this technique are possible (Pilant, 1979). The data analysis approach adopted here is similar to that of Brune et. al. (1960).

7.4.2 Experimental Arrangement

A cylindrical lens of 5 cm focal length was used to produce a line focus on the surface of a 99% pure aluminium plate, producing preferential ultrasonic wave propagation perpendicular to the line (Aindow et. al., 1982). Generation was accomplished in the thermoelastic regime with an incident laser energy of $\sim$ 7 mJ. The Lamb waves were detected at the focus of the interferometer, at a distance of 24 mm away from the acoustic source.

7.4.3 Results

The laser ultrasonic source generated both symmetric and antisymmetric Lamb waves. Since the interferometer was sensitive to out of plane surface motion, it was more suited for the detection of antisymmetric waves, but had sufficient sensitivity to record the symmetric arrival. Fig. (7.10) shows a waveform obtained on a 425 μm thick aluminium sheet. There is clear frequency dispersion of the large amplitude antisymmetric mode, with the higher frequency components arriving first after about 8 μs. There is also evidence of dispersion in the smaller amplitude symmetric mode, which arrives after approximately 5 μs. For the case of a sample of 80 μm in thickness, fig. (7.11) shows that the symmetric arrival is a relatively brief event, while the antisymmetric arrival again shows characteristic frequency dispersion. Measurement of the sheet

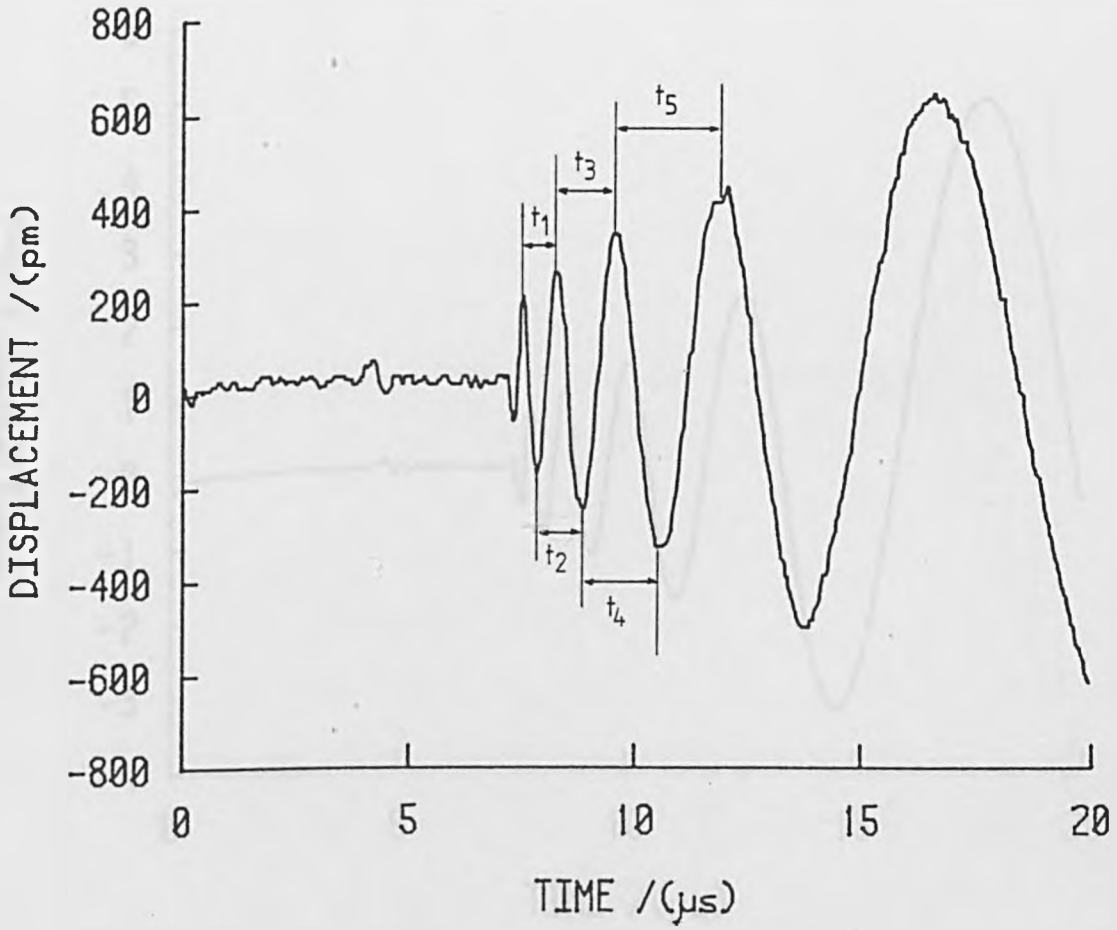

Fig. (7.9) Illustration of the analysis of a Lamb waveform for plate thickness estimation. The frequency of a component is evaluated from 1/t, and the corresponding arrival time from the mean time between the two peaks of the component.

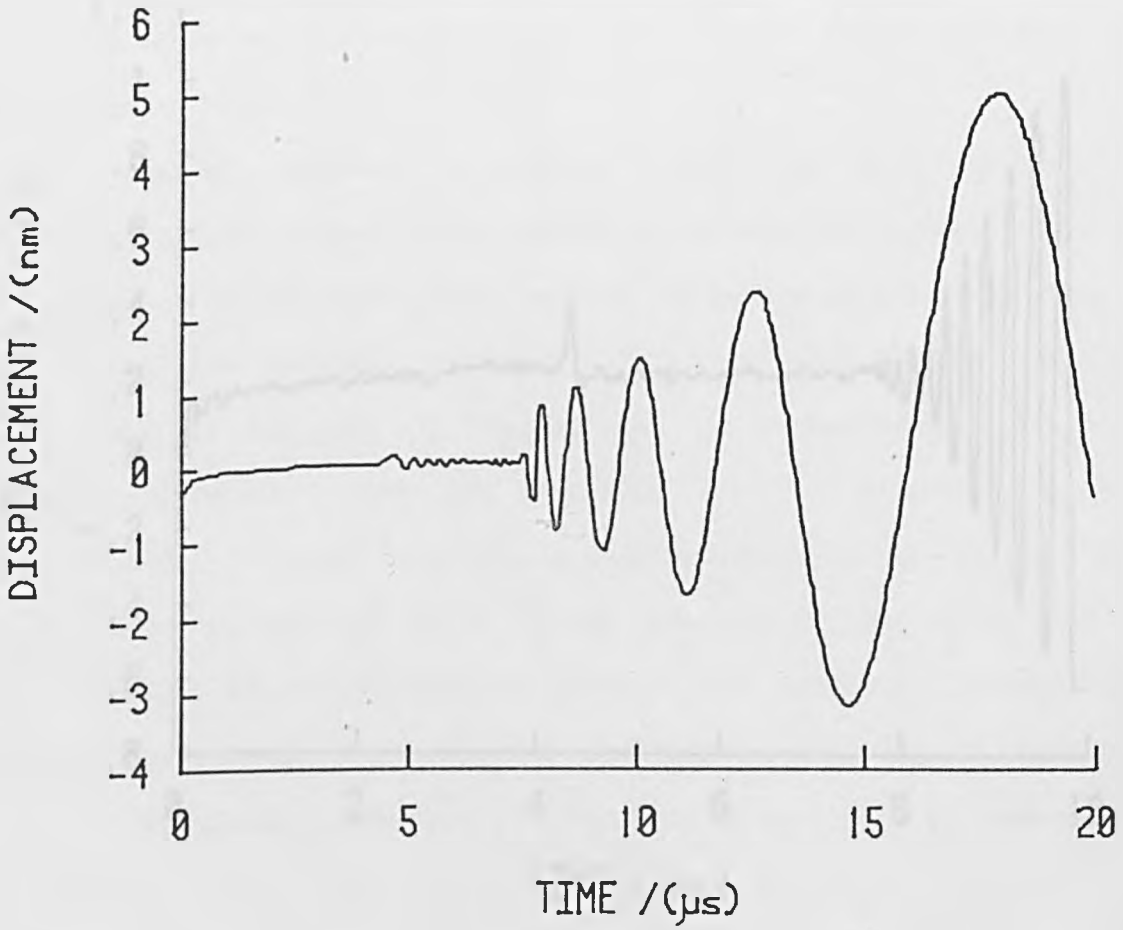

Fig. (7.10) Lamb waves detected at a distance of 24 mm away from the acoustic source in an aluminium plate of thickness 425 μm.

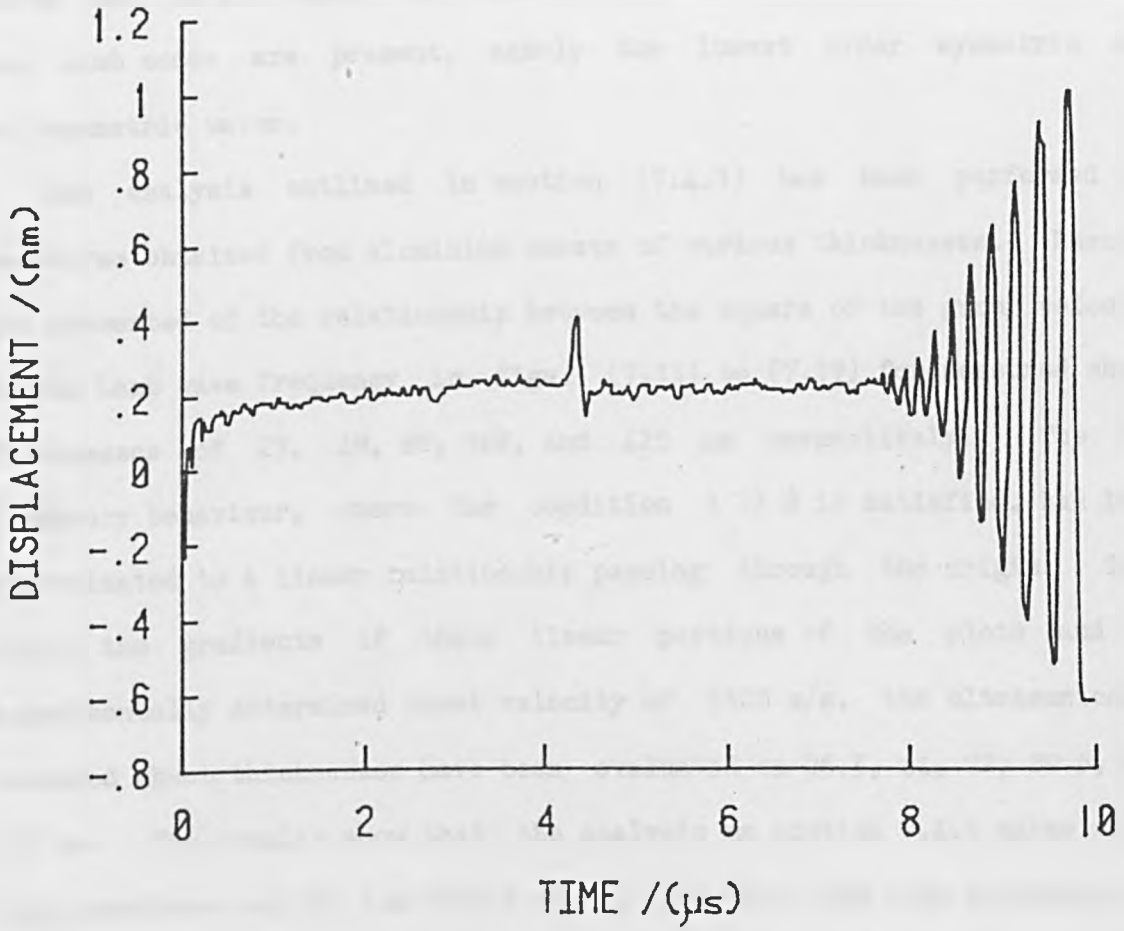

Fig. (7.11) Lamb waves detected at a distance of 24 mm away from the acoustic source in an aluminium plate of thickness 80 μm.

velocity from fig. (7.11) yields a value of 5500 ± 60 m/s, which can be compared with a value of 5531 m/s from evaluation of equation (7.9) for an accepted longitudinal velocity of 6400 m/s and a shear velocity of 3111 m/s in aluminium. Fig. (7.12) shows the dispersion relationship for plate thicknesses of 49, 102, and 425 μm. Comparison with the experimental dispersion curves obtained by Worlton (1961) in aluminium shows that in all cases, the values of fd measured necessitates that only two Lamb modes are present, namely the lowest order symmetric and antisymmetric waves.

The analysis outlined in section (7.4.1) has been performed on waveforms obtained from aluminium sheets of various thicknesses. Results are presented of the relationship between the square of the group velocity versus Lamb wave frequency in figs. (7.13) to (7.17) for measured sheet thicknesses of 27, 49, 80, 102, and 425 μm respectively. The low frequency behaviour, where the condition $\lambda >> d$ is satisfied, has been approximated to a linear relationship passing through the origin. Thus using the gradients of these linear portions of the plots and an experimentally determined sheet velocity of 5500 m/s, the ultrasonically measured sheet thicknesses have been evaluated as 26.5, 44, 72, 89.5, and 300 μm. The results show that the analysis on section 7.4.1 makes valid approximations only at low values of fd, for which the Lamb wavelength is large compared with the sample thickness, and discrepancies should be expected at higher values as seen in fig. (7.17) for the 425 μm sample. A comparison between thickness measurements using the Lamb wave technique, the pulse-echo measurements and micrometer measurements are summarised in table (7.1).

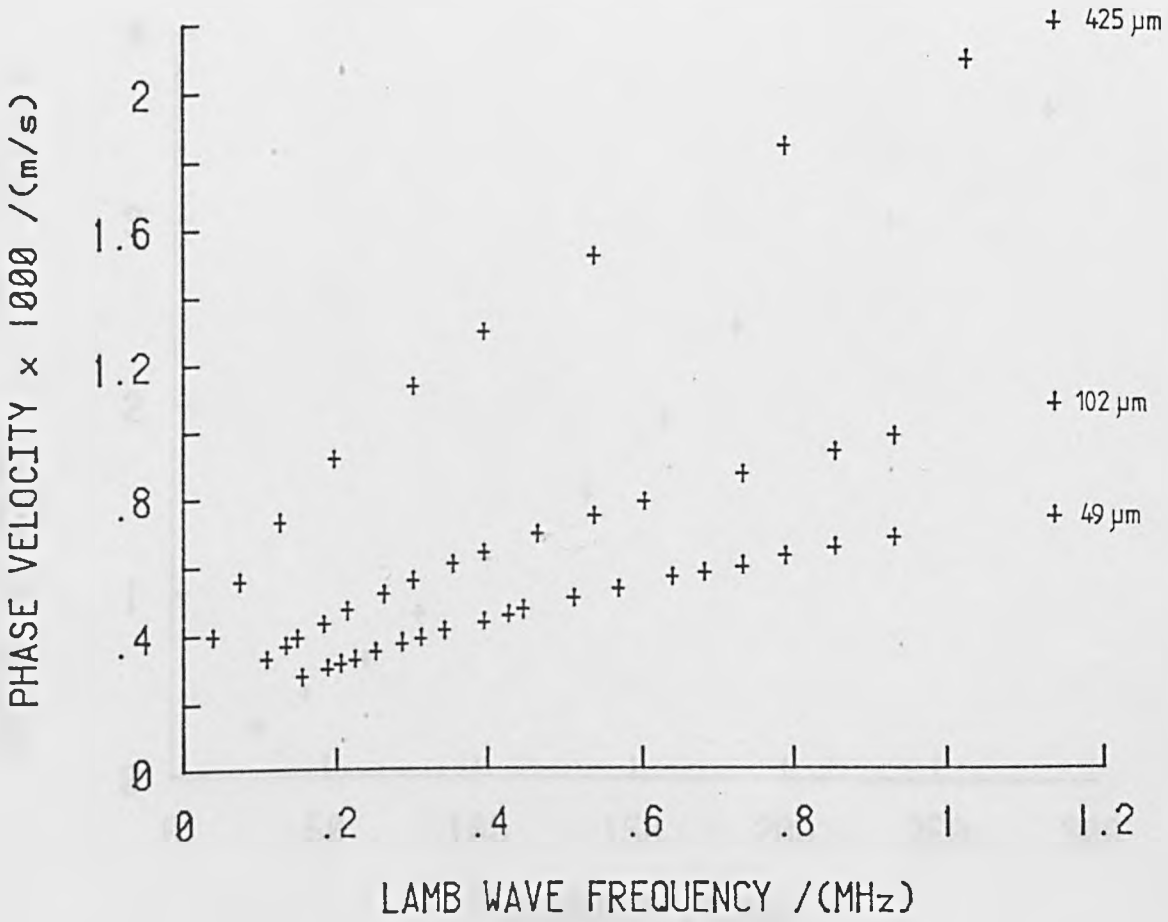

Fig. (7.12) Dispersion curves for aluminium samples of thickness 425, 102, and 49 µm.

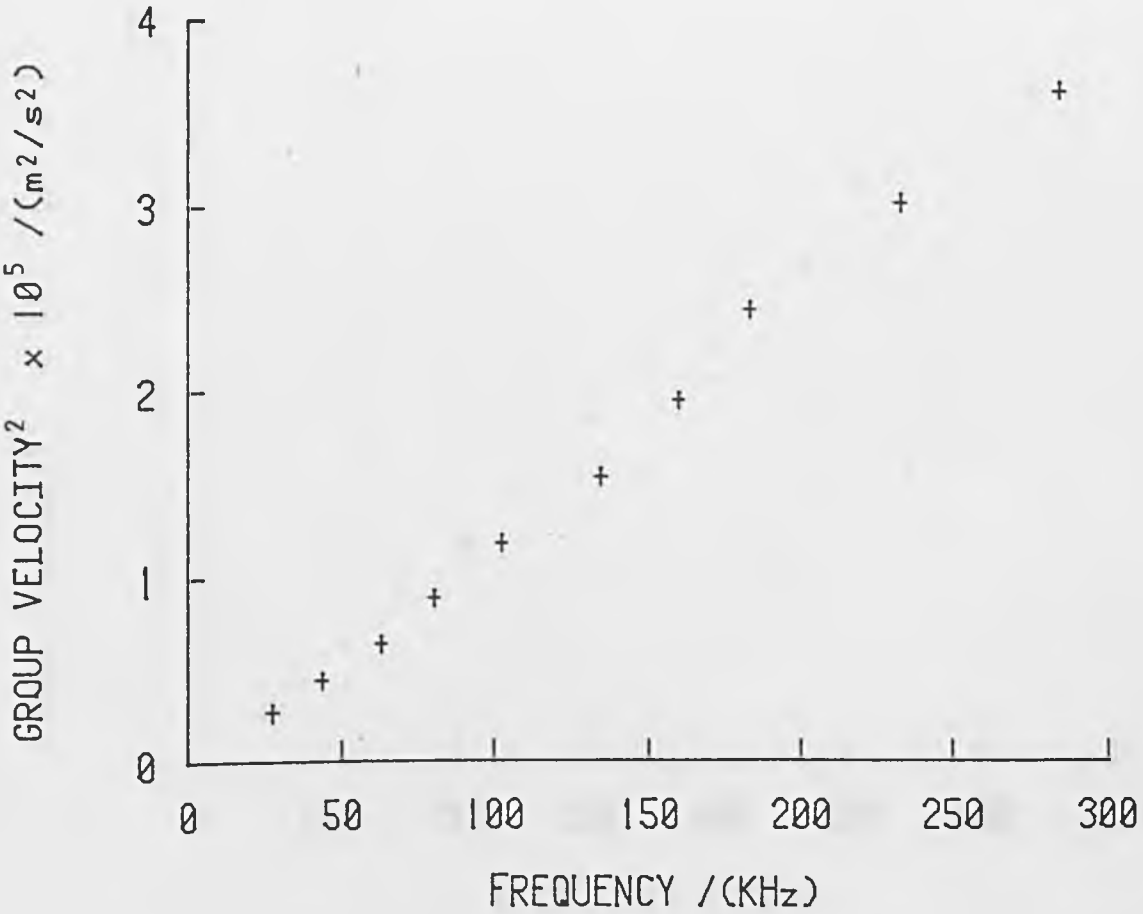

Fig. (7.13) Frequency dependence of the square of the group velocity. A least squares fit through the origin and the low frequency data gives a thickness estimate of 26.5 μm, compared with a micrometer measurement of 27 μm.

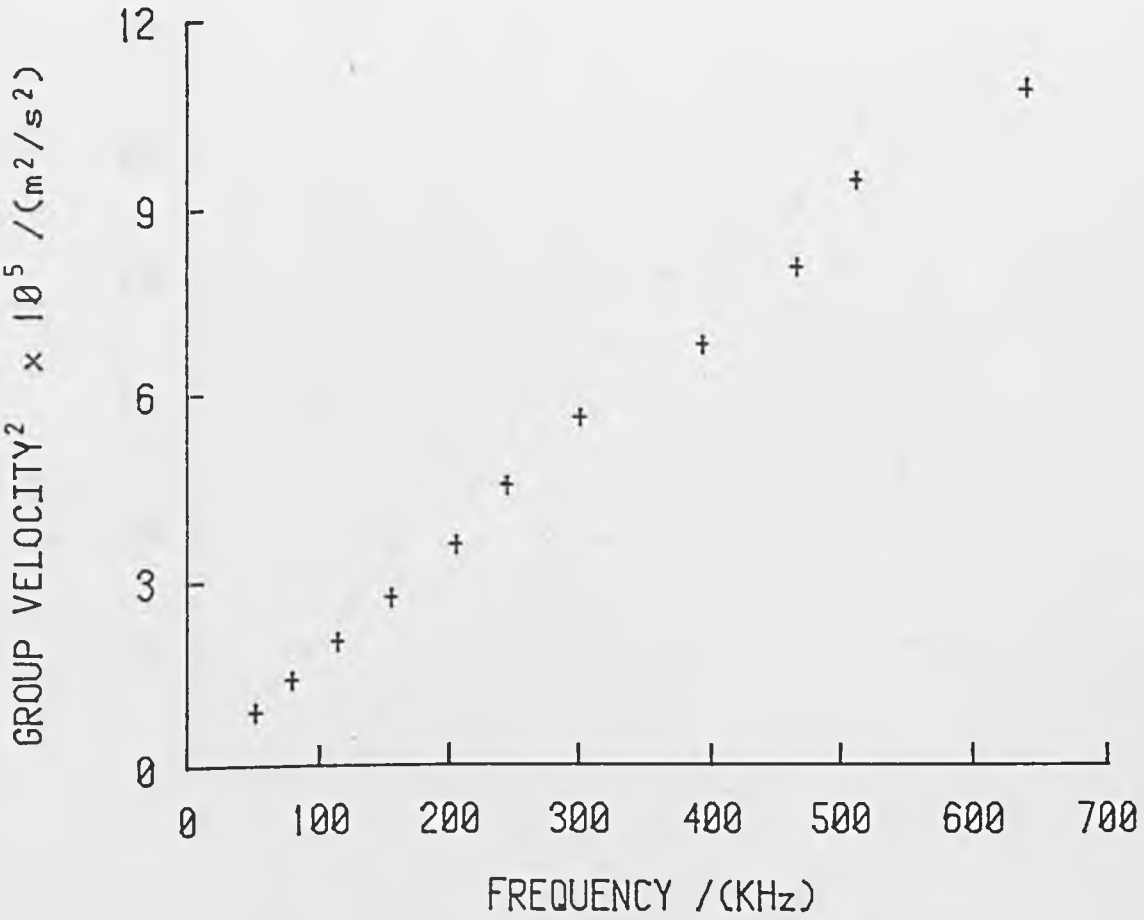

Fig. (7.14) Frequency dependence of the square of the group velocity for a 49 μm thick sample. Estimated thickness is 44 μm.

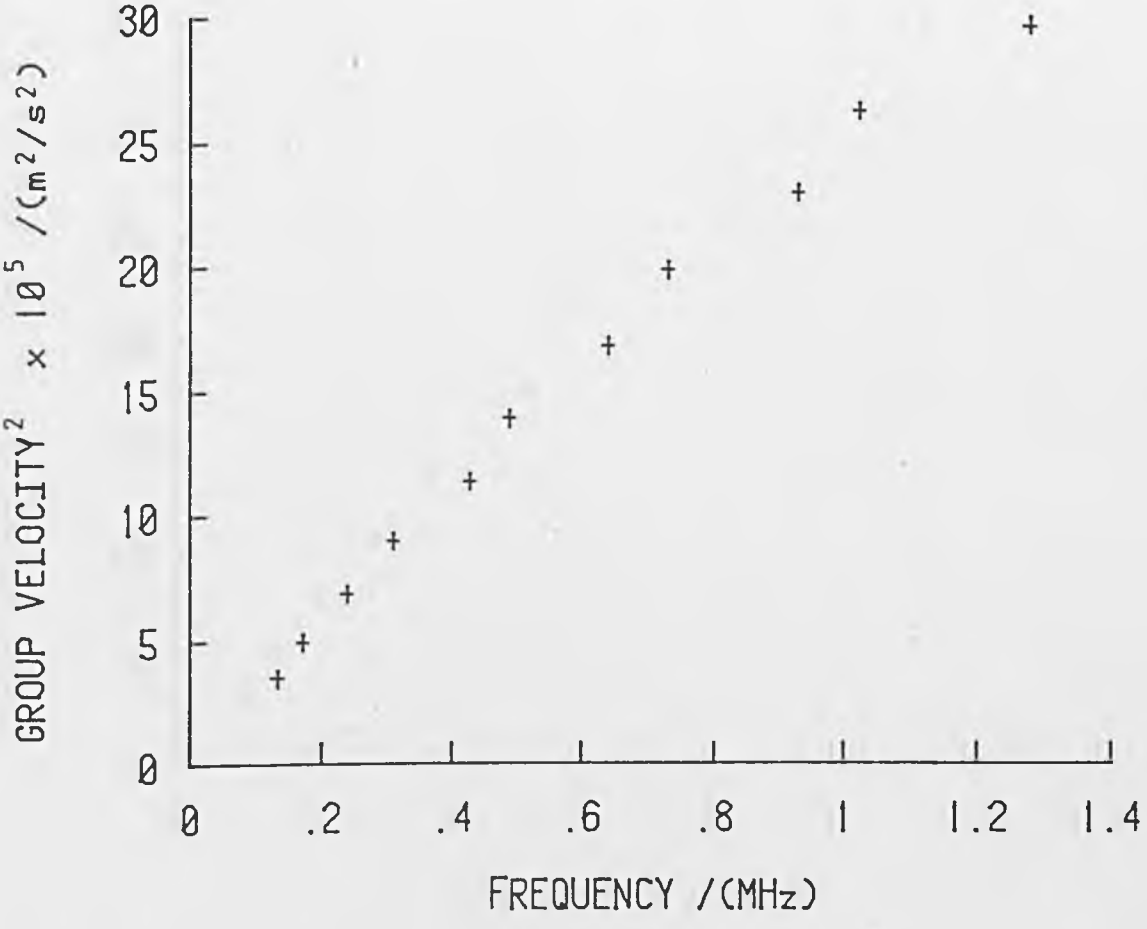

Fig. (7.15) Frequency dependence of the square of the group velocity for an 80 μm thick sample. Estimated thickness is 72 μm.

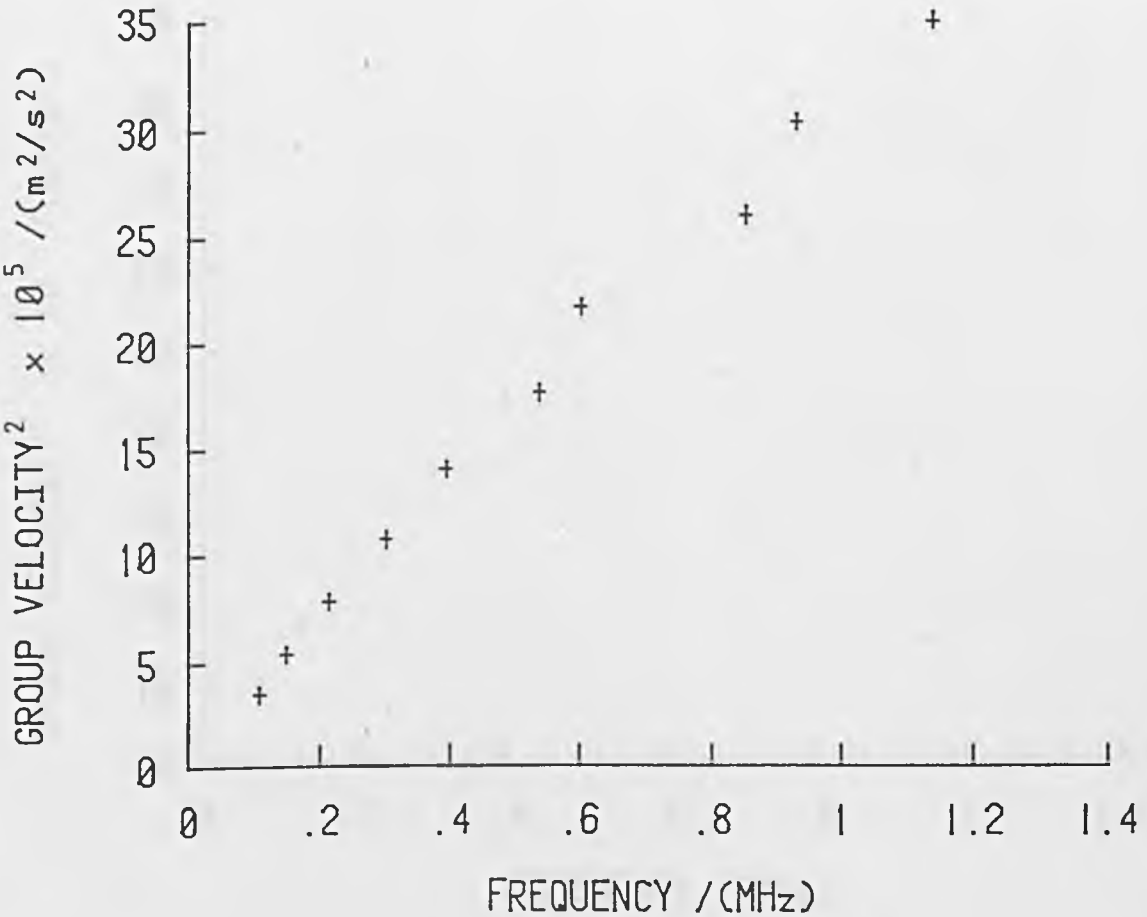

Fig. (7.16) Frequency dependence of the square of the group velocity for a 102 μm thick sample. Estimated thickness is 89.5 μm.

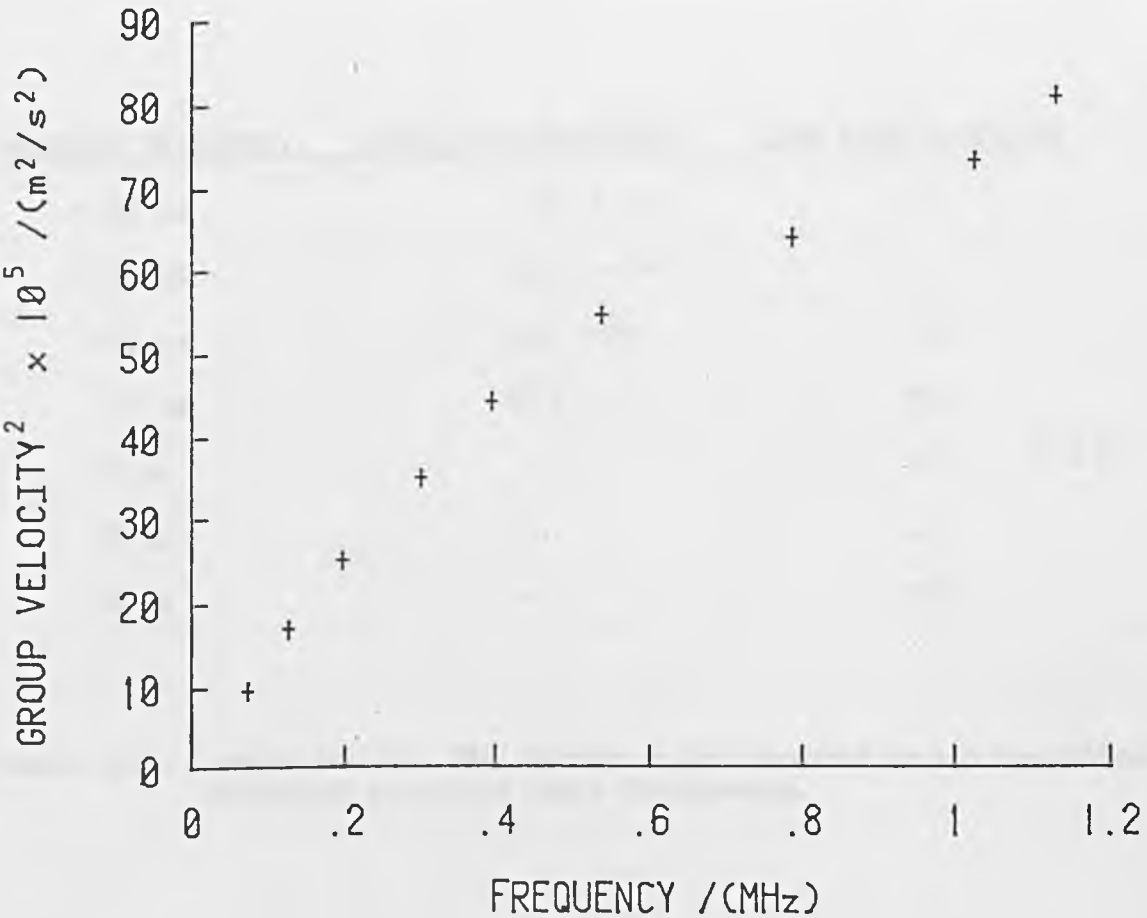

Fig. (7.17) Frequency dependence of the square of the group velocity for a 425 μm thick sample. Estimated thickness is 300 μm.

MEASURED THICKNESS	PULSE-ECHO TECHNIQUE	LAMB WAVE TECHNIQUE	
1.98 mm	1.94 ±0.07	-	
0.90 mm	0.97 ± 0.07	-	
425 µm	468 ± 70	300	
102 µm	80 ± 9	89.5	
80 µm	-	72	± 2%
49 µm	-	44	
27 µm	-	26.5	

Table (7.1) Comparison of the mechanically measured and ultrasonically estimated aluminium plate thicknesses.

7.5 Conclusion

The pulse-echo technique has provided accurate thickness gauging on samples of 0.5 mm thick and greater. Difficulties arise for thinner samples due to the limited temporal resolution attainable with the 50 ns duration Nd:YAG laser pulses.

Laser generation and interferometric detection of Lamb waves has been studied in aluminium plates of different thickness. It has been shown that the thickness of thin metal sheet can be estimated from analysis of a single dispersive Lamb waveform. Preliminary studies have shown that an accuracy of better than 2% is achieved, for sheets of less than 30 μm in thickness. The results suggest that the accuracy of the technique improves with decreasing plate thickness, as would be expected from the long wavelength approximation used.

One point of interest is that since the high frequency data are least likely to satisfy the condition implied by equation (7.15) that $\lambda >> d$, then extraction of signal from noise at the front end of the acoustic waveform is not required, nor desirable. The more reliable thickness estimate is obtained from the later arriving low frequency components, although eventually problems may be encountered with signal interference resulting from side or end wall acoustic reflections.

7.6 References

A. M. Aindow, R. J. Dewhurst and S. B. Palmer, Opt. Comm. 42 116 (1982).

J. N. Brune, J. Nafe and J. Oliver, J. Geophys. Res. 65 287 (1960).

G. W. Farnell, in "Acoustic Surface Waves" (Edited by A. A. Oliner, Springer-Verlag, Berlin) p. 23 (1978).

J. Krautkramer and H. Krautkramer, in "Ultrasonic Testing of Materials" (Springer-Verlag, Berlin) 3rd Edition, p. 197 (1983).

H. Lamb, Proc. Roy. Soc. Lond. A90 114 (1916).

W. L. Pilant, in "Elastic Waves in the Earth" (Elsevier Scientific Publishing Company, Amsterdam) p. 246 (1979).

Lord Rayleigh, Proc. Lond. Math. Soc. 20 225 (1889).

W. R. Reynolds and R. L. Smith, J. Phys. D. 17 109 (1984).

H. Sontag and A. C. Tam, Appl. Phys. Lett. 46 725 (1985).

A. C. Tam, Appl. Phys. Lett. 45 510 (1984).

I. A. Viktorov, in "Rayleigh and Lamb Waves" (Plenum Press, New York, 1967).

D. C. Worlton, J. Appl. Phys. 32 967 (1961).

CHAPTER 8

Summary and Future Work

Historically, piezoelectric transducers have been relied upon for the generation and detection of ultrasound. However, as was described in chapter 2, these devices have some serious limitations when repeatable, quantitative data is required, or even for qualitative data from materials at elevated temperatures and in other hostile environments. The possiblities offered by the use of laser generation and detection of ultrasound is therefore of great practical importance.

The laser technique is capable of generating ultrasonic transients of wide bandwidths, limited only by the generating laser pulse risetime. The distribution of energy into longitudinal, shear, and surface acoustic modes can be altered simply by varying the laser spot diameter or incident laser energy. In the case of Rayleigh waves, the generating laser beam can be readily focussed to a point to give an omnidirectional source of Rayleigh waves, or a line if a directional beam is required. Additionally, longitudinal, shear and Rayleigh waves are all generated from the same source.

For non-contact detection of ultrasound, many interferometers have been developed for possible applications in the field of nondestructive evaluation as discussed in chapter 2. Of these interferometers, a variation of the Michelson design has been developed for the work of this thesis which incorporated versatility and high sensitivity. In chapter 3, the design and operating principles of the stabilised Michelson interferometer was described. The inherent disadvantage of the device was that its high sensitivity of operation required a significant

proportion of the laser light incident on the sample, to be back scattered into the receiving optics, necessitating the use of polished surfaces. However, for the purpose of investigating ultrasonic phenomena in the laboratory, the interferometer has proved invaluable. It was shown both theoretically and experimentally that for interference with multi-mode lasers, high fringe visibility can be achieved for the zero path length condition, and in addition, at path length differences equal to an integer multiple of twice the laser cavity length. Furthermore the effects of laser relaxation oscillations and intermode beating have been reduced with the use of a balanced photodetection system. These two results eliminate the need for an expensive stabilised single frequency laser. Further studies would benefit from the development of a photodetection system based on avalanche photodiodes to further increase the sensitivity and bandwidth of the interferometer.

Interferometric studies of laser generated bulk and surface waves in the thermoelastic and plasma regimes were shown to be in agreement with wave propagation theory in chapter 4. The absolute calibration of the interferometer and a capacitance transducer have been shown to be in excellent agreement. A comparison of the interferometer with a capacitance transducer, EMATs and a piezoelctric transducer was undertaken. As expected the piezoelectric transducer had the highest sensitivity, but it was shown that the non-contacting and wideband operation of the interferometer would in some situations be advantageous. Although the EMATs performed worst in the series of experiments, their operation on rough surfaces combined with a portable laser fibre-optic delivery system may prove to be a viable system for materials inspection.

In chapter 5, the interaction of laser generated Rayleigh pulses with surface breaking slots was examined. It has been shown that slot depths

of 5 mm and less, having widths of less than 0.3 mm, can be accurately estimated from laser generation in the thermoelastic and plasma regimes on duraluminium and mild steel samples. This study has brought together both experimental and numerical model data generated for identical configurations. The resulting data comparison has been in good agreement, and has provided an improved understanding of the various Rayleigh wave interactions with surface breaking slots. Possibilities for further work include the development of a computer controlled scanning mirror for rapid material inspection, with a view to imaging both surface and bulk defects.

The inspection of materials at elevated temperatures is assuming increasing importance as a means of ensuring high quality products, with a good yield. Various attempts to overcome the problems associated with ultrasonic generation and detection at elevated temperatures have been reviewed in chapter 6. A non-contact study using lasers has evaluated the variation in longitudinal velocity with temperature in duraluminium, aluminium, iron, stainless steel and graphite. For duraluminium and iron additional results were presented for the shear wave velocity. Measurements at temperatures of up to $\sim$ 1000 ^{0}C were performed on both iron and stainless steel. The surfaces of the samples were slightly damaged through repetitive ablation of material at the same spot during ultrasonic generation. This was more severe than would be experienced in measurements during operational applications where only one laser shot would occur at a particular point. It would seem feasible in future work, to measure the frequency dependence of attenuation and its variation with temperature, due to the broadband nature of both source and receiver.

The thickness of thin aluminium sheets has been estimated by pulse-echo and Lamb wave techniques. It has been shown that for accurate

thickness measurements of thin materials, < 0.5 mm, using a pulse-echo technique, high temporal resolution is required. The use of picosecond pulses would greatly decrease the thickness of material that could accurately be measured, provided the acoustic sensor had an equally fast response.

Thickness estimates using Lamb waves have shown an accuracy of better than 2% for sheets of 30 μm thickness and less. A more rigorous theoretical plate wave analysis is required which includes additional terms in the hyperbolic tangent expansion. This will increase the validity of equation (7.15) for the case of thicker plates.

Ultrasonics is, at present, a subject of active academic study. The combination of laser source and laser detector has been used to confirm and extend existing wave propagation theory. A disadvantage of laser systems presently used in the laboratory is their lack of portability, which precludes their use in the field. Recent work by Dewhurst (1983) has shown that a portable battery operated Nd:YAG laser may be developed for use in such applications. However, the link between academic studies and the development of industrial non-contacting laser nondestructive evaluation techniques is still rather weak, mainly due to the lack of convenient and portable optical sensing systems. However, with the continuing development of sensitive optical devices that will operate on rough surfaces, the role of optical sensing of ultrasound may soon play an important role in industrial nondestructive evaluation.

8.1 References

R. J. Dewhurst, NDT Commun. 1 93 (1983).

Appendices

Appendix 1

The program given below was written in Tektronix basic, and runs on a Tektronix MS4101 computer system. The program was used to graph fig. (4.6b) for the surface displacement observed in the plasma regime on epicentre, for the application at the surface of a Heaviside force loading. The program uses the equations derived by Knopoff in 1958.

```
10 CLEAR
20 Z1 = 0
30 PRINT "Input the longitudinal velocity in m/s"\INPUT PV
40 PRINT "Input the shear velocity in m/s"\INPUT SV
50 PRINT "Input the sample thickness in mm"\INPUT Z\Z = Z/1000
60 PRINT "Input the time period of interest in μs"\INPUT TP\TP = TP*10^-6
70 DIM I1(511),I2(511),I3(511)
80 PAGE
90 WAVEFORM WI IS I1,DS,H$,V$
100 FOR T = 0 TO TP STEP TP/512
110 DS = TP/512
120 Y = SV*T/Z\W = PV*T/Z
130 IF T <= Z/PV THEN HP = 0\IF T >Z/PV THEN HP = 1
140 IF T <= Z/SV THEN HS = 0\IF T >Z/SV THEN HS = 1
150 IF T <= 3*Z/PV THEN HR = 0\IF T >3*Z/PV THEN HR =1
160 A = SV/PV
170 D0 = (Y^2 - 1)
180 W2 = W^2
190 V = W/3
200 D1 = ((2*W2) - 2 + (1/A^2))
```

```
210 D2 = SQR(W2 - 1 + (1/A^2))*(W2 - 1)*4*W
220 D3 = (Y^2 + A^2 -1)
230 D4 = (2*Y^2-1)
240 D5 = (D4^2) - (4*Y*D0*SQR(D3))
250 D6 = (2*V^2 - 2 + (1/A^2))
260 D7 = (V^2-1)
270 D8 = SQR(V^2 - 1 + 1/A^2))
280 N1 = (W2*D1^2*1/A^2*HP)
290 N2 = (D1^2 - D2)
300 N3 = 4*Y^2*D0*D3*HS
310 N4 = (D4^2 - 4*Y*D0*SQR(3))
320 N5 = (D6^2 + 4*V*D7*D8)
330 N6 = 1/3*V^2*D6*1/A^4*HR
340 N7 = D6^2 - 4*V*D7*D8
350 U1 = N1/N2^2
360 U2 = N3/N4^2
370 U3 = (N5^2*N6)/N7^4
380 I1(Z1) = U1 - U2 + U3
390 Z1 = Z1 + 1
400 NEXT T
410 SETGR GRAT 3,3,1,1
420 PAGE
430 GRAPH WI
440 END
```

Appendix 2

The program given below was written in Tektronix basic, to run on a Tektronix MS4101 computer system. The program was used to graph fig. (4.10) for the displacement at the surface of a half space produced by the application at the surface of a normal point loading, having a Heaviside time dependence. The program uses the equations derived by Pekeris (1955).

```
10 Rem Calculate surface displacement from Pekeris (1955)
20 CLEAR
30 PAGE
40 DIM U(511)
50 PRINT "Input the shear velocity in m/s"\INPUT SH
60 PRINT "Input the source to detector separation in mm"\INPUT R\R = R/1000
70 PRINT "Input the time period of interest in μs"\INPUT TP\TP = TP*10^-6
80 PAGE
90 Z = 0
100 WAVEFORM WU IS U,D1,H$,V$
110 FOR T1 = 0 TO TP STEP TP/512
120 T = T1*SH/R
130 D1 = TP/512
140 IF T <=1/SQR(3) THEN GOTO 160
150 IF T > 1/SQR(3) THEN GOTO 170
160 U(Z) = 0\GOTO 300
170 IF T <= 1 THEN GOTO 190
180 IF T > 1 THEN GOTO 240
190 A = SQR(3)/SQR(T^2 - 0.25)
200 B = SQR(3*SQR(3) + 5)/SQR(0.75 + 0.25*SQR(3) - T^2)
210 C = SQR(3*SQR(3) - 5)/SQR(T^2 + 0.25*SQR(3) - 0.75)
```

```
220 U(Z) = -1/32*(6 - A - B + C)
230 GOTO 300
240 IF T <= 0.5*SQR(3 + SQR(3)) THEN GOTO 260
250 IF T > 0.5*SQR(3 + SQR(3) THEN GOTO 290
260 N = SQR(3*SQR(3) + 5)\D = SQR(0.75 + 0.25*(SQR(3)) - T^2)
270 U(Z) = -1/16*(6 - N/D)
280 GOTO 300
290 U(Z) = -3/8
300 Z = Z +1
310 NEXT T1
320 PAGE
330 SETGR GRAT 3,3,1,1
340 GRAPH WU
350 END
```

Appendix 3

Rayleigh Wave Interactions with 90° and 270° corners

The theoretical and experimental study of Rayleigh wave scattering at surface irregularities is one of the classic problems in the theory of elastic waves. The transmission and reflection of Rayleigh waves at vertical discontinuities is of fundamental importance to seismologists investigating the earth's crust (Mal and Knopoff, 1965), and interest has developed in the use of grooves as reflecting elements in surface acoustic wave filters (Williamson and Smith, 1973). More recently, the use of Rayleigh waves as a means of nondestructively evaluating the depth of surface breaking slots has been demonstrated by Cooper et. al. (1986). Up to present, the subject of Rayleigh wave interactions with discontinuities has been discussed extensively in the literature. In 1961, Lapwood theoretically considered the problem of Rayleigh waves transmitted around a 90° corner, and transmission and reflection of Rayleigh waves at a corner of a wedge was investigated by Hudson and Knopoff (1964) including the cases of wedges with 90° and 270° corners.

Experimental reflection and transmission coefficients of Rayleigh waves for various configurations have been investigated by de Bremaecker (1958), Pilant et. al. (1964) and Knopoff and Gangi (1960) by employing piezoelectric transducers. Some appreciable differences exist in the values reported for the theoretical and experimental results. The discrepancies between some calculated values and measured ones would appear to result mainly from over simplification of the boundary conditions in some of the theoretical analyses (Fujii et. al., 1984). In addition, the wide range of materials used in these investigations with their differing values of Poisson's ratio has contributed to the difficulty of comparing results.

Table (A3.1) shows some values for the reflection and transmission coefficients at a 90° corner calculated by different authors, with table (A3.2) showing the same for a 270° corner. Gautesen (1985) has shown that the value for the transmission coefficient at a 90° corner is approximately independent of Poisson's ratio as borne out by the majority of results in table (A3.1).

Reference	Poisson's ratio	Reflection coefficient	Transmission coefficient
de Bremaecker (1958)	0.17	0.38	0.63
Pilant et. al. (1964)	0.25	0.252	0.670
Gautesen (1985)	0.25	0.32	0.68
Munasinghe et. al. (1973a)	0.245	0.36	0.64
Bond (1979)	0.24	0.43	0.57
Viktorov (1962)	0.34	0.60	0.70
Cuozzo et. al. (1977)	0.34	0.42	0.72
Bond (1979)	0.34	0.47	0.59
Achenbach et. al. (1980)	0.33	0.40	0.60
Jungerman et. al. (1983)	0.34	0.40	-
Gautesen (1985)	0.33	0.39	0.67
From this thesis	0.34	0.40	0.55

Table (A3.1) Summary of results obtained for Rayleigh wave reflection and transmission coefficients at a 90° corner.

Reference	Poisson's ratio	Reflection coefficient	Transmission coefficient
Mal. et. al. (1965)	0.25	-	0.25
Munasinghe et. al. (1973b)	0.245	0.09	0.28
Knopoff et. al. (1960)	0.25	-	0.28
Georgiou et. al. (1987)	0.29	-	0.27
Cuozzo et. al. (1977)	0.34	0.15	0.13
Bond (1978)	0.34	0.11	0.23
From this thesis	0.33	0.09	0.17

Table (A3.2) Summary of results obtained for Rayleigh wave reflection and transmission coefficients at a 270° corner.

A noncontacting optical measurement of the Rayleigh wave reflection coefficient can be made by positioning the laser interferometer spot in the near field of a discontinuity, and in between the discontinuity and the laser source. Since the detector is a laser spot, no correction is required for attenuation when the incident Rayleigh pulse passes through the surface under the interferometer spot, before it strikes the discontinuity. Also, since the measurement can be made close to the discontinuity, diffraction and attenuation corrections to the reflection coefficient are not significant (Jungerman et. al., 1983).

The Rayleigh wave reflection and transmission coefficients at 90° and 270° corners, assumed to be frequency independent (Bond ,1986), have been estimated by dividing the peak to peak amplitude of the reflected (or transmitted) Rayleigh pulse by that of the incident Rayleigh pulse. The waveform of fig. (A3.1) has been used to determine the reflection coefficient at a 90° corner with the interferometer situated ~ 1.5 mm from the corner. The experimentally measured value was 0.40 ± 0.03. Using the first waveform in fig. (5.17b) (3 mm from corner) the transmission coefficient at a 90° corner has been calculated as 0.55 ± 0.03. From analysis of figs. (5.18b) and (5.20b) the transmission coefficient at a 270° corner has been evaluated as 0.17 ± 0.05, with the reflection coefficient evaluated from fig. (5.19b) as being 0.09 ± 0.05. A finite difference method has been used by Bond (1978) to model the interaction of pulsed Rayleigh waves with sharp 90° and 270° corners in aluminium. This author evaluated the reflection and transmission coefficients at a 90° corner as 0.47 ± 0.05 and 0.59 ± 0.05 respectively, and those for a 270° corner as 0.11 ± 0.03 and 0.23 ± 0.03 respectively. The experimentally estimated values for both the reflection and transmission coefficient are in agreement with those of Bond (1978) within the limits of experimental error.

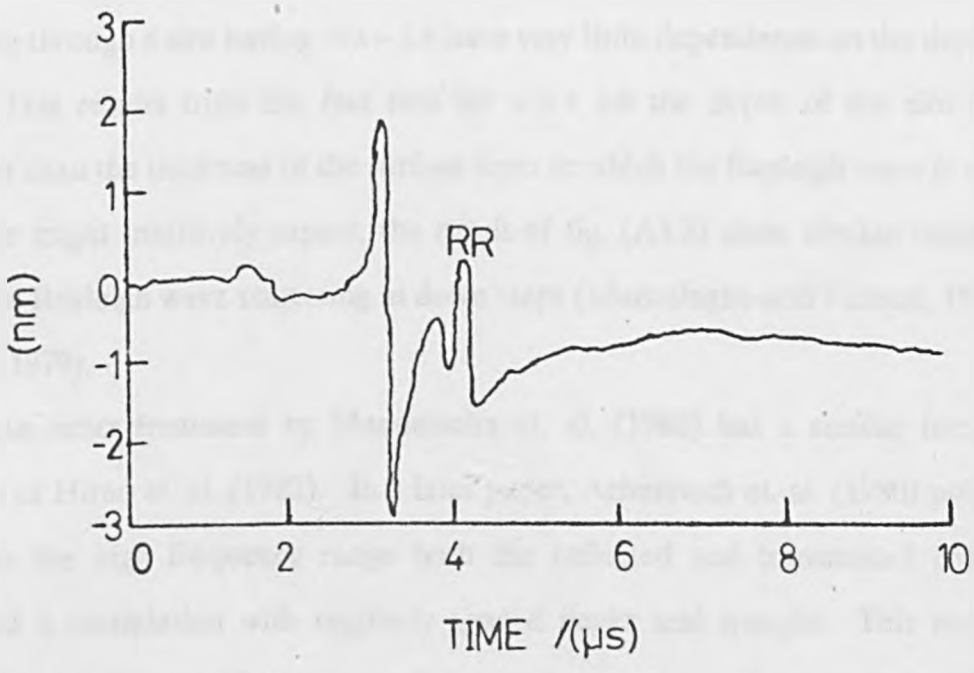

Fig. (A3.1) Waveform showing the reflected Rayleigh pulse (RR) from a 90° corner.

Rayleigh Wave Interactions with Surface Breaking Slots

Viktorov (1958) studied the interaction of Rayleigh waves with a surface breaking slot in duraluminium. Both his reflection and transmission data are in good agreement with values obtained by Hirao et. al. (1982) using a finite difference method. The calculated reflection and transmitted coefficients versus the slot depth measured in units of wavelength, are shown in fig. (A3.2) (Hirao et. al., 1982). The curves show that both the reflection and transmission coefficients for a Rayleigh wave passing through a slot having $d/\lambda > 1.6$ have very little dependence on the depth of the slot. This results from the fact that for $d/\lambda > 1.6$ the depth of the slot becomes greater than the thickness of the surface layer to which the Rayleigh wave is confined. As one might intuitively expect, the result of fig. (A3.2) show similar behaviour to that for Rayleigh wave scattering at down steps (Munasinghe and Farnell, 1973a, and Bond, 1979).

An exact treatment by Mendelsohn et. al. (1980) has a similar form to the results of Hirao et. al. (1982). In a later paper, Achenbach et. al. (1980) pointed out that in the high frequency range both the reflected and transmitted coefficients showed a modulation with regularly spaced peaks and troughs. This modulation indicates a resonance phenomenon due to surface motions of the crack faces, and the same authors show that for $d/\lambda > 1$ the crack depth may be estimated.

From results presented in chapter 5, fig. (A3.3) shows the Rayleigh wave reflection coefficients, and fig. (A3.4) shows the Rayleigh wave transmission coefficients as a function of d/λ, and evaluated for a Rayleigh pulse interacting with a slot of depth 0.50 mm. These figures were calculated by dividing the reflected (or transmitted) frequency spectra of fig. (5.11) with the incident frequency spectra. Also shown in figs. (A3.3) and (A3.4) are the theoretical curves predicted by Hirao et. al. (1982). Some of the experimental points have large percentage errors.

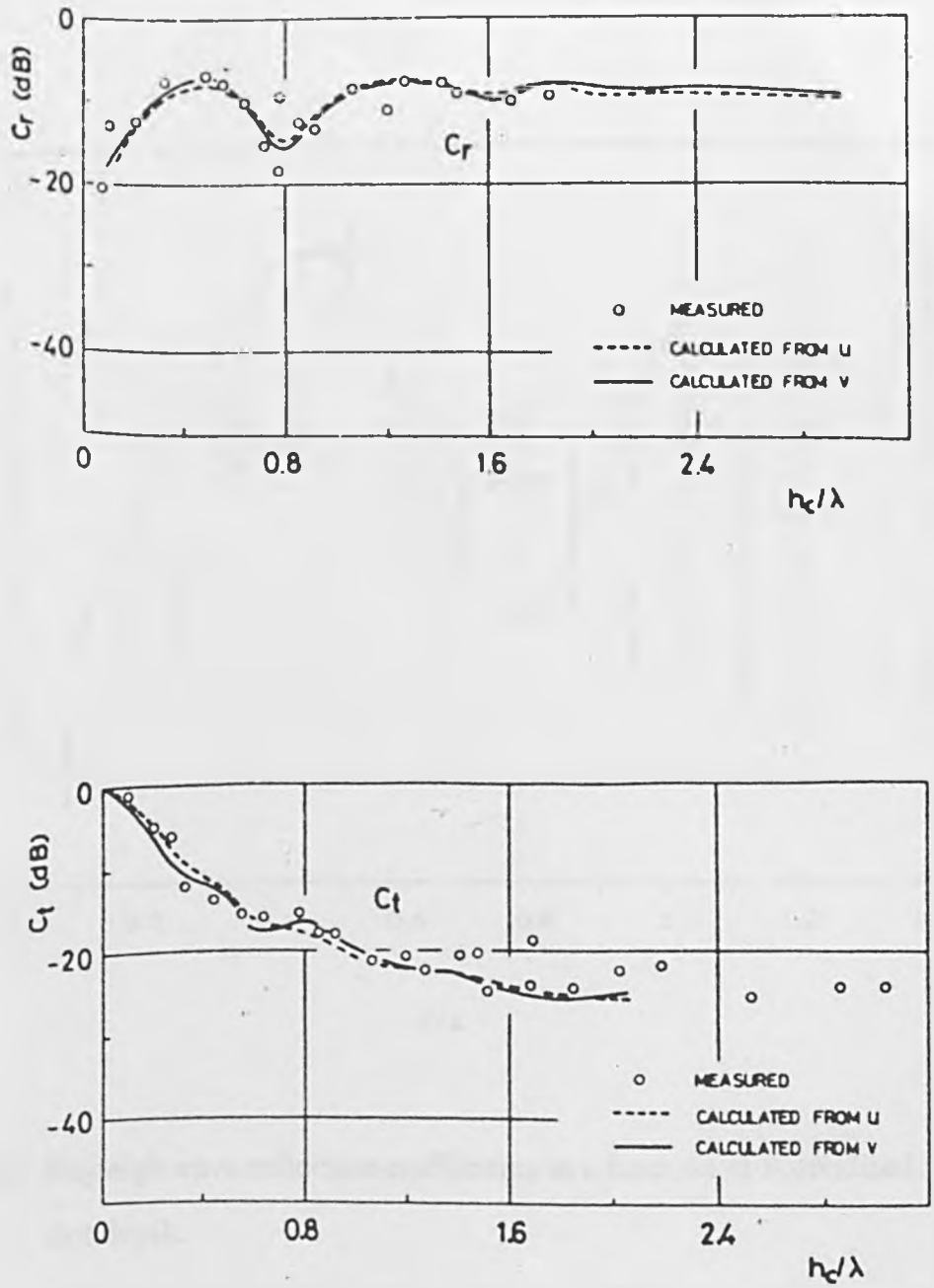

Fig. (A3.2) Rayleigh wave reflection and transmission coefficients as a function of normalised slot depth (after Hirao et. al., 1982).

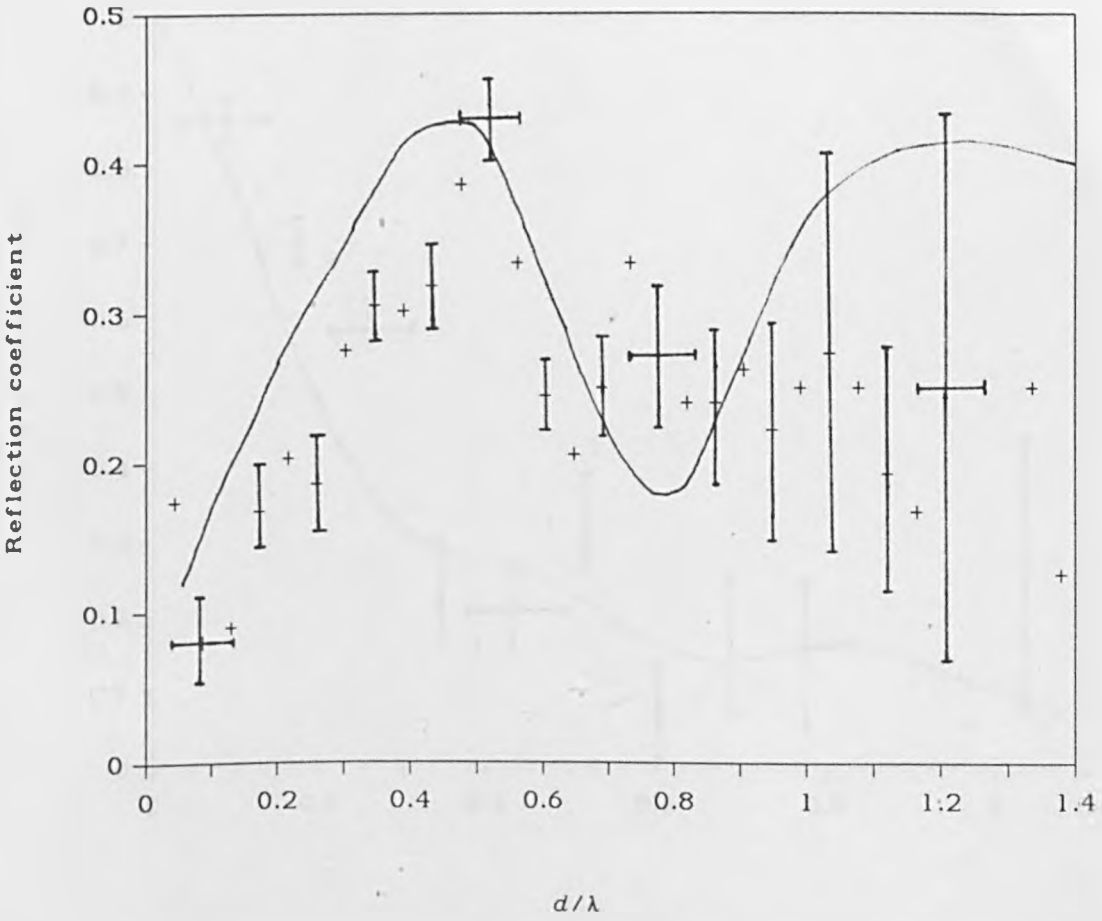

Fig. (A3.3) Rayleigh wave reflection coefficients as a function of normalised slot depth.

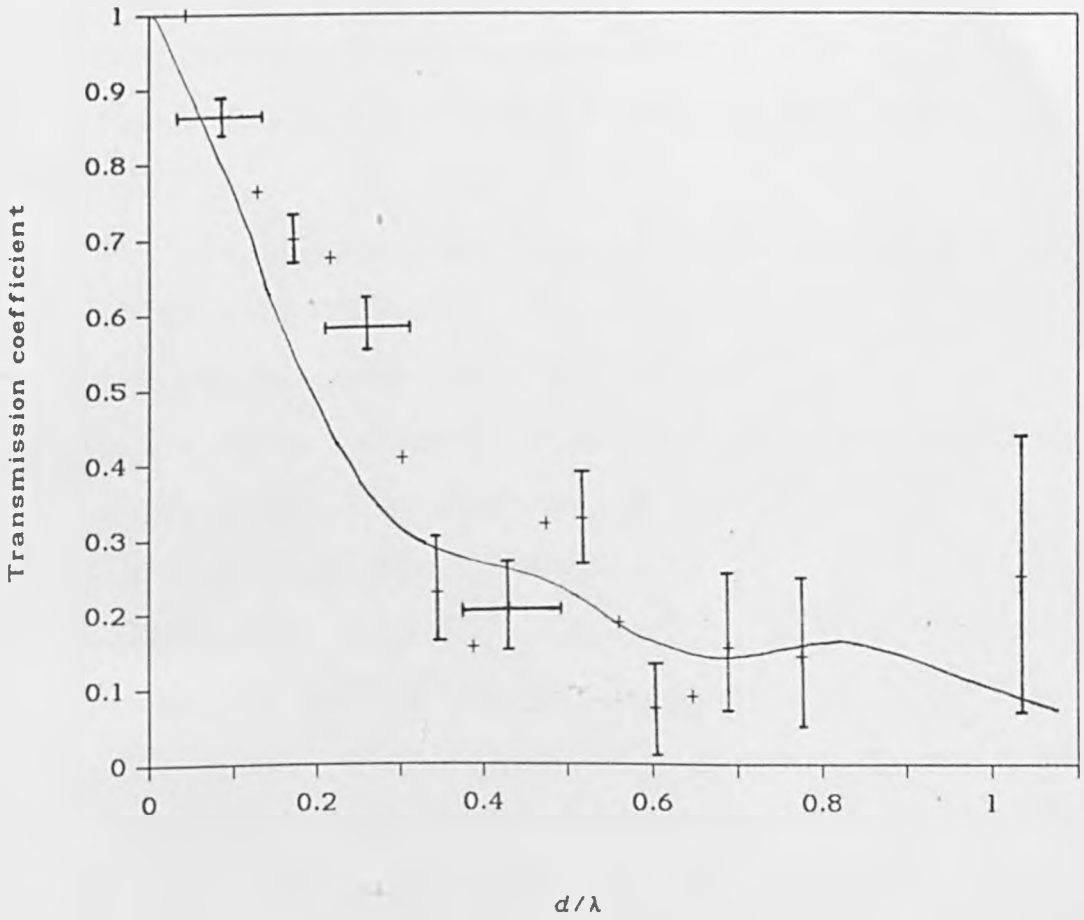

Fig. (A3.4) Rayleigh wave transmission coefficients as a function of normalised slot depth.

Nevertheless, it can be concluded that the experimental points are not in disagreement with the theoretical predictions for both the reflection and transmission coefficients.

References

J. D. Achenbach, A. K. Gautesen and D. A. Mendelsohn, IEEE Tans. Son. and Ultrason. SU-27 124 (1980).

L. J. Bond, Ph.D thesis (The City University, London, UK, 1978).

L. J. Bond, Ultrasonics 17 71 (1979).

L. J. Bond, in discussion after Cooper et. al. (1986).

J. A. Cooper, R. J. Dewhurst and S. B. Palmer, Phil. Trans. Roy. Soc. Lond. A 320 319 (1986).

F. C. Cuozzo, E. L. Cambiaggio, J. P. Damiano and E. Rivier, IEEE Trans. Son. and Ultrason. SU-24 280 (1977).

J. C. de Bremaecker, Geophysics 23 258 (1958).

K. Fujii, S. Takeuchi, Y. Okano and M. Nakano, Bull. Seism. Soc. Am. 74 41 (1984).

G. A. Georgiou and L. J. Bond, Ultrasonics 25 328 (1987).

A. K. Gautesen, J. Appl. Mech. 52 664 (1985).

M. Hirao, H. Fukuoka and Y. Miura, J. Acoust. Soc. Am. 72 602 (1982).

J. A. Hudson and L. Knopoff, J. Geophys. Res. 69 281 (1964).

R. L. Jungerman, B. T. Khuri-Yakub and G. S. Kino, in "Review of Progress in Quantitative Nondestructive Evaluation" 3B 791 (1983).

L. Knopoff and A. F. Gangi, Geophysics 25 1203 (1960).

E. R. Lapwood, Geophys. J. Roy. Astr. Soc. 4 174 (1961).

A. K. Mal and L. Knopoff, Bull. Seism. Soc. Am. 55 319 (1965).

D. A. Mendelsohn, J. D. Achenbach and L. M. Keer, Wave Motion 2 277 (1980).

M. Munasinghe and G. W. Farnell, J. Geophys. Res. 78 2454 (1973a).

M. Munasinghe and G. W. Farnell, J. Appl. Phys. 44 2025 (1973b).

W. L. Pilant, L. Knopoff and F. Schwab, J. Geophys. Res. 69 291 (1964).

R. C. Williamson and H. I. Smith, IEEE Trans. Micro. Theory Tech. MTT-21 195 (1973).

I. A. Viktorov, Sov. Phys. Acoust. 8 119 (1962).

I. A. Viktorov, Sov. Phys. Doklady 3 304 (1958).